Study of Non-Standard Neutrino Interactions with Atmospheric Neutrino Data in Super-Kamiokande

Gaku Mitsuka

February 9, 2009

Abstract

The atmospheric neutrino data show the apparent deficit in upward-going ν_μ events, which was called as the atmospheric neutrino problem. They have been well explained by the 2-flavor $\nu_\mu \leftrightarrow \nu_\tau$ oscillation scheme and also the Δm_{23}^2 and $\sin^2 2\theta_{23}$ parameters have been measured. Neutrino oscillations in atmospheric neutrinos play a very important role in particle physics because they present the clear evidence for physics beyond the standard model.

In addition to neutrino oscillations, a lot of attempts have been proposed to account for the atmospheric neutrino problem. Considering that atmospheric neutrino data are well fitted by neutrino oscillations, the contribution of the other models would be at most sub-dominant. In this thesis, we focus on the additional neutrino interactions with matter, which are forbidden in the standard model. The phenomena driven by such interactions in the Earth are assumed to be dependent on the matter density and independent of the energy of neutrinos. We call them non-standard neutrino interactions.

Our goals are, first, to measure the dominance of standard neutrino oscillations compared to the possible presence of non-standard interactions, and next, to search for the signal of non-standard interactions using large number of atmospheric neutrino data in Super-Kamiokande. The analysis is performed with the two schemes: (1) Standard 2-flavor $\nu_\mu \leftrightarrow \nu_\tau$ oscillation with non-standard neutrino interactions in the $\nu_\mu - \nu_\tau$ sector, and (2) Standard 2-flavor $\nu_\mu \leftrightarrow \nu_\tau$ oscillation with non-standard neutrino interactions in the $\nu_e - \nu_\tau$ sector. Scheme (1) assume that the flavor transition is only occurred between ν_μ and ν_τ, whereas ν_e flux is kept as is. To the contrary, scheme (2) allows the flavor transition with all flavored neutrinos. The effects of non-standard neutrino interactions have never been evaluated simultaneously with neutrino oscillations in the neutrino oscillation experiments. Then this analysis is the first experimental approach to investigate their effects.

Our approach requires more accurate analysis than that with only neutrino oscillations, since our interests would exist as sub-dominant effects. Not only improved atmospheric neutrino flux model and neutrino interaction theories are employed in the simulation, but also the absolute energy scale is precisely examined using various calibration sources. Furthermore, the systematic uncertainties are carefully inspected to investigate the possible signal of non-standard neutrino interactions.

As a result of the analyses with the atmospheric neutrino data from the Super-Kamiokande-I (1996-2001) and Super-Kamiokande-II (2003-2005), no significant signal of non-standard neutrino interactions has been observed and the limits on parameters for non-standard neutrino interactions have been obtained.

Acknowledgments

Contents

Chapter 1

Introduction

This thesis aims to evaluate the dominance of the solution with pure neutrino oscillations in the atmospheric neutrino data against the possible presence of non-standard neutrino interactions. Also we purpose to investigate the signal of non-standard neutrino interactions. First we explain the feature of atmospheric neutrinos which work as the probe in this thesis. In Chapter 1.2 neutrino oscillations in atmospheric neutrinos are discussed. Non-standard neutrino interactions are introduced in Chapter 1.3. At the end of this chapter, our motivations and goals are presented.

1.1 Atmospheric Neutrinos

When primary cosmic rays interact with nuclei in the atmosphere of the Earth, secondary particles, mostly pions and some kaons, are produced in hadronic showers. Atmospheric neutrinos are produced from the decay of those secondary particles, dominantly by the following decay chains of pions :

$$
\begin{aligned}
\pi^+ &\rightarrow \mu^+ + \nu_\mu \\
& \hookrightarrow e^+ + \nu_e + \overline{\nu}_\mu
\end{aligned}
\tag{1.1}
$$

$$
\begin{aligned}
\pi^- &\rightarrow \mu^- + \overline{\nu}_\mu \\
& \hookrightarrow e^- + \overline{\nu}_e + \nu_\mu
\end{aligned}
\tag{1.2}
$$

Two muon neutrinos and one electron neutrino are generated by the decay of a charged pion. Therefore, the flux ratio $(\nu_\mu + \overline{\nu}_\mu)/(\nu_e + \overline{\nu}_e)$ is expected to be two for relatively low energy neutrinos. For high energy neutrinos above a few GeV, this flux ratio becomes greater than two because high energy muons reach the ground without decay and the number of electron neutrinos decreases. In Figure 1.1, the left-hand figure shows the flux ratio, $(\nu_\mu + \overline{\nu}_\mu)/(\nu_e + \overline{\nu}_e)$, as a function of the neutrino energy, which is calculated by M. Honda *et al.* [1, 2, 3].

Since the primary cosmic rays isotropically pour on the Earth and the Earth has a spherical form, the atmospheric neutrino flux is expected to be up-down symmetric. In Figure 1.1, two figures on the right panel show the neutrino flux as a function of the zenith angle of neutrino arrival direction where $\cos \Theta = -1$ ($\cos \Theta = +1$) indicates upward-going (downward-going) directions. The flux of low energy neutrinos is affected by the rigidity (=momentum/charge)
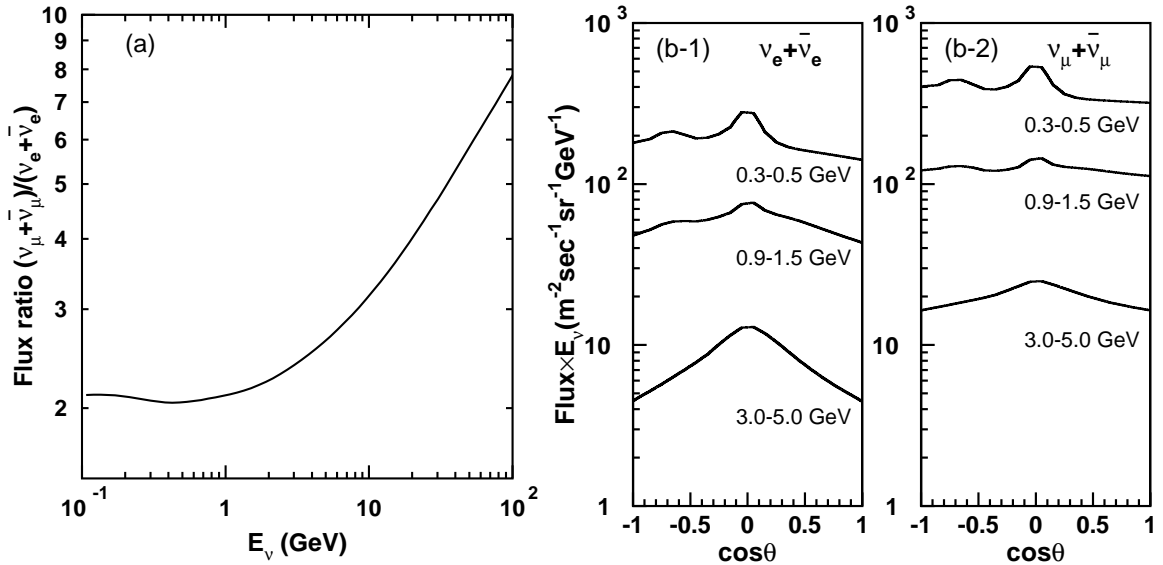
Figure 1.1: Flux ratio of $\nu_\mu + \overline{\nu}_\mu$ to $\nu_e + \overline{\nu}_e$ as a function of the neutrino energy (a), and the zenith angle dependence of atmospheric neutrino for $\nu_e + \overline{\nu}_e$ (b-1) and $\nu_\mu + \overline{\nu}_\mu$ (b-2). The flux is calculated by M. Honda *et al.* [1, 2, 3].

cutoff of the primary cosmic rays due to the geomagnetic field. Since the geomagnetic field around Super-Kamiokande is stronger than the average, the up-down symmetry is broken in low energy neutrinos. For energies above a few GeV, the geomagnetic effect is negligible. The flight length of atmospheric neutrinos ranges from $\sim 15\,\mathrm{km}$ to $\sim 13000\,\mathrm{km}$ depending on the zenith angle of the arrival direction.

The detailed explanation about the expectation of the atmospheric neutrino flux is described in Chapter 3.2.

1.2   Neutrino Oscillations in Atmospheric Neutrinos

The expected total flux of atmospheric neutrinos has $\sim 10\,\%$ uncertainty which mostly comes from the uncertainties on cross sections of hadronic interactions and on fluxes of primary cosmic ray components [2]. However, the flux ratio $(\nu_\mu + \overline{\nu}_\mu)/(\nu_e + \overline{\nu}_e)$ can be predicted more accurately with only $3\,\%$ uncertainty thanks to the cancellation of each error. This ratio has been measured by several underground experiments and reported in the style of a double ratio $R \equiv (N_\mu/N_e)_{Data}/(N_\mu/N_e)_{MC}$, where N_μ (N_e) is the number of muon (electron) events produced by charged current interactions.

The double ratio R obtained by underground Cherenkov detectors, Kamiokande [4, 5, 6] and IMB [7, 8] and an iron calorimeter detector Soudan 2 [9] was significantly lower than 1. This was called as the *atmospheric neutrino problem*. Also it was known that the smallness of R was caused by the observed zenith angle dependent deficit of ν_μ and $\overline{\nu}_\mu$. MACRO [10], Kamiokande [12] and Super-Kamiokande [11] have studied the upward-going muons produced by energetic ν_μ charged current neutrino interactions in the rock surrounding the detector and their data are consistent with the 2-flavor $\nu_\mu \leftrightarrow \nu_\tau$ oscillation.

Neutrino oscillation hypothesis is described as follows: In the standard model of elementary particles, neutrinos are regarded as exactly massless particles [13, 14, 15]. However, there is no fundamental reason to forbid the finite masses of neutrinos. Neutrino oscillation has been proposed by Maki, Nakagawa and Sakata in 1962 as a consequence of the finite masses of neutrinos [16].

If neutrinos have finite masses, their flavor eigenstates can be written as the superpositions of the mass eigenstates as follows :

$$|\nu_\alpha\rangle = \sum_{i=1}^{3} U_{\alpha i}|\nu_i\rangle, \tag{1.3}$$

where $|\nu_\alpha\rangle$ represents the flavor eigenstates ν_e, ν_μ and ν_τ and $|\nu_i\rangle$ represents the mass eigenstates ν_1, ν_2 and ν_3. $U_{\alpha i}$ is a 3×3 unitary mixing matrix known as the MNS matrix. The mixing matrix U can be written as a product of three rotation matrices using the mixing angle θ_{12}, θ_{23} and θ_{13} for each flavor and a CP-violating phase δ as follows :

$$\mathrm{U} = \begin{pmatrix} 1 & 0 & 0 \\ 0 & c_{23} & s_{23} \\ 0 & -s_{23} & c_{23} \end{pmatrix} \begin{pmatrix} c_{13} & 0 & s_{13}e^{-i\delta} \\ 0 & 1 & 0 \\ -s_{13}e^{i\delta} & 0 & c_{13} \end{pmatrix} \begin{pmatrix} c_{12} & s_{12} & 0 \\ -s_{12} & c_{12} & 0 \\ 0 & 0 & 1 \end{pmatrix}, \tag{1.4}$$

where $c_{ij} \equiv \cos\theta_{ij}$, $s_{ij} \equiv \sin\theta_{ij}$. The time evolution of the flavor eigenstates is represented as :

$$|\nu_\alpha(t)\rangle = \sum_i U_{\alpha i} \exp(-iE_i t)|\nu_i(t=0)\rangle \tag{1.5}$$

$$= \sum_i \sum_{\alpha'} U_{\alpha i} U^*_{\alpha' i} \exp(-iE_i t)|\nu'_\alpha(t=0)\rangle, \tag{1.6}$$

where E_i is an eigenvalue of the mass eigenstate $|\nu_i\rangle$. Therefore the probability for flavor eigenstate ν_α at $t=0$ to change the state ν_β at time t, is calculated as :

$$P(\nu_\alpha \to \nu_\beta) = |\langle\nu_\beta(t)|\nu_\alpha(0)\rangle|^2 \tag{1.7}$$

$$= \left|\sum_i U_{\beta i} U^*_{\alpha i} \exp(-iE_i t)\right|^2 \tag{1.8}$$

$$= \sum_i |U_{\alpha i} U_{\beta i}|^2 + \sum_{i\neq j} U_{\alpha i} U^*_{\beta i} U^*_{\alpha j} U_{\beta j} \exp(-i(E_i - E_j)t). \tag{1.9}$$

Thus, due to the flavor mixing of massive neutrinos, the flavor transition phenomenon, neutrino oscillation could occur.

In the two-flavor mixing case, the mixing matrix U is simplified as follows :

$$\mathrm{U} = \begin{pmatrix} \cos\theta & \sin\theta \\ -\sin\theta & \cos\theta \end{pmatrix}. \tag{1.10}$$

The transition probability for $\nu_\alpha \to \nu_\beta$ (eq.(1.9)) is expressed in a simpler form :

$$P(\nu_\alpha \to \nu_\beta) = \sin^2 2\theta \sin^2\left(\frac{(E_i - E_j)t}{2}\right). \tag{1.11}$$

If neutrinos have finite masses, the following approximation can be used :

$$
\begin{aligned}
E_i - E_j &= \sqrt{m_i^2 + p_i^2} - \sqrt{m_j^2 + p_j^2} \\
&\simeq \left(p + \frac{m_i^2}{2p} \right) - \left(p + \frac{m_j^2}{2p} \right) \\
&\simeq \frac{\Delta m_{ij}^2}{2E},
\end{aligned}
\tag{1.12}
$$

where $\Delta m_{ij}^2 \equiv m_i^2 - m_j^2$ is the mass-squared difference of neutrino mass eigenstates. Finally using the neutrino flight length L_ν and the neutrino energy E_ν, the survival probability of ν_α in the two-flavor mixing case is written as follows :

$$
\begin{aligned}
P(\nu_\alpha \to \nu_\alpha) &= 1 - \sin^2 2\theta \sin^2 \left(\frac{\Delta m_{ij}^2 L_\nu}{4E_\nu} \right) \tag{1.13} \\
&= 1 - \sin^2 2\theta \sin^2 \left(\frac{1.27 \Delta m_{ij}^2 (\mathrm{eV}^2) L_\nu (\mathrm{km})}{E_\nu (\mathrm{GeV})} \right) \tag{1.14} \\
&= 1 - \sin^2 2\theta \sin^2 \left(\pi \frac{L_\nu}{l} \right), \tag{1.15}
\end{aligned}
$$

where $l \equiv 4\pi E_\nu / \Delta m_{ij}^2$ is the oscillation length. The oscillation probability is characterized by the mixing angle θ, the mass squared difference Δm_{ij}^2, the neutrino flight length L_ν and the neutrino energy E_ν. The oscillation amplitude is maximum when $L_\nu[\mathrm{km}]/\mathrm{E}_\nu[\mathrm{GeV}] = \pi/2.53 \cdot \Delta m_{ij}^2[\mathrm{eV}^2]$. Survival probability as a function of flight length of neutrino is demonstrated in Figure 1.2, where $\sin^2 2\theta = 1.0$ and $\Delta m^2 = 2.2 \times 10^{-3} \mathrm{eV}^{-2}$ are assumed.

In 1998, Super-Kamiokande reported that the zenith angle distributions of muon neutrino events were asymmetric and concluded that their measurement results gave an evidence for neutrino oscillation [17]. Super-Kamiokande also presented the observation of an oscillation signature with L/E dependence [18], which is well described by the hypothesis that ν_μ oscillates to ν_τ with a probability of the nearly maximal mixing. Since typical atmospheric neutrino experiments have the neutrino energies above several hundred MeV, the observation of atmospheric neutrinos is sensitive to Δm^2 down to $10^{-4} \mathrm{eV}^2$ according to the relation between L_ν, E_ν and Δm^2. Figure 1.3 summarize the recent measurements of the neutrino oscillation parameters, $\sin^2 2\theta$ and Δm_{23}^2, by the atmospheric and accelerator neutrino experiments.

1.3   Non-Standard Interactions in Atmospheric Neutrinos

In addition to neutrino oscillations, a lot of attempts have been proposed to explain the atmospheric neutrino problem [22]. Among many alternative models, we focus on the additional neutrino interactions where the neutrinos take part in the flavor changing and non universal processes in matter. Flavor changing neutral current (FCNC) represents the neutrino interactions with fermion f in matter, $\nu_\alpha + f \to \nu_\beta + f$. Figure 1.4 shows a possible diagram for FCNC off d-quark. Lepton non universality (NU) is defined as the difference in the amplitude of the neutral current scattering between ν_α and ν_β, which are exactly same under the standard model. These interactions are forbidden in the standard model, however the theories concerning
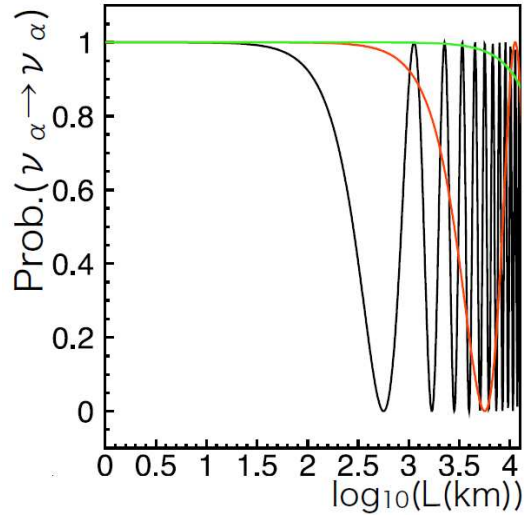
Figure 1.2: Survival probability of $\nu_\alpha \to \nu_\alpha$ as a function of flight length. Horizontal axis is the propagation length $\log_{10}(L_\nu(\mathrm{km}))$. (Black curve) E_ν=1GeV. (Red curve) E_ν=10GeV. (Green curve) E_ν=100GeV. $\sin^2 2\theta = 1.0$ and $\Delta m^2 = 2.2 \times 10^{-3}\mathrm{eV}^2$ are assumed.
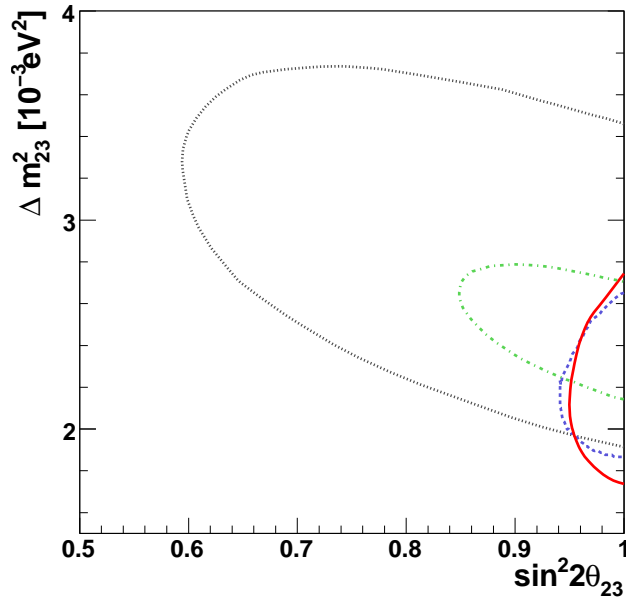
Figure 1.3: 90 % confidence level allowed regions of oscillation parameters for $\nu_\mu \leftrightarrow \nu_\tau$ oscillation. The horizontal axis shows $\sin^2 2\theta_{23}$ and the vertical axis shows Δm^2_{23}. The results are taken from Super-Kamiokande[19] (solid curve), SK L/E [19] (dashed curve), K2K experiment [20] (dotted curve) and MINOS experiment[21] (dash-dotted curve).
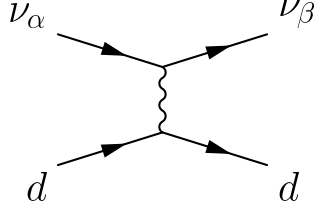
Figure 1.4:

about neutrino masses predict them, for example the case in which neutrino masses follow from the admixture of isosinglet neutral heavy leptons [23]. For simplicity, we call these interactions *non-standard neutrino interactions* (NSI) in the following text. Although NSI is predicted by these theories, the expected phenomena driven by NSI itself do not depend on any model except for the assumption that NSI is dependent on the density of matter, while is independent of the neutrino energy.

In the *standard model*, the weak interaction Hamiltonian is described as

$$H_W = \frac{G_F}{\sqrt{2}} \left(J_\mu^\dagger J_\mu + \rho J_\mu^{NC} J_\mu^{NC} \right) \tag{1.16}$$

where J_μ and J_μ^{NC} are the weak current. The part of eq.(1.16) relevant to $\nu_\alpha + f$ scattering is

$$
\begin{aligned}
H_W^{eff} &= \frac{G_F}{\sqrt{2}} \left[\bar{f}\gamma_\mu(1-\gamma_5)\nu_\alpha \right] \left[\bar{\nu}_\alpha \gamma^\mu(1-\gamma_5)f \right] \\
&+ \sqrt{2}G_F\rho \left[\bar{\nu}_\alpha \gamma_\mu \frac{1}{2}(1-\gamma_5)\nu_\alpha \right] \left[\bar{f}\gamma^\mu(g_V - g_A\gamma_5)f \right]
\end{aligned} \tag{1.17}
$$

where $g_V = g_L + g_R = -1/2 + 2\sin^2\theta_W$, $g_A = g_L - g_R = -1/2$ and $\rho = 1$. L, R are the left-handed and right-handed fermion, respectively. θ_W is the Weinberg angle.

After the Fierz transformation of the first term,

$$H_W^{eff} = \frac{G_F}{\sqrt{2}} \left[\bar{\nu}_\alpha \gamma_\mu(1-\gamma_5)\nu_\alpha \right] \left[\bar{f}\gamma^\mu(c_V - c_A\gamma_5)f \right] \tag{1.18}$$

where

$$
\begin{array}{ccc}
 & \alpha = f & \alpha \neq f \\
c_V = & g_V + 1 & g_V \\
c_A = & g_A + 1 & g_A
\end{array} \tag{1.19}
$$

When neutrinos propagate through matter, they are refracted due to the interaction with matter. In it, neutrinos receive the extra energy V. Using eq.(1.18), V for the fermion f is given as

$$V_{SM} = \sqrt{2}G_F c_V N_f \tag{1.20}$$

with the fermion density in matter N_f. Suppose the interaction in $\alpha \neq f$,

$$V_{SM} = \sqrt{2}G_F c_V N_f = \sqrt{2}G_F g_V N_f = \sqrt{2}G_F(g_L(f) + g_R(f))N_f \tag{1.21}$$

Now, we extend eq.(1.21) to the case in NSI. In this case, V is replaced with

$$V_{NSI} = \sqrt{2}G_F(\varepsilon_{\alpha\beta}^{fL} + \varepsilon_{\alpha\beta}^{fR})N_f \qquad (1.22)$$

where $\varepsilon_{\alpha\beta}^{fP}$ $(P = L, R)$ is the parameter to describe the strength of NSI. Note that NSI allow the flavor transition through the neutral current interaction such as $\nu_\alpha + f \rightarrow \nu_\beta + f$. As seen in eq.(1.22), NSI coupling parameter $\varepsilon_{\alpha\beta}^{fP}$ corresponds to the neutral current coupling $g_P(f)$ of the standard model. We cannot distinguish NSI to the left-handed and right-handed fermion in atmospheric neutrinos, so $\varepsilon_{\alpha\beta}^{fP}$ is replaced with $\varepsilon_{\alpha\beta}^f \equiv \varepsilon_{\alpha\beta}^{fL} + \varepsilon_{\alpha\beta}^{fR}$. Also, since we assume fermion f as d-quark in matter, hereafter we remove the superscript $f(= d)$ and use $\varepsilon_{\alpha\beta}$ for simplicity. Thus the effective potential induced by 2-flavor NSI in the $\nu_\alpha - \nu_\beta$ sector can be written as

$$H(r) = H_0 + V_{eff} \qquad (1.23)$$

$$= \begin{pmatrix} p & 0 \\ 0 & p \end{pmatrix} + \sqrt{2}G_F N_f(\vec{r}) \begin{pmatrix} \varepsilon_{\alpha\alpha} & \varepsilon_{\alpha\beta}^* \\ \varepsilon_{\alpha\beta} & \varepsilon_{\beta\beta} \end{pmatrix} \qquad (1.24)$$

where p is the neutrino momentum, G_F is the Fermi coupling constant, $\varepsilon_{\beta\beta} - \varepsilon_{\alpha\alpha}$ represents the difference in the amplitude of NC interaction between ν_α and ν_β, and $\varepsilon_{\alpha\beta}$ represents the amplitude of FCNC. $N_f(\vec{r})$ is the fermion (d-quark) density as a function of the position $\vec{r}$ along the neutrino path. The solution of the Schrödinger equation is written as:

$$|\psi(t)\rangle = \exp\left(-i\int_0^L H(r)dr\right)|\psi(0)\rangle \qquad (1.25)$$

where L is the flight length of neutrino. The integration is carried out along the neutrino path. The survival probability of ν_α is written as

$$P(\nu_\alpha \rightarrow \nu_\alpha) = 1 - \frac{\varepsilon_{\alpha\beta}^2}{\varepsilon_{\alpha\beta}^2 + (\varepsilon_{\beta\beta} - \varepsilon_{\alpha\alpha})^2/4}\sin^2\left(\sqrt{2}G_F X_f\sqrt{\varepsilon_{\alpha\beta}^2 + (\varepsilon_{\beta\beta} - \varepsilon_{\alpha\alpha})^2/4}\right) \qquad (1.26)$$

where X_f is the column density of the fermions f along the neutrino path

$$X_f = \int_0^L N_f(\vec{r})dr \qquad (1.27)$$

We obtain the oscillating form of neutrino survival probability, however the survival probability is a function of the column density of the fermions, and has no dependence on the neutrino energy. Survival probability $\nu_\alpha \rightarrow \nu_\alpha$ as a function of propagation length is presented in Figure 1.5, where the matter density profile in the Earth is taken from the PREM model [24].

1.4 Motivations

NSI in the matter of the Earth gives the flavor transitions which possibly account for the atmospheric neutrino problem. However, the solution with pure NSI was strongly ruled out because of the inconsistency between data and expectation in the high energy region [25]. That is, the observed high energy data well explained by neutrino oscillations show the small flavor
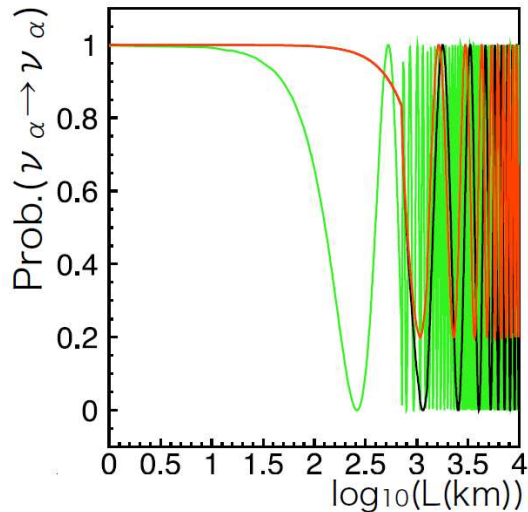
Figure 1.5: Survival probability of $\nu_\alpha \to \nu_\alpha$ as a function of the propagation length in the matter of the Earth. Horizontal axis is the propagation length $\log_{10}(L_\nu(\mathrm{km}))$. (Black curve) $\varepsilon_{\alpha\beta}$=1.0 and $\varepsilon_{\beta\beta} - \varepsilon_{\alpha\alpha}$=0.01. (Red curve) $\varepsilon_{\alpha\beta}$=1.0 and $\varepsilon_{\beta\beta} - \varepsilon_{\alpha\alpha}$=1.0. (Green curve) $\varepsilon_{\alpha\beta}$=10.0 and $\varepsilon_{\beta\beta} - \varepsilon_{\alpha\alpha}$=0.1. $N_f(\vec{r})$ is replaced with the average matter density along the path of neutrino $\langle N_f(\vec{r}) \rangle$ to simplify the calculation.

transition due the condition $\Delta m^2 L / 4E_\nu \ll 1$, whereas NSI can give rise to the sizable transition wherever the fermion column density is sufficient.

Nevertheless, this result only states that the atmospheric neutrino problem cannot be explained by the pure NSI and NSI is most unlikely the dominant component of the characteristics of the problem. In other words, NSI can coexist with neutrino oscillations although its effect is at most sub-dominant.

Presence of NSI simultaneously with neutrino oscillations can be the test how neutrino oscillations are robust to the atmospheric neutrino data by comparing the allowed neutrino oscillation parameters between two cases, pure neutrino oscillations and the mixed with NSI (we call it the *hybrid model*). Furthermore, suppose neutrino oscillations are stable enough or the *true* solution of the problem, neutrino oscillations capably act as the probe of NSI by measuring the deviation of the hybrid model from pure neutrino oscillations. The situation where NSI and neutrino oscillations coexist simultaneously has never been tested by the neutrino oscillation experiments so far, thus this thesis will give the first experimental results.

Propagation of three flavored neutrinos $\nu(t)$ in the hybrid model are derived from the solution of the Schrödinger equation,

$$i\frac{d}{dt}|\nu(t)\rangle = H|\nu(0)\rangle \tag{1.28}$$

with the effective hamiltonian H for neutrinos $(+)$ and anti-neutrinos $(-)$

$$H = \frac{1}{2E_\nu} U \begin{pmatrix} 0 & 0 & 0 \\ 0 & \Delta m_{21}^2 & 0 \\ 0 & 0 & \Delta m_{31}^2 \end{pmatrix} U^\dagger + V_{\mathrm{MSW}} \pm \sqrt{2} G_F N_f(\vec{r}) \begin{pmatrix} \varepsilon_{ee} & \varepsilon_{e\mu}^* & \varepsilon_{e\tau}^* \\ \varepsilon_{e\mu} & \varepsilon_{\mu\mu} & \varepsilon_{\mu\tau}^* \\ \varepsilon_{e\tau} & \varepsilon_{\mu\tau} & \varepsilon_{\tau\tau} \end{pmatrix} \tag{1.29}$$

8

where the first and second term are given by neutrino oscillations and the third term by NSI. For convenience, the first and second term are called as the *vacuum term* and *matter term*, respectively. Under the standard model, only ν_e receives an extra contribution from the electron in matter. This effect is called as the MSW mechanism [26, 27, 28] and denoted as V_{MSW}.

As an example, we briefly review the expected phenomena of the most simple case in which 2-flavor neutrino oscillation and NSI in the $\nu_\mu - \nu_\tau$ sector are taken into account simultaneously. In this case, the effective hamiltonian can be reduced to

$$H = \frac{1}{2E_\nu} U \begin{pmatrix} 0 & 0 \\ 0 & \Delta m_{32}^2 \end{pmatrix} U^\dagger \pm \sqrt{2} G_F N_f(\vec{r}) \begin{pmatrix} \varepsilon_{\mu\mu} & \varepsilon_{\mu\tau}^* \\ \varepsilon_{\mu\tau} & \varepsilon_{\tau\tau} \end{pmatrix} \tag{1.30}$$

where V_{MSW} is not appeared since the reduced H decouples to ν_e.

In the matter of the Earth, a contribution to the neutrino propagation can be known by the size of their eigenvalues derived from the diagonalization of eq.(1.30), where the eigenvalues vary according to the neutrino energy. Assuming all of $\varepsilon_{\alpha\beta}$ have a equivalent size to the standard model ($\varepsilon_{\alpha\beta} \sim 1$), the vacuum term dominates below 1 GeV, while the matter term plays the leading role above a few GeV. In the energy range where the matter term has the dominant contribution, deficit of ν_μ events is enhanced or decreased and hence the zenith angle distributions are changed due to nonzero $\varepsilon_{\alpha\beta}$.

Considering these expected phenomena, the features of atmospheric neutrinos advantageously work in the tests: (i) They have the wide energy range from a few hundred MeV to a hundred TeV, (ii) neutrinos incoming from the upward direction propagate in the dense matter of the Earth, and (iii) almost full mixing between ν_μ and ν_τ. The advantage of (i) is understood by recalling that the inconsistency between NSI and neutrino oscillations is appeared in the high energy events while NSI shows better agreement with the low energy events. (ii) enhances the amplitude of NSI compared to neutrino oscillations, and derive the conspicuousnes of NSI. (iii) helps us to obtain the natural ν_τ beam oscillated from the atmospheric ν_μ flux, where we note that NSI couplings to ν_τ, i.e. $\varepsilon_{\alpha\tau}$, have been poorly constrained due to the lack of abundant ν_τ beam.

Finally, let us summarize the motivation of this study:

(1) Test of the robustness of neutrino oscillations to the atmospheric neutrino data.

(2) Investigation of the possible presence of NSI. If we would not able to obtain the signal of NSI, we derive the constraints to them.

This study is, in a sense, equivalent to measure the deviation between atmospheric neutrino data and the solution with pure neutrino oscillations, then a highly accurate analysis is required. In order to achieve the study, not only improved atmospheric neutrino flux model and neutrino interaction theories are employed in the simulation, the absolute energy scale is adjusted accurately, but also the systematic uncertainties are carefully inspected. We emphasize that the analysis assuming the existence of NSI is the first attempt among the neutrino oscillation experiments so far.

Chapter 2

The Super-Kamiokande Detector

Super-Kamiokande is a cylindrical 50 kt water Cherenkov detector located at Kamioka Observatory in Gifu Prefecture, Japan. The geographic coordinates of the site are 36°25'N and 137°18'E, and the altitude above sea level is 370 m. The detector lies in a zinc mine under the peak of Mt.Ikenoyama, where the mean rock overburden is ~ 1000 m (2700 m water equivalent). This overburden serves as a shield against cosmic ray muon background. The cosmic ray muon flux at the Super-Kamiokande site is reduced by 5 orders of magnitude compared to that on the surface of the earth.

The main scientific purposes of the Super-Kamiokande experiment are the searches for nucleon decays and the studies of various types of neutrinos: atmospheric neutrinos, solar neutrinos, and the neutrinos from supernovae and the other astrophysical sources. The Super-Kamiokande detector is also used as a target of the artificial neutrino beam in long-baseline neutrino oscillation experiments, the K2K experiment and the forthcoming T2K experiment [29]. The Super-Kamiokande experiment started taking data in April, 1996 and continued the observation for five years within the running period referred to SK-I till the detector maintenance in July, 2001. During refilling water after the maintenance, an accident occurred in November, 2001 in which more than a half of the PMTs were destroyed. The Super-Kamiokande detector was rebuilt after the accident with the half of the original PMT density in the inner detector and resumed observation from October, 2002, which is referred to the SK-II running period. The SK-II continued the physics measurement for three years and finished in October 2005 for the reconstruction work to put the PMT density back to the SK-I level. The Super-Kamiokande detector has restarted observation in June, 2006.

In this thesis, the data observed in the SK-I (1996-2001) and the SK-II running periods (2002-2005) are used.

2.1   Cherenkov Radiation

The Super-Kamiokande detector observes relativistic charged particles in water by detecting the emitted Cherenkov light. The Cherenkov photons are radiated when the velocity of a charged particle exceeds the light velocity in the medium :

$$v \geq \frac{c}{n},$$

(2.1)
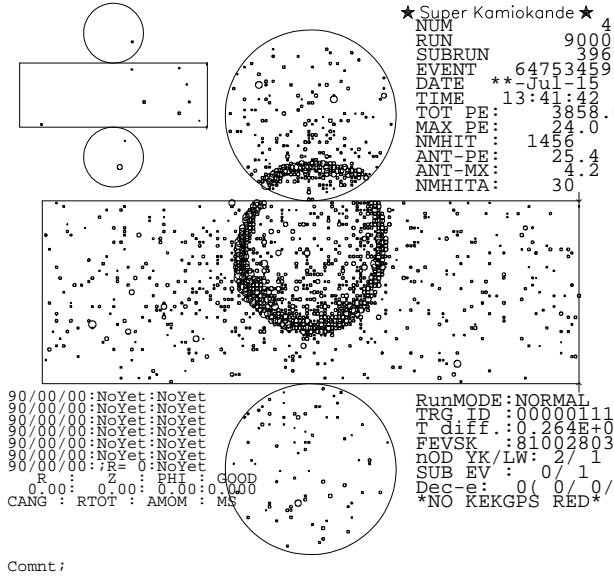
Figure 2.1: A typical observed neutrino event in Super-Kamiokande. The size of small circles in the unrolled cylinder represents the amount of Cherenkov photons detected in each photo-multiplier tube. The Cherenkov ring image is clearly visible.

where v is the velocity of the charged particle, n is the refractive index of the medium and c is the light velocity in vacuum [30]. The momentum threshold of Cherenkov radiation is determined by the refractive index of the medium and the mass of the particle. Since the refractive index of water is about 1.34, the momentum thresholds of Cherenkov radiation for electrons, muons and charged pions are 0.57, 118 and 156 MeV/c, respectively. As for proton, because of its large mass the momentum thresholds is about 1.07 GeV/c.

Cherenkov light is emitted on a cone with a characteristic half opening angle θ_C along the direction of the particle. The opening angle, called Cherenkov angle, is determined as follows :

$$\cos \theta_C = \frac{1}{n\beta}, \tag{2.2}$$

where $\beta = v/c$. For the particle with $\beta \simeq 1$ in water, the Cherenkov angle is about $42°$.

The number of photons emitted by Cherenkov radiation is given as a function of the wavelength λ as follows :

$$\frac{d^2N}{dxd\lambda} = \frac{2\pi\alpha}{\lambda^2}\left(1 - \frac{1}{n^2\beta^2}\right), \tag{2.3}$$

where x is the path length of the charged particle and α is the fine structure constant. About 340 photons/cm are emitted between the wavelength of 300 nm to 600 nm, which is the sensitive wavelength region of the PMTs used in the Super-Kamiokande detector.

Particles emitting Cherenkov light project ring images on the wall inside the detector. Super-Kamiokande detects the Cherenkov photons by the PMTs arranged on the wall and the Cherenkov rings can be recognized. Figure 2.1 shows a visual display of a typical neutrino event in the Super-Kamiokande detector.
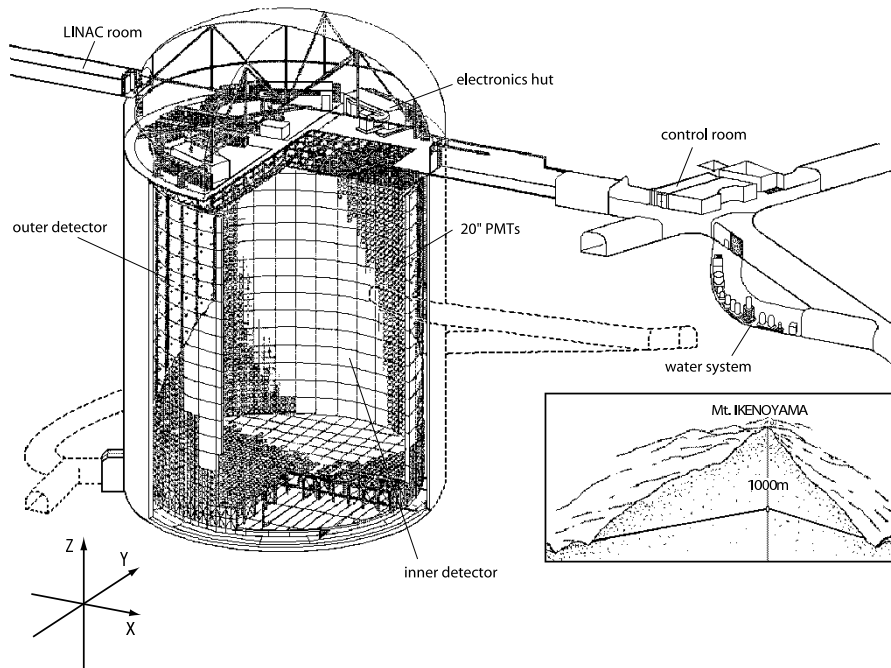
Figure 2.2: Super-Kamiokande detector and its location.

2.2 Detector

2.2.1 Water Tank

A schematic view of the detector is shown in Figure 2.2. The whole size of the water tank is 41.4 m in the hight and 39.3 m in the diameter, in which 50 kt highly pure water is filled. The water tank is optically separated into two concentric cylindrical regions by a PMT support structure and a pair of opaque sheets as shown in Figure 2.3.

The inner region, this part of the detector is referred to the inner detector (ID), contains 32 kt water with the size of 36.2 m in the hight and 33.8 m in the diameter. 11,146 inward-facing 20-inch PMTs are attached to the supporting frame uniformly at intervals of 70 cm for SK-I. The effective photocathode coverage of the ID is about 40 %, and the rest of the surface is covered with black polyethylene terephthalate sheet, called "black sheet". For SK-II, 5,182 20-inch PMTs are attached at one intervals to the supporting frame and the photocathode coverage of the ID is about 20 %.

The outer region completely surrounds the ID with the thickness of 2.05 m on top and bottom and 2.2 m along the barrel wall. This region, called the outer detector (OD), is monitored by 1,885 outward-facing 8-inch PMTs attached to the outer side of the supporting frame. To improve the light collection efficiency, each PMT in the OD is attached to a 60 cm × 60 cm wavelength shifting plate, and the walls are covered with reflective material called "tyvek sheet". The OD is used to veto entering cosmic ray muons and to tag the outgoing charged particles. Furthermore, the 2 m thickness water layer itself serves as a shield to attenuate gamma ray and neutron fluxes from the rock.

The inner and outer volumes are separated by a 55 cm thick dead region. This region is not

12
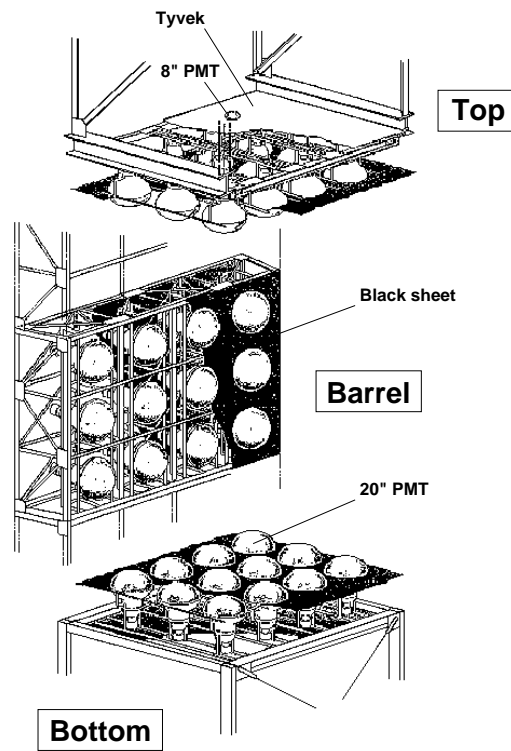
Figure 2.3: Supporting frame of PMTs.

instrumented with any PMT. Stainless steel frames and signal and HV cables of the ID and OD PMTs are contained in this dead region.

2.2.2 Inner detector photomultiplier tube

The photomultiplier tubes used in the ID, product name Hamamatsu R3600, have photo-cathode with a diameter of 50 cm (20 inch). This 20 inch PMT was originally developed by Hamamatsu Photonics K.K. in cooperation with the Kamiokande collaborators [31]. Later, the dynode structure and the bleeder circuit were modified for Super-Kamiokande to improve timing response and photon collection efficiency [32]. A schematic view of the PMT is shown in Figure 2.4 and the specifications are summarized in Table 2.1.

The photocathode of the PMT is coated by bialkali (Sb-K-Cs) owing to the high spectral sensitivity to Cherenkov light and the low thermionic emission. The quantum efficiency of the PMT together with the Cherenkov spectrum is shown in Figure 2.5, in which the peak is 22 % at 360-400 nm (Figure 2.6). The dynode structure and the bleeder circuit are optimized to achieve high collection efficiency, fast timing response and good energy resolution. The averaged value of the collection efficiency at the first dynode is 70 %, which is uniform within a difference of $\pm 7\%$ everywhere on the photocathode. The gain of the ID PMTs is 10^7 at a supply high voltage from 1500 V to 2000 V. Figure 2.7 shows the charge distribution for the single photoelectron signal in which a clear 1 p.e. peak can be seen. The transit time spread of the single photoelectron signal is about 2.2 nsec. The average dark noise rate at the 0.25 p.e.s threshold used in Super-Kamiokande is about 3 kHz.

The magnetic field over 100 mG affects photoelectron trajectories in the PMT and makes the timing resolution worse, while geomagnetic field at the detector site is about 450 mG. To compensate for the magnetic field, 26 sets of horizontal and vertical Helmholtz coils are arranged around the tank. As the result, the magnetic field inside the detector is reduced to about 50 mG.

On November 12th, 2001 while refilling the SK tank after completing the upgrade work, one ID PMT on the bottom of the tank imploded, which triggered a cascade of implosions. About 60 % of the ID and OD PMTs were destroyed. To avoid a chain reaction of implosion, all of the inner PMTs are instrumented with acrylic covers in SK-II. A clear 12 mm thick UV-transparent acrylic dome is put over the photo-cathode area of each PMT and the side of the PMT is protected by the fiberglass shield with holes, which let water flow into the case freely as shown in Figure 2.8. Figure 2.9 shows the transparency of the acrylic cover for photons with normal incidence in water, which is mode than 96 % above 350 nm of wavelength and the effect of the PMT case is small. 11,146 and 5,182 PMTs are used in SK-I and SK-II, respectively.

2.2.3 Outer detector photomultiplier tube

1,885 8-inch PMTs, Hamamatsu R1408, are used in the OD. For SK-I, the OD PMTs were reused from the IMB experiment [33] after finishing that experiment. The photocathode of the OD PMT is fitted with 60 cm $\times$ 60 cm $\times$ 1.3 cm wavelength shifter plate. The wavelength shifter increases the light collection efficiency by 60 %. The timing resolution at single photoelectron is about 13 nsec without the wavelength shifter and about 15 nsec with the plate. However, since the OD is used as a veto counter, rather than a particle tracker, The extra photons are of importande while the poor timing resolution is of little consequence.
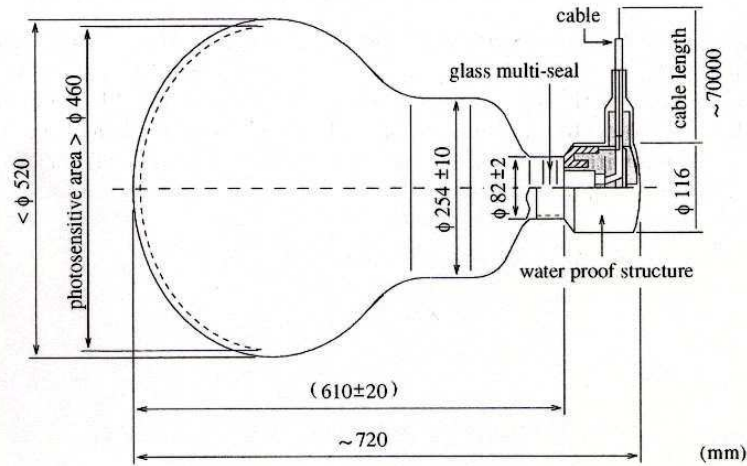
Figure 2.4: A schematic view of a 20-inch PMT.

Shape	Hemispherical
Photocathode area	50 cm diameter
Window material	Pyrex glass $(4 \sim 5\,\mathrm{mm})$
Photocathode material	Bialkali (Sb-K-Cs)
Quantum efficiency	$22\,\%$ at $\lambda = 390\,\mathrm{nm}$
Dynodes	11 stage Venetian blind type
Gain	10^7 at $\sim 2000\,\mathrm{V}$
Dark current	$200\,\mathrm{nA}$ at 10^7 gain
Dark pulse rate	$3\,\mathrm{kHz}$ at 10^7 gain
Cathode non-uniformity	$< 10\,\%$
Anode non-uniformity	$< 40\,\%$
Transit time	$90\,\mathrm{nsec}$ at 10^7 gain
Transit time spread	$2.2\,\mathrm{nsec}$ $(1\,\sigma)$ for 1 p.e. equivalent signals
Weight	$13\,\mathrm{kg}$
Pressure tolerance	$6\,\mathrm{kg/cm^2}$ water proof

Table 2.1: Specifications of 20-inch PMT.
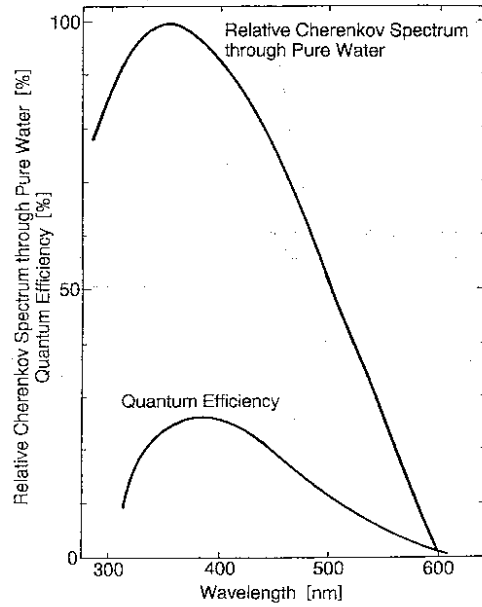
Figure 2.5: The spectrum shape of Cherenkov light through pure water and the quantum efficiency of 20-inch PMT as a function of wavelength.
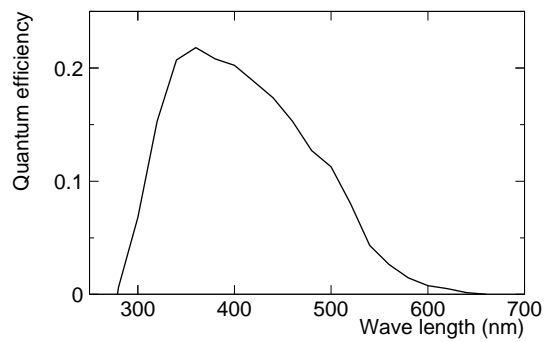
Figure 2.6: the quantum efficiency of ID 20-inch PMT as a function of wavelength.
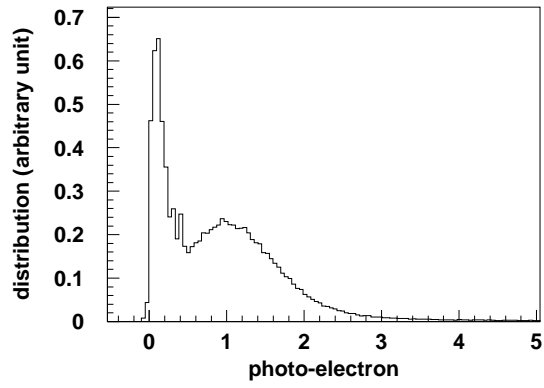
Figure 2.7: Single photoelectron distribution of a typical 20-inch PMT.

Figure 2.8: PMT case attached to the inner PMT after SK-II experiment
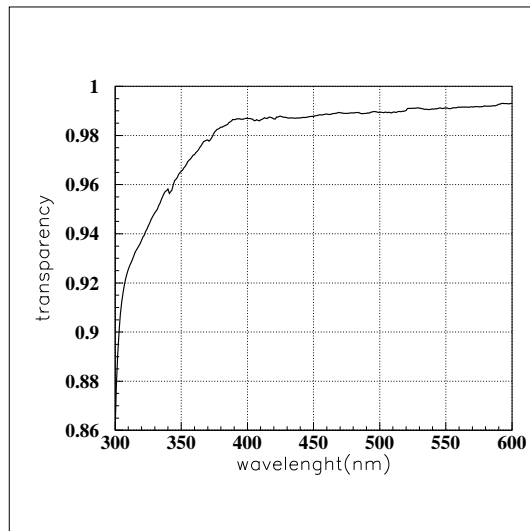
Figure 2.9: The transparancy of the acylic case as a function of wavelength

17

2.3　Water Purification System

The water for the Super-Kamiokande experiment is produced from abundant spring water in the mine. The water in the tank is continuously circulated through the water purification system to keep the high attenuation length. It is also an important purpose of this system to remove the radioactive materials, especially radon (Rn), which is a background source for the solar neutrino observation in the MeV energy range. The water is constantly circulated through the purification system with flow rate of about 35 ton/hour. The outline of the system is shown in Figure 2.10. The system consists of the following components.

- 1μm mesh filter　　　　removes dust and small particles which reduce the water transparency.

- Heat exchanger　　　　cools water to suppress the growth of bacteria. The water temperature in the detector is kept at 14 °C.

- Cartridge polisher　　　　eliminates ions which also reduce water transparency.

- Ultra-Violet sterilizer　　　　kills bacteria.

- Radon-reduced air dissolving tank　　dissolves radon-reduced air into the water to increase radon removal efficiency at the vacuum degasifier stage which follows.

- Reverse osmosis filter　　　　removes particulates.

- Vacuum degasifier　　　　removes dissolved gases in water, such as the oxygen and radon.

- Ultra filter　　　　removes minute particles of the order of 10 nm.

- Membrane degasifier　　　　removes radon dissolved in water.

The typical number of particles larger than 0.2μm is reduced to 6 particles/cc and the light attenuation length is achiedved to be $\sim$100 m after purification. The resistivity of the water entering the purification system from the detector is about 11 MΩ·cm. After the purification, the water has an average resistivity of 18.20 MΩ·cm, approching the chemical limit.

2.4　Radon Hut and Air Purification System

It is also essential to have clean air in the detector and the experimental area to minimize the radon level in the detector water. The radon concentration of the mine air in the access tunnel to the experimental site has a strong seasonal variation of $2{,}000 \sim 3{,}000$ Bq/m^3 during summer and $100 \sim 300$ Bq/m^3 during winter as shown in Figure 2.11. This is caused by the seasonal variation of the air flow inside the mine.

Fresh air from outside the mine is continuously pumped into the SK dome area at the rate of 10 m^3/minute through an air duct along the 1.8 km Atotsu access tunnel to the SK experimental area. As a result, the typical radon concentration in the SK dome air is $20 \sim 30$ mBq/m^3.
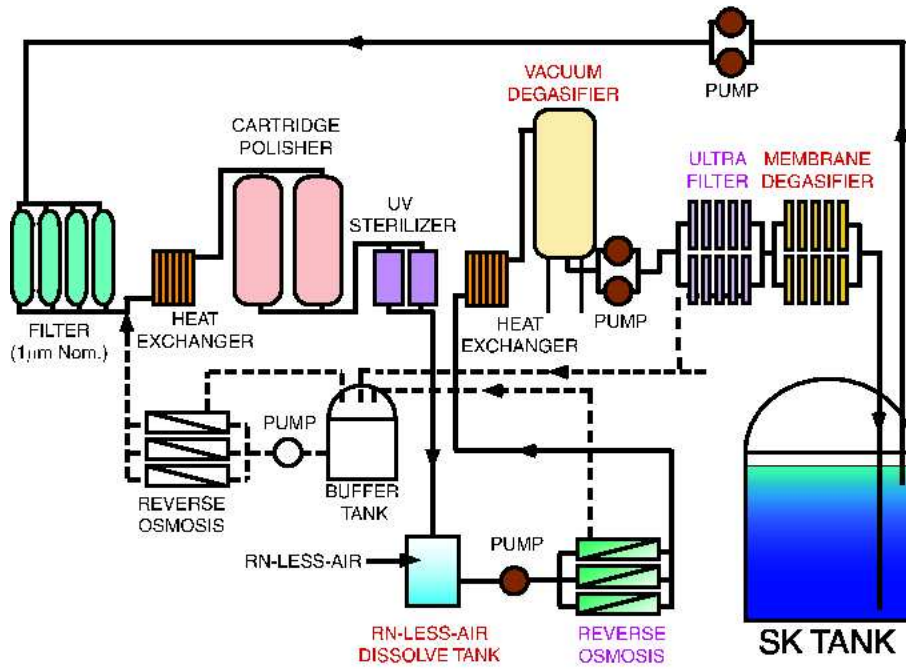
Figure 2.10: The water purification system for Super-Kamiokande.
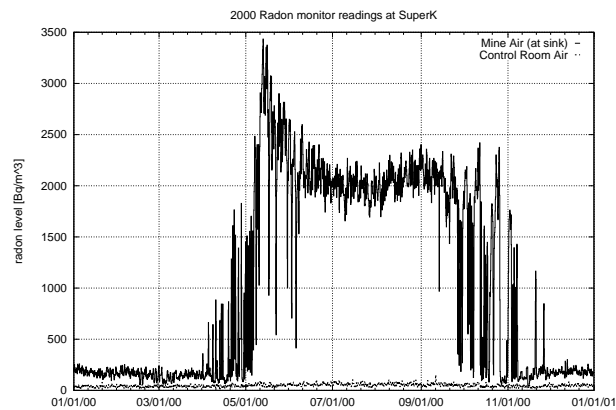
Figure 2.11: The upper histogram (solid curve) shows the measured radon concentration levels in the mine air [34]. The lower histogram (dashed curve) shows the corresponding radon levels in the SK dome.
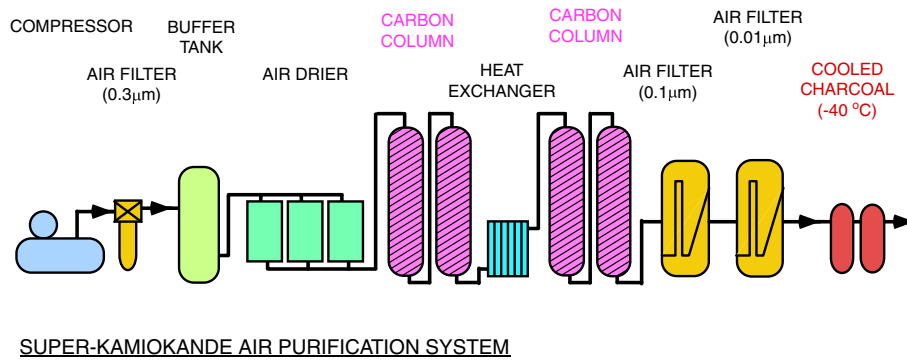
Figure 2.12: A schematic view of the radon-reducing air system.

Furthermore, to keep the radon level inside the detector absolute minimum, radon-free air is produced by the air purification system in the mine and is continuously pumped into the space above the water surface inside the tank at a positive pressure to prevent radon in the SK dorm air from entering the detector and dissolving into the purified water [35]. A schematic view of the air purification system is shown in Figure 2.12. The radon concentration of the radon-free air is less than $3\,\mathrm{mBq/m^3}$. The air purification system consists of compressors, a buffer tank, driers, and the filters. The air flow rate is about $18\,\mathrm{m^3/hour}$. The process of the air purification system is described as follows:

- **Compressor:**
  Compresses air to $7 \sim 8.5$ atmospheric pressure.

- **Air Filter:**
  Removes dusts in sizes of $\sim 0.3\,\mu\mathrm{m}$.

- **Buffer Tank:**
  Stores the air.

- **Air Drier:**
  Dries the air and removes CO_2 gas to improve the radon removal capability in Carbon Columns.

- **Carbon Columns:**
  Removes radon gas using activated charcoal.

- **Air Filter:**
  Further Removes small dust and particles of $\sim 0.01\,\mu\mathrm{m}$.

- **Cooled Charcoal Columns:**
  Further removes the remaining radon gas with the charcoal cooled down to –40°C.
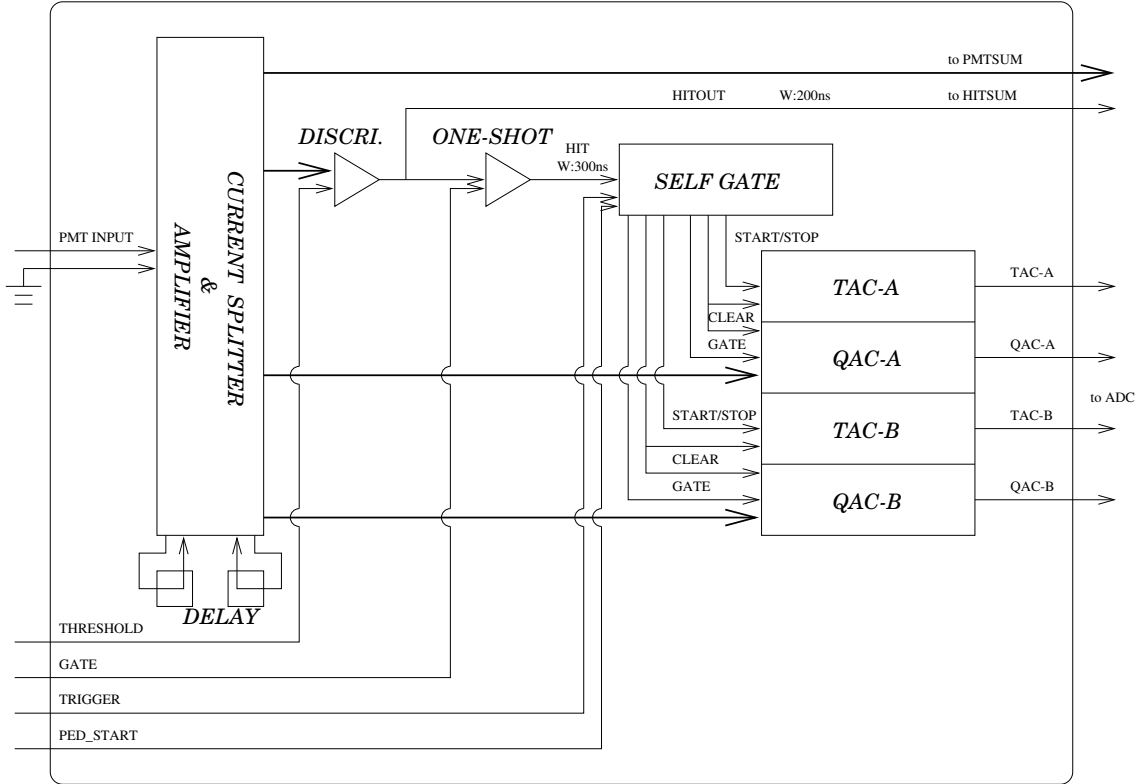
Figure 2.13: A block diagram of analog input part of ATM.

2.5 Electronics and Data Acquisition System

2.5.1 Inner detector electronics and data acquisition

ID PMT signals are processed by custom built electronics modules called ATM (Analog-Timing-Module) of the TKO standard (TRISTAN KEK Online) [36, 37]. The ATM module records the integrated charge and the arrival timing information of each PMT signal.

Figure 2.13 shows the block diagram of the analog input part of the ATM module. Each PMT input channel of ATM has two switching pairs of QAC (Charge to Analog Converter) and TAC (Time to Analog Converter) to minimize the electronics dead time in the data taking for two successive events, such as a muon followed by its decay electron. Each PMT signal sent to ATM is amplified 100 times, and then divided into four signals. One of them is sent to the discriminator. When the pulse height of the PMT signal exceeds the threshold level, which is set to $0.25\,\mathrm{p.e.s}$, a $400\,\mathrm{nsec}$ gate signal for QAC and a start signal for TAC are generated. At the same time, rectangular signal called HITSUM($200\,\mathrm{ns}$ width and $15\,\mathrm{mV}$ pulse hight) is sent to a global trigger module. Other two branches of the splitted PMT signal are fed to QAC. If a global trigger is issued, a stop signal is sent to TAC and the information in QAC and TAC is digitized by ADC. The digitized charge and timing information is stored in internal FIFO memory in ATM. If a global trigger is not issued within $1.3\,\mu\mathrm{sec}$, all the information in QAC and TAC is cleared. ATM has $450\,\mathrm{pC}$ dynamic range with a resolution of $0.2\,\mathrm{pC}$, and $1.3\,\mu\mathrm{sec}$

21

dynamic range with a resolution of 0.4 nsec. The remaining one signal becomes an output signal of ATM called PMTSUM.

Figure 2.14 shows a schematic view of the ID data acquisition system. Signals from 12 PMTs are fed to an ATM board to be processed. There are in total 946 ATM boards installed in 48 TKO crates. The digitized data in ATM FIFO memory are sent to VME memory modules called SMP (Super Memory Partner) every 16 events. 48 SMP are installed in 8 VME crates, and one SMP module handles the data of 20 ATMs. The data in SMP memories are read out by 8 slave computers and sent to the online host computer.

2.5.2 Outer detector electronics and data acquisition

Figure 2.15 shows a schematic view of the OD data acquisition system [38]. The paddle cards distribute high voltage from the main frame to the OD PMTs. A coaxial cable is used to supply the high voltage to an OD PMT and to send a signal from the PMT. These cards also pick off the PMT signals through a high voltage capacitor. Signals from the OD PMTs are sent to QTC (Charge to Time Converter) modules. A QTC module converts the PMT signal to a rectangular pulse whose width is proportional to the input charge. At the same time, a rectangular HITSUM signal is generated by QTC and sent to a global trigger module. The threshold of QTC modules is set to 0.25 p.e.. If a global trigger is received, the leading edge and the width of the rectangular pulse are converted to the timing and charge information by a LeCroy 1877 multi-hit TDC module. TDC module can record up to 8 QTC pulses with a resolution of 0.5 nsec. The dynamic range is set to 16 μsec which starts from 10 μsec before the global trigger timing. The digitized data stored in TDC are read by a slave computer through VME memory module called DPM (Dual Port Memory) and then sent to the online host computer.

2.5.3 Trigger

Figure 2.16 shows a overview of the ID trigger scheme. An ATM module generates a rectangular HITSUM signal with 15 mV in pulse height and 200 nsec in width if an ID PMT signal exceeds the threshold. These signals are analog-summed over all PMTs to generate an ID-HITSUM signal. The pulse height of the ID-HITSUM signal is proportional to the number of hit PMTs within 200 nsec time window. There are three types of trigger signals derived from the ID-HITSUM signal. In SK-I, the high energy (HE) trigger is generated when the pulse hight of ID-HITSUM signal exceeds a threshold of -340 mV, which corresponds to 31 hits within a 200 nsec time window. The threshold for the low energy (LE) trigger is set to -320 mV, which corresponds to 29 hits. This is equivalent to a signal expected from a 5.7 MeV electron assuming 50 % of trigger efficiency . The trigger rates for HE and LE triggers are ~ 5 Hz and ~ 11 Hz, respectively. The super low energy (SLE) trigger was implemented in May 1997 in order to lower the solar neutrino analysis threshold. The threshold is set to 4.6 MeV equivalent. The SLE triggered events are not used in atmospheric neutrino analysis. In SK-II, the same trigger scheme with the different thresholds is used. The threshold energies for the SK-II HE and LE triggers are 10 MeV and 8 MeV, respectively.

The OD trigger is generated by a similar procedure. When an OD PMT signal exceeds a threshold, a QTC module generates a rectangular pulse with 20 mV in height and 200 nsec in width. These signals are also analog summed up to generate an OD-HITSUM signal. The threshold for the OD trigger is set to 19 hits within a 200 nsec time window.

Figure 2.14: A schematic view of the inner detector data acquisition system.
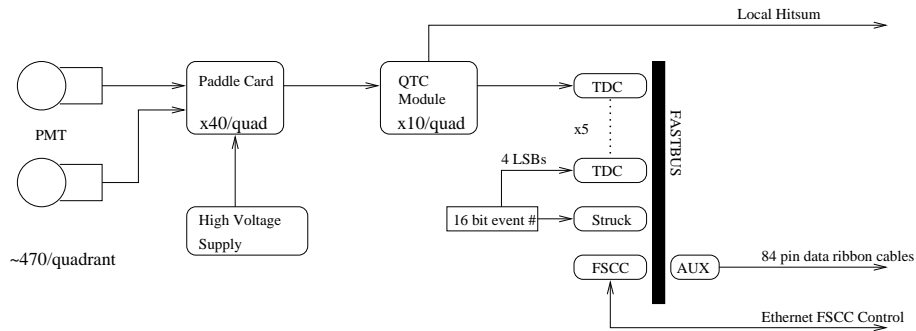
Figure 2.15: A schematic view of the outer detector data acquisition system.

These four types of trigger signals (HE, LE, SLE and OD) are fed to a hardware trigger module called TRG. The TRG module generates a global trigger signal when any one of the trigger signals is issued.
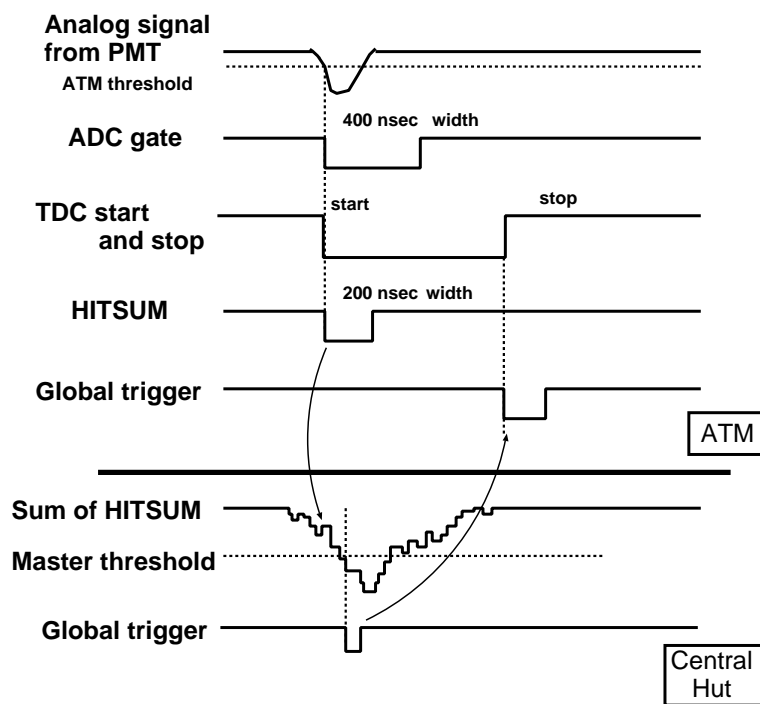
Figure 2.16: An overview of the ID trigger scheme.

Chapter 3

Simulation of Atmospheric Neutrino Events

3.1 Overview

Atmospheric neutrino events in Super-Kamiokande are simulated by a Monte Carlo method, in which all of the important factors are accurately simulated. Monte Carlo simulation consists of three constituents: neutrino flux, neutrino interactions and particle tracking in the detector. First, we expect number of events occured in the detector during a certain period by means of the products of neutrino flux and cross sections. The kinematics of the neutrino interactions are simulated following the atmospheric neutrino energy spectrum, and then the generated particles are tracked in water with the detector simulation program.

Neutrino oscillations and the other physical features of atmospheric neutrinos are studied by comparing the observed data with the prediction by the Monte Carlo simulation.

3.2 Atmospheric Neutrino Flux

There have been several models for atmospheric neutrino flux, which are calculated by M. Honda *et al.* [1, 2, 3] (Honda flux), G. Battistoni *et al.* [39] (Fluka flux) and G. Barr *et al.* [40] (Bartol flux). In our Monte Carlo simulation program, the Honda flux is adopted as a default model and other two flux calculations are used to estimate the systematic uncertainties in the flux calculation.The way of estimating systematic uncertainlies are discussed in Chapter 7.3.1. The energy range supported by the Honda flux is up to 10 TeV, so the Volkova flux [41] is adopted to simulate the event above 10 TeV. In order to connect the Volkova flux with the Honda flux smoothly at 10 TeV, we adjust the absolute normalization of the Volkova flux.

The primary cosmic ray flux model as an input of the neutrino flux calculation is determined based on the experimental measurements. Current status of the measurements of cosmic ray proton flux is shown in Figure 3.1 with the model used in the Honda flux calculation. The primary cosmic ray spectrum has been precisely measured by BESS and AMS experiments up to 100 GeV [42, 43]. The cosmic ray flux changes depending on the turbulence of the solar wind, which is higher when the solar activities are high (solar maximum) than when the solar activities are low (solar minimum). The difference of the cosmic ray flux at solar maximum and solar minimum is more than a factor of two for 1 GeV cosmic rays, while it decrease to $\sim 10\,\%$

for 10 GeV. The effect of geomagnetic field is represented as the rigidity (= momentum/charge) cutoff. The geomagnetic field works as a shield, by which cosmic ray with lower momentum than the cutoff cannot arrive at the Earth. Cosmic ray flux above 100 GeV, which are responsible for ≥ 10 GeV neutrinos, is not affected by the solar activity nor the geomagnetic field.
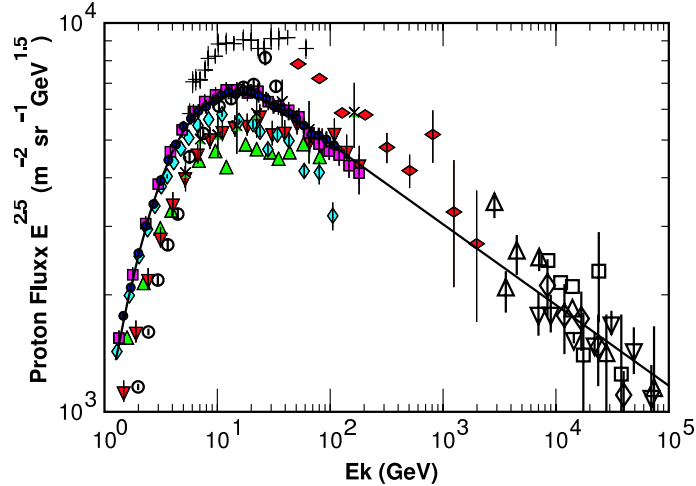
Figure 3.1: Measurements of primary cosmic ray proton flux and the model used in Honda flux calculation. The data are taken from Webber [44] (crosses), LEAP [45] (upward triangles), MASS1 [46] (open circles), CAPRICE [47] (vertical diamonds), IMAX [48] (downward triangles), BESS98 [42] (circles), AMS [43] (squares), Ryan [49] (horizontal diamonds), JACEE [50] (downward open triangles), Ivanenko [51] (upward open triangles), Kawamura [52] (open squares) and Runjob [53] (open diamonds).

In the atmosphere, primary cosmic ray protons and nuclei interact with air nuclei, and secondary particles, mostly pions and some kaons, are consequently generated. In the Honda flux the US Standard Atmosphere model [54] is employed for the density structure of the atmosphere and the structure gives the zenith angle dependence of the atmospheric neutrinos. Geomagnetic filed effects are calculated based on the IGRF2005 model [55].

In the hadronic interactions of the cosmic rays with air nuclei, the two theoretical models: NUCRIN [56] simulation program is used for the primary cosmic ray energies < 5 GeV and DPMJET-III [57] is used for > 5 GeV. Mesons, mostly pions and some kaons, generated through the hadronic interactions create atmospheric neutrinos when they decay in the atmosphere.

Likewise, secondary cosmic ray muons are generated through the decay of mesons. The flux of the secondary cosmic ray muons have been measured by several experiments such as BESS [58] or L3+C [59]. These observations capably work for the calibration of the hadronic interaction model by comparing the momentum spectrum with the expectation. DPMJET-III employed in the Honda flux is modified using the measurements by BESS and L3+C as follows: first, tunable parameters are assigned to a valence quark and the average energy of produced meson, for example π^+, is expressed as

$$\langle E_{\pi^+} \rangle = (1 + c_u) \langle E_{\pi^+}^0 \rangle \tag{3.1}$$

where E_{π^+} is the modified energy of π^+, $E_{\pi^+}^0$ is the original energy, and c_u is the tunable

parameter for u-quark. Produced mesons, $\pi^{\pm}$, π^0, K^+, etc, are connected through such tunable parameters. Second, determine the best-fit tunable parameters by adjusting the predicted muon spectrum to be consistent with the observations. After that, nucleon spectrum is derived to keep the energy conservation. Figure 3.2 shows the ratio of cosmic ray muon spectrum after the modification, and results in that the hadronic interaction model agrees with the measurement within $\lesssim 10\%$ in the $1{\sim}100\,\mathrm{GeV}$ muon energy range.
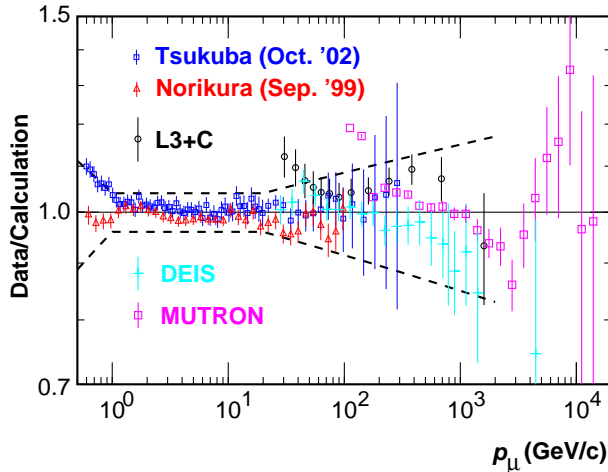
Figure 3.2: Secondary cosmic ray muon fluxes normalized by the calculation [60]. Data are observed at Tsukuba(open box) and Norikura(open triangle) with the BESS detector [61, 62], and at CERN(open circle) with the L3 detector [59]. For reference, DEIS [63] and MUTRON [64] are plotted. Dashed lines represent the sum of errors in data and calculation. Figure is taken from [60].

In the calculation of neutrino flux, interactions and propagation of particles are treated in a 3-dimensional way, including the curvature of charged particles in geomagnetic field. An advantage of the 3-dimensional way compared to the 1-dimension is discussed. The prominent features of the 3-dimensional calculation in comparison with the 1-dimensional one are (1) an enhancement of neutrino flux for near-horizontal direction and (2) lower production height of neutrinos in the atmosphere which is also prominent for near-horizontal direction. The first feature is explained as a difference of the effective area for primary cosmic rays which generate horizontally incoming neutrinos, as illustrated in Figure 3.3. This effect is important for low energy neutrinos ($< 1\,\mathrm{GeV}$), in which transverse momentum of the secondary particles in hadronic interactions and the bending of muons in the geomagnetic field are considerable. Figure 3.4 shows the zenith angle distributions of the Honda and Bartol 3-dimensional atmospheric neutrino flux and the Honda 1-dimensional neutrino flux, using 1-dimensional approximation with older primary flux and hadronic interaction model. Since the geomagnetic field above Super-Kamiokande is stronger than the average, neutrino flux below a few GeV is predicted to be up-down asymmetry. This up-down asymmetry for low energy neutrinos is smeared due to the small angular correlation in neutrino interactions and cannot be observed in charged leptons. The reason of the second feature is explained as follows. The primary cosmic rays from horizontal direction travel a longer distance in atmosphere than the vertically incoming cosmic

rays to reach the same altitude. Therefore, interaction vertex of the vertically incoming cosmic rays have a lower altitude compared to the horizontal one. Unlike a 1-dimensional calculation, the incidence angle of primary cosmic rays which produce horizontally going neutrinos is not restricted to be horizontal direction in a 3-dimensional calculation. As a result, production height of neutrinos in the 3-dimensional calculation is lower than that in the 1-dimensional calculation for near-horizontal direction. This effect is also prominent for low energy neutrinos ($< 1\,\mathrm{GeV}$). The simulations for neutrino production height from the Honda flux and Honda-1D flux are shown in Figure 3.5.
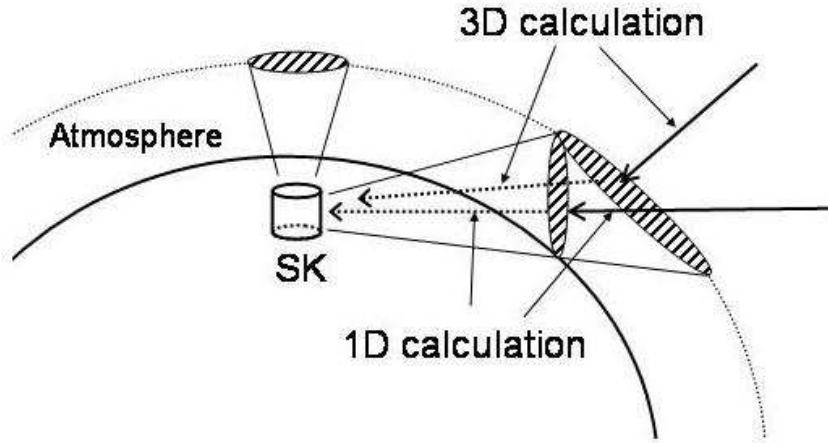
Figure 3.3: A schematic view of the effective areas of primary cosmic rays interacting with air nuclei for 1-dimensional and 3-dimensional calculations. Arrows written by solid lines show the primary cosmic rays and dotted lines show the neutrinos. The 3-dimensional calculation gives larger areas for near-horizontal direction.

The calculated energy spectrum of atmospheric neutrinos at the Super-Kamiokande site for the Honda flux, Fluka flux and Bartol flux is shown in Figure 3.6, in which the flux of $\nu_e + \overline{\nu}_e$ to $\nu_\mu + \overline{\nu}_\mu$ is averaged over all of the direction. The flavor ratio is about two up to a few GeV energy regions, however it becomes larger than two as the neutrino energy increases because more cosmic ray muons reach the ground before decaying. The flavor ratio highly depends on the zenith angle of incoming neutrinos as seen in Figure 3.7. The zenith angle dependence of the flavor ratio plays the key role in 3-flavor neutrino oscillation analysis.
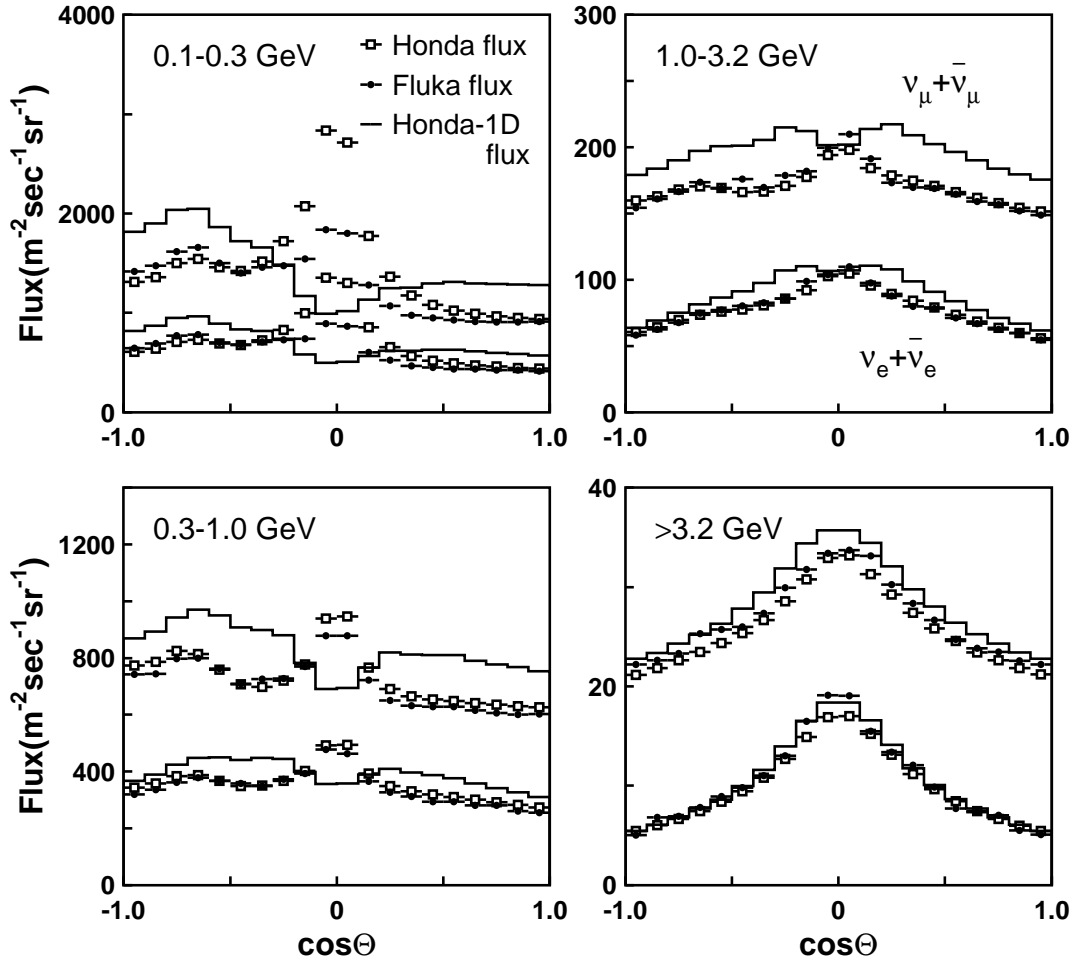
Figure 3.4: Zenith angle dependence of the atmospheric neutrino flux. Boxes show the Honda flux, dots show the Bartol flux and solid lines show the Honda-1D flux. The higher flux is for $\nu_\mu + \overline{\nu}_\mu$ and the lower flux for $\nu_e + \overline{\nu}_e$ in each plot. An enhancement of the neutrino flux is seen for near-horizontal directions at energies below 1 GeV in 3-dimensional calculations, the Honda flux and the Fluka flux. On the other hand, no enhancement is seen in the Honda-1D flux.
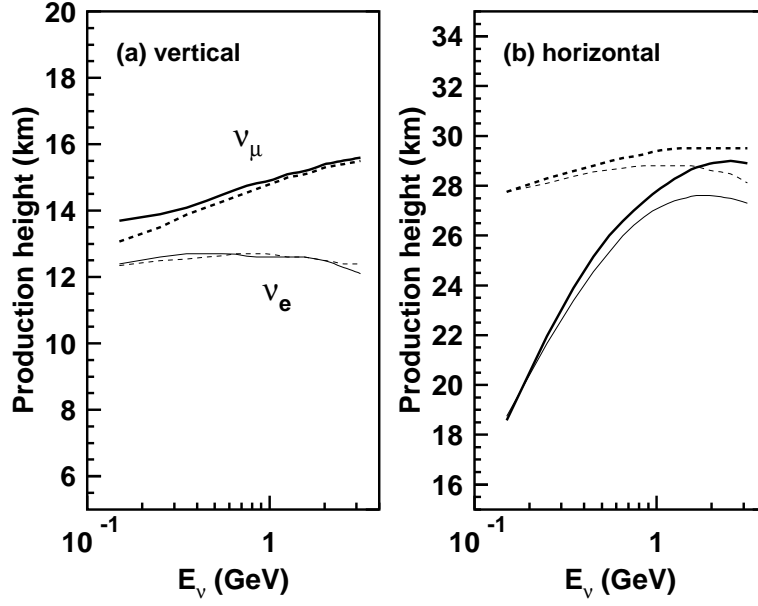
Figure 3.5: 50 % accumulation probability of neutrino production height for (a) near-vertical ($\cos\theta > 0.95$) and (b) near-horizontal ($|\cos\theta| < 0.05$) directions. Thick and thin solid curves are for ν_μ and ν_e by the 3-dimensional calculation, and thick and thin dashed curves are for ν_μ and ν_e by the 1-dimensional calculation, respectively.
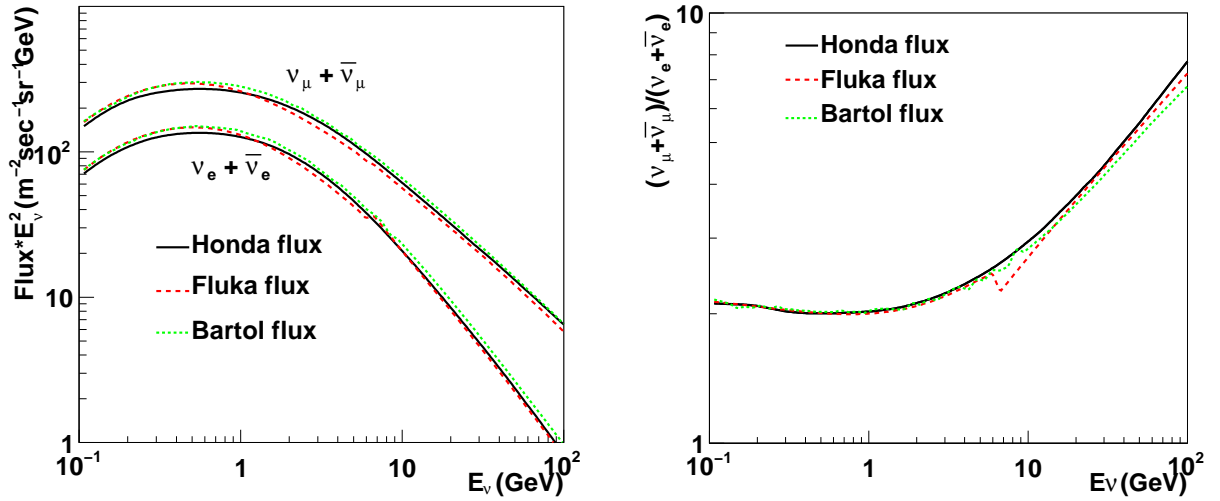
Figure 3.6: Predictions of the direction averaged atmospheric neutrino flux (Left) and the flavor ratio (Right). Solid curves show the Honda flux, dashed curves show the Fluka flux and dotted curves show the Bartol flux.
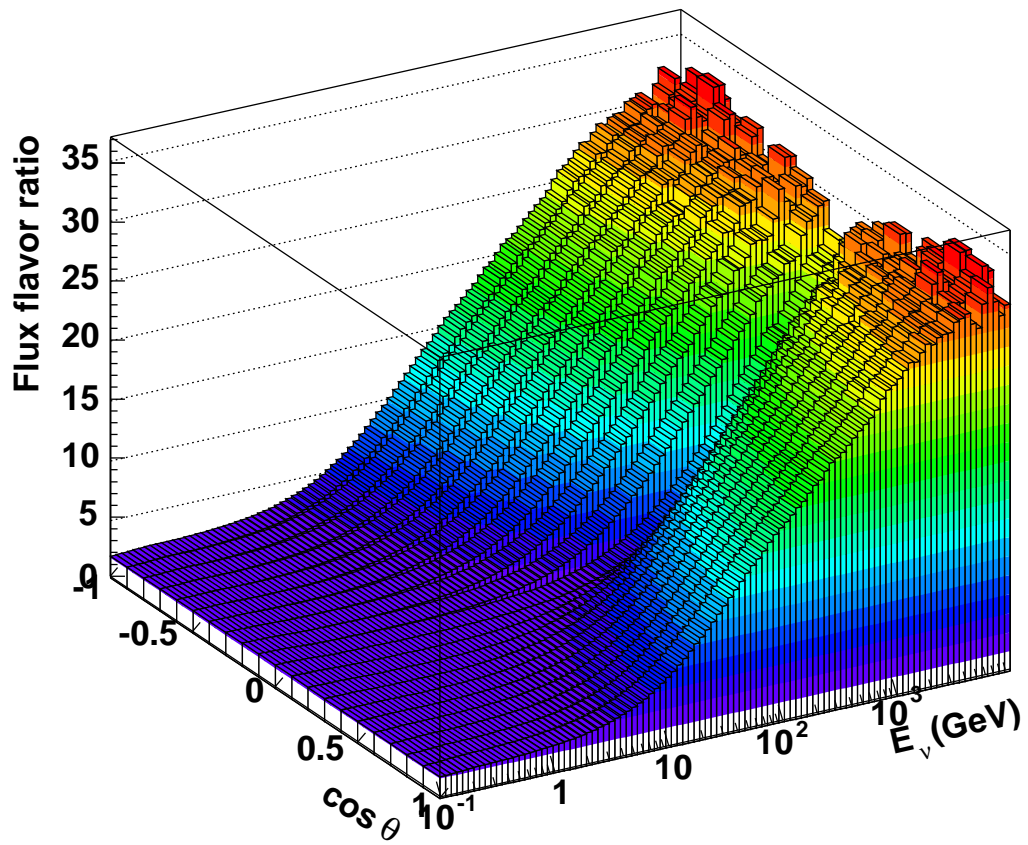
Figure 3.7: Flavor ratio $(\nu_\mu + \overline{\nu}_\mu)/(\nu_e + \overline{\nu}_e)$ as a function of neutrino energy and zenith angle. Calculation is based on the Honda flux.

3.3 Neutrino Interaction

Atmospheric neutrinos interact with nucleons and electrons in water. The neutrino interactions are treated using the NEUT program library [66, 67] in our Monte Carlo simulation. This library was first developed to study atmospheric neutrinos as a background of nucleon decay analysis in the Kamiokande experiment, and then it was inherited to the Super-Kamiokande experiment with a lot of modifications. In the NEUT library, the following charged current (CC) and neutral current (NC) interactions are simulated :

CC/NC (quasi-)elastic scattering $\quad \nu + N \rightarrow l + N'$

CC/NC single meson production $\quad \nu + N \rightarrow l + N' + meson$

CC/NC single gamma production $\quad \nu + N \rightarrow l + N' + \gamma$

CC/NC deep inelastic interaction $\quad \nu + N \rightarrow l + N' + hadrons$

CC/NC coherent pion production $\quad \nu + {}^{16}\text{O} \rightarrow l + {}^{16}\text{O} + \pi$

where N and N' are nucleons (proton or neutron) and l is a lepton.

Since the cross section of neutrino-electron elastic scattering is about 10^3 times smaller than that of the neutrino-nucleon interactions at a neutrino energy of $\sim 1\,\text{GeV}$, this interaction mode is neglected in our simulation.

3.3.1 Elastic and Quasi-Elastic Scattering

The amplitude of the CC quasi-elastic scattering (CCQE) for free protons (i.e. hydrogen atom in water) is described by the product of the hadron and lepton weak currents:

$$T = \frac{G_F}{\sqrt{2}} \overline{u}_l(k_2) \gamma^\mu (1 - \gamma_5) u_\nu(k_1) \langle N'(p_2)|J_\mu^{hadron}|N(p_1)\rangle \tag{3.2}$$

where G_F is the Fermi coupling constant, $p_1(p_2)$ is a initial(final) nucleon 4–momentum, and $k_1(k_2)$ is a initial(final) lepton 4–momentum, respectively. The hadronic weak current J_μ^{hadron} is expressed as:

$$\langle N'(p_2)|J_\mu^{hadron}|N(p_1)\rangle = \cos\theta_c \overline{u}_{N'}(p_2) \left[\gamma_\mu F_V^1(q^2) + \frac{i\sigma_{\mu\nu}q^\nu \xi F_V^2(q^2)}{M} + \gamma_\mu\gamma_5 F_A(q^2) \right] \tag{3.3}$$

where M is the mass of the target nucleon, θ_c is the Cabbibo angle, q is the 4–momentum transfered of the lepton. We use dipole-type form factors both for vector form factors, $F_V^1(q^2)$ and $F_V^2(q^2)$, and axial vector form factor, $F_A(q^2)$, which are given as :

$$F_V^1(q^2) = \left(1 - \frac{q^2}{4M^2}\right)^{-1} \left[G_E(q^2) - \frac{q^2}{4M^2} G_M(q^2) \right] \tag{3.4}$$

$$\xi F_V^2(q^2) = \left(1 - \frac{q^2}{4M^2}\right)^{-1} \left[G_E(q^2) - G_M(q^2) \right] \tag{3.5}$$

$$F_A(q^2) = -g_A \left(1 - \frac{q^2}{M_A^2}\right)^{-2} \tag{3.6}$$

$$G_E(q^2) = (1+\xi)^{-1} G_M(q^2) = \left(1 - \frac{q^2}{M_V^2}\right)^{-2} \tag{3.7}$$

G_E and G_M are the electric and magnetic form factor, M_V and M_A are the vector and axial vector mass.

Hence, the differential cross section is written as [68] :

$$\frac{d\sigma^{\nu(\bar{\nu})}}{dq^2} = \frac{M^2 G_F^2 \cos^2\theta_c}{8\pi E_\nu^2}\left[A(q^2) \mp B(q^2)\frac{s-u}{M^2} + C(q^2)\frac{(s-u)^2}{M^4}\right] \tag{3.8}$$

where E_ν is the neutrino energy, and s and u are Mandelstam variables [68]. The factors A, B and C are given as :

$$
\begin{aligned}
A(q^2) &= \frac{m^2 - q^2}{4M^2}\left[\left(4 - \frac{q^2}{M^2}\right)|F_A|^2 - \left(4 + \frac{q^2}{M^2}\right)|F_V^1|^2\right. \\
&\quad - \frac{q^2}{M^2}|\xi F_V^2|^2\left(1 + \frac{q^2}{4M^2}\right) - \frac{4q^2 F_V^1 \xi F_V^2}{M^2} \\
&\quad \left. - \frac{m^2}{M^2}\left((F_V^1 + \xi F_V^2)^2 + |F_A|^2\right)\right] \tag{3.9}
\end{aligned}
$$

$$B(q^2) = \frac{q^2}{M^2}\left(F_A(F_V^1 + \xi F_V^2)\right) \tag{3.10}$$

$$C(q^2) = \frac{1}{4}\left(|F_A|^2 + |F_V^1|^2 - \frac{q^2}{4M^2}|\xi F_V^2|^2\right) \tag{3.11}$$

where m is the lepton mass, ξ is defined by means of anomalous magnetic moment $\mu \equiv \mu_p - \mu_n = 3.71$. In our simulation the vector mass M_V is set to be $0.84\,\text{GeV}$ and the axial vector mass M_A is set to be $1.21\,\text{GeV}$ according to the experimental results [69, 70, 71]. Common M_A value is also used for single meson productions. g_A is the axial vector coupling constant which is measured in (polarized) nucleon beta-decay [72] and set to be 1.232 in the NEUT library. World average g_A value is 1.2673 ± 0.0035 [73], although the change of cross section caused by the different g_A value is less than 5%. In addition to the dipole form factor, several types of form factor have been proposed [74, 75, 76]. The difference of the cross section between their models and dipole form factor is at most 10%.

For larger M_A values, interactions with higher Q^2 values (and therefore larger scattering angles) are enhanced. M_A value which we use is decided to be consistent with the data from the other experiment, K2K and MiniBooNE. The uncertainty of the value is estimated to be 10% following the total uncertaintiy addopted to the K2K and MiniBooNE results. The results of various measurements and the weighted average except for K2K and MiniBooNE results are shown in Figure 3.8.

For the scattering off bound nucleons in ^{16}O, nuclear effects such as the Fermi motion of the nucleons or the Pauli exclusion principle must be considered. We follow the Smith and Moniz [78] model to treat nuclear effects. In this model the Pauli exclusion principle is explained as follows: Since nucleons are fermions, the outgoing momentum of the nucleons in the interactions is required to be larger than the Fermi surface momentum to allow quasi-elastic scattering to occur. In the NEUT library, the Fermi surface momentum is set to be $225\,\text{MeV/c}$ which is determined to reproduce the quasi-elastic peak in electron scattering, while the corresponding value in association with the Spectral function [79], more sophisticated way to treat the Pauli exclusion principle, is $209\,\text{MeV/c}$.
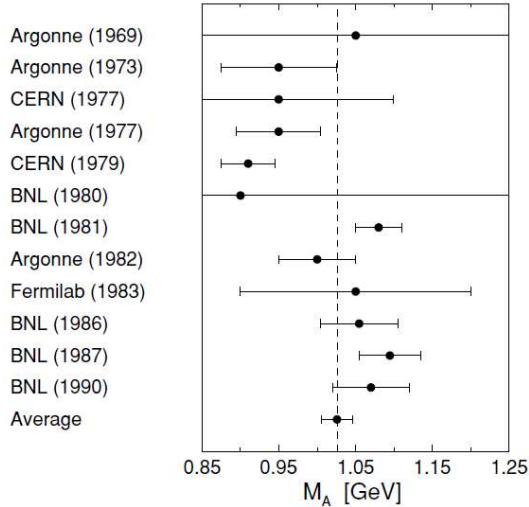
Figure 3.8: Axial vector mass M_A extractions from (quasi-)elastic neutrino and anti-neutrino scattering experiments. The weighted average except for the K2K and MiniBooNE results is $M_A=1.026\pm0.021$GeV. Figure is taken from [77].

Various theoretical models have been proposed to account for nuclear effects in the neutrino interactions at intermediate energies besides the Smith and Moniz model, for example Nieves *et al.* [80], and Nakamura *et al.* [81] and so on. These models are used to estimate the systematic uncerteinties of the neutrino interaction and nuclear effects.

The cross sections for neutral current elastic scatterings are estimated from the following relations [82, 83] :

$$\sigma(\nu p \rightarrow \nu p) = 0.153 \times \sigma(\nu n \rightarrow e^- p) \tag{3.12}$$

$$\sigma(\bar{\nu} p \rightarrow \bar{\nu} p) = 0.218 \times \sigma(\bar{\nu} p \rightarrow e^+ n) \tag{3.13}$$

$$\sigma(\nu n \rightarrow \nu n) = 1.5 \times \sigma(\nu p \rightarrow \nu p) \tag{3.14}$$

$$\sigma(\bar{\nu} n \rightarrow \bar{\nu} n) = 1.0 \times \sigma(\bar{\nu} p \rightarrow \bar{\nu} p) \tag{3.15}$$

Figure 3.9 shows the cross section of the quasi-elastic scattering for the experimental data and the calculation by the NEUT library, where solid and dashed curve indicate the scattering off free and bound nucleon, respectively.

3.3.2 Single Meson Production

The single meson productions via baryon resonances are the dominant hadron production processes in the region where the invariant mass of the hadron system (W) is less than about 2.0 GeV/c^2. Our simulation for the process is based on the model of Rein and Sehgal [90]. This model was originally developed for single pion productions, however in the NEUT library their method is extended with some modification so as to simulate single η and K productions.

This method assumes an intermediate baryon resonances :

$$\begin{aligned} \nu + N &\rightarrow l + N^* \\ N^* &\rightarrow N' + \text{meson} \end{aligned} \tag{3.16}$$
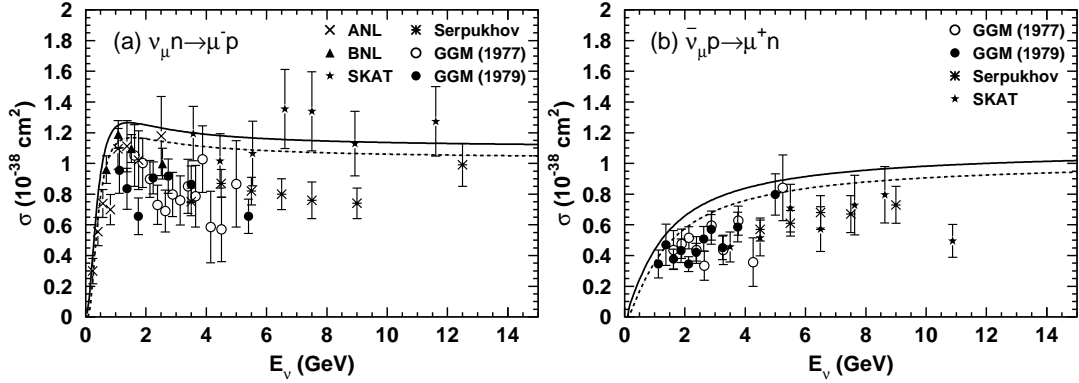
Figure 3.9: cross sections of (a) ν_μ and (b) $\overline{\nu}_\mu$ with the experimental data from ANL [84], Gargamelle [85, 86], BNL [87], Serpukhov [88] and SKAT [89].

where N and N' are nucleons and N^* is a baryon resonance. The amplitude of a baryon excitation is described as:

$$T(\nu N \rightarrow lN^\star) = \frac{G_F}{\sqrt{2}}\overline{u}_l\gamma^\mu(1 - \gamma_5)u_\nu\langle N^\star|J_\mu^{hadron}|N\rangle \tag{3.17}$$

Where $\langle N^*|J_\mu^{hadron}|N\rangle$ is the weak hadron current for this process. The matrix elements of the hadron current are calculated using FKR (Feynman-Kislinger-Ravndal) baryon model [91] in which the baryon is described by a relativistic three-body system. The differential cross section of single meson production is a product of the amplitude of each resonance production and the probability of the baryon resonance decay to this meson. For negligible decay width of a baryon resonance (N^*), the differential cross section is :

$$\frac{d^2\sigma}{dq^2dE_\nu} = \frac{1}{32\pi ME_\nu^2} \cdot \frac{1}{2} \sum_{j,spin} \left|T(\nu N \rightarrow lN_j^*)\right|^2 \delta(W^2 - M_j^2) \tag{3.18}$$

where M is the mass of the target nucleon, E_ν is neutrino energy, W is the invariant mass of the hadronic system (or the mass of the intermediate baryon resonance), and M_j is the mass of the baryon resonance (N_j^*). Intermediate baryon resonances with invariant mass W less than $2\,\mathrm{GeV/c^2}$, totally 28 resonances, and 3 background terms are considered in the simulation as listed in Table 3.1. For W larger than $2\,\mathrm{GeV}$, the interactions are simulated as deep inelastic scattering as described in Section 3.3.3.

Lepton mass effects from the non-conservation of lepton current and the pion-pole term in the hadronic axial vector current dictated by PCAC are adopted to the CC interactions [92, 93], which induce the supression of the cross section in lower Q^2.

The differential cross section for the resonance with finite decay width Γ can be derived by replacing the δ-function with a Breit-Wigner factor :

$$\delta(W^2 - M_j^2) \quad \rightarrow \quad \frac{1}{2\pi} \cdot \frac{\Gamma}{(W - M_j)^2 + \Gamma^2/4} \tag{3.19}$$

For a single meson production, the axial vector mass M_A is also set to be $1.21\,\mathrm{GeV}$ due to the same reason as (quasi-)elastic scattering.

(a) $\nu_\mu p \to \mu^- p \pi^+$

(b) $\nu_\mu n \to \mu^- n \pi^+$

(c) $\nu_\mu n \to \mu^- p \pi^0$

(d) The list of the experiments in this figure
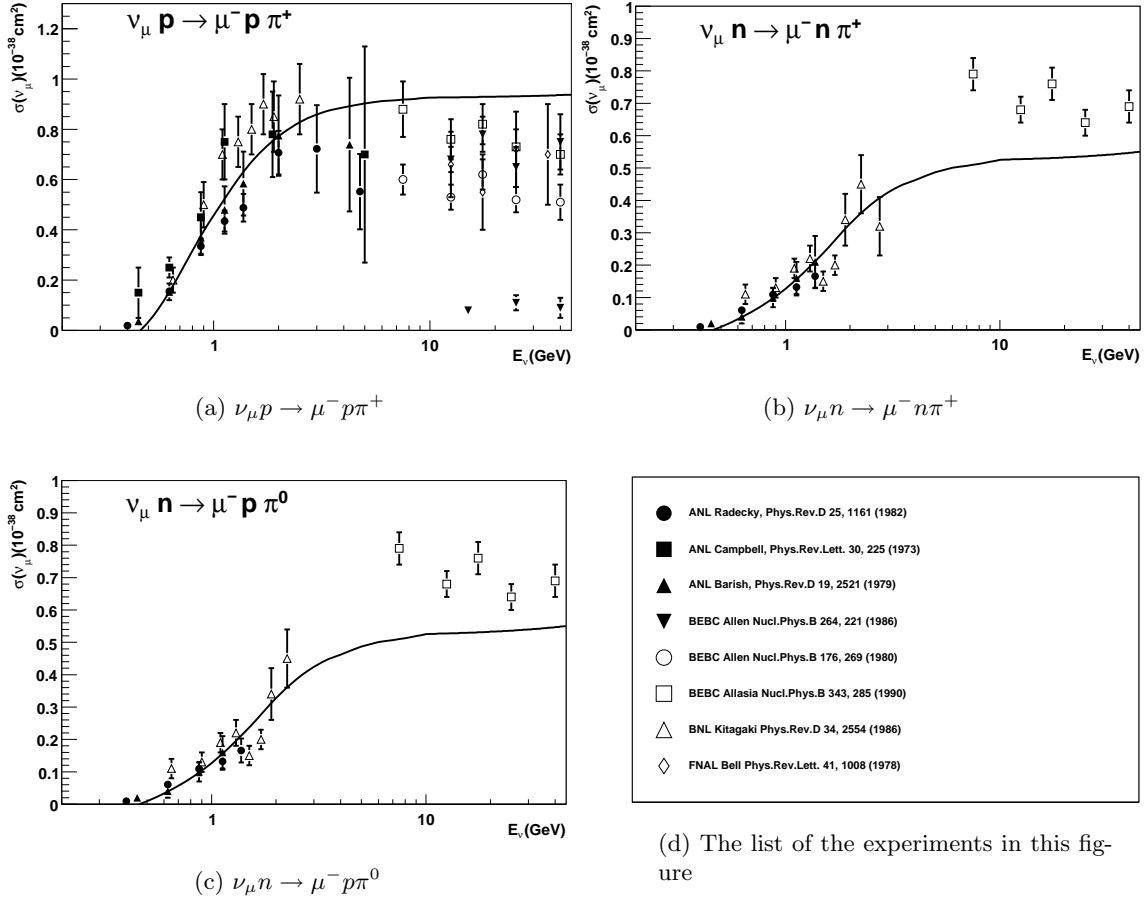
Figure 3.10: Cross sections for charged current single pion productions of ν_μ. Solid curves indicate our calculations. Experimental data are summarized in the panel (d).

To determine the angular distribution of a pion in the final state, Rein's method [94] is used for the $P_{33}(1232)$ resonance. For other resonances, the directional distribution of the generated pion is set to be isotropic in the resonance rest frame. The angular distribution of π^+ has been measured for $\nu_\mu \, p \to \mu^- \, p \, \pi^+$ [95] and the results agree well with the NEUT's prediction.

The Pauli exclusion principle in the decay of the baryon resonance is considered for the interaction off bound nucleon by requiring the momentum of the nucleon to be greater than the Fermi surface momentum.

Is is known that a baryon resonance in a nucleus can dissapear without meson emission via the following interaction:

$$N^* + N \to N' + N'' \tag{3.20}$$

where N^* is a baryon resonance and N, N', N'' are nucleons. The rate of the interactions is estimated from the theoreticl calculation [96]. In our simulation 20% of resonances in ^{16}O is assumed to dissapear without meson emission.

Figures 3.10, 3.11 and 3.12 show the cross sections of charged current and neutral current single meson productions with our calculations and the experimental data.

(a) $\overline{\nu}_\mu p \rightarrow \mu^+ p \pi^-$

(b) $\overline{\nu}_\mu n \rightarrow \mu^+ n \pi^-$

(c) $\overline{\nu}_\mu p \rightarrow \mu^+ n \pi^0$

(d) The list of the experiments in this figure
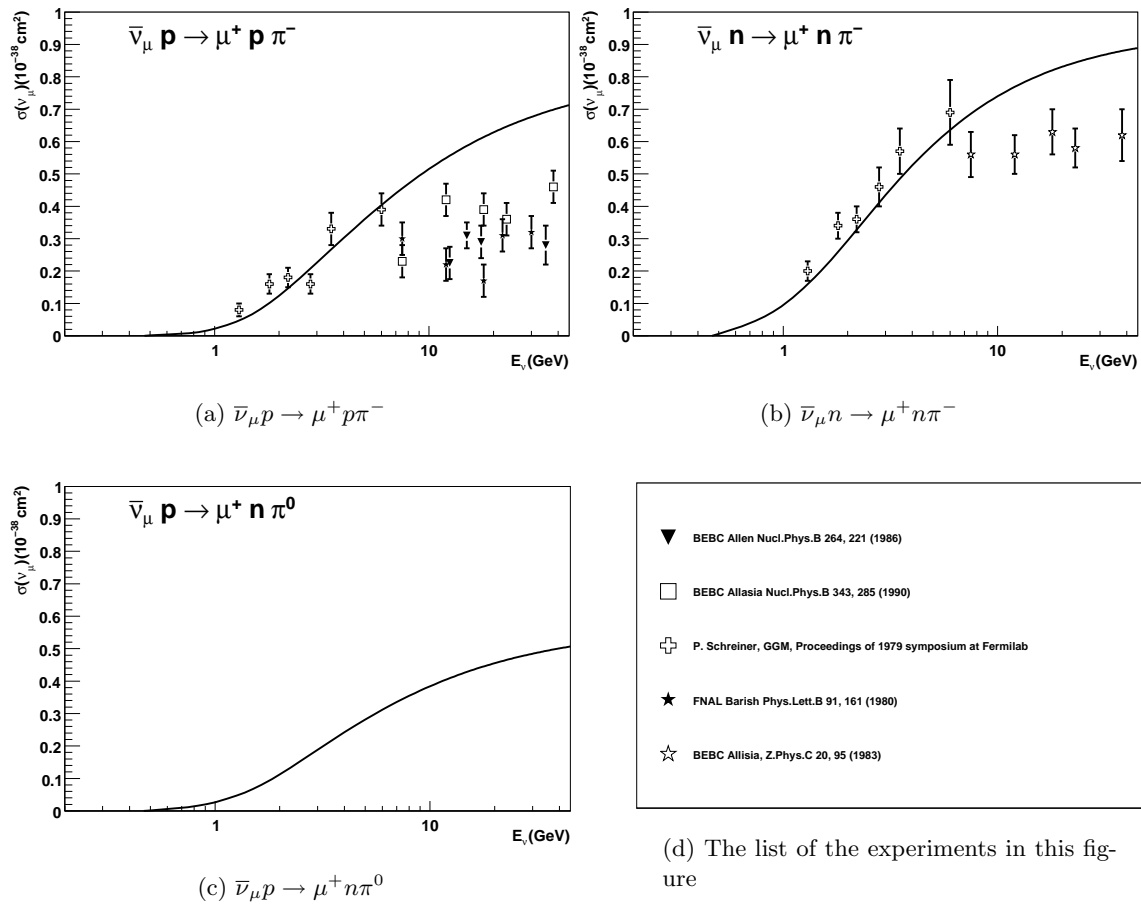
Figure 3.11: Cross sections for charged current single pion productions of $\overline{\nu}_\mu$. Solid curves show our calculations.
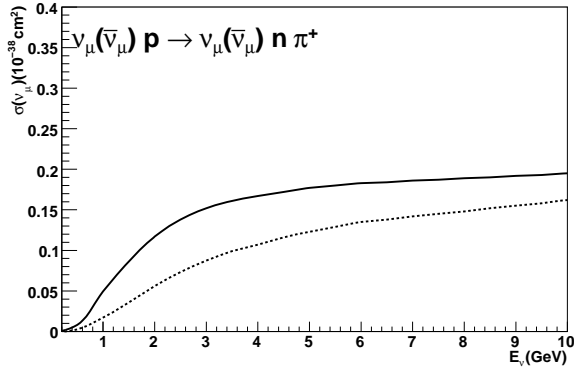
(a) Neutral current π^+ production
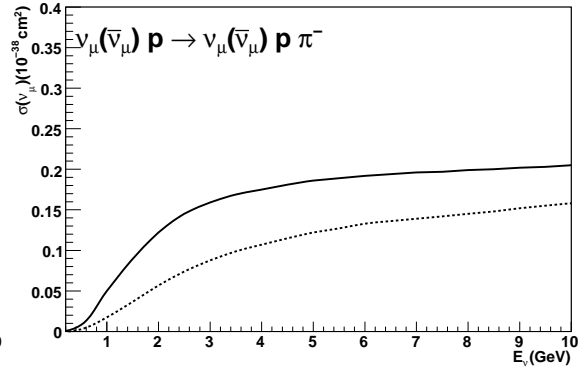
(b) Neutral current π^- production
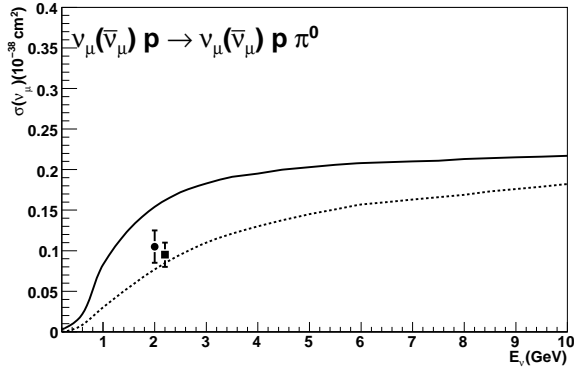
(c) Neutral current π^0 production
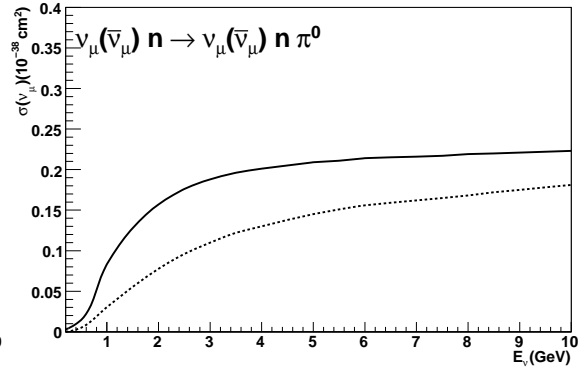
(d) Neutral current π^+ production

Figure 3.12: Cross sections for neutral current single pion productions of ν_μ (solid curve) and $\overline{\nu}_\mu$ (dashed curve). Experimental data are taken from [97] (dot) and [98] (box).

3.3.3 Deep Inelastic Scattering

The cross section of CC deep inelastic scattering is calculated by integrating the following equation in the range of the invariant mass $W > 1.3\,\mathrm{GeV}/c$ [99] :

$$
\begin{aligned}
\frac{d^2\sigma^{\nu,\bar{\nu}}}{dxdy} &= \frac{G_F^2 M_N E_\nu}{\pi}\left((1 - y + \frac{y^2}{2} + C_1)F_2(x, q^2) \pm y(1 - \frac{y}{2} + C_2)xF_3(x, q^2)\right) \\
C_1 &= \frac{yM_l^2}{4M_N E_\nu x} - \frac{xyM_N}{2E_\nu} - \frac{m_l^2}{4E_\nu^2} - \frac{m_l^2}{2M_N E_\nu x} \\
C_2 &= -\frac{m_l^2}{4M_N E_\nu x}
\end{aligned}
\tag{3.21}
$$

where x and y, Bjorken parameters, are defined as $x = -q^2/(2M(E_\nu - E_l))$ and $y = (E_\nu - E_l)/E_\nu$, M_N is the nucleon mass, m_l is the outgoing lepton mass, E_ν and E_l are the energy of incoming neutrino and outgoing lepton in the laboratory frame, respectively. The nucleon structure functions F_2 and xF_3 are taken from the Parton distribution function(PDF) GRV98 [100], where the correction function given by A. Bodek and U. K. Yang [101] are adopted to improve the implementation of the PDF in lower Q^2 region.

In our simulation, the cross section of deep inelastic scattering induced by the neutral current interactions are assumed to have the following relations which are estimated from experimental results [102, 103] :

$$
\frac{\sigma(\nu N \to \nu X)}{\sigma(\nu N \to \mu^- X)} = \begin{cases} 0.26 & (\ E_\nu < 3\,\mathrm{GeV}\ ) \\ 0.26 + 0.04\,(E_\nu/3 - 1) & (\ 3\,\mathrm{GeV} \leq E_\nu < 6\,\mathrm{GeV}\ ) \\ 0.30 & (\ E_\nu \geq 6\,\mathrm{GeV}\ ) \end{cases}
\tag{3.22}
$$

$$
\frac{\sigma(\bar{\nu} N \to \bar{\nu} X)}{\sigma(\bar{\nu} N \to \mu^+ X)} = \begin{cases} 0.39 & (\ E_\nu < 3\,\mathrm{GeV}\ ) \\ 0.39 - 0.02\,(E_\nu/3 - 1) & (\ 3\,\mathrm{GeV} \leq E_\nu < 6\,\mathrm{GeV}\ ) \\ 0.37 & (\ E_\nu \geq 6\,\mathrm{GeV}\ ) \end{cases}
\tag{3.23}
$$

The kinematics of the hadronic system is simulated by two different methods according to the range of invariant mass. In the region of $1.3\,\mathrm{GeV}/\mathrm{c}^2 < W < 2.0\,\mathrm{GeV}/\mathrm{c}^2$, only pions are considered as outgoing mesons. The mean multiplicity of pions is estimated from the result of Fermilab 15-foot hydrogen bubble chamber experiment [104] :

$$
\langle n_\pi \rangle = 0.09 + 1.83\ln(W^2)
\tag{3.24}
$$

The number of pions in each event is determined by using the KNO (Koba-Nielsen-Olsen) scaling. Since the range of W overlaps with that in single pion production, $n_\pi \geq 2$ is required in this W region. The forward-backward asymmetry of pion multiplicity in the hadronic center of mass system is included using the results from BEBC experiment [105] :

$$
\frac{n_\pi^F}{n_\pi^B} = \frac{0.35 + 0.41\ln(W^2)}{0.5 + 0.09\ln(W^2)}
\tag{3.25}
$$

In the region of $W > 2.0\,\mathrm{GeV}/\mathrm{c}^2$, the kinematics of the hadronic system are calculated by PHYTIA/JETSET package [106]. This package treats not only π but also K, η, ρ and so on.

Cross section of the CC ν_μ and $\bar{\nu}_\mu$ interactions are plotted in Figure 3.13.
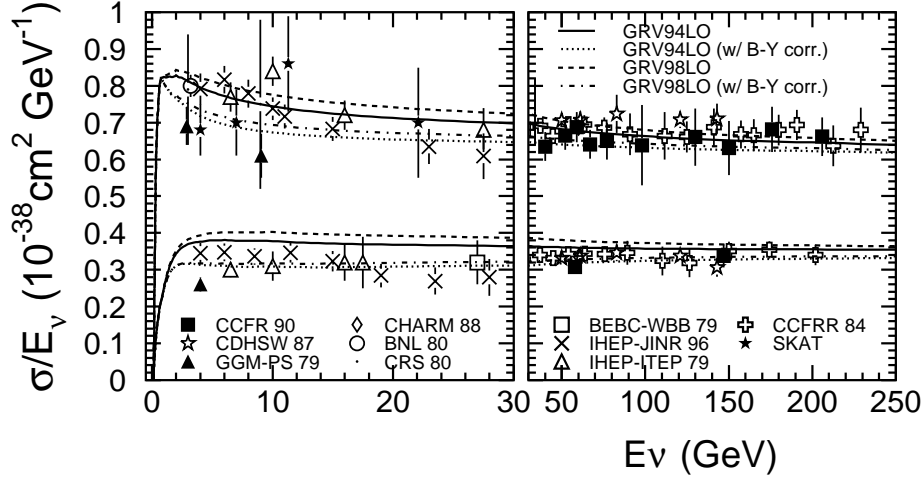
Figure 3.13: Cross sections for charged current ν_μ and $\overline{\nu}_\mu$ interactions. Upper(lower) curves are $\nu_\mu(\overline{\nu}_\mu)$.

3.3.4 Coherent Pion Production

The coherent pion production is a neutrino interaction with a oxygen nucleus, which remains intact, and one pion with the same charge as the incoming weak current is produced. Since very little momentum is transferred to the oxygen nucleus, the angular distributions of the outgoing leptons and pions are peaked in the forward direction. The formalism developed by Rein and Sehgal [107] is adopted to simulate the interactions, and the differential cross section is given by :

$$
\frac{d^3\sigma}{dQ^2 dy dt} = \beta \times \frac{G_F^2 M}{2\pi^2} f_\pi^2 A^2 E_\nu (1-y) \frac{1}{16\pi} (\sigma_{total}^{\pi N})^2
$$
$$
\times (1+r^2) \left(\frac{M_A^2}{M_A^2 + Q^2} \right)^2 e^{-b|t|} F_{abs} \tag{3.26}
$$
$$
r = Re(f_{\pi N}(0))/Im(f_{\pi N}(0)) \tag{3.27}
$$

where β is the axial vector couping constant and is 1 (2) for NC (CC) interactions, G_F is the weak coupling constant, M is the nucleon mass, f_π is pion decay constant and is $0.93\,m_\pi$, A is the atomic number ($=16$ for oxygen), E_ν is the neutrino energy, y is the lepton fractional energy loss, $\sigma_{total}^{\pi N}$ is the averaged pion-nucleon cross section, b is in the order of the nucleus transverse dimensions and is $80\,\text{GeV}^{-2}$, M_A is the axial-vector mass, Q^2 is the square of the 4–momentum transfer of the lepton, t is the square of the 4-momentum transfer to the nucleus, and F_{abs} is a t-independent factor to account for the absorption of pions in the nucleus. $f_{\pi N}(0)$ in r is the πN scattering amplitude.

The measurement by the K2K-SciBar detector sets the upper limit on the cross section of CC coherent pion production [108]. The upper limit was significantly lower than the predicted cross section by Rein and Sehgal. Therefore some modification is necessary to obtain the reasonable expectation. In NEUT library, the modification by Rein and Sehgal [109] is introduced to account
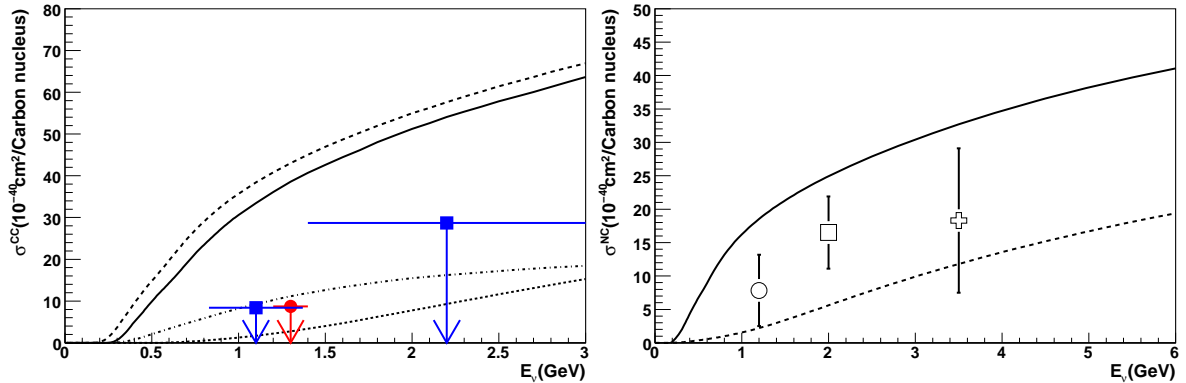
Figure 3.14: The cross sections of coherent pion production off the carbon nucleus. (Left) The charged current interaction. Solid and dashed curve indicate Rein and Sehgal with and without lepton mass effects, respectively. Dotted and dashed-dotted curve represent Kartavtsev *et al.* [110] and Alvarez-Russo *et al.* [111], respectively. The arrow indicates the experimental upper limit by K2K [108] (circle) and SciBooNE [112] (boxes). The experimental limits are converted from the cross section ratio $\sigma_{coherent}/\sigma_{CCtotal}$ with the NEUT prediction. (Right) Solid curve indicate Rein and Sehgal. Dashed curve indicate Kartavtsev *et al.*. Experimental data are taken from MiniBooNE [113] (open circle), Aachen-Padova [114] (open box) and Gargamelle [115] (open cross).

for the non-vanishing lepton masses in CC interactions which suppress the cross section, in case of ν_μ, about 25% at 1.3GeV due to the interference of the axial vector and pseudoscalar(pion-exchange) amplitudes.

3.3.5 Nuclear Effects

It is also important to simulate the secondary interactions of mesons produced in neutrino interactions with nucleons inside the ^{16}O nuclei. All of the mesons produced within the ^{16}O nuclei are tracked from their production points until they exit or are absorbed in the nuclei. This is applied to π, K and η by using a cascade model in our simulation. The interactions of pions are especially important since the cross section of neutrino interactions accompanied with pion production are large for $E_\nu > 1$ GeV, and the pion-nucleon interaction cross section is also large. The pion interactions in ^{16}O nuclei considered in our simulation are : inelastic scattering, charge exchange, and absorption. First, the initial pion production point in the nucleus, where neutrino-nucleon interactions occur, is determined by the Wood-Saxon density distribution [116] :

$$\rho(r) = \frac{Z}{A}\rho_0 \frac{1}{1 + \exp\left(\dfrac{r - c}{a}\right)} \tag{3.28}$$

where ρ_0 is the average density of the nucleus, a and c are the density parameters, Z is the atomic number, and A is the mass number. For ^{16}O nucleus : $\rho_0 = 0.48\,m_\pi^3$, $a = 0.41$ fm, $c = 2.69$ fm, $Z = 8$ and $A = 16$ [117]. A type of pion interaction is determined from the calculated mean free path of each interaction, which is modeled by L. Salcedo *et al.* [118]. The mean free path of pions depends on their momentum and positions in the nucleus. In the interactions, the
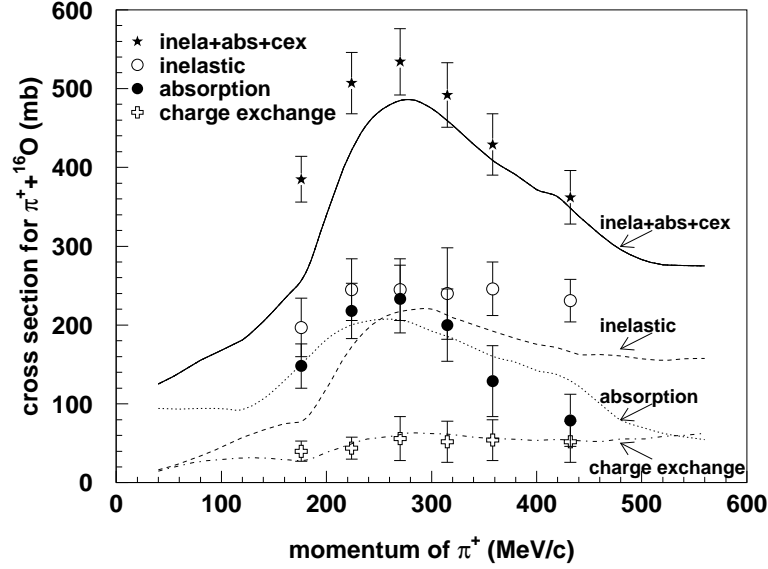
Figure 3.15: The cross sections of π^+-^{16}O scattering as a function of π^+ momentum. The lines are the cross sections calculated by our simulation for each interaction mode, and the experimental data points are taking from [121].

Fermi motion of the nucleus and the Pauli exclusion principle are considered, and the outgoing nucleon must have the energy above the Fermi surface momentum defined by :

$$p_F(r) = \left(\frac{3}{2}\pi^2\rho(r)\right)^{\frac{1}{3}}. \qquad (3.29)$$

The angular and momentum distributions of the outgoing pions are determined by using the results of a phase shift analysis from π - N scattering experiments [119]. The pion interaction simulation is tested using the experimental data for the following three interactions : π - ^{12}C scattering, π -^{16}O scattering, and pion photo-production ($\gamma+^{12}$C $\rightarrow \pi^- + X$) [120, 121] as shown in Figure 3.15. For kaons, the elastic scattering and charge exchange interactions are considered using the results from the cross sections measured by the $K^{\pm}$-N scattering experiments [122, 123, 124]. For η mesons, the absorption ($\eta N \rightarrow N^* \rightarrow \pi(\pi)N$) is considered [125]. These pions are tracked as described above.

Nucleons generated in nucleus often cause secondary interactions with nucleons bound in nucleus. The nucleon-nucleon elastic scattering cross section is based on the measurements by Bertini [126], which is used in GCALOR. The pion production caused by the decay of produced deltas is also taken into account, according to the isobar production model by Lindenbaum *et al.* [127].

Probability of nucleon-nucleon interaction in ^{16}O is shown in Fig. 3.16. The production of nucleons with nucleon momentum below 225MeV/c is suppressed by the Pauli exclusion principle. In the momentum range above 300MeV/c, a half of nucleons interact mainly by elastic scattering, therefore more than one nucleon escapes from Oxygen.

Mean deflection angle is shown in Fig. 3.17, where the nucleon momentum is from 500MeV/c to 1000MeV/c. The deflection angle has a peak around 40 degrees.
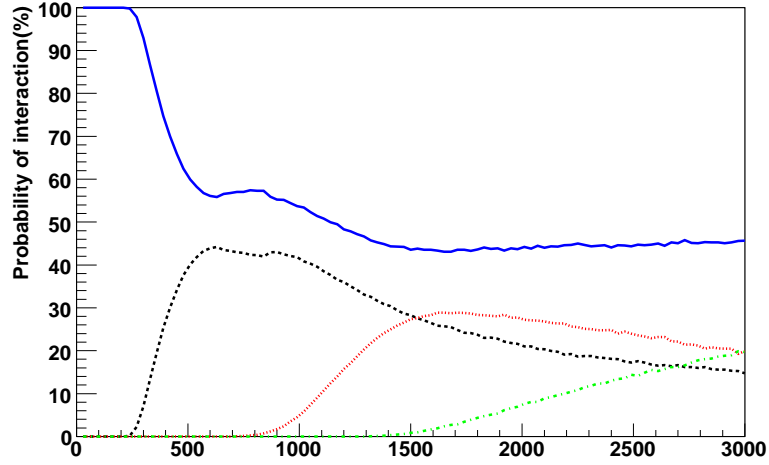
Figure 3.16: Probability of nucleon-nucleon inteactions as a function of incoming nucleon momentum(MeV/c). No interaction(solid curve), elastic scattering(dashed curve), single π production(dotted curve), and two π production(dashed-dotted curve) are plotted.
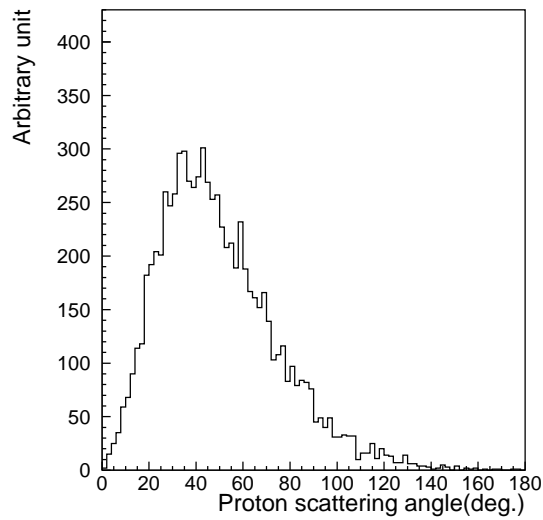
Figure 3.17: Deflection angle of proton by secondary interactions in ^{16}O nucleus. Proton momentum is distributed from 500MeV/c to 1000MeV/c.

44

The concept of formation zone(length) is also considered for all hadrons produced in nucleus. This is a distance or time from the neutrino interaction point to the hadron production point. The intermediate states are assumed to be non-bound quark states. The formation length of each hadron is expressed as follows:

$$L = p/\mu^2 \tag{3.30}$$

where p is the momentum of tha hadron and μ^2=0.08GeV^2 is a fitted constant from the SKAT experiment [128]. We can see the nucleon-nucleon intearction in nucleus has large effect and results in the significant distortion of the geometry of particles observed in the detector.

3.4 Detector Simulation

The produced particles in neutrino interactions are fed into a detector simulation code, which simulates (1) the tracks of particles, (2) the generation and propagation of Cherenkov photons in water, and (3) the PMT response and the readout electronics.

3.4.1 Particle Tracking

The detector simulation has been developed based on the GEANT package [129]. Table 3.2 lists various processes which are considered in our simulation program. The hadronic interactions in water are simulated using the CALOR package [130]. This package is known to reproduce the pion interactions well including low energy region ($\sim 1\,\mathrm{GeV}/c$). For still lower energy region ($p_\pi \leq 500\,\mathrm{MeV}/c$), a custom program [131] based on experimental data from $\pi-^{16}$O scattering [132] and $\pi - p$ scattering [133] is used in our simulation code.

The uncertainty in the hadron simulation is estimated by comparing the model used in our detector simulation, CALOR [130], and the FLUKA model. The uncertainty affects the contamination of NC interactions, especially for the ν_μ-enriched samples. The difference from the FLUKA model is assumed to be a systematic error.

The number of generated Cherenkov photons, the direction of each photons and its wavelength are calculated using Eq.(2.2) and Eq.(2.3). The Cherenkov photons are only generated between 300nm and 700nm because PMTs are only sensitive to this region.

3.4.2 Cherenkov photon tracking in water

We take into account the dispersion of the refractive index. The group velocity

$$v_g = \frac{c}{n(\lambda) - \lambda\frac{\partial n(\lambda)}{\partial \lambda}} \tag{3.31}$$

where c is light velocity in vacuum, λ is light wavelength, is used for the light velocity in the water. The generated Cherenkov light can be scattered and absorbed in water. The water transparency as a function of wavelength is determined as follows:

Short wavelength
The relation

$$C \propto \lambda^{-4} \tag{3.32}$$

is employed, where C is the scattering coefficient and λ is wavelength. If the size of particles with which a Cherenkov photon interacts is small compared to the wavelength, the scattering length is propotional to the fourth power of light wavelength. This is Rayleigh scattering.

Long wavelength

We use the data taken from [134].

The absolute water transparency is determined to be consistent with the direct measurement of pure water. When the Cherenkov light arrives at the surface of a PMT or black sheet, reflection on the surface can occur. The calculated reflection value, including the polarization, is used for the simulation. The reflection by black sheet is calculated and measured in water, which are consistent each other.

3.4.3 Response of the PMT

The average value of the collection efficiency of PMT is treated as a tunable parameter. This is used for the final adjustment of the entire scale.

Charge and timing resolution of PMTs are considered. The charge value of each hit PMTs is simulated by the random number distributed to follow the measured one photon distribution shown in Figure 2.7. The timing distribution dependent on the charge is measured using a laser. In the simulation, the timing of each PMT is a Gaussian random variable with the sigma shown in Figure 4.5.

3.5 Upward-Going Muon

Upward-going muon (UPMU) is the event which muon produced by the charged current interactions of the upward-going muon neutrinos enters the inner detector. For such events, there are two targets in the neutrino interactions: water in the outer detector and rock around the entire Super-Kamiokande detector. About 85% of UPMU events are induced by the interaction in rock, and the others are in water. Hereafter, we mention only the case in rock, since the interaction in water is identical to the simulation we saw above.

As for the neutrino interaction taking place in the rock, the follwing rock profiles are assumed in the simulation, $\rho = 2.65\text{g/cm}^3$, $Z = 11$, and $A = 22$. These profiles are based on the "standard rock" [135]. The propagation of daughter muons through rock is simulated by the routines developed by [136].

Each UPMU has an associated volume through which it may traverse

$$V^\mu(E_\mu) = \frac{4\pi}{3} R_{eff}^3 \qquad (3.33)$$

where $R_{eff}(E_i, E_{min})$ is the effective muon range, E_i is the initial UPMU energy, and $E_{min} = 1.6\text{GeV}$ is the energy threshold for UPMU event. The effective detection volume V_{eff}, consisting of the rock around the detector which is much bigger than the detector volume, is given by the product of the effective detector area $A_{eff}(\theta)$ as a function of zenith angle θ and the muon range $R_{eff}(E_i, E_{min})$.

$$V_{eff}(E_0, \theta, E_{min}) = A_{eff}(\theta) R_{eff}(E_i, E_{min}) \qquad (3.34)$$

Effective area is approximately 1200 m^2 for all θ.

We are thus able to constrain the volume around the detector for which events can be generated by requiring that for each event the ratio of V_{eff} to $V^\mu(E_\mu)$ exceeds a random number on [0,1] (denoted as ζ).

$$V_{eff}(E_0, \theta, E_{min})/V^\mu(E_\mu) > \zeta \qquad (3.35)$$

46

We can visualize this requirement by embedding the volume associated with V_{eff} inside $V^\mu(E_\mu)$. We pick random point inside $V^\mu(E_\mu)$ and accept it if and only if it also lies within V_{eff}.

Resonance/Background	Msss(GeV/c)	Width(GeV/c)
$P_{33}(1234)p,n$	1.232	0.115
$D_{13}(1525)p$	1.520	0.125
$D_{13}(1525)n$	1.520	0.125
$S_{11}(1540)p$	1.535	0.150
$S_{11}(1540)n$	1.535	0.150
$S_{31}(1620)p,n$	1.620	0.140
$S_{11}(1640)p$	1.650	0.150
$S_{11}(1640)n$	1.650	0.150
$D_{13}(1670)p$	1.700	0.100
$D_{13}(1670)n$	1.700	0.100
$D_{15}(1680)p$	1.675	0.155
$D_{15}(1680)n$	1.675	0.155
$D_{33}(1730)p,n$	1.700	0.250
$P_{11}(1450)p$	1.440	0.200
$P_{11}(1450)n$	1.440	0.200
$P_{33}(1640)p,n$	1.600	0.370
$F_{15}(1680)p$	1.680	0.125
$F_{15}(1680)n$	1.680	0.125
$P_{11}(1710)p$	1.710	0.110
$P_{11}(1710)n$	1.710	0.110
$P_{13}(1740)p$	1.720	0.200
$P_{13}(1740)n$	1.720	0.200
$P_{31}(1920)p,n$	1.910	0.220
$F_{35}(1920)p,n$	1.905	0.300
$F_{37}(1950)p,n$	1.950	0.240
$P_{33}(1960)p,n$	1.920	0.250
$F_{17}(1970)p$	1.990	0.325
$F_{17}(1970)n$	1.990	0.325
Background Proton	0.940	3.000
Background Neutron	0.940	3.000
Background J=3/2	0.940	3.000

Table 3.1: List of resonances and background terms taken into account

γ	(e^+, e^-) pair production
	Compton scattering
	Photoelectric effect
$e^\pm$	Multiple scattering
	Ionization and δ-rays production
	Bremsstrahlung
	Annihilation of positron
	Generation of Cherenkov radiation
$\mu^\pm$	Decay in flight
	Multiple scattering
	Ionization and δ-rays production
	Bremsstrahlung
	Direct (e^+, e^-) pair production
	Nuclear interaction
	Generation of Cherenkov radiation
Hadrons	Decay in flight
	Multiple scattering
	Ionization and δ-rays production
	Hadronic interactions
	Generation of Cherenkov radiation

Table 3.2: List of the processes considered in simulator.

Chapter 4

Calibration

4.1 Relative Gain Calibration

The high voltage value of each PMT is set to provide approximately uniform gain for all PMTs in the detector. The uniformity of the PMT gain is necessary to determine the momentum without systematic difference depending on its vertex position or direction.

Figure 4.1 shows a schematic view of the relative gain calibration system. Light generated by a Xe lamp is passed through an ultraviolet (UV) filter and neutral density (ND) filter and then split into four. One is injected into a scintillator ball via an optical fiber. The others are used to monitor the intensity of the Xe light and to make a calibration trigger. The scintillator ball is made of acrylic resin mixed with BBOT wavelength shifter and MgO powder diffuser. BBOT wavelength shifter absorbs UV light and emits light with a peak at 440 nm, which is a typical wavelength of Cherenkov light.

The high voltage value of each PMT is adjusted to give the same gain with the others. The relative gain G_i of the i-th PMT is obtained by :

$$G_i = \frac{Q_i}{Q_0 f(\theta)} \cdot l_i^2 \cdot \exp\left(\frac{l_i}{L}\right) \tag{4.1}$$

where Q_i is the charge detected by the i-th PMT, l_i is the distance from the light source to the PMT, $f(\theta)$ is the PMT acceptance as a function of the photon incidence angle θ, L is the attenuation length and Q_0 is the normalization factor. This measurement is performed for several positions of the scintillator ball, changing the voltage.

Figure 4.2 shows the relative gain distribution of all the PMTs after adjusting high voltage values. The relative gain spread is about 7 %. The remaining gain difference is corrected in software.

4.2 Absolute Gain Calibration

The absolute gain calibration is necessary to convert the charge detected by each PMT in pico Coulomb (pC) into the number of photoelectrons. The absolute gain is determined using the charge distribution of single photoelectron signals.

The low energy γ-ray generated from neutron capture on Nickel nucleus is used as a calibration source to measure the single photoelectron distributions. The schematic view of the Nickel
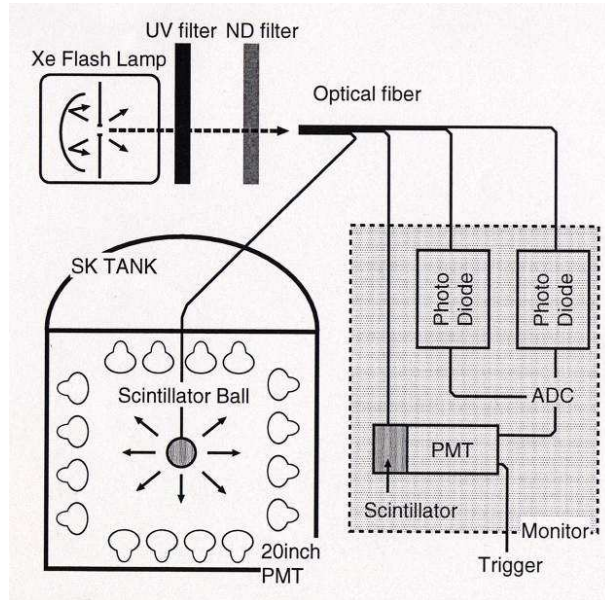
Figure 4.1: A schematic view of the relative gain measurement system using a Xe lamp.
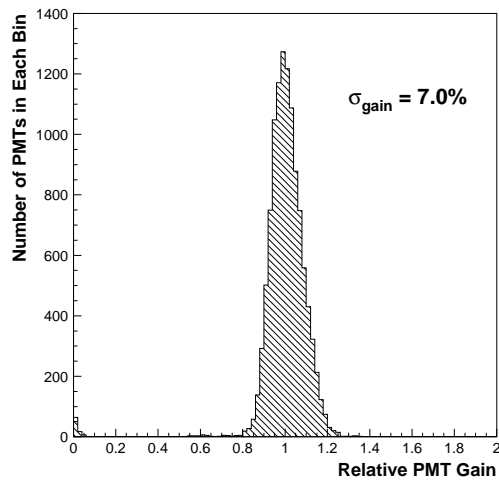
Figure 4.2: The relative gain distribution of all the ID PMTs, measured in 1996.
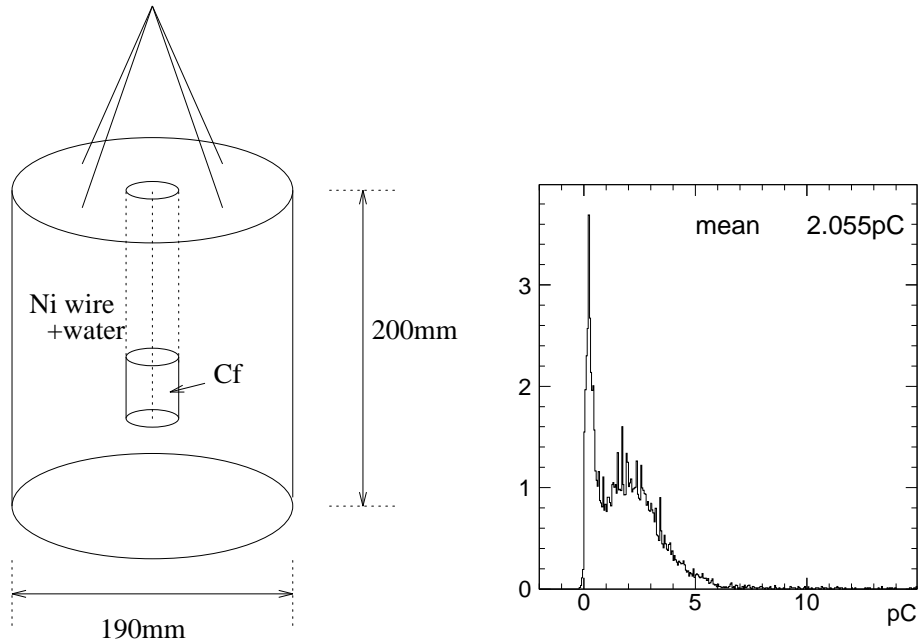
Figure 4.3: Schematic view of an Nickel calibration source (left) and charge distribution of a typical ID PMT (right).

calibration source is shown in Figure 4.3. Neutrons produced by spontaneous fission of ^{252}Cf are captured on surrounding Ni wires in polyethylene vessel, and low energy ($6 \sim 9\,\mathrm{MeV}$) γ-rays are generated simultaneously. The number of hit PMT is about $50 \sim 80$ in total, so that the number of p.e. detected by each PMT is at most one. The charge distribution of a typical PMT is also shown in Figure 4.3. The sharp peak near zero is caused by electrons that are emitted from the photocathode but miss the first dynode, and the peak around $2\,\mathrm{pC}$ corresponds to that of single photoelectrons. The mean value $2.055\,\mathrm{pC}$ is used as a constant to convert the PMT charge from pico Coulomb to the number of p.e.s.

4.3   Relative Timing Calibration

The relative timing calibration is important for the vertex position reconstruction. The timing response of the PMT depends on not only the length of the signal cable but also the detected charge because of the slewing effect of discriminator. The large signal tends to exceed the threshold earlier than the small one.

Figure 4.4 shows the schematic view of the relative timing calibration system. N_2 laser generator emits intense light with $337\,\mathrm{nm}$ wavelength within a time width of $3\,\mathrm{nsec}$. The wavelength of the laser light is converted to $384\,\mathrm{nm}$ by a dye laser module. The PMT is most sensitive to this wavelength. Then the light is split into two. One is injected into a diffuser ball in the ID via an optical fiber and the other is used to monitor the light intensity. The schematic view of the diffuser ball is also shown in Figure 4.4. The laser light injected to the diffuser ball is first diffused by a TiO_2 diffuser tip at the center and then further diffused by the surrounding
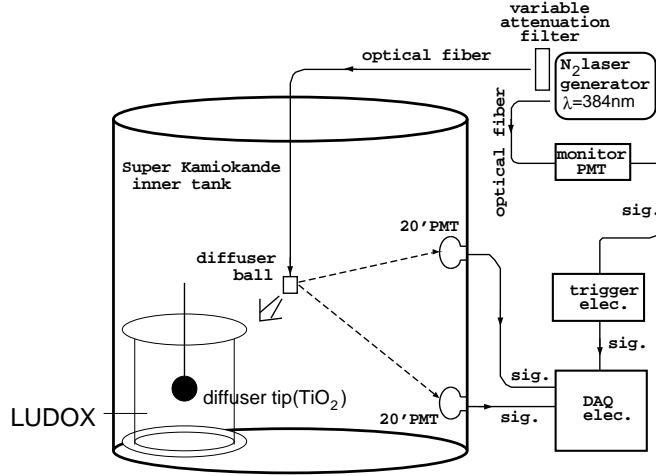
Figure 4.4: A schematic view of the timing measurement system using a laser.

LUDOX silica gel made of 20 nm glass fragments. The PMT timing response is measured with various light intensity from 1 p.e. to a few hundreds of p.e. using an adjustable attenuation filter. The results are shown as a scatter plot of the timing and the charge called TQ-map in Figure 4.5. Each dot represents one measurement, and the open circles are the average timing with respect to charge for a PMT.The TQ-map is made for all ID PMTs and used to correct the timing information.

4.4 Water Transparency Measurement

Water transparency is the length scale of the optical attenuation in water, which represents the combined effect of absorption and scattering on the intensity of the light. Water transparency in Super-Kamiokande is measured using N_2 laser beam injected into the detector. The wavelength dependence of the attenuation length can be measured by changing the dye of the laser. The absorption and scattering coefficients are separately measured by this method. Further, the water transparency is independently measured using Cherenkov light from cosmic ray muons. The time variation of the water transparency can be monitored by this method without disturbing the normal data taking.

4.4.1 Light scattering measurement using a laser

The light attenuation length in water can be described as $L = (\alpha_{abs} + \alpha_{scat})^{-1}$, where α_{abs} and α_{scat} are the absorption coefficient and scattering coefficient, respectively. The absorption and scattering coefficients are separately measured using a N_2 laser [137]. Figure 4.6 shows a schematic view of the measurement system. Each laser, wavelength of 337, 371, 400 and 420 nm, fires every 6 seconds during normal data taking. The light from the laser is injected into the ID via an optical fiber toward the bottom of the tank. A typical event by the laser light is also shown in Figure 4.6. The PMT hits clustered at the bottom of the tank are due to the direct (unscattered) photons.
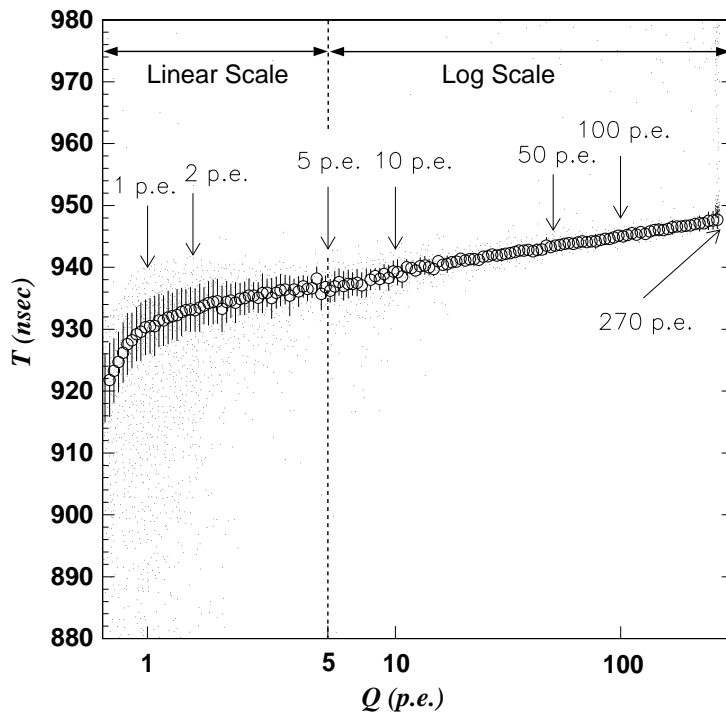
Figure 4.5: TQ-map, a measured two-dimensional plot of timing vs. charge distribution.
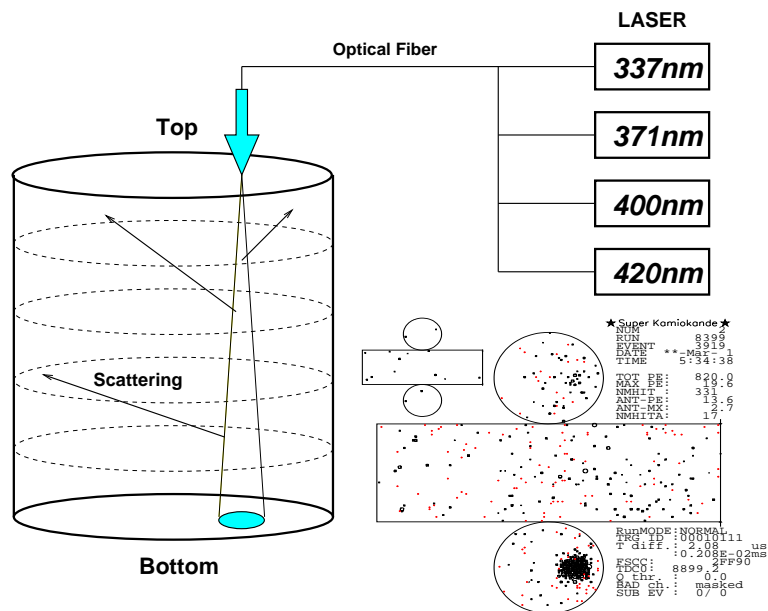
Figure 4.6: A schematic view of the scattering and absorption parameter measurement using laser systems, and a typical laser event.
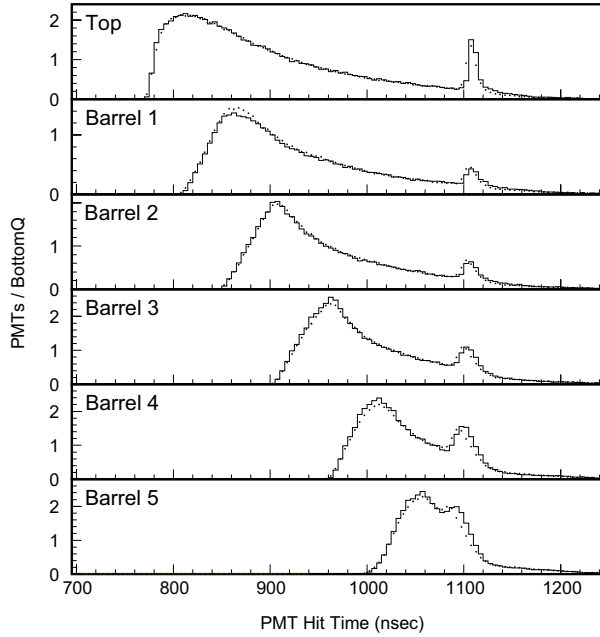
Figure 4.7: PMT hit time distributions of 337 nm-laser events in each detector region for the data (dots) and the Monte Carlo events which is tuned by the scattering and absorption parameters (histograms).

In the analysis, the detector is separated into 6 regions, top and 5 in barrel, as shown in Figure 4.6. The total charge of bottom PMTs is used for the normalization of the light intensity. Figure 4.7 shows the PMT hit timing distributions in each region for data and Monte Carlo simulation. These PMT hits on the top and barrel wall are due to the photons scattered in water, or the photons reflected by surfaces of bottom PMTs or black sheets. The first peaks and slopes are characterised by the absorption and scattering coefficients and the second peaks around 1100 nsec are due to the photons reflected by the PMTs or black sheets. For the Monte Carlo simulation, the absorption and scattering coefficients are adjusted so that the PMT hit time distributions are in agreement with data. The attenuation length in water is calculated using the measured absorption and scattering coefficients.

The attenuation coefficients (L^{-1}) obtained by this method are plotted in Figure 4.8 with a star symbol. The lines shows a model used in the Monte Carlo simulation, which are determined by fitting the measurements from this method.

4.4.2 Measurement using cosmic ray muons

Water transparency is also measured by using Cherenkov light from cosmic ray muons passing through the detector. Since the energy deposit of such a energetic muon is almost constant (about 2 MeV/cm), cosmic ray muons can be used as a calibration source.

Only vertical downward muons are selected for this measurement. The muon track is reconstructed by connecting the entrance and the exit points in the ID. Under the assumption that the light detected by each PMT is not scattered, the detected charge (photoelectrons) is
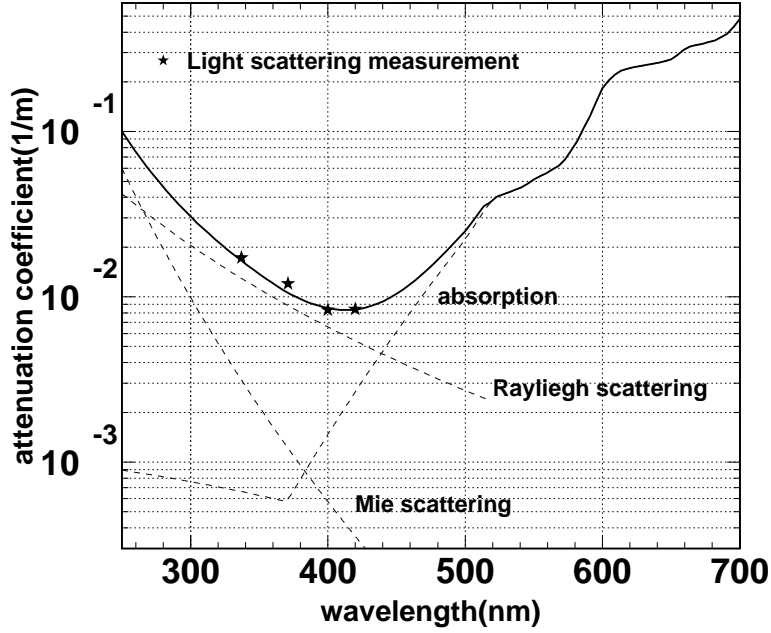
Figure 4.8: Wavelength dependence of attenuation coefficients (L_{atten}^{-1}) obtained by the light scattering measurement (points) together with a model in the detector simulation (lines, see Chapter 3.4).

expressed by :

$$Q = Q_0 \cdot \frac{f(\theta)}{l} \cdot \exp\left(-\frac{l}{L}\right) \tag{4.2}$$

where Q_0 is a constant, $f(\theta)$ is the PMT acceptance, l is the photon path length and L is the attenuation length. The left panel on Figure 4.9 show the schematic view of the measurement. The right panel on Figure 4.9 shows $\log\left(Q \cdot l/f(\theta)\right)$ as a function l in a typical run. The attenuation length is estimated to be 95 m for this data set.

Since the cosmic ray muons are measured during the normal data taking, continuous check of the water transparency is possible by this method. Figure 4.10 shows the time variation of the attenuation length. This time variation is corrected in event reconstruction processes.

This measurement also works for the tuning of the charge scale of the Monte Carlo simulation. Figure 4.11 shows the intersection of the effective observed charge at $l \to 0$ in the right panel on Figure 4.9 as a function of elapse days. The variation of the attenuation length is negligible at the small path length, so the effective observed charge at $l \sim 0$ is stable during the data taking. The charge scale (intersection) of the Monte Carlo simulation is adjusted to be consistent with the measured value by changing the number of photons generated by the traversing charged particle and the acceptance of PMT, where the acceptance is defined to be independent of the photon incident angle. The charge scale is adjusted within 0.4% between the Monte Carlo simulation and data. The residual of the adjustment is smaller than the statistical error of data.
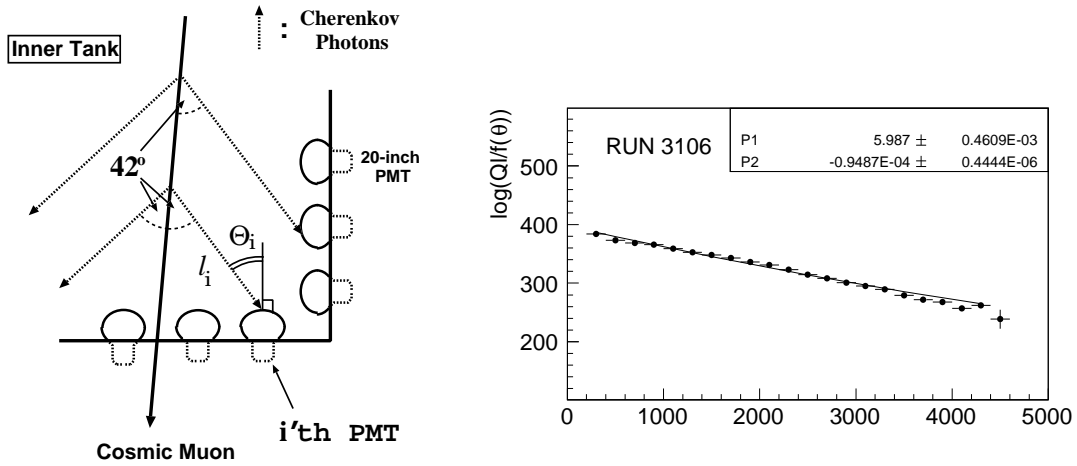
Figure 4.9: (Left) Schematic view of the attenuation length measurement using vertically penetrating cosmic ray muons. Dotted arrows show the trajectories of Cherenkov photons and l_i shows the flight length of the Cherenkov photons detected by the i-th PMT. (Right) Effective observed charge ($\log(Ql/f(\theta))$) for through-going muons as a function of the photon path length (l) where Q is the detected charge and $f(\theta)$ is the PMT acceptance.
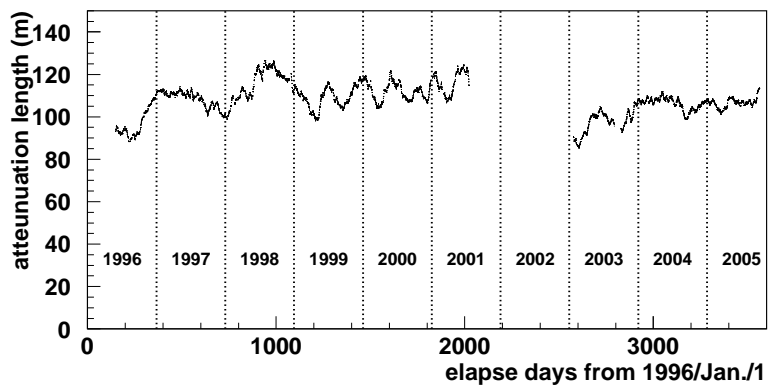
Figure 4.10: Time variation of water attenuation length.

57
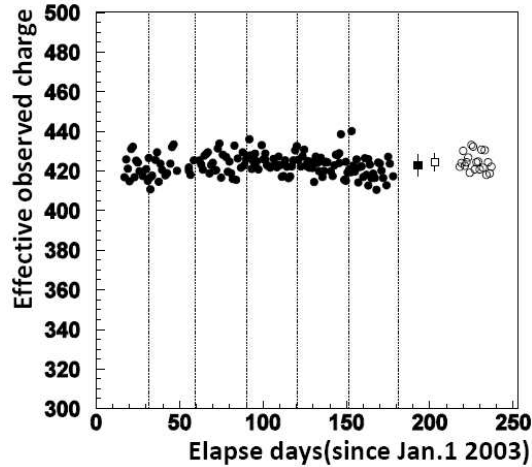
Figure 4.11: Effeftive charge $\log(Ql/f(\theta))$ at $l \to 0$ as a function of elapse days. Black circle is the observed data and black box is the average of the data with RMS. White circle is the Monte Carlo simulation and white box is its average with RMS. This figure is the case for SK-II.

4.5 Absolute Energy Calibration

The momentum of a particle is determined by the charge information of PMTs. Since the systematic uncertainty in the absolute energy scale affects the atmospheric neutrino analysis, it is essential to understand the absolute energy scale as accurte as possible. Four kind of methods are employed in momentum range from a few tens of MeV/c to about $10 \, \mathrm{GeV/c}$ by using independent calibration sources: decay electrons from stopping muons, π^0 events, low and high energy stopping muons.

The residuals between the data and Monte Carlo simulation are not corrected in the analysis, but are combined with the time variation of the energy scale, and considered as the systematic uncertainty in the absolute energy scale calibration.

4.5.1 Decay electrons

Many electron events produced by the decay of cosmic ray muons are observed in Super-Kamiokande. The energy and angular spectrum of the electron is expressed as

$$\frac{1}{\Gamma}\frac{\Gamma}{dx\,d\cos\theta} = 4x^2\left[3x(1-x) + \frac{2}{3}\rho(4x-3) - P_\mu\xi\cos\theta\left(1-x+\frac{2}{3}\delta(4x-3)\right)\right] \qquad (4.3)$$

where P_μ is the polarization of muon, $x = (2E_e/m_\mu)$, and θ is the angle between the spin of muon and the electron momentum. ρ, ξ and δ are called as the Michel parameters. In the $V - A$ theory, the Michel parameters are

$$\rho = \delta = \frac{3}{4}, \quad \xi = 1 \qquad (4.4)$$

x is restricted to be less than 1, so the electon produced by the muon decay is distributed up to $\sim m_\mu/2. \sim 53$ MeV, which is so called the Michel spectrum. The validity of this formula has
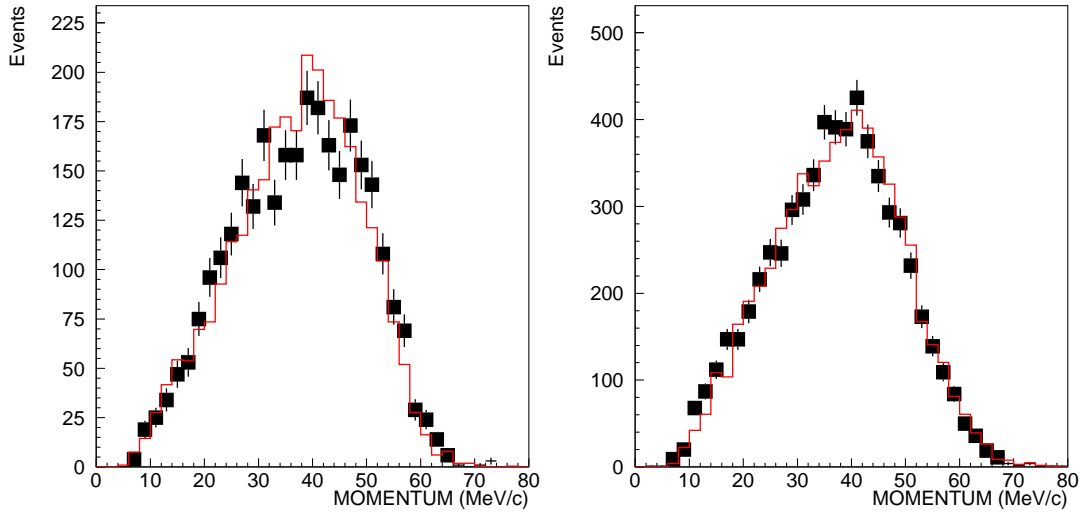
Figure 4.12: The momentum distribution of decay electrons of the data (dot) and the Monte Carlo (line) for SK-I (left) and SK-II (right). Monte Carlo events are normalized by the number of observed data.

been confirmed by the various high precision experiments using the polarized muon beam, for example [138]. Thus the well known energy spectrum are used to check the absolute energy scale by comparing the energy spectrum between the observed data and Monte Carlo simulation.

Decay electrons are selected by the following criteria :

1. The time interval from a stopping muon event is $1.5\,\mu$sec to $8.0\,\mu$sec.

2. The number of hit PMT in a $50\,$nsec time window is larger than $60(30)$ for SK-I (SK-II).

3. The goodness of the vertex fit is greater than 0.5.

4. The vertex position is reconstructed more than $2\,$m away from the ID wall.

Figure 4.12 shows the momentum spectra of decay electrons compared with the prediction from the Monte Carlo simulation. The momentum distribution is distorted from the Michel spectrum, for example as clearly seen in the tail of the spectrum extending up to ∼70 MeV. This is caused by the case of μ^- in which almost all μ^- is trapped by a oxygen atom in K-shell orbit and the decay electron is influenced by electric potential of the oxygen nuclei and orbital motion of the parent μ^- [139]. Criterion (2) rejects ∼6 MeV γ-rays from μ^- capture on the nucleon. In the simulation, measured μ^+/μ^- ratio of 1.37 [140] and the effect of μ^- capture by oxygen nuclei are considered.

We use the vertex fitter which has been devised and developed for the low energy neutrino observations such as solar and supernova neutrinos [141]. In this fitter, the vertex of electron is reconstructed using the timing information of hit PMTs, where the timing resolution of PMT is taken into account. In the ideal case the goodness becomes 1.

The mean values of data agree with the Monte Carlo prediction within $0.6\,\%(1.6\,\%)$ for SK-I (SK-II).

4.5.2 Neutrino induced π^0 events

The π^0 events produced in the interactions of the atmospheric neutrino are used for the energy scale calibration in the several hundred MeV energy range. Since a π^0 decays immedeately into two γ-rays, the invariant mass of π^0 is obtained by the reconstructed momentum of two γ-rays, $P_{\gamma 1}$ and $P_{\gamma 2}$, and the opening angle θ as follows:

$$M_{\pi^0} = \sqrt{2P_{\gamma 1}P_{\gamma 2}(1 - \cos\theta)} \tag{4.5}$$

The π^0 events are selected from the atmospheric neutrino sample by the following criteria :

1. Two Cherenkov rings are recognized and both of them are identified as electron-like.

2. Electrons from muon decay is not detected.

3. The vertex position is reconstructed more than $2\,\mathrm{m}$ away from the ID wall.

Criterion (2) rejects the contamination of $\pi^+\pi^0$ or $\mu^{\pm}\pi^0$ events. A typical π^0 event is displayed in Figure 4.13. Figure 4.14 shows the invariant mass distribution of π^0 events, which is compared with the prediction from the Monte Carlo simulation. A peak of the mass distribution, for example in SK-I they are 139.5MeV/c (data) and 138.7MeV/c (MC), is slightly shited from the π^0 mass ~ 135MeV/c toward a higher mass because of mainly two reasons: First, when a π^0 is produced in the oxygen nucleus, the remaining nucleus is often left in the excited state and then emit the de-excitation γ-rays which add a small number of photons, i.e. energy, to an event. Second, the two γ-rays as decay products of a π^0 do not convert into the electromagnetic showers right after the decay. Thus the reconstructed vertex tends to be pulled toward the particle direction. This causes the reconstructed opening angle of the two γ-rays to be slightly larger than the true opening angle, resulting in the larger π^0 invariant mass. The de-excitation of oxygen nucleus is considered in the Monte Carlo simulation.

The peak position of the data is $0.6\,\%(1.6\,\%)$ higher than that of the Monte Carlo simulation for SK-I (SK-II).

4.5.3 Low energy stopping muons

The Cherenkov angle of charged particles is expressed as a function of the momentum:

$$\cos\theta_C = \frac{1}{n\beta} = \frac{1}{n}\sqrt{1 + \frac{m^2}{p^2}} \tag{4.6}$$

where θ_C, n, β, m and p are the Cherenkov angle, the refraction index of water, v/c, mass and momentum. Since the Cherenkov angle has a large dependence on the momentum for low energy stopping muons ($< 400\,\mathrm{MeV/c}$), the momentum can be estimated by measuring the Cherenkov angle. The momentum estimated from the detected charge ($\mathrm{P}_{p.e.}$) is used to check the systematic uncertainty in the momentum determination by comparing it with the momentum derived from the Cherenkov angle (P_θ). This method is not applicable to the electrons or the high energy muons because the Cherenkov angle approaches a limit when the momentum is high compared to its mass. Low momentum stopping muon events are selected for this study by the following criteria:
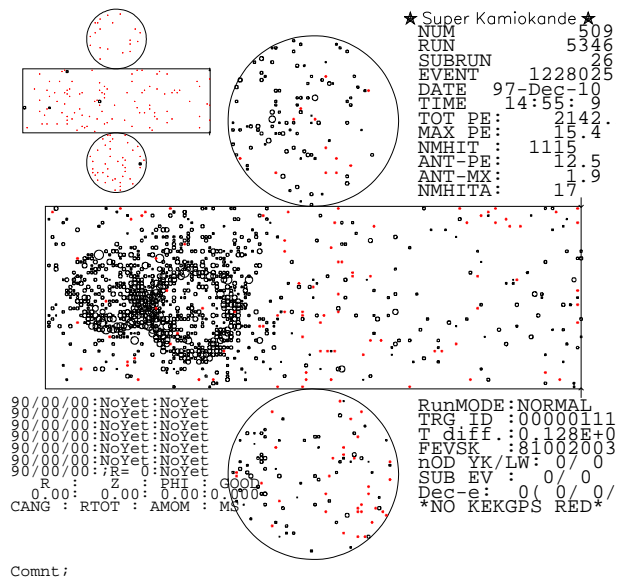
Figure 4.13: A typical π^0 event. Two Cherenkov rings from the γ-rays are found.
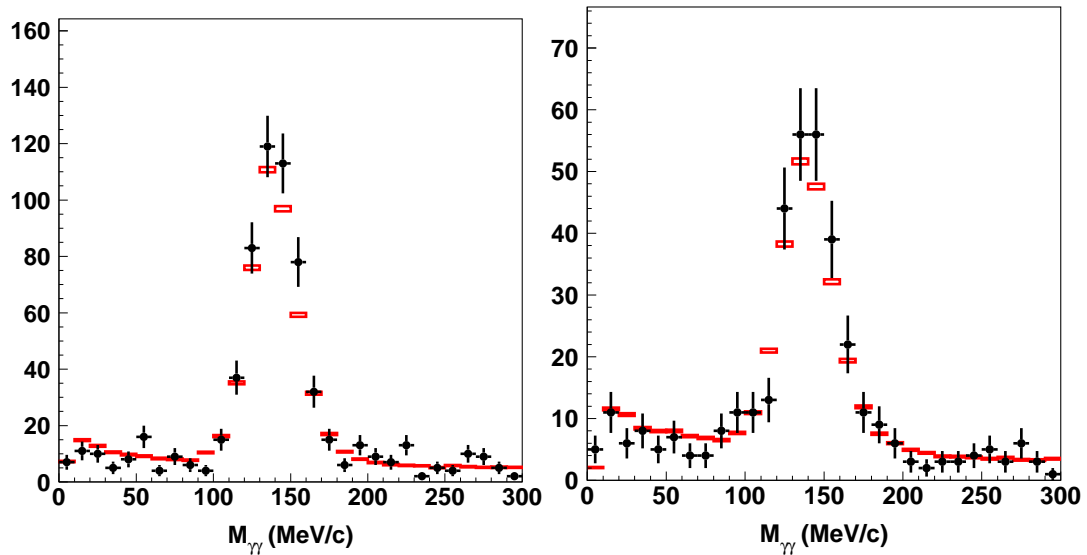
Figure 4.14: Invariant mass distribution of neutrino induced π^0 events of the observed data (dot) and the atmospheric neutrino Monte Carlo events (boxes) for SK-I (left) and SK-II (right). The peak position is fitted by a Gaussian distribution. Monte Carlo events are normalized by the livetime of observed data.

1. The total number of p.e.s in the ID is less than 1500 p.e.s for SK-I (750 for SK-II)

2. One cluster of hit PMTs in the outer detector.

3. The entrance point is on the top wall.

4. The direction is downward ($\cos\theta > 0.9$).

5. One decay electron event is detected.

Criterion (1) selects low momentum muon events. Criterion (2) requires an entrance point of a muon in the OD, namely the stopping muons. Criteria (3) and (4) select the muon events which are straight downgoing.

The upper left panel on Figure 4.15 shows the reconstructed momentum distribution for the events passed through the above criteria. On the other hand, the upper right panel shows the reconstructed opening angle distribution. In both panels, the Monte Carlo simulation is normalized by the number of measured data. The correlation between $P_{p.e.}$ and P_θ is shown in the lower panel on Figure 4.15. Since the expected momentum tends to show the smaller value compared to the reconstructed momentum, these two momentums do not relate exactly one by one in the low momentum region, although it does not affect the result of the calibration.

The energy scale of the data is compared with that of the Monte Carlo simulation by comparing the ratios of $P_{p.e.}/P_\theta$. Figure 4.16 shows the averaged $P_{p.e.}/P_\theta$ for the data and the Monte Carlo simulation and the MC/data ratio as a function of the expected momentum P_θ. They agree within 0.7 % for SK-I and 1.3 % for SK-II.

4.5.4 High energy stopping muons

The momentum for high energy stopping muons can be estimated from its track length because the range of the muon track is well understood and approximately proportional to the momentum. Since the measurement of the range is independent of the momentum reconstructed using the observed charge, the estimated momentum from its range is used for checking the energy scale from $1\,\mathrm{GeV}/c$ up to $10\,\mathrm{GeV}/c$. Stopping muon events are selected by the following criteria:

1. The entrance point is on the top wall.

2. The direction is downward ($\cos\theta > 0.94$).

3. One decay electron event is detected.

4. The reconstructed range of muon track is greater than $7\,\mathrm{m}$.

The range of the muon is defined as the distance between the entrance position of the stopping muon and the vertex position of the subsequent decay electron. Figure 4.17 shows the averaged value of the ratio momentum/range as a function of the range for the data and the Monte Carlo simulation. The momentum loss per cm is about $2.3\,\mathrm{MeV}/c$. The comparison of the momentum/range between the data and the Monte Carlo simulation is also shown in Figure 4.17. Although the momentum dependence is seen, the deviations from unity are less than 0.7 % for SK-I and 1.1 % for SK-II.
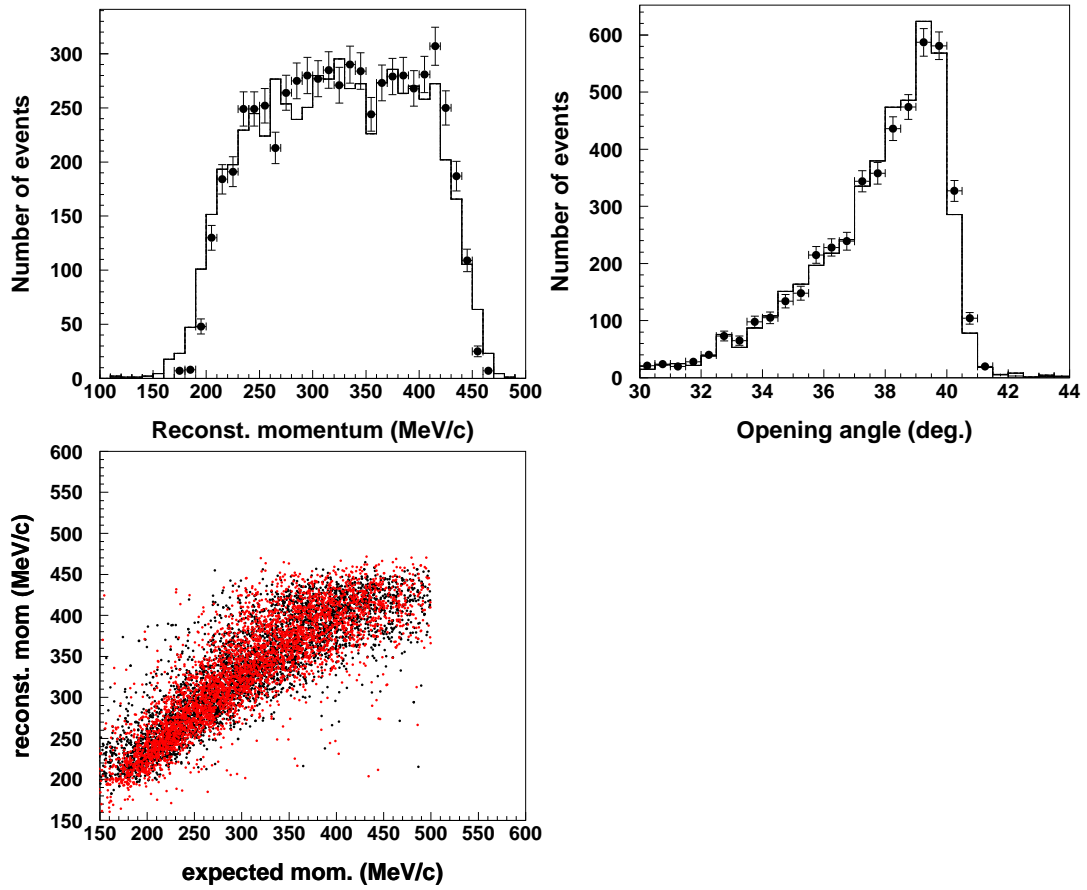
Figure 4.15: (Upper left) The reconstructed momentum distribution $P_{p.e.}$ for the data (circle and error) and the Monte Carlo simulation (histogram). (Upper right) The reconstructed opening angle distribution. (Lower) The correlation between the two momentum P_{θ} (horizontal axis) and $P_{p.e.}$ (vertical axis). Black dot represents the data and red dot for the simulation.
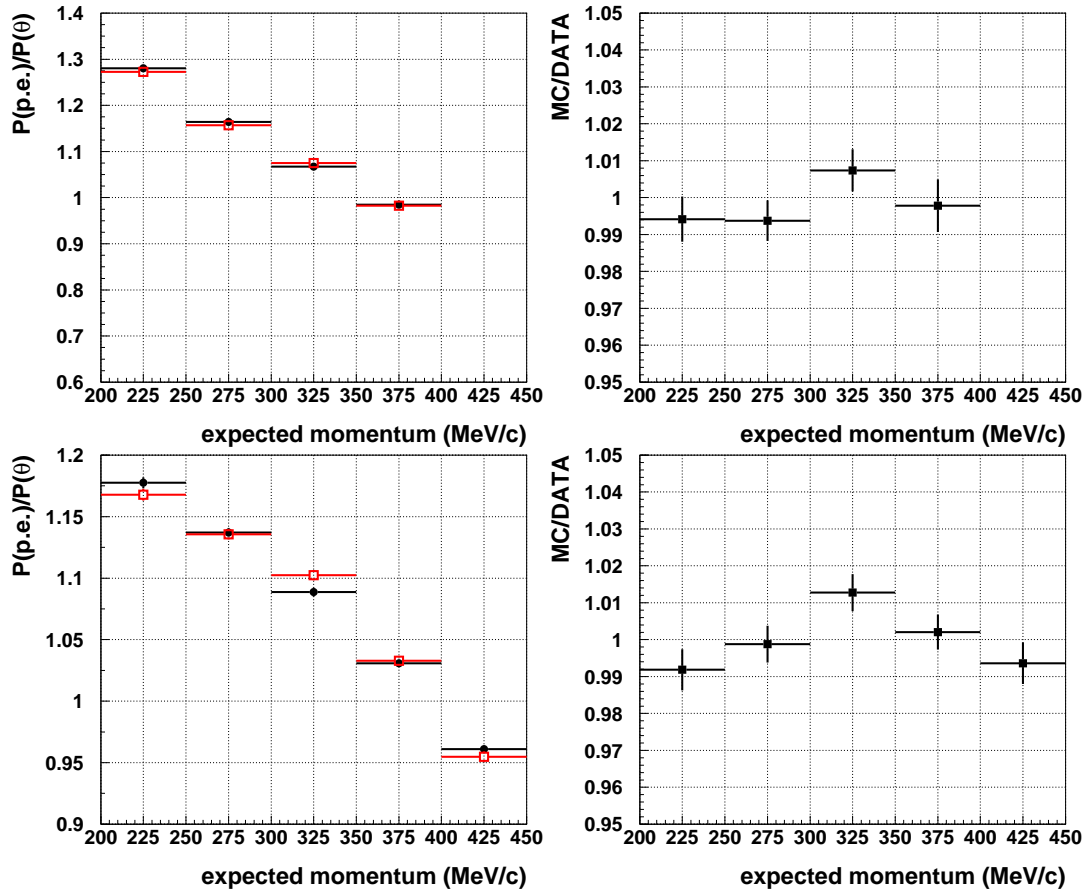
Figure 4.16: Figure on left panel shows the averaged ratio of the momentum derived from the charge to that from the opening angle ($P_{p.e.}/P_\theta$) as a function of the momentum P_θ for the data (black points) and the Monte Carlo events (open boxes), and figure on right panel shows the ratio of the data to the Monte Carlo events. The top two panels show for SK-I and the bottom two panels show for SK-II.

64
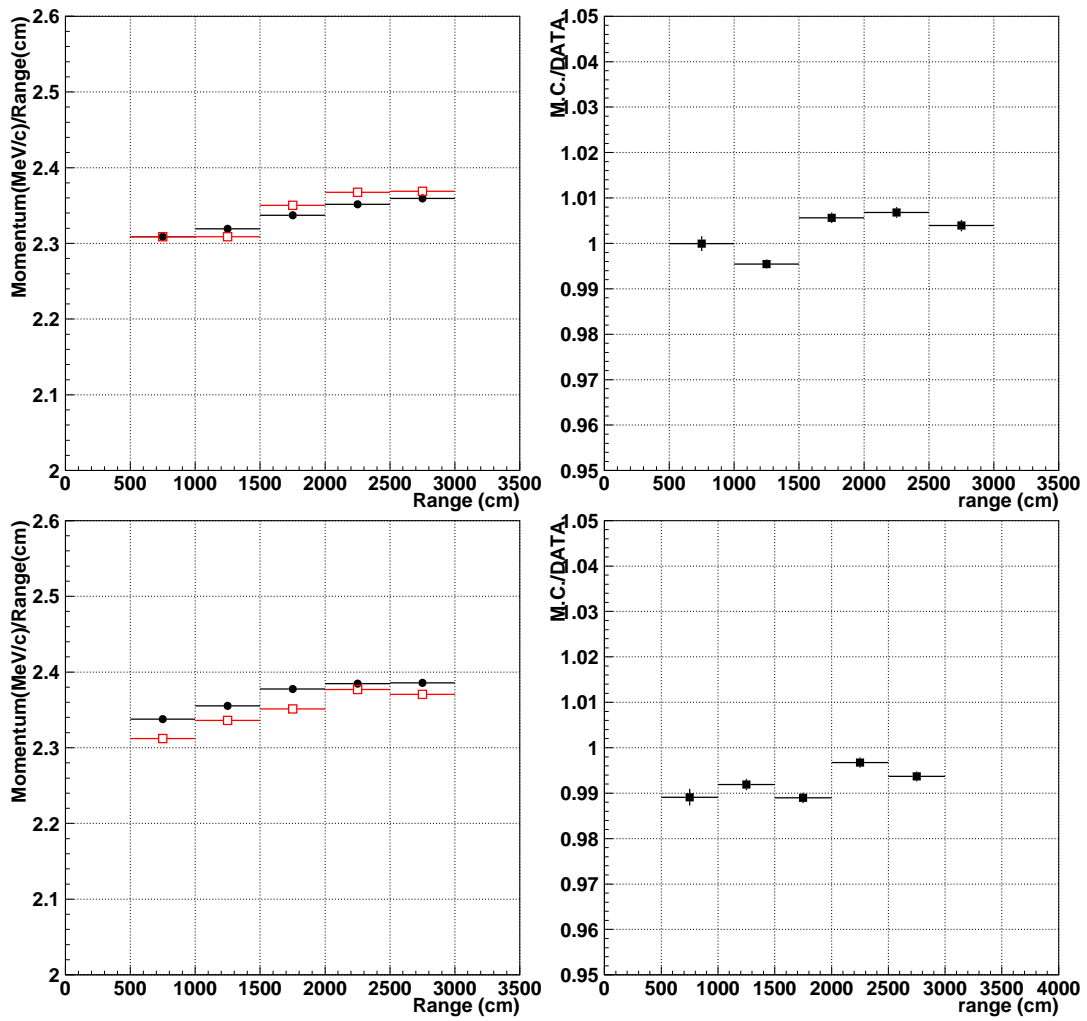
Figure 4.17: Figure on left panel shows the range v.s. averaged momentum/range of stopping muon events for the data (black points) and the Monte Carlo events (open boxes), and figure on right panel shows the ratio of the Monte Carlo events to the data for SK-I (top) and SK-II (bottom).
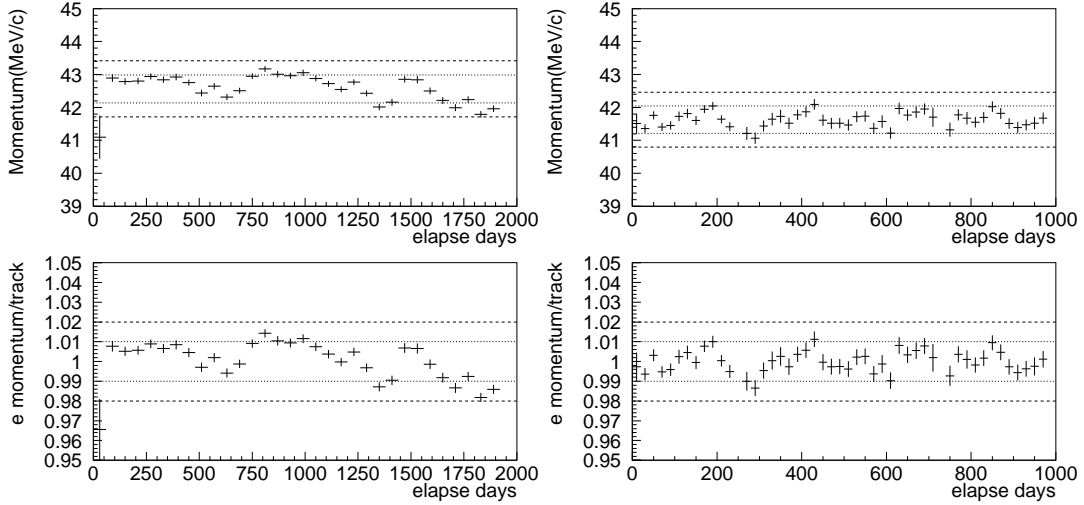
Figure 4.18: The time variation of the reconstructed momentum (top) and the averaged momentum/range (bottom) of the *decay electrons* as a function of elapse days from April, 1996(October, 2002) for SK-I(SK-II). Left panel shows distributsions for SK-I and right panel for SK-II.

4.5.5 Time variation of energy scale

The stability of the energy scale is also monitored by the stopping muons and the decay electrons. Figures 4.18 and 4.19 show the time variation of the averaged momentum/range and the reconstructed momentum for the stopping muons and decay electrons as a function of elapse days from April 1st, 1996. Energy scale variation is determined by the reconstructed momentum of the decay electrons (Upper two panels on Figure 4.18) and the averaged momentum/range of the stopping muons (Lower two panels on Figure 4.19). The RMS of the variation is given as 0.9 % (0.6 %) for SK-I (SK-II).

4.5.6 Uniformity of Energy Scale

The uniformity of the detector is measered using the decay electrons from the cosmic ray muons. They are good calibration sources to check the detector uniformity, because the vertex is distributed uniformly in the fiducial volume and the momentum distribution is almost uniform in all directions. To take into account the muon polarization, only electrons whose direction is perpendicular to the parent muon direction are used. This condition is $-0.25 < \cos\Theta_{e\leftrightarrow\mu} < 0.25$, where $\cos\Theta_{e\leftrightarrow\mu}$ is the opening angle between the electron and muon directions. Figure 4.20 shows the averaged momentum of decay electrons for the Monte Carlo events normalized by that for data as a function of the zenith angle of the electrons. From this figure, the detector gain is uniform within ± 0.6 % for SK-I and SK-II.

4.5.7 Summary of the absolute energy calibration

Figure 4.21 shows the summary of the absolute energy calibration. The absolute energy scale is checked by various methods over a wide energy range. The uncertainty of the energy scale is estimated to be less than 0.7 % and 1.6% for the momentum range from a few tens of MeV/c to
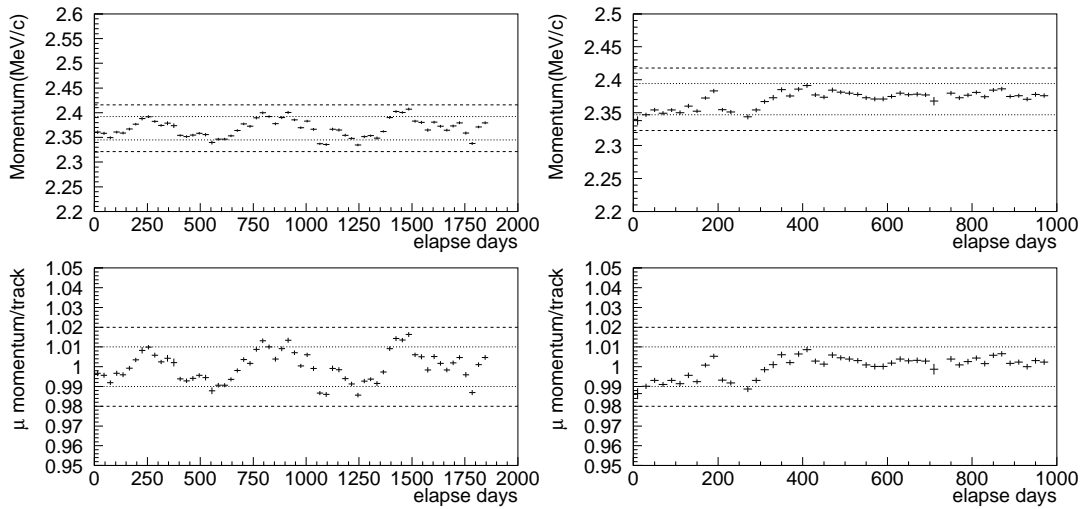
Figure 4.19: The time variation of the reconstructed momentum (top) and the averaged momentum/range (bottom) of the *stopping muons*.
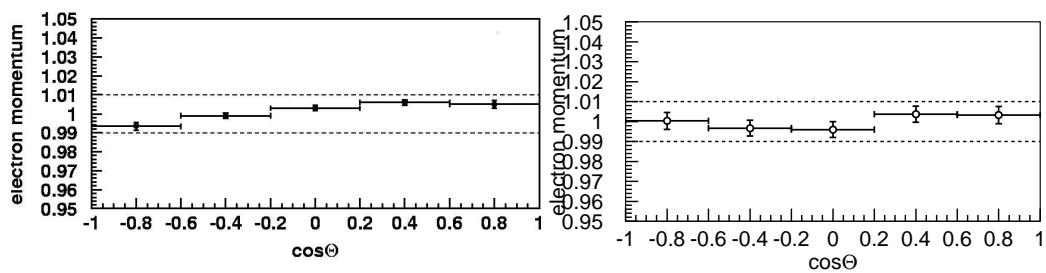
Figure 4.20: The uniformity of the detector gain as a function of zenith angle for SK-I (left) and SK-II (right). The vertical axes in the two figures are the averaged momentum of decay electron events.

about $10\,\mathrm{GeV}/c$ for SK-I and SK-II, respectively. Combined with the RMS of the time variation of the energy scale, $1.1\,\%$ ($1.7\,\%$) is adopted to the systematic error for SK-I (SK-II).
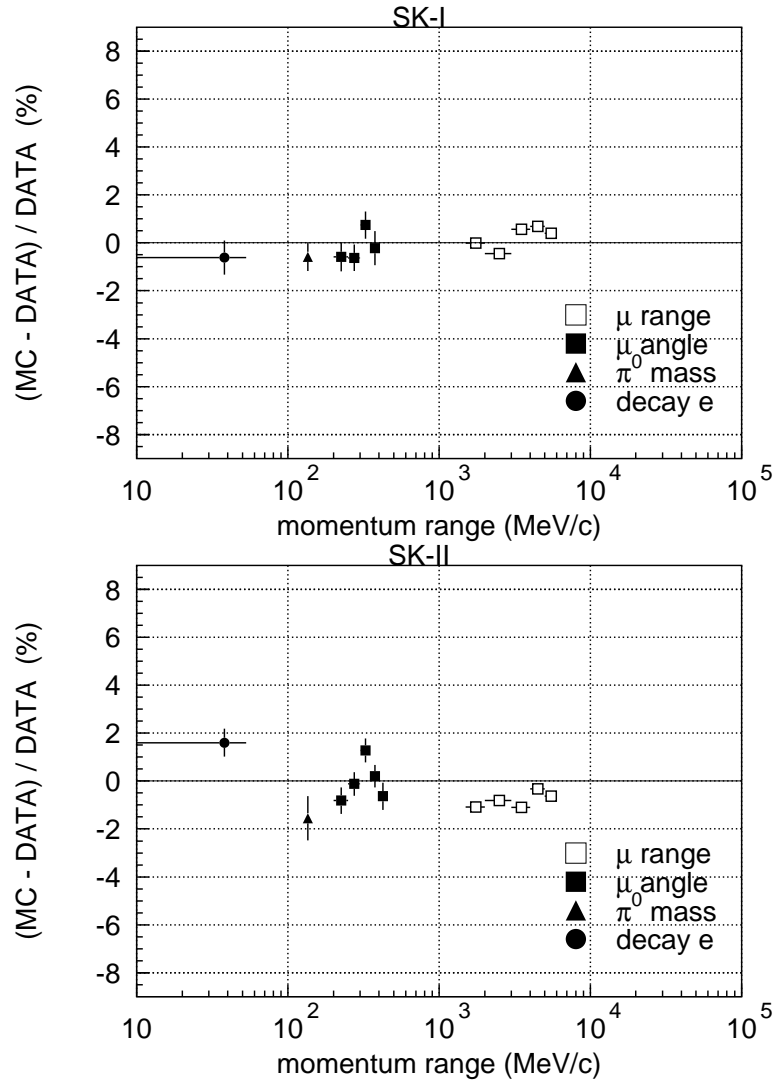
Figure 4.21: The summary of the absolute energy scale calibration for SK-I (top) and SK-II (bottom). The horizontal axis shows the momentum range of each source and the vertical axis shows the deviation of the data from the Monte Carlo predictions.

69

Chapter 5

Data Reduction
and Event Reconstruction

5.1 Data Reduction

About 10^6 events are collected by the Super-Kamiokande detector per day, however most of the events are cosmic ray muons and low energy backgrounds from radioactivities such as radon decay. The efficient event selection is necessary for selecting neutrino events from a huge quantity of data.

The atmospheric neutrino events observed in Super-Kamiokande consist of the following four categories; fully contained (FC), partially contained (PC), upward stopping muons (UPMU stopping) and upward through-going muons (UPMU through) as shown in Figure 5.1. For FC and PC events, the vertices of neutrino interactions are required to be within a fiducial volume, 2 m inside from the ID wall. If the tracks of entire particles are contained inside the ID, the event is classified into FC. If one of the particles exits the ID and deposits energy in the OD, the event is classified into PC. The UPMU events are produced by the atmospheric muon neutrinos via charged current interactions in the rock surrounding the detector. Since the downward-going neutrino-induced muons cannot be distinguished from the cosmic ray muons, only muons traveling in the upward-going direction are selected. The UPMU stopping enter from outside the detector and stop inside the ID, while the UPMU through enter the detector and exit the ID.

Expected energy range for each event class are, $\sim 1\,\mathrm{GeV}$ for FC, $\sim 10\,\mathrm{GeV}$ for PC, $\sim 10\,\mathrm{GeV}$ for UPMU stopping, and $\sim 100\,\mathrm{GeV}$ for UPMU through. Figure 5.2 shows the expected number of neutrino events as a function of neutrino energy.

A data sample for each event class goes through a different reduction process. To separate FC and PC events, the number of hit PMTs in the OD hit cluster (NHITAC, see Appendix C.2.2) is employed, where hit cluster is defined as the spatial cluster of neighboring hit PMTs. Figure 5.3 shows the NHITAC distribution for both FC and PC final samples in the fiducial volume. FC and PC events are clearly separated at NHITAC = 10 (16) for SK-I (SK-II). Since the reflective sheet covered on the OD wall is exchanged to a new one improving the reflectivity in SK-II, the number of the OD hits is increased and the cut criterion is tuned. The systematic uncertainties for FC/PC separation are estimated to be 0.6 % for SK-I and 0.5 % for SK-II by comparing the NHITAC distributions for the data and the Monte Carlo events.

70
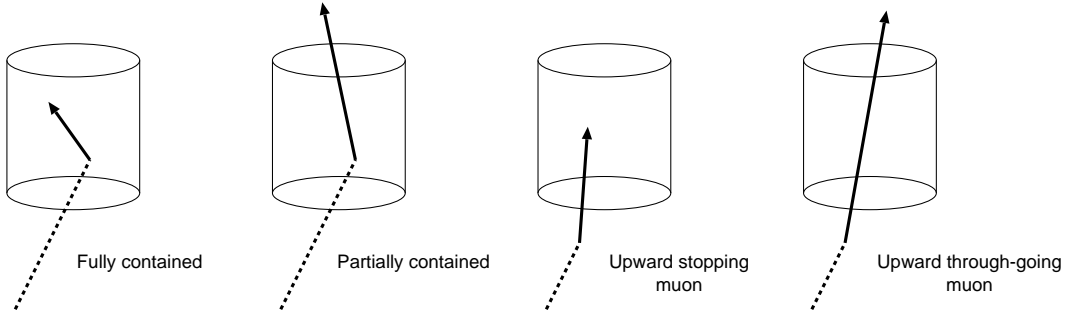
Figure 5.1: Categories of atmospheric neutrino events in Super-Kamiokande. Dashed lines show trajectories of primary neutrinos, and solid arrows show those of secondary charged particles.
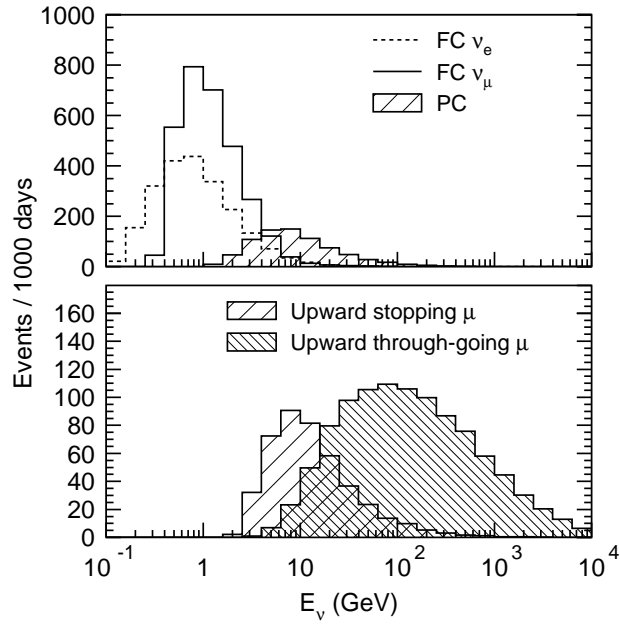
Figure 5.2: The expected parent neutrino energy distribution for each event class.
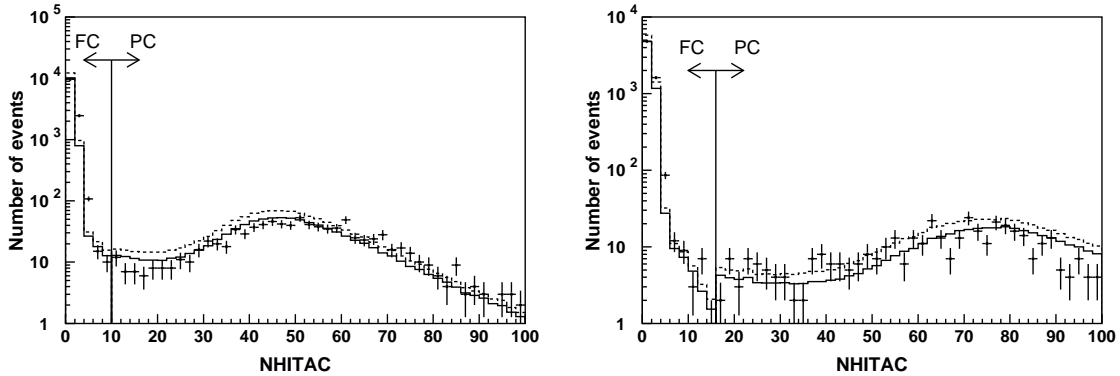
Figure 5.3: NHITAC distributions for FC and PC final samples for SK-I (left) and SK-II (right). The points show the observed data, and histograms show the atmospheric neutrino Monte Carlo events assuming no oscillation (dashed lines) and $\nu_\mu \leftrightarrow \nu_\tau$ 2-flavor oscillation with $(\sin^2 2\theta, \Delta m^2) = (1.00, 2.1 \times 10^{-3}\,\mathrm{eV}^2)$ (solid lines).

The reduction processes are basically automated and are the same for SK-I and SK-II except for some of the event selection criteria because of the difference in the number of the ID PMTs.

As we mentioned, the UPMU events are classified into two categories : (i) upward stopping muon events with only an entrance point in the OD (UPMU stopping) and (ii) upward through-going muon events with an entrance point and exit point in the OD (UPMU through). In order to separate the UPMU stopping events and the UPMU through events, the number of hit OD PMTs within 8 m from the exit position (NHITEX) is used. Figure 5.4 shows the NHITEX distributions for UPMU stopping and UPMU through final samples. The events with NHITEX less than 10 (16 for SK-II) are regarded as stopping muons and the rest of events are categorized to through-going muons. In SK-II, the cut criterion is shifted larger due to the change for the OD responses. The systematic uncertainty for the stopping/through-going separation is estimated to be 0.4 % both for SK-I and SK-II, respectively, by comparing the NHITEX distributions for the observed data and the Monte Carlo events. Low energy events and downward-going muon events are rejected by the automated reduction process and the remaining background after automated process, mainly mis-reconstructed horizontal-going cosmic ray muons are rejected by physicists with eye-scanning.

Detail of the data reduction processes for FC, PC, and UPMU are described in Appendix C.

5.2   Event Reconstruction

Event reconstruction processes are applied to the atmospheric neutrino events which pass through the data reduction processes. The common programs are applied for both the observed data and the atmospheric neutrino Monte Carlo events. The event reconstruction process is fully automated.

The outline of the reconstruction process for FC and PC events is described below and the flowchart of the processes is shown in Figure 5.5:

(1) Vertex Reconstruction
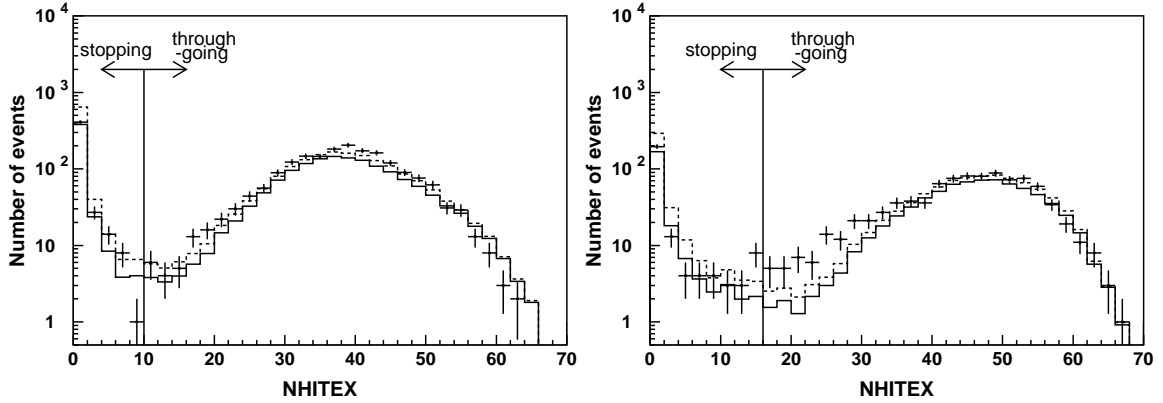
Figure 5.4: NHITEX distributions for UPMU stopping and UPMU through final samples for SK-I (left) and SK-II (right). The points show the observed data, and histograms show the atmospheric neutrino Monte Carlo events assuming no oscillation (dashed lines) and $\nu_\mu \leftrightarrow \nu_\tau$ 2-flavor oscillation with $(\sin^2 2\theta,\, \Delta m^2) = (1.00,\, 2.1 \times 10^{-3}\,\mathrm{eV}^2)$ (solid lines).

The vertex position is determined as the point where the timing residual distribution of hit PMTs has the sharpest peak. The direction and the outer edge of the dominant ring are also reconstructed.

(2) Ring Counting

Other possible rings are searched using the vertex and direction information of the dominant ring determined by the vertex reconstruction. The ring candidates are tested whether the ring is true or false by a likelihood method, and the number of rings is determined.

(3) Particle Identification

Candidate ring is classified into two types, a showering type ($e^\pm, \gamma$) and non-showering type ($\mu^\pm, \pi^\pm$), according to the ring pattern and the opening angle. For the sake of simplicity, the showering type and the non-showering type is denoted as e-like and μ-like, respectively.

(4) Precise Vertex Reconstruction (only for single ring event)

The precise vertex position is obtained using the Cherenkov ring pattern assuming the particle type, a showering type(e-like) or a non-showering type(μ-like). This precise vertex fitter is called MS-fit.

(5) Decay Electron finding

Primary event induced decay electrons are searched.

(6) Momentum Reconstruction

The momentum of each ring is determined from the charge detected inside a Cherenkov cone. The conversion from the charge to the momentum is determined based on a Monte Carlo simulation and the detector calibration.

(7) Ring Number Correction

Rings which have the low momentum and overlapped with other energetic rings are discarded as fitting mistakes.

(8) π^0 Reconstruction

Other ring candidate of π^0 events is searched among the single ring e-like events.

Detail of the event reconstruction processes are described in Appendix D.

FC and PC samples

Vertex reconstruction

point-fit
ring edge search
TDC-fit

Ring counting

Estimation of the number
of Cherenkov rings and its
directions

Particle Identification

Classification according
to the ring pattern

Single ring event   *Multi ring event*

Precise
vertex reconstruction

Precise vertex and
direction reconstruction
using PID information

Decay electron search

Momentum reconstruction

Determination of the
momentum of each ring

Ring number correction
(FC only)

Check low momentum ring
and overlapped ring with
other energetic one

pi0 reconstruction(FC only)

Search and reconstruction
of pi0-like ring

Figure 5.5: Flowchart of the event reconstruction for FC and PC samples

Chapter 6

Data set

We summarize here our data sets for this analysis : FC, PC and UPMU data during the SK-I period (1489.2 days exposure for FC and PC, 1645.9 days for UPMU) and the SK-II period (798.6 days for FC and PC, 827.7 days for UPMU). Since the reconstruction of muon with long path length is less sensitive to the detector condition, the live time of the UPMU data is larger than that of FC and PC data. The statistics of the atmospheric neutrino Monte Carlo events amounts to an exposure of 500 years for SK-I and SK-II.

6.1 Event Classification

Final samples of FC and PC events are selected and cateagorized by the following criteria after event reconstruction processes :

- FC samples

  (1-1) Number of hit PMTs in the OD hit cluster (NHITAC) < 10 (16 for SK-II)

  (1-2) Distance from vertex to the nearest ID wall (D_{wall}) > 200 cm, i.e. Fiducial volume cut

  (1-3) Visible energy assuming electrons (E_{vis}) > 30 MeV

    – FC Single-ring μ-like samples

    (1-4) $p_\mu > 200 \,\mathrm{MeV}/c$

    – FC Single-ring e-like samples

    (1-5) $p_e > 100 \,\mathrm{MeV}/c$

    – FC Multi-ring μ-like sample

    (1-6) The most energetic ring is identified as μ-like and the momentum $p_\mu > 600 \,\mathrm{MeV}/c$ and $E_{vis} > 600 \,\mathrm{MeV}$

    – FC Multi-ring e-like sample

    (1-7) The most energetic ring is identified as e-like and $E_{vis} > 1330 \,\mathrm{MeV}$

- PC samples

(2-1) NHITAC $\geq$ 10 (16 for SK-II)

(2-2) $D_{wall} > 200\,cm$

(2-3) $E_{vis} > 350\,MeV$

   – PC OD stopping sample

(2-4) The maximum number of p.e.s observed in the OD in a sliding $500\,nsec$ time window from $-400\,nsec$ to $+600\,nsec$ (PE_{anti}) is less than $PE_{exp}/1.5$, where PE_{exp} is the expected number of p.e.s in the OD from the potential track length in the OD

(2-5) The most energetic ring or the second one should be identified as μ-like

   – PC OD through-going sample

(2-6) $PE_{anti} > PE_{exp}/1.5$

FC and PC samples are separated by the number of hit PMTs in the OD hit cluster (NHITAC). The fiducial volume for the FC and PC samples is defined by $D_{wall} > 200\,cm$ which corresponds to $22.5\,kton$. The visible energy (E_{vis}) is defined as the sum of the energy of each ring assuming all rings are produced by electrons. The criterion (1-3) is introduced to reject remaining low energy background events.

First FC events are divided into Single-ring and Multi-ring samples according to the number of Cherenkov rings. Next the Single-ring sample is separated into "Sub-GeV sample" with $E_{vis} < 1.33\,GeV$ and "Multi-GeV sample" with $E_{vis} > 1.33\,GeV$. At last the Single-ring Sub-GeV sample is classified into e-like and μ-like samples according to the particle identification result. As only for Single-ring Sub-GeV samples, more finer classifications are adopted to increase the purity of a certain neutrino interaction mode in each sample according to number of decay electrons and the π^0 reconstruction information(see Appendix D.5 and D.8). For Multi-ring sample the most energetic ring is used to identify the particle type.

For PC events, first the criterion (2-3) $E_{vis} > 350\,MeV$, which corresponds to muon momentum $\gtrsim 530\,MeV/c$, is adopted. This cut is sufficiently safe for PC events because the exiting muons must have at least momentum of $700\,MeV/c$ to reach the OD. PC events are separated into two categories, "OD stopping sample" and "OD through-going sample" using the observed p.e.s in the OD and the expected charge derived from the track length, where the criteria (2-4), (2-5) and (2-6) are applied. Muons in the "OD stopping sample" are assumed to be stopped in the OD, while more energetic muons in the "OD through-going sample" are assumed to pass through the OD.

The UPMU stopping and UPMU through samples are selected by requiring the following criteria after data reduction and event reconstruction processes :

- UPMU stopping sample

(3-1) Number of hit OD PMTs within $8\,m$ from the muon exit point (NHITEX) < 10 (16 for SK-II)

(3-2) Reconstructed ring direction is upward (zenith angle $\cos\Theta \leq 0$)

(3-3) $p_\mu \geq 1.6\,GeV/c$ (corresponds to track length of $7\,m$ for muon)

- UPMU through sample

(4-1) NHITEX $\geq$ 10 (16 for SK-II)
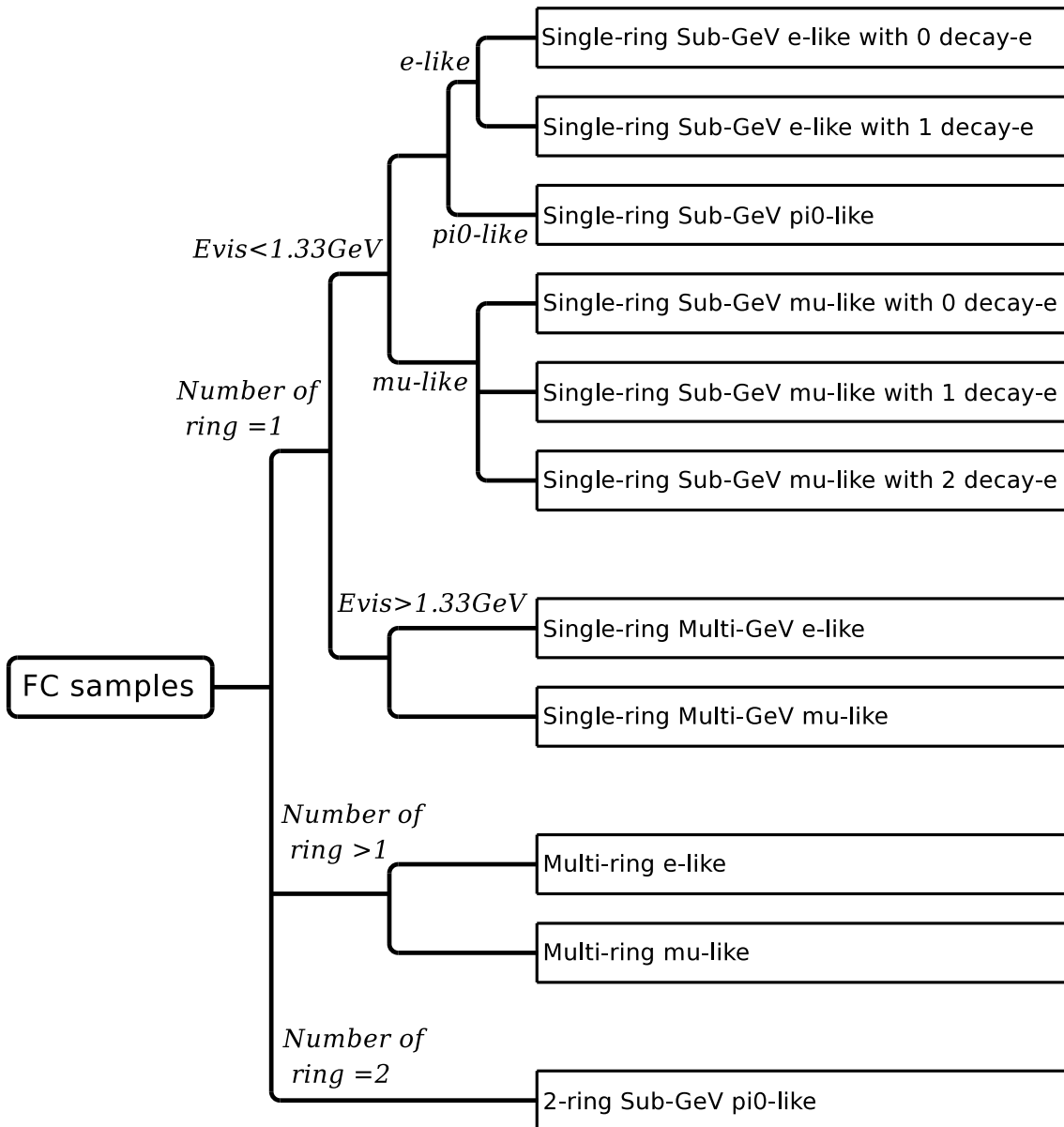
Figure 6.1: Classification of FC samples.

(4-2) Reconstructed ring direction is upward (zenith angle $\cos\Theta \leq 0$)

(4-3) Distance from the muon entrance point to the exit point $\geq 7\,\mathrm{m}$

UPMU stopping and through samples are separated by the number of hit OD PMTs near the exit point (NHITEX). The third criteria, (3-3) and (4-3), are adopted to keep the performance of the event reconstruction. The track length is determined by the distance between the entrance and exit points for UPMU through samples. The UPMU through sample is further separated into showering muon sample and non-showering muon sample. The showering muon events consist of the high energy muons which lose energy through radiative processes such as bremsstrahlung, e^+e^- pair production and photo-nuclear interactions and the energy of the parent neutrino is approximately $1\,\mathrm{TeV}$. The momentum of UPMU stopping is determined from the observed charge by the same way as that for FC and PC events (see Appendix D.6).

The number of events for the atmospheric neutrino data in each final sample is shown in Table 6.1 together with the Monte Carlo predictions.

6.2 Vertex Distribution

Figures 6.2 and 6.3 show the reconstructed vertex distributions for the FC and PC samples projected to $R^2 = (X^2 + Y^2)$ and Z axes. Points show the observed data and histograms show the atmospheric neutrino Monte Carlo events assuming no oscillation and 2-flavor $\nu_\mu \leftrightarrow \nu_\tau$ oscillation with $(\sin^2 2\theta, \Delta m^2) = (1.0, 2.1 \times 10^{-3}\,\mathrm{eV}^2)$. The live time of the Monte Carlo events is normalized to that of the observed data. The vertex distributions of the data and the Monte Carlo events with neutrino oscillation agree well in the fiducial volume, which are shown with arrows. For Sub-GeV samples observed data (points) show the little higer statistics than the Monte Carlo events taking account of neutrino oscillation (solid lines), which can be understood as follows: the calculated neutrino flux corresponding to this energy range may be smaller than the actual neutrino flux as indicated by the comparison between hadronic interaction model and observed $\mu^+ + \mu^-$ data (see Figure 3.2, where $p_\mu \lesssim 3\mathrm{GeV}$ corresponds to Sub-GeV neutrino events). These amounts of excesses are within the systematic uncertainty in the absolute normalization. For Multi-GeV Single-ring μ-like events the excess due to the cosmic ray muons at $Z = 1810\,\mathrm{cm}$, the upper edge of the inner detector, is seen in Z distribution for both SK-I and SK-II, but they are rejected by the fiducial volume cut.

6.3 Number of Ring and Momentum Distribution

Figure 6.4 shows the distribution of the number of rings for data and Monte Carlo events. Figures from 6.5 to 6.7 show the distribution of the momentum for data and Monte Carlo events. The distributions for data and the oscillated Monte Carlo events are consistent.

6.4 Zenith angle Distribution

Figures from 6.8 to 6.12 show the zenith angle distributions. The data (dots and errors) are compared with the Monte Carlo expectation without oscillations (dashed lines) and the best-fit expectation for 2-flavor $\nu_\mu \leftrightarrow \nu_\tau$ oscillations (solid lines). The 2-flavor $\nu_\mu \leftrightarrow \nu_\tau$ oscillation hypothesis provides a consistent explanation to all data samples.

	SK-I		SK-II	
	Data	Monte Carlo	Data	Monte Carlo
FC Sub-GeV				
Single-ring				
e-like	3426	3065.7	1841	1816.6
0μedecay	2984	2663.1	1605	1456.6
1μedecay	275	210.9	155	119.5
π^0-like	167	191.8	81	100.9
μ-like	3219	4321.9	1686	2343.0
0μedecay	1034	1412.3	563	801.4
1μedecay	2035	2745.3	1043	1457.1
2μedecay	150	164.3	80	84.5
2-ring π^0-like	528	615.0	284	322.1
FC Multi-GeV				
Single-ring				
e-like	829	894.1	417	478.4
μ-like	694	1028.9	379	557.3
Multi-ring				
e-like	433	492.0	260	278.8
μ-like	617	920.0	361	484.7
PC	898	1185.4	430	589.6
UPMU				
stopping	417.7	705.2	208.6	359.2
non-showering	1544.8	1482.8	771.2	763.0
showering	296.5	289.3	105.4	105.9

Table 6.1: Summary of atmospheric neutrino events for data and Monte Carlo events of FC, PC and UPMU samples for SK-I and SK-II. The live time of FC and PC is 1489.2 days for SK-I and 798.6 days for SK-II and the live time of UPMU samples is 1645.9 days for SK-I and 827.7 days for SK-II. The number of the Monte Carlo events is normalized by the live time of the data.

		FC Sub-GeV Single-ring e-like				FC Sub-GeV 2-ring π^0-like
		0μedecay	1μedecay	π^0-like	all	
	Q.E.	77.7 %	3.8 %	10.6 %	68.4 %	2.7 %
CC	single meson	12.5 %	50.7 %	7.2 %	14.8 %	3.7 %
$\nu_e + \overline{\nu}_e$	multi π	1.0 %	10.1 %	2.0 %	1.7 %	0.6 %
	coherent π	1.3 %	8.5 %	0.5 %	1.7 %	0.7 %
CC $\nu_\mu + \overline{\nu}_\mu$		0.6 %	15.2 %	7.0 %	2.0 %	2.5 %
NC		6.8 %	11.2 %	72.0 %	11.1 %	89.4 %

		FC Sub-GeV Single-ring μ-like			
		0μedecay	1μedecay	2μedecay	all
	Q.E.	71.3 %	78.5 %	5.8 %	73.4 %
CC	single meson	12.9 %	15.6 %	66.4 %	16.7 %
$\nu_\mu + \overline{\nu}_\mu$	multi π	1.1 %	1.6 %	15.7 %	2.0 %
	coherent π	0.8 %	1.5 %	8.6 %	1.6 %
CC $\nu_e + \overline{\nu}_e$		1.8 %	<0.1 %	<0.1 %	0.6 %
NC		11.8 %	2.6 %	3.3 %	5.7 %

Table 6.2: Fraction of each neutrino interaction mode in FC Sub-GeV Single-ring and Sub-GeV π^0-like atmospheric neutrino Monte Carlo events.

		FC Multi-GeV Single-ring e-like	FC Multi-GeV Multi-ring e-like
	Q.E.	33.6 %	3.3 %
CC	single meson	23.9 %	22.9 %
$\nu_e + \overline{\nu}_e$	multi π	13.7 %	39.8 %
	coherent π	2.0 %	1.0 %
CC $\nu_\mu + \overline{\nu}_\mu$		5.4 %	10.6 %
NC		13.6 %	17.0 %

Table 6.3: Fraction of each neutrino interaction mode in FC Multi-GeV e-like atmospheric neutrino Monte Carlo events.

		FC Multi-GeV Single-ring μ-like	FC Multi-GeV Multi-ring μ-like
	Q.E.	51.2 %	5.1 %
CC	single meson	32.5 %	38.0 %
$\nu_\mu + \overline{\nu}_\mu$	multi π	12.3 %	43.2 %
	coherent π	2.7 %	2.0 %
CC $\nu_e + \overline{\nu}_e$		0.3 %	2.7 %
NC		0.3 %	7.4 %

Table 6.4: Fraction of each neutrino interaction mode in FC Multi-GeV μ-like atmospheric neutrino Monte Carlo events.

		PC	UPMU		
			stop	shower	non-shower
	Q.E.	20.8 %	16.1 %	1.3 %	4.0 %
CC	single meson	25.3 %	22.8 %	2.9 %	7.7 %
$\nu_\mu + \overline{\nu}_\mu$	multi π	49.4 %	60.0 %	95.8 %	88.3 %
	coherent π	1.7 %	0.3 %	0.0 %	0.0 %
CC $\nu_e + \overline{\nu}_e$		2.0 %	0.6 %	0.0 %	0.0 %
NC		0.9 %	0.2 %	0.0 %	0.0 %

Table 6.5: Fraction of each neutrino interaction mode in PC and UPMU atmospheric neutrino Monte Carlo events.
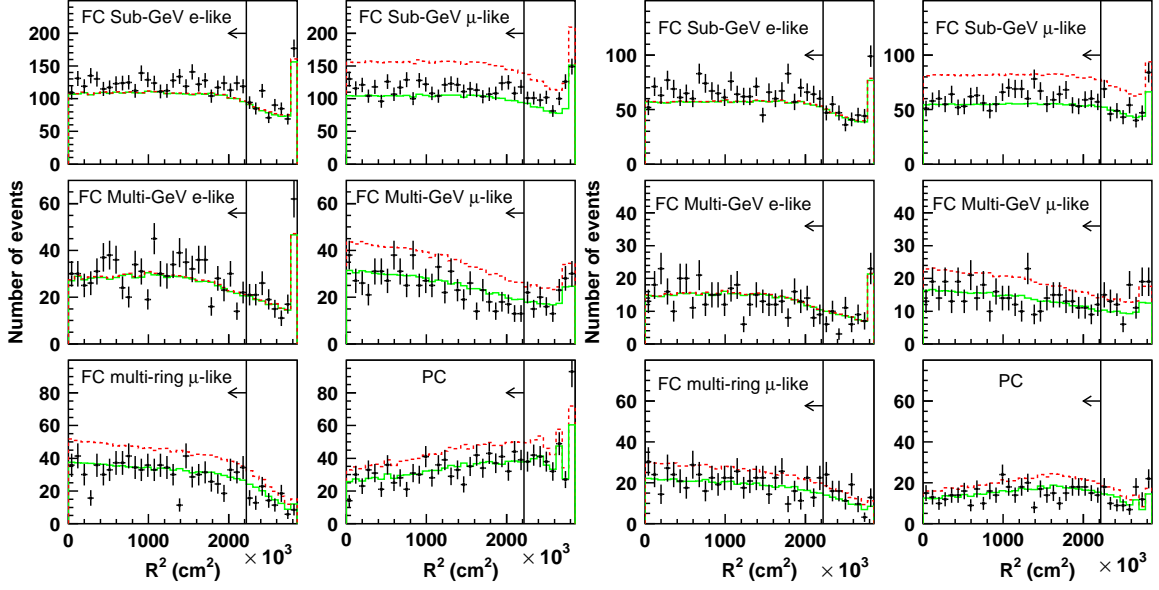
Figure 6.2: The vertex distributions projected on R^2 axis for data (dot) and Monte Carlo events assuming no oscillation (dashed line) and 2-flavor $\nu_\mu \leftrightarrow \nu_\tau$ oscillation with $(\sin^2 2\theta, \Delta m^2) = (1.0,\ 2.1 \times 10^{-3}\,\mathrm{eV}^2)$ (solid line). The left six panels show those for SK-I and the right panels show those for SK-II. Excess of data compared to the Monte Carlo events (solid line) shown in the entire Sub-GeV sample distribution is mentioned in the text.

Figure 6.13 shows the angular resolution of the neutrino directions as a function of the momentum. The angular resolution is defined as the angular difference between the parent neutrinos and the reconstructed direction of outgoing leptons in which 68 % of the events are included.
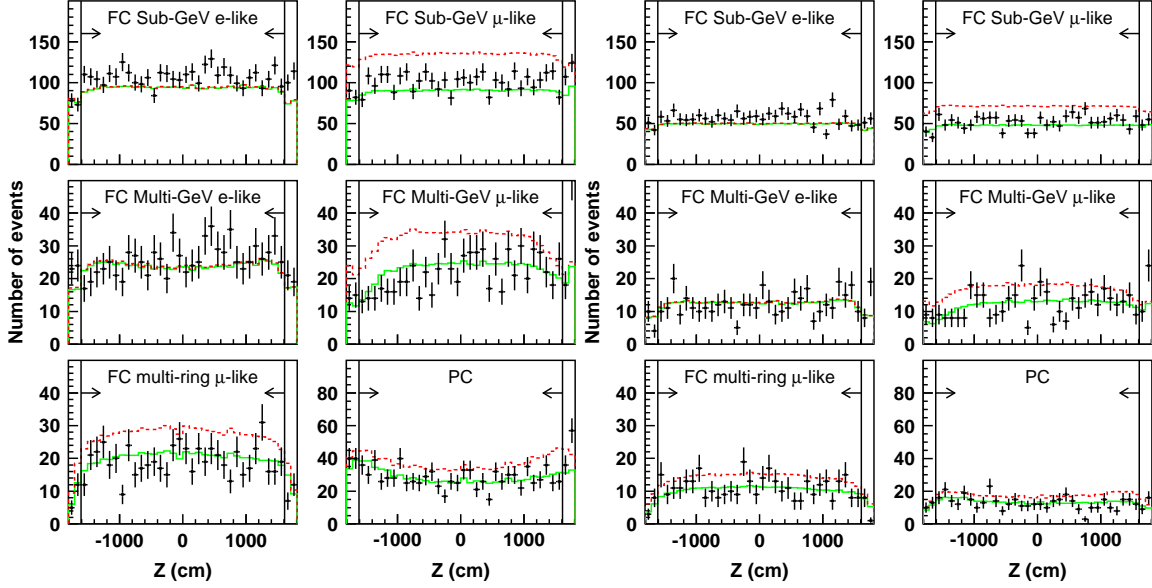
Figure 6.3: The vertex distributions projected on Z axis for data (dot) and Monte Carlo events assuming no oscillation (dashed line) and 2-flavor $\nu_\mu \leftrightarrow \nu_\tau$ oscillation with $(\sin^2 2\theta, \Delta m^2) = (1.0, 2.1 \times 10^{-3}\,\mathrm{eV^2})$ (solid line). The left six panels show those for SK-I and the right panels show those for SK-II. Excess of data compared to the Monte Carlo events (solid line) shown in the entire Sub-GeV sample distribution is mentioned in the text.
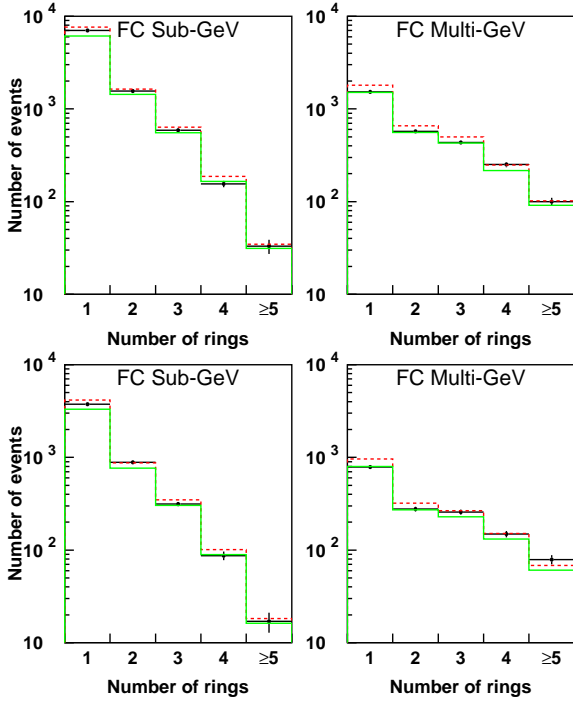
Figure 6.4: The number of rings for data (dot) and Monte Carlo events assuming no oscillation (dashed line) and 2-flavor $\nu_\mu \leftrightarrow \nu_\tau$ oscillation with $(\sin^2 2\theta, \Delta m^2) = (1.0, 2.1 \times 10^{-3}\,\mathrm{eV^2})$ (solid line) for Sub-GeV events (left) and Multi-GeV events (right). The upper two panels show those for SK-I and the bottom panels show those for SK-II.

84
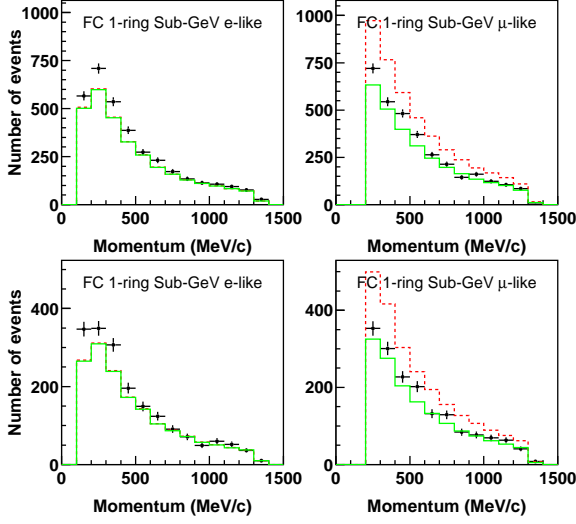
Figure 6.5: The momentum distributions for FC Sub-GeV Single-ring e-like samples (left panel) and FC Sub-GeV Single-ring μ-like samples (right panel). Upper panels for SK-I and lower panels for SK-II. Dot stands for data, dashed line for Monte Carlo events assuming no oscillation, and solid line for 2-flavor $\nu_\mu \leftrightarrow \nu_\tau$ oscillation with $(\sin^2 2\theta, \Delta m^2) = (1.0, 2.1 \times 10^{-3} \, \mathrm{eV}^2)$.
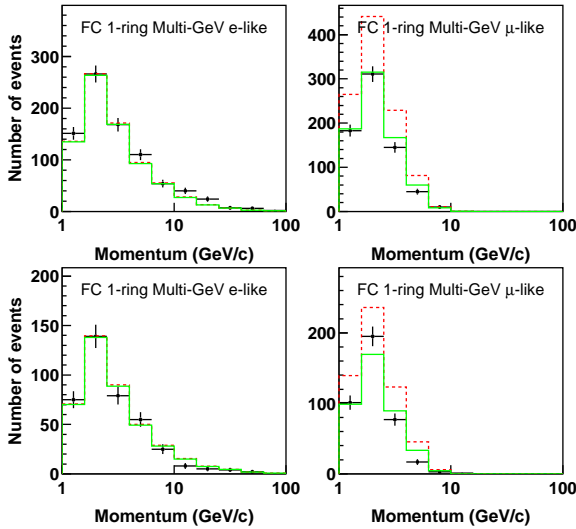
Figure 6.6: The momentum distributions for FC Multi-GeV Single-ring e-like samples (left panel) and FC Multi-GeV Single-ring μ-like samples (right panel). Upper panels for SK-I and lower panels for SK-II. Dot stands for data, dashed line for Monte Carlo events assuming no oscillation, and solid line for 2-flavor $\nu_\mu \leftrightarrow \nu_\tau$ oscillation with $(\sin^2 2\theta, \Delta m^2) = (1.0, 2.1 \times 10^{-3} \, \mathrm{eV}^2)$.
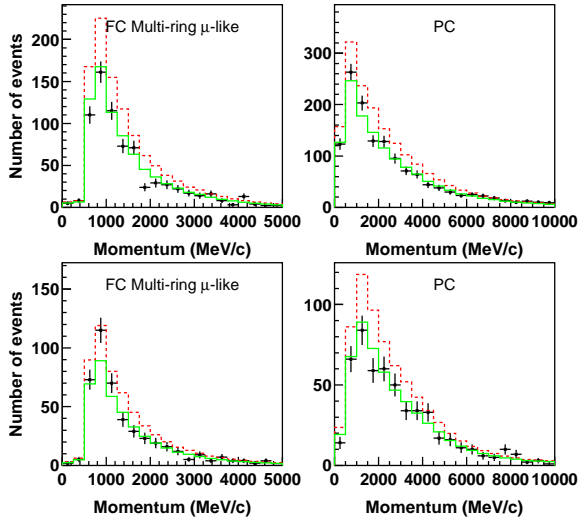
Figure 6.7: The momentum distributions for FC Multi-ring μ-like samples (left panel) and PC samples (right panel). Upper panels for SK-I and lower panels for SK-II. Dot stands for data, dashed line for Monte Carlo events assuming no oscillation, and solid line for 2-flavor $\nu_\mu \leftrightarrow \nu_\tau$ oscillation with $(\sin^2 2\theta,\, \Delta m^2) = (1.0,\, 2.1 \times 10^{-3}\,\mathrm{eV}^2)$.
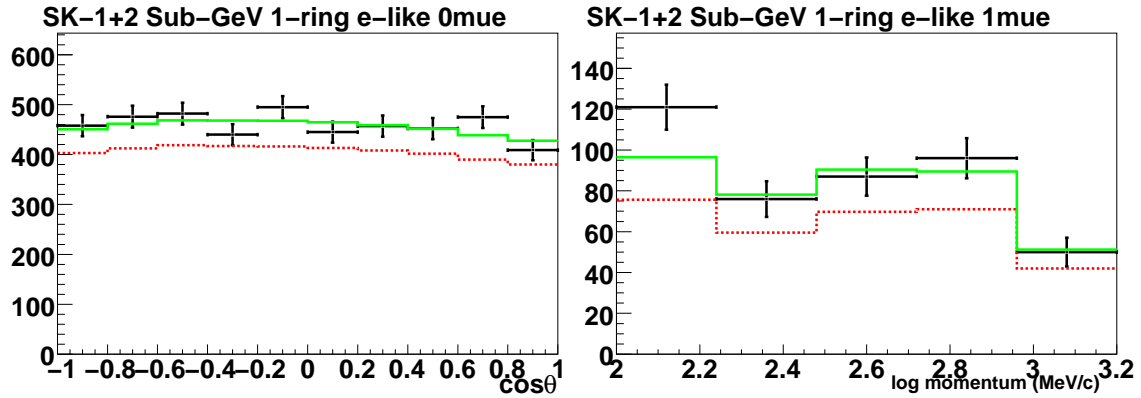
(a) Sub-GeV Single-ring e-like 0 decay-electron

(b) Sub-GeV Single-ring e-like 1 decay-electron
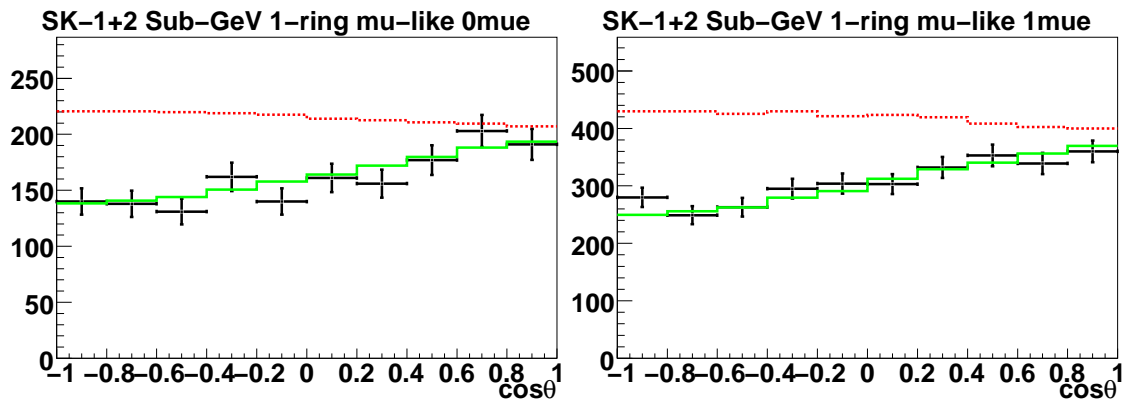
(c) Sub-GeV Single-ring μ-like 0 decay-electron

(d) Sub-GeV Single-ring μ-like 1 decay-electron
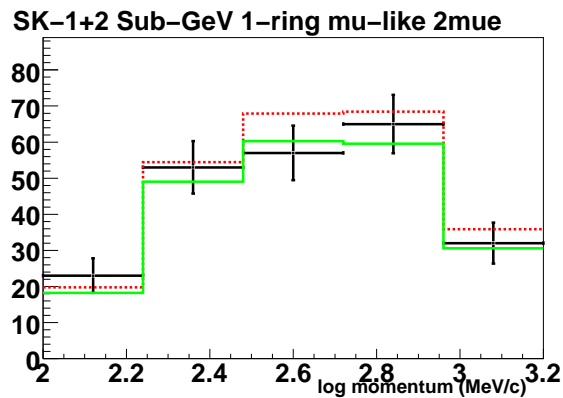
(e) Sub-GeV Single-ring μ-like 2 decay-electron

Figure 6.8: Zenith angle and momentum distributions of the observed data (points with statistical errors) and the Monte Carlo expectations (solid and dashed lines). Dashed line indicates the expectation assuming the best-fitted 2-flavor $\nu_\mu \leftrightarrow \nu_\tau$ oscillations, while solid line assumes the expectation with null oscillation.

(a) Sub-GeV Single-ring π^0-like   (b) Sub-GeV 2-ring π^0-like
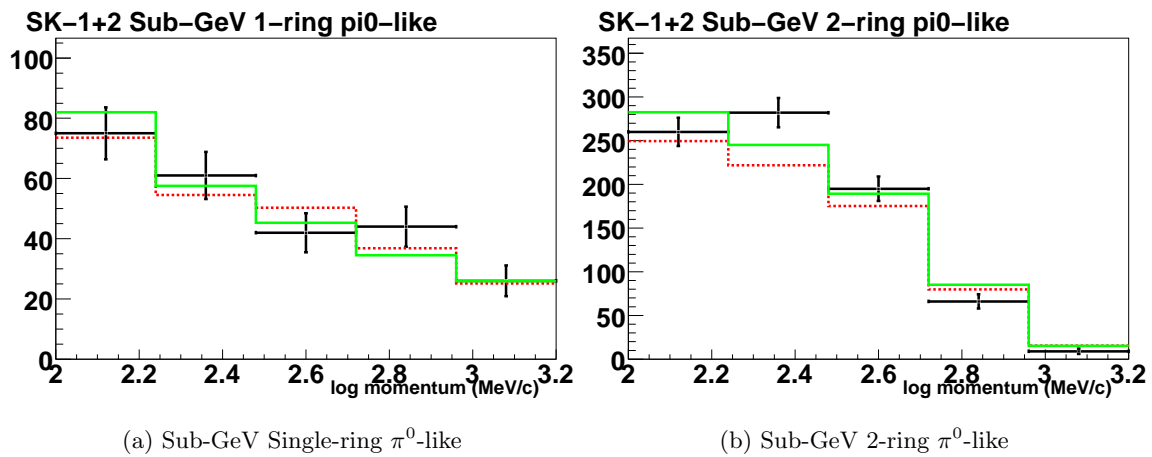
Figure 6.9: Momentum distributions of the observed data (points with statistical errors) and the Monte Carlo expectations (solid and dashed lines). Dashed line indicates the expectation assuming the best-fitted 2-flavor $\nu_\mu \leftrightarrow \nu_\tau$ oscillations, while solid line assumes the expectation with null oscillation.

(a) Multi-GeV Single-ring e-like

(b) Multi-GeV Single-ring μ-like

(c) Multi-GeV Multi-ring e-like

(d) Multi-ring e-like
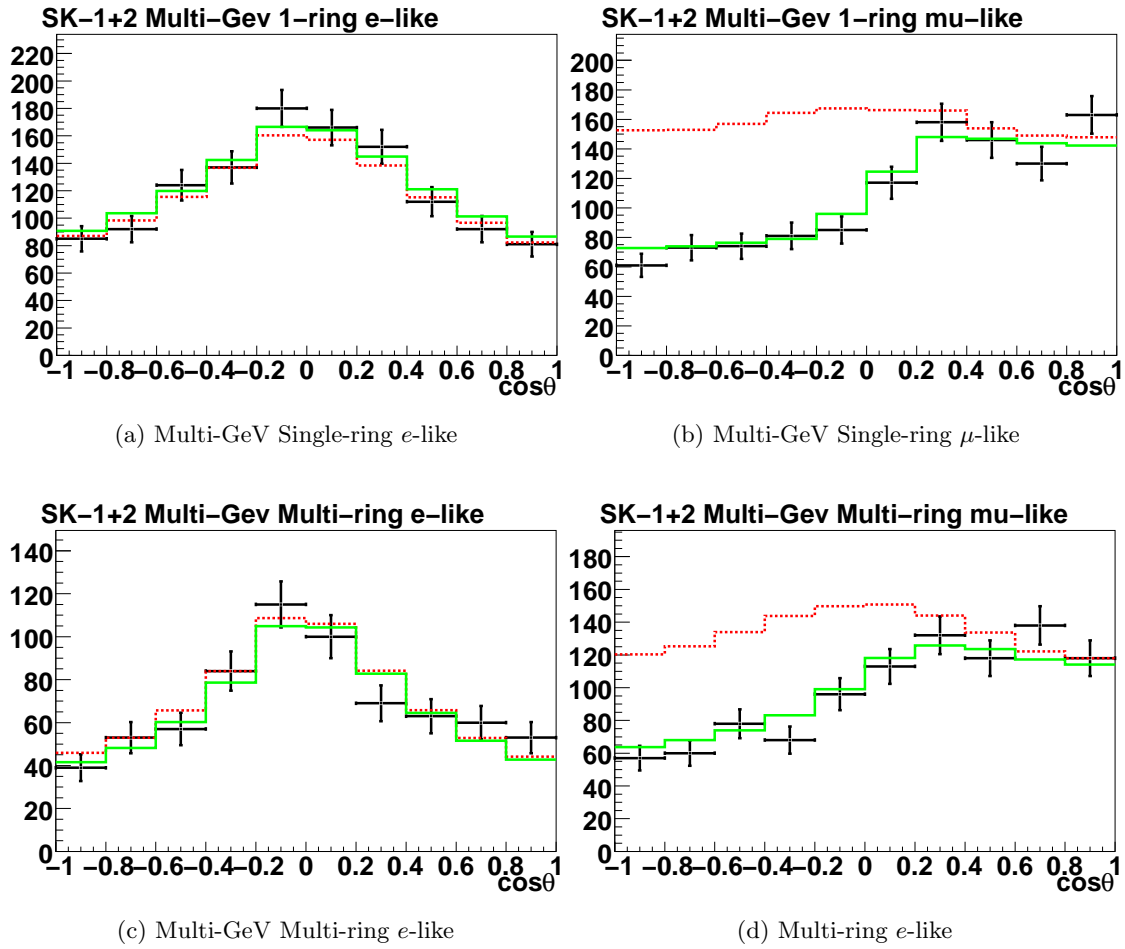
Figure 6.10: Momentum distributions of the observed data (points with statistical errors) and the Monte Carlo expectations (solid and dashed lines). Dashed line indicates the expectation assuming the best-fitted 2-flavor $\nu_\mu \leftrightarrow \nu_\tau$ oscillations, while solid line assumes the expectation with null oscillation.

(a) PC OD stopping   (b) PC OD through going
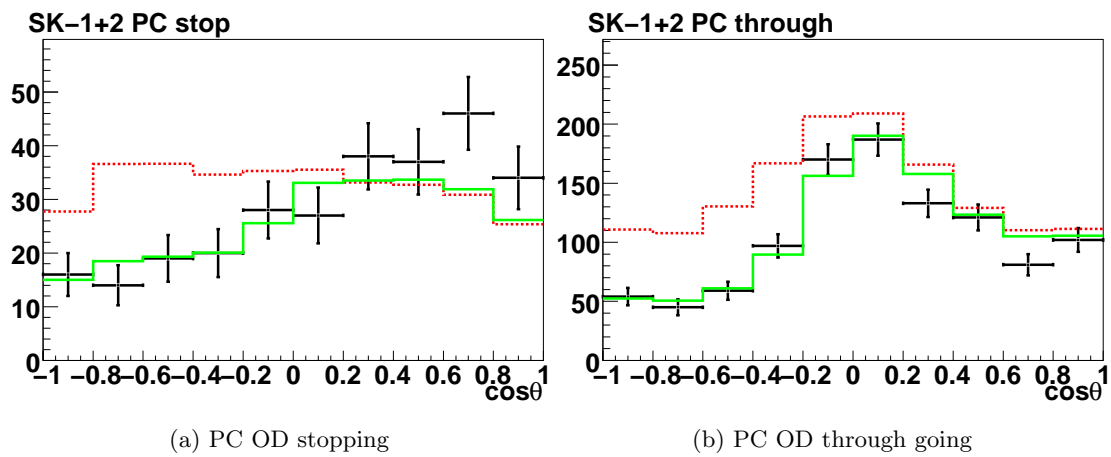
Figure 6.11: Zenith angle distributions of the observed data (points with statistical errors) and the Monte Carlo expectations (solid and dashed lines). Dashed line indicates the expectation assuming the best-fitted 2-flavor $\nu_\mu \leftrightarrow \nu_\tau$ oscillations, while solid line assumes the expectation with null oscillation.

(a) UPMU stopping

(b) UPMU through non shower-like

(c) UPMU through shower-like
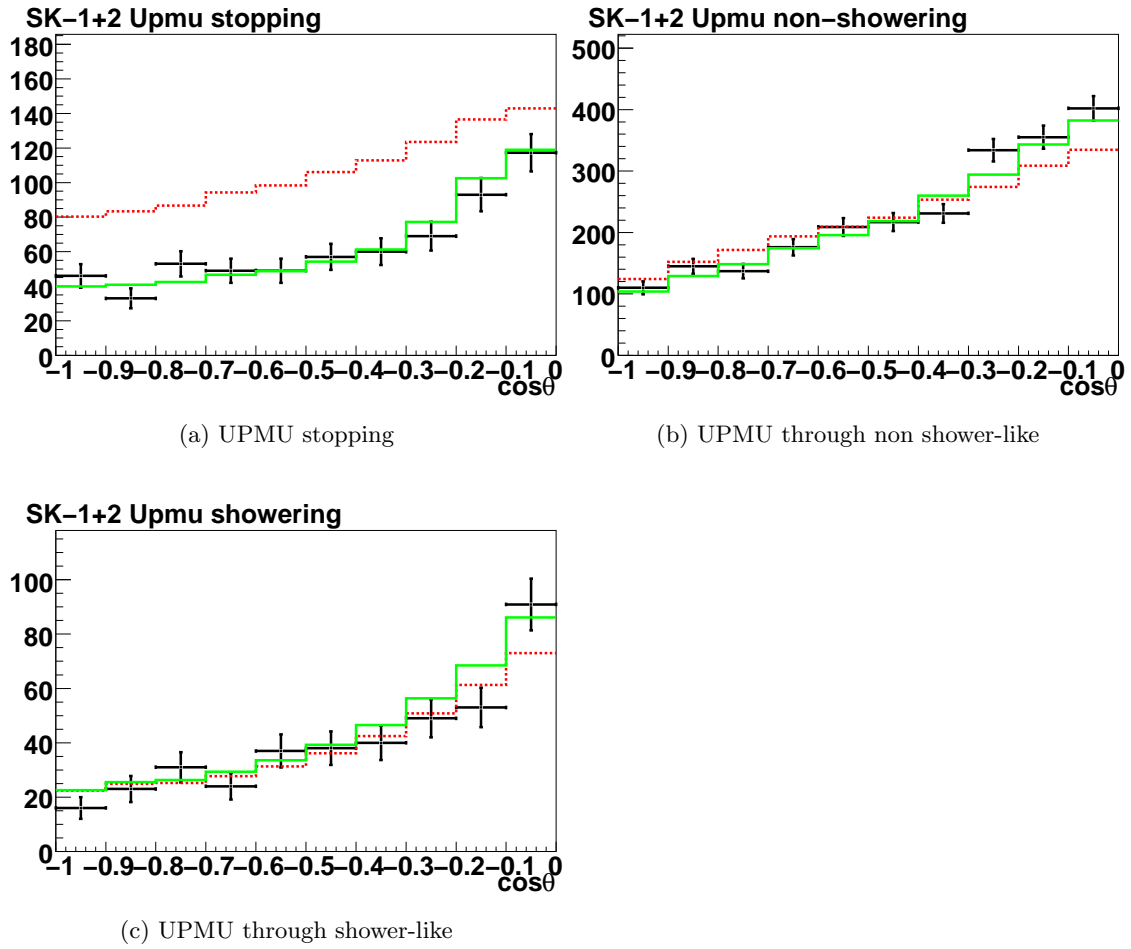
Figure 6.12: Zenith angle distributions of the observed data (points with statistical errors) and the Monte Carlo expectations (solid and dashed lines). Dashed line indicates the expectation assuming the best-fitted 2-flavor $\nu_\mu \leftrightarrow \nu_\tau$ oscillations, while solid line assumes the expectation with null oscillation.
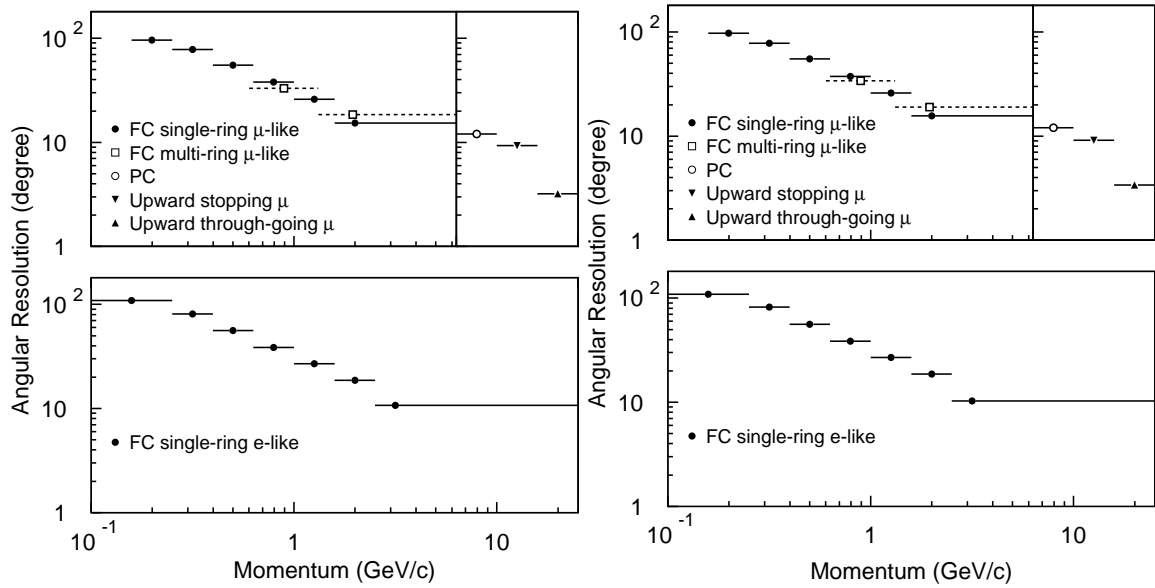
Figure 6.13: Angular resolution of the neutrino direction as a function of the outgoing charged lepton momentum for SK-I (left) and SK-II (right).

Chapter 7

Analysis Method and Systematic Uncertainties

We evaluate an agreement of the fitting by χ^2 test, which is performed with the FC, PC and UPMU samples of the SK-I and SK-II atmospheric neutrino data. These samples are divided into 400 bins for SK-I and 350 bins for SK-II according to the reconstructed event type, momentum and zenith angle. The SK-I and SK-II data are individually handled due to the difference in the detector response and the solar modulation effect in the atmospheric neutrino flux. First, we define the formulation of χ^2, and next, analysis binning is presented in Chapter 7.2. Finally systematic uncertainties are discussed.

7.1   Definition of χ^2

Atmospheric neutrino data are divided into fine bins to have the high sensitivity depending on the neutrino energy and zenith angle, i.e. propagation length. In order to treat the finer binning, the likelihood is based on Poisson probabilities. Suppose we have totally n bins for data indexed by i, the likelihood can be expressed as

$$\mathcal{L}(N^{exp}, N^{obs}) = \prod_{i=1}^{n} \frac{e^{-N_i^{exp}} N_i^{exp^{N_i^{obs}}}}{N_i^{obs}!} \tag{7.1}$$

where N_i^{exp} and N_i^{obs} is the number of expected and observed events in i-th bin, respectively. The log likelihood ratio gives χ^2,

$$\chi^2 \equiv -2 \ln \frac{\mathcal{L}(N^{exp}, N^{obs})}{\mathcal{L}(N^{obs}, N^{obs})} = 2 \sum_{i=1}^{n} \left(N_i^{exp} - N_i^{obs} + N_i^{obs} \ln \frac{N_i^{obs}}{N_i^{exp}} \right) \tag{7.2}$$

The effects of independent systematic uncertainties are included into the bin following "pull-method" [143]. The number of expected events in a bin varies according to the systematic uncertainty, thus N_i^{exp} is replaced with

$$N_i^{exp} \to N_i^{exp}(1 + \sum_{j}^{m} f_j^i \epsilon_j) \tag{7.3}$$

where ϵ_j is a variation of j-th systematic uncertainty and f_j^i is the fractional change of the event rate in the i-th bin due to the j-th systematic uncertainty. m is the total number of systematic uncertainties.

For each uncertainty, the parameter ϵ_j is estimated during the fit to χ^2 and the resulting quantity $\epsilon_j/\sigma_j^{sys}$ follows Gaussian distribution, where σ_j^{sys} is an estimated 1σ value of the j-th systematic uncertainty. In order to constrain the range of ϵ_j and hence the effect of systematic uncertainty, additional term

$$\sum_j^m \left(\frac{\epsilon_j}{\sigma_j^{sys}}\right)^2 \tag{7.4}$$

is added to eq.(7.2). Thus the χ^2 with totally $n = 750$ bins and $m = 90$ systematic uncertainties is defined as

$$\chi^2 = 2\sum_{i=1}^{750}\left(N_i^{exp}(1+\sum_{j=1}^{90}f_j^i\epsilon_j) - N_i^{obs} + N_i^{obs}\ln\frac{N_i^{obs}}{N_i^{exp}(1+\sum_{j=1}^{90}f_j^i\epsilon_j)}\right) + \sum_{j=1}^{90}\left(\frac{\epsilon_j}{\sigma_j^{sys}}\right)^2 \tag{7.5}$$

In this equation, 90's ϵ_j are varied to minimize χ^2 for each choice of oscillation parameters. The minimum χ^2 is obtained when $\partial\chi^2/\partial\epsilon_l = 0$ is realized for every ϵ_l with $l = 1-90$. $\partial\chi^2/\partial\epsilon_l = 0$ can be reduced to

$$\sum_i N_i^{exp}f_l^i - \frac{\sum_i N_i^{obs}f_l^i}{1+\sum_j f_j^i\epsilon_j} + \sum_j \frac{\epsilon_j}{(\sigma_j^{sys})^2}\delta_{jl} = 0 \tag{7.6}$$

Here we add

$$\sum_j \sum_i N_i^{obs}f_j^i f_l^i \epsilon_j \tag{7.7}$$

to the both hands in eq.(7.6), and obtain the form

$$\sum_j\left(\sum_i N_i^{obs}f_j^i f_l^i + \frac{1}{(\sigma_j^{sys})^2}\delta_{jl}\right)\epsilon_j = \sum_i N_i^{obs}f_l^i\left(\frac{1}{1+\sum_j f_j^i\epsilon_j} + \sum_j f_j^i\epsilon_j - \frac{N_i^{exp}}{N_i^{obs}}\right) \tag{7.8}$$

This means that the solution of $\partial\chi^2/\partial\epsilon_l = 0$ can be deduced from the matrix equation

$$\sum_j \mathcal{M}_{lj}\epsilon_j = \nu_l \tag{7.9}$$

where $\mathcal{M}_{lk}$ and ν_l are expressed by means of eq.(7.8)

$$\sum_i N_i^{obs}f_j^i f_l^i + \frac{1}{(\sigma_j^{sys})^2}\delta_{jl} \rightarrow \mathcal{M}_{lj} \tag{7.10}$$

$$\sum_i N_i^{obs}f_l^i\left(\frac{1}{1+\sum_j f_j^i\epsilon_j} + \sum_j f_j^i\epsilon_j - \frac{N_i^{exp}}{N_i^{obs}}\right) \rightarrow \nu_l \tag{7.11}$$

In the actual calculation, the first term of ν_l is computed by the series expansion upto $\mathcal{O}(\epsilon_j^5)$. The matrix $\mathcal{M}_{lk}$ is symmetric and invertible. If the number of bins (n) is much larger than the number of systematic uncertainties (m), this approach has the advantage rather than the

covariance matrix approach due to the difference between the inverse matrix $m \times m$ (pull-method) and $n \times n$ (covariance). Since ν_l contains ϵ_j itself, eq.(7.9) is solved iteratively beginning with $\epsilon_j = 0$ for every j until the value of χ^2 stabilizes.

The effect of systematic uncertainties is taken into account through the coefficients f_j^i in eq.(7.5). These f_j^i are calculated in advance using the Monte Carlo simulation. If we write the bin contents with only j-th uncertainty as $(N_i^{exp})_j$, and assume f_j^i to be linear on the bin content and taken to be the slope of the line between its content at $\pm \sigma_j^{sys}$, the coefficients f_j^i are defined as

$$f_j^i = \frac{(N_i^{exp})_{j(+\sigma)} - (N_i^{exp})_{j(-\sigma)}}{2(N_i^{exp})_{j(0)}} \tag{7.12}$$

As a most simple case, we mention the uncertainty in the total cross section of single meson production ($j = 18$). As is discussed later, this uncertainty is estimated to be 20%. It turns out the change of bin contents $\pm 20\%$, then f_{18}^i is given as

$$f_{18}^i = \frac{1.2 - 0.8}{2 \times 1.0} = 0.2 \tag{7.13}$$

While for the energy dependent uncertainty, for example, f_j^i of the absolute normalization uncertainty below 1 GeV ($j = 1$, see Figure 7.5) is expressed as

$$f_1^i = -0.2 E_\nu(\text{GeV}) + 0.27 \tag{7.14}$$

During the fit, the values of f_j^i are taken from the table prepared in advance.

7.2 Analysis Binning

In order to obtain the high sensitivity the binning should be sufficiently fine. However, too narrow binning causes the decrease of the number of expected events in a bin and then the contribution to the χ^2 grows up due to the increase of the error.

If the true number of expected events in a bin is assumed to be N_{true} with livetime L, the number of expected events N_{MC} of a Monte Carlo simulation with livetime αL will be αN_{true}. Suppose we can observe $\tilde{N}_{true}$ with livetime L and $\tilde{N}_{MC}$ with livetime αL in a bin, they will not be exactly N_{true} or αN_{true}, but distribute following Poisson statistics about their true values. We define the probability to observe $\tilde{N}_{true}$ and $\tilde{N}_{MC}$ events from a Poisson distribution of mean N_{true} and N_{MC} as $P(\tilde{N}_{true}|N_{true})$ and $P(\tilde{N}_{MC}|N_{MC}) = P(\tilde{N}_{MC}|\alpha N_{true})$, respectively. By means of the probabilities the average contribution to the reduced χ^2 is expressed as an average over the possible values of $\tilde{N}_{MC}$ and $\tilde{N}_{true}$,

$$h(N_{true}) = \sum_{\tilde{N}_{true}=0}^{\infty} P(\tilde{N}_{true}|N_{true}) \sum_{\tilde{N}_{MC}=0}^{\infty} P(\tilde{N}_{MC}|\alpha N_{true}) \chi^2(\tilde{N}_{true}, \tilde{N}_{MC}/\alpha) \tag{7.15}$$

where χ^2 is taken from eq.(7.2).

Figure 7.1 shows the average contribution to the reduced χ^2 for varying amounts of uncertainty in the expected number of events. For less than three expected events, the contribution to the χ^2 is considerably greater than 1. Around five expected events the curve begins to flatten and continues smoothly as increase in the number of expected events. Therefore the analysis
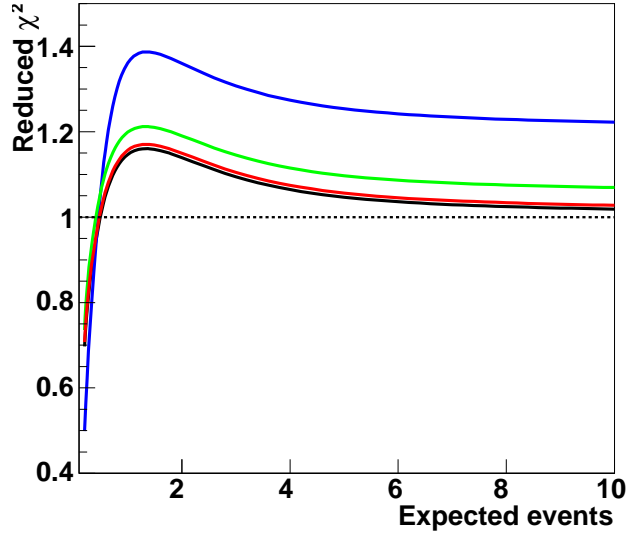
Figure 7.1: Average contribution to the reduced χ^2 as a function of the expected number of events in a bin. The factor of Monte Carlo simulation to the observation is 5 for blue curve, 20 for green curve, 100 for red curve, and no error for black curve.

binning has been chosen to avoid the feature at low expectation. The expected number of events in a bin in SK-II is smaller than that in SK-I, then the different binning are employed between SK-I and SK-II to avoid the binning effect on the fitting results, especially in higher energy regions which have less statistics. Also we can see the small factor of Monte Carlo simulation to the observation yields the large reduced χ^2. In order to perform the precise analysis, we prepare the Monte Carlo simulation corresponding to the 500 years of livetime for both SK-I and SK-II, in which the factors are approximately 120 for SK-I and 230 for SK-II. Therefore the statistics of Monte Carlo simulation is sufficient.

Figures 7.2 and 7.3 show the definition of the binning for SK-I and SK-II, respectively. The SK-I and SK-II data are individually handled due to the difference in the detector response and the solar modulation effect in the atmospheric neutrino flux. A total of 750 bins are considered in the calculation of χ^2 with their associated sets of the observations and the Monte Carlo predictions. In this thesis, we employ the common binning to the other atmospheric neutrino analysis in Super-Kamiokande to evaluate the results based on the same framework.

For the FC samples, the Sub-GeV Single-ring e-like 1μedecay, Sub-GeV Single-ring μ-like 2μedecay, and Sub-GeV π^0-like samples are divided only by the momentum due to the small statistics and poor angular correlation for NC events. Other FC samples are further divided into 10 zenith angle bins equally spaced between $\cos\Theta = -1$ and $\cos\Theta = +1$, where $\cos\Theta$ is cosine of zenith angle of Cherenkov ring direction. The PC samples are similarly divided into 10 bins equally spaced between $\cos\Theta = -1$ and $\cos\Theta = +1$.

7.3 Systematic Uncertainties

We describe the systematic uncertainties in this chapter. The systematic uncertainties of the event selection, detector response, and solar moduration effect in the atmospheric neutrino
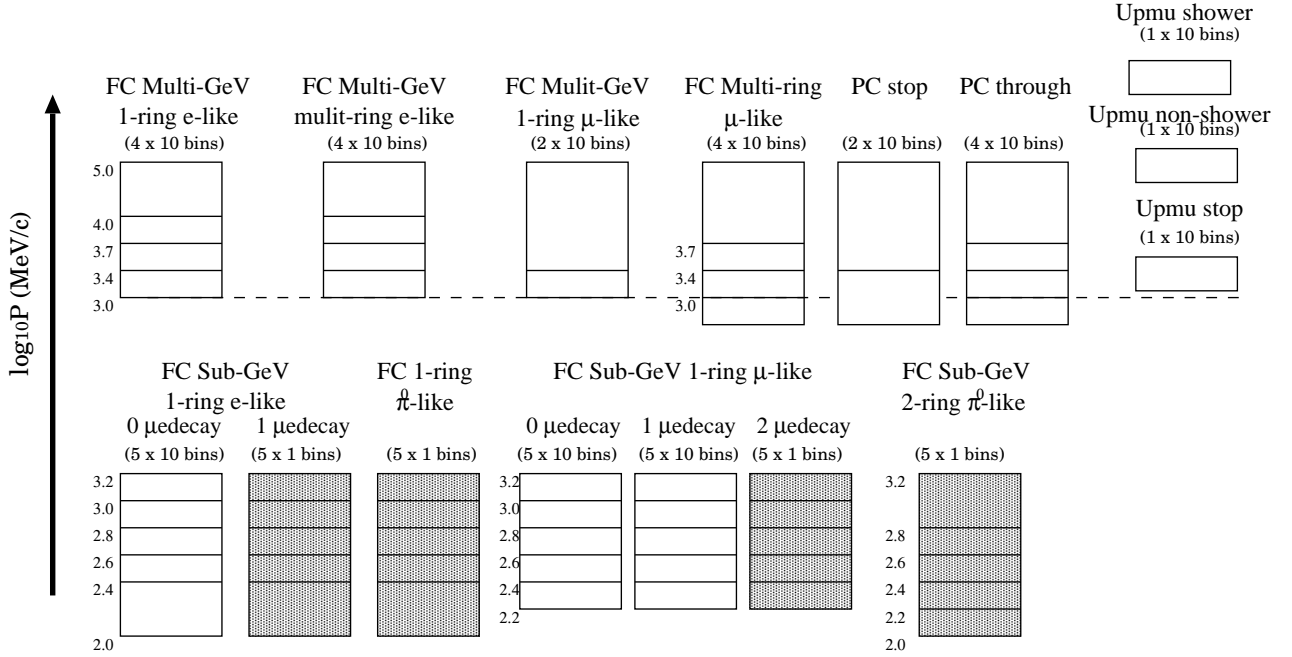
Figure 7.2: The definition of the binning for the SK-I data for the neutrino oscillation analysis : 310 bins for the FC samples, 60 for the PC samples, 30 for the upward-going muon samples. The momentum bins shown in white boxes are divided into 10 bins equally spaced between $\cos\Theta = -1$ and $\cos\Theta = +1$. The FC Single-ring e-like 1μedecay sample, the μ-like 0μedecay sample and the π^0 samples are not divided by the zenith angle bins.
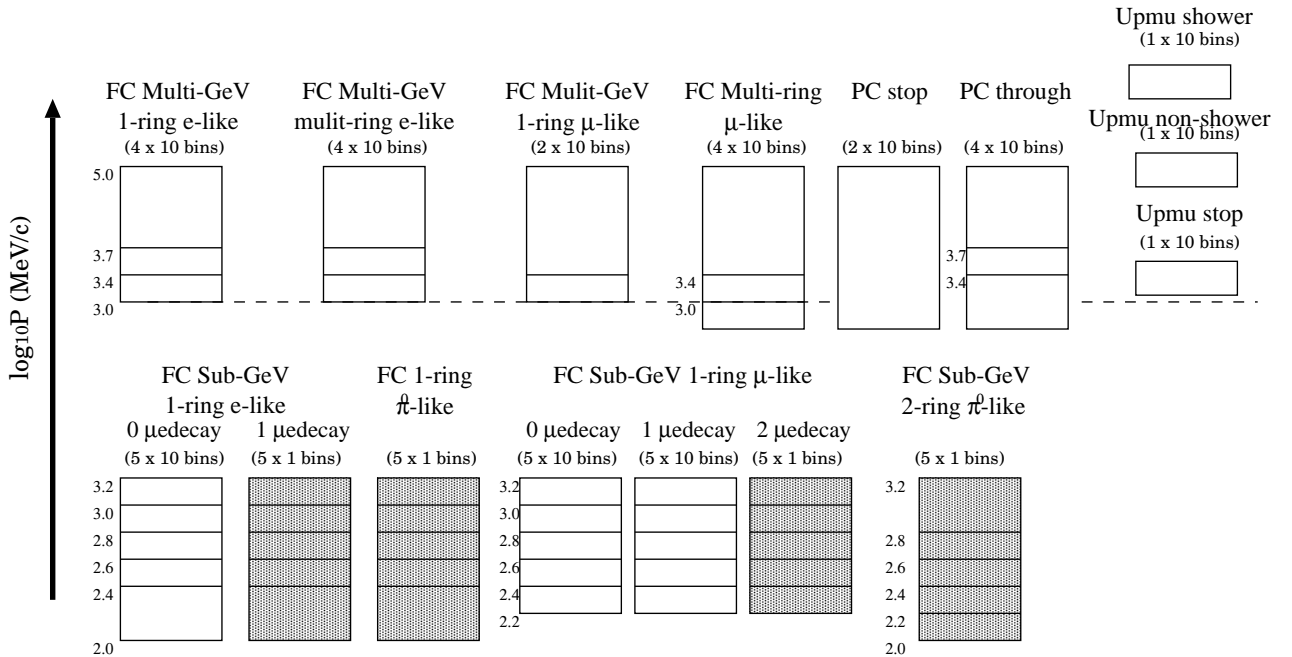
Figure 7.3: The definition of the binning for the SK-II data for the neutrino oscillation analysis : 280 bins for the FC samples, 40 for the PC samples and 30 for the upward-going muon samples.

flux are individually considered between SK-I and SK-II, while others are identical for SK-I and SK-II. Among 90 systematic uncertainties, 19's are for the neutrino flux, 15's for the neutrino interaction, 28's for the SK-I detector response and 28's for the SK-II detector response.

In this chapter, only uncertainties contributory to the analysis results are presented and others are summarized in Appendix A. The effect of systematic uncertainty is taken into account analysis bin by bin, while all uncertainties are treated as uncorrelated each other.

7.3.1 Atmospheric Neutrino Flux

We discussed the atmospheric neutrino flux in Chapter 3.2. Systematic uncertainties in the prediction of the atmospheric neutrino flux are estimated by the comparison of the Honda flux [3] with other flux models, the FLUKA flux [39] and the Bartol flux [40]. The systematic uncertainties in the atmospheric neutrino flux are listed in Table 8.1 and 8.2 in Chapter 8.

- Absolute normalization
  The origin of the uncertainties in the atmospheric neutrino flux calculation is studied in [3]. Figure 7.4 shows the uncertainty of each error source and their sum, in which δ_π accounts for an uncertainty due to pion production in the hadronic interaction model, δ_K for Kaon production uncertanty, δ_σ for hadronic interaction cross section uncertainty, and δ_{air} for atmosphere density profile uncertainty. Uncertainties due to pion production and Kaon production are dominant sources above a few GeV of neutrino energy, while the contribution of interaction cross section uncertainty grows up below 1GeV.

  The sum of δ_π and δ_σ is considered in this uncertainty term as shown in the Figure 7.5, although the uncertainties of Kaon production and atmosphere density profile are included in other term. Note that absolute normalization uncertainty is divided into two terms, below 1 GeV and above 1 GeV, because the major error source is different below and above 1 GeV.

- Flavor ratio
  The flavor ratio $(\nu_\mu + \overline{\nu}_\mu)/(\nu_e + \overline{\nu}_e)$ of the atmospheric neutrino flux is estimated by the comparison of the Honda flux with the FLUKA and the Bartol flux. According to the comparison shown in the Figure 7.6, systematic uncertainty is estimated to be 2 % for E_ν <1 GeV, 3 % for 1 GeV< E_ν <10 GeV, and 5 % for 10 GeV< E_ν <30 GeV. Above 30 GeV, the uncertainty increases almost linearly with $\log E_\nu$ from 5 % (30 GeV) to 30 % (1 TeV). In the low energy region, the uncertainty mainly comes from the pion spectrum in the primary hadronic interactions, while in the high energy region, the uncertainty originates in the K/π production ratio. Due to the difference of error source in each energy region, flavor ratio uncertainty is divided into three terms: E_ν <1 GeV, 1 GeV< E_ν <10 GeV, and E_ν >10 GeV.

- K/π ratio
  As seen in Figure 7.7, atmospheric neutrinos are mainly produced by π^+/π^- below 10 GeV of neutrino energy, while K's contribution is sizable around a few tens of GeV, and dominant above 100 GeV. According to the SPY experiment [144], the measurement of the K/π ratio has been performed achieving an accuracy of 3%, where K and π momentum ranges from 7 GeV/c to 135 GeV/c. According to the measurement of the SPY experiment and the correspondance between hadron momentum and neutrino energy, we estimate the
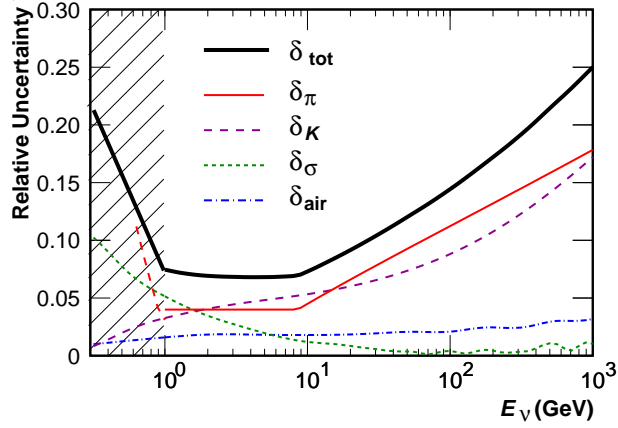
Figure 7.4: The uncertainty of each error source for atmospheric neutrino flux and their sum [3]. In this study, δ_π is estimated from the comparison of the observation and the calculation of the atmosoheric muon flux, however this method loses the validity below 1 GeV(shaded region). Note the statistical and systematic uncertainties are not shown in this figure. Figure is taken from [3].
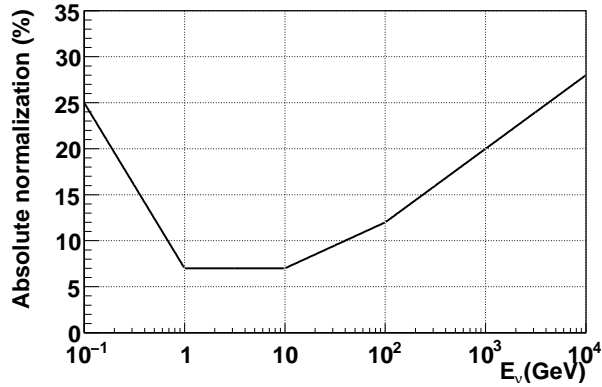
Figure 7.5: Absolute normalization uncertainty due only to δ_π and δ_σ as a function of neutrino energy. δ_K and δ_{air} are not included in this figure. The uncertainty is indivisually considered below and above 1 GeV due to the difference of their origin.
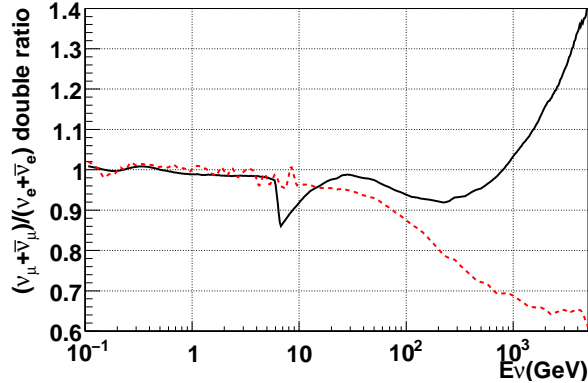
Figure 7.6: The flavor ratio $(\nu_\mu + \overline{\nu}_\mu)/(\nu_e + \overline{\nu}_e)$ of the atmospheric neutrino flux. Vertical axis stands for the double ratio, FLUKA flux/Honda flux(solid) and Bartol flux/Honda flux(dashed). A kink in the FLUKA flux around 8 GeV due to the technical treatment in the original calculation is corrected in the application.

uncertainty of K/π ratio to be 5% below E_ν=100GeV and 20% above E_ν=1TeV. The uncertainty is assumed to increase linearly from 5% to 20% between 100GeV and 1TeV.

- Sample-by-sample normalization
  An energy dependence is inevitable in the comparison using several flux models and can not be explained by a simple spectral index uncertainty as seen in Figure 7.8. From a comparison of the predicted number of events among three flux models, 5% is assigned as the relative normalization uncertanty for these samples.

7.3.2 Neutrino Interactions

Much work has been done to understand theoretically and experimentally the neutrino-nucleus interactions. Estimation of systematic uncertainties are based on their studies. The systematic uncertainties in the neutrino interactions are listed in Table 8.3.

- Nuclear Effect in pion spectrum
  The systematic uncertainty of the predicted pion energy spectrum is estimated by the comparison of NEUT [66, 67], our simulation library, and other neutrino interaction simulator, NUANCE [145] in which nuclear effects are treated based on [146].

7.3.3 Event Selections

- PC stop/through separation
  PC events are classified into two categories, PC stop and through events, according to the energy deposit in OD region. The uncertainty of PC stop/through separation is estimated as follows: PE_{anti}/PE_{exp} distribution of MC events is shifted so as the mean value of the distribution is consistent with that of data, where PE_{anti} stands for the observed p.e.s in the OD and PE_{exp} for the expected p.e.s from the potential track length in the OD. The fractional change in number of events between nominal MC and shifted MC in each category is considered as the systematic uncertainty of the separation. The uncertainty is

100
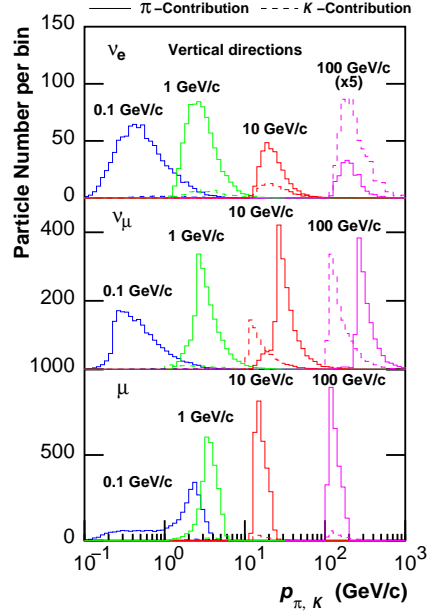
Figure 7.7: The momentum distributions of π's and K's relevant to the atmospheric μ's and ν's with fixed momenta, 0.1, 1.0, 10, 100 GeV/c. Figure is taken from [60].
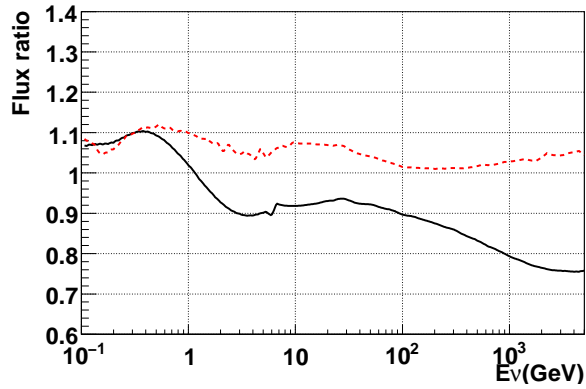
Figure 7.8: The ratio of the calculated neutrino flux in which the fluxes calculated in Bartol (solid line) and FLUKA (dashed line) are normalized by the Honda flux. Also see $\nu_\mu + \overline{\nu}_\mu$ spectrum shown in the left panel of Figure 3.6.

estimated in OD bottom, barrel, and top region separately because of the possible position dependence of OD calibration.

- Background subtraction of Upward going muon events
  The main background for upward going muon is cosmic ray muons. Most of thse events are rejected in the UPMU reduction. After the reduction, the precise fitter gives more accurate fitting informations and rejects downward going muon. The remaining backgrounds after the selection from the precise fitter are eliminated by eye-scanning. Nevertheless, there may still exist some background in near horizontal direction due to the finite fitter resolution and multiple scattering of muons inthe nearby the rock. The cosmic ray contamination is estimated by the shape of zenith angle distribution above horizon which is extrapolated by fitting the zenith angle distribution below horizon. The contamination is estimated for upward stopping muon, upward through-going shower-like, and upward through-going nonshower-like events separately.

7.3.4 Event Reconstructions

Effects of systematic uncertainty related to the event reconstruction are small in this analysis.

Chapter 8

Analysis with 2-Flavor Hybrid Model

We test non standard neutrino interactions (NSI) with the whole atmospheric neutrino data in SK-I and SK-II. NSI consist of either flavor changing neutral current (FCNC) and lepton non universality (NU) in the matter of the Earth. FCNC represents the neutrino interactions with matter as $\nu_\alpha + f \rightarrow \nu_\beta + f$ which allow the flavor transition through the neutral current interactions, and NU indicates the difference between the $\nu_\alpha + f$ and $\nu_\beta + f$ neutral current elastic forward scattering amplitudes, where f denote the fermion in matter.

The scheme we focus on this chapter is that of NSI in the $\nu_\mu - \nu_\tau$ sector coexist with 2-flavor $\nu_\mu \leftrightarrow \nu_\tau$ standard neutrino oscillations, here we call it the *2-flavor Hybrid model*. Propagation of neutrinos from source to the detector assuming the 2-flavor hybrid model is expressed as in Figure 8.1. In this scheme, the flavor transition is only occurred between ν_μ and ν_τ, whereas ν_e flux is kept as is. The *3-flavor hybrid model* with 2-flavor $\nu_\mu \leftrightarrow \nu_\tau$ standard neutrino oscillations and NSI in the $\nu_e - \nu_\tau$ sector is discussed in Chapter 9.

Our interests in this chapter are

(1) Test of the robustness of neutrino oscillations in the atmospheric neutrino data.

(2) Investigation of the possible presence of NSI. If we would not able to obtain the signal of NSI, we derive the constraints to them.

where we use the robustness of the implementation of 2-flavor $\nu_\mu \leftrightarrow \nu_\tau$ neutrino oscillations to the atmospheric neutrinos as a probe of NSI.

First, we explain the formalism of this model in Chapter 8.1. Expected phenomena are discussed in Chapter 8.2, and results of this test are presented in Chapter 8.4.

8.1 Formalism

For the sake of the convenience for the latter discussion, we introduce the complete, i.e. 3-flavor, formula of Hamiltonian to govern the propagation of ν_α to ν_β:

$$H_{\alpha\beta} = \frac{1}{2E} U_{\alpha j} \begin{pmatrix} 0 & 0 & 0 \\ 0 & \Delta m_{21}^2 & 0 \\ 0 & 0 & \Delta m_{31}^2 \end{pmatrix} (U^\dagger)_{k\beta} + V_{\mathrm{MSW}} + \sqrt{2} G_F N_f(\vec{r}) \begin{pmatrix} \varepsilon_{ee} & \varepsilon_{e\mu}^* & \varepsilon_{e\tau}^* \\ \varepsilon_{e\mu} & \varepsilon_{\mu\mu} & \varepsilon_{\mu\tau}^* \\ \varepsilon_{e\tau} & \varepsilon_{\mu\tau} & \varepsilon_{\tau\tau} \end{pmatrix} \quad (8.1)$$
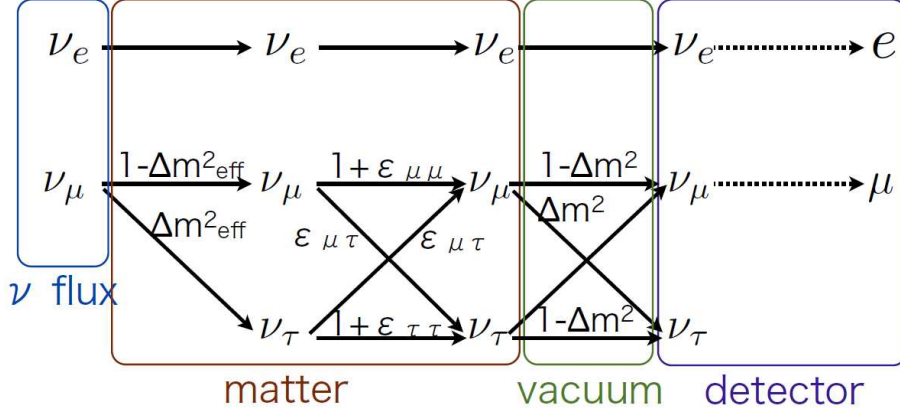
Figure 8.1: Propagation of neutrinos from source to the detector within the 2-flavor hybrid model.

where U is the PMNS matrix and V_{MSW} is the MSW potential in the flavor basis. The first and second term represent neutrino oscillations and the third term is the NSI contribution. $N_f(\vec{r})$ is the fermion number density of the medium along the neutrino trajectory $\vec{r}$, here we assume d-quark density in the matter of the Earth just for the convenience when we compare our results to the bounds given by neutrino scattering experiments. Note that the first term is energy dependent, while the second and third term is energy independent and matter dependent.

We reduce eq.(8.1) to that of the 2-flavor hybrid model we focus on this chapter. In this work we follow the formalism by M.C. Gonzalez-Garcia and M. Maltoni [147], where the propagation of neutrinos($+$) and anti-neutrinos($-$) is governed by the following Hamiltonian:

$$H \equiv \frac{\Delta m^2}{4E} U_\theta \begin{pmatrix} -1 & 0 \\ 0 & 1 \end{pmatrix} U_\theta^\dagger \pm \sqrt{2} G_F N_f(\vec{r}) U_{\xi,\pm\eta} \begin{pmatrix} -1 & 0 \\ 0 & 1 \end{pmatrix} U_{\xi,\pm\eta}^\dagger \tag{8.2}$$

The matrics U_θ and $U_{\xi,\pm\eta}$ are given by:

$$U_\theta = \begin{pmatrix} \cos\theta & \sin\theta \\ -\sin\theta & \cos\theta \end{pmatrix} \tag{8.3}$$

$$U_{\xi,\pm\eta} = \begin{pmatrix} \cos\xi & \sin\xi e^{\pm i\eta} \\ -\sin\xi e^{\mp i\eta} & \cos\xi \end{pmatrix} \tag{8.4}$$

$$\xi = \frac{1}{2} \arctan\left(\frac{\varepsilon_{\mu\tau}}{(\varepsilon_{\tau\tau} - \varepsilon_{\mu\mu})/2} \right) \tag{8.5}$$

where a possible non-vanishing relative phase $\eta(\equiv \delta(\varepsilon_{\mu\tau}))$ is considered. $\sqrt{2} G_F N_f(\vec{r})\varepsilon_{\mu\tau}$ is the amplitude of the flavor changing neutral current(FCNC) process $\nu_\mu + f \rightarrow \nu_\tau + f$, while $\sqrt{2} G_F N_f(\vec{r})(\varepsilon_{\tau\tau} - \varepsilon_{\mu\mu})$ is the amplitude of lepton non universality(NU). These interactions are defined in Chapter 1.3. Note that V_{MSW} is not appeared in the $\nu_\mu - \nu_\tau$ sector.

If the matter profile in the Earth is constant along the neutrino trajectory, $P_{\nu_\mu \rightarrow \nu_\mu}$ is expressed as:

$$P_{\nu_\mu \rightarrow \nu_\mu} = 1 - P_{\nu_\mu \rightarrow \nu_\tau} = 1 - \sin^2 2\Theta \sin^2\left(\frac{\Delta m^2 L}{4E} R \right) \tag{8.6}$$

104
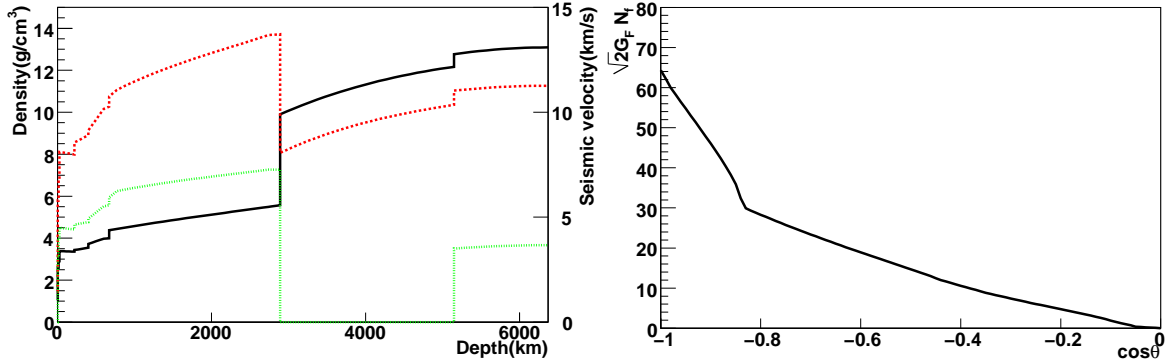
Figure 8.2: (Left) PREM predicted matter density (solid line) and seismic velocity (dashed line for P-wave and dotted line for S-wave) as a function of the depth, where depth = 0 km is the surface of the Earth. (Right) The average fermion number density as a function of zenith angle.

where the effective mixing angle Θ and NSI's correction factor to the oscillation wavelength, R, are given as

$$\sin^2 2\Theta = \frac{1}{R^2}(\sin^2 2\theta + R_0^2 \sin^2 2\xi + 2R_0 \sin 2\theta \sin 2\xi \cos \eta), \qquad (8.7)$$

$$R = \sqrt{1 + R_0^2 + 2R_0(\cos 2\theta \cos 2\xi + \sin 2\theta \sin 2\xi \cos \eta)}. \qquad (8.8)$$

R_0 gives the ratio between standard oscillation and NSI to the oscillation wavelength

$$R_0 = \pm \frac{\lambda_{matter}}{2} \frac{4E}{\Delta m^2} \qquad (8.9)$$

NSI effect λ_{matter} is given as:

$$\lambda_{matter} = 2\sqrt{2}G_F N_f(\vec{r})F$$

$$\equiv 4.58 \times 10^{-22}(2 - Y_p)\frac{\rho(\vec{r})_{Earth}}{3g/cm^3}F\,\mathrm{GeV} \qquad (8.10)$$

$$F = \sqrt{|\varepsilon_{\mu\tau}|^2 + \frac{(\varepsilon_{\tau\tau} - \varepsilon_{\mu\mu})^2}{4}} \qquad (8.11)$$

We employ the PREM model [24] to describe the matter density profile and chemical composition, as shown in Figure 8.2, where the proton/nucleus ratio in the mantle and core are set to be $Y_p = 0.497$ and 0.468, respectively. The fermion f in the above formulae are assumed to be d-quark. This assumption is just for convenience when we compare our results to the bounds given by neutrino scattering experiments. In the calculations we take the average matter density along the path of neutrino.

8.2   Expected Phenomena

In this section we describe expected phenomena driven by NSI. As explicitly expressed in eq.(8.2), the first term (standard 2-flavor oscillations) depends on the neutrino energy, while the
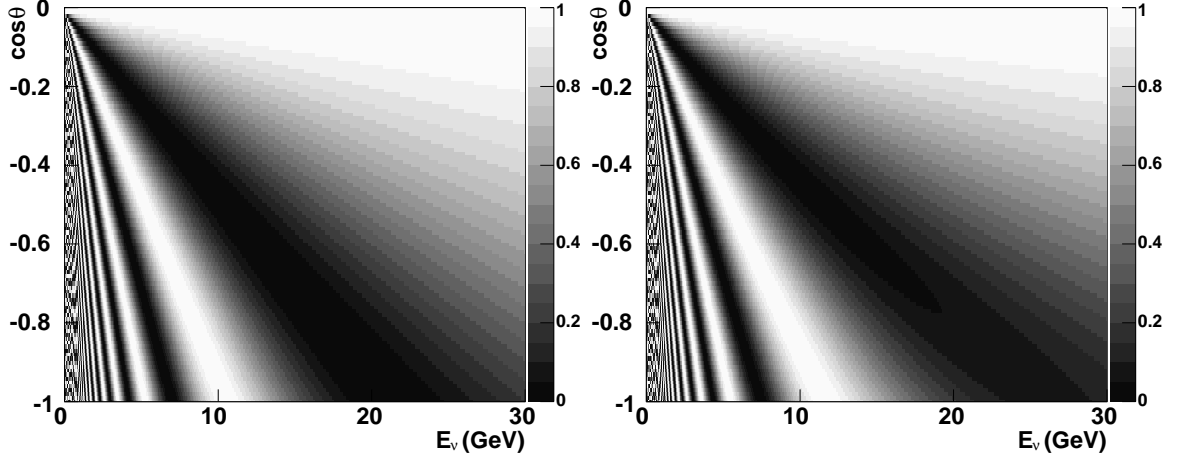
Figure 8.3: Survival probability of $\nu_\mu \rightarrow \nu_\mu$ for standard 2-flavor oscillation (left panel) and the 2-flavor hybrid model (right panel). In both panels $\Delta m^2 = 2.1 \times 10^{-3} \text{eV}^2$ and $\theta = 45°$ are assumed. Only in the right panel $\varepsilon_{\mu\tau}$(FCNC)=0.015 and $\varepsilon_{\tau\tau} - \varepsilon_{\mu\mu}$(NU)=0.05, corresponding to the present limits, are assumed. For simplicity, the matter density is assumed to be constant, $\rho = 5.0 \text{g/cm}^3$.

second term (NSI) is energy independent and matter dependent, thus the relative effect of NSI in the hybrid model is expected to vary according to the neutrino energy. First we demonstrate the survival probability of $\nu_\mu \rightarrow \nu_\mu$ for standard 2-flavor oscillation and the 2-flavor hybrid model in Figures 8.3 and 8.4, where only the upward region is presented because NSI is effective only in matter, so no difference is found in the angular region from downward to horizon.

We discuss how NSI affects the atmospheric neutrino oscillations in three energy ranges, (1) $E_\nu <$1GeV, (2) $1< E_\nu <$30GeV, (3) $E_\nu >$30GeV.

(1) $E_\nu <$1GeV

As seen in Figure 8.5, an eigenvalue of the vacuum term in eq.(8.2), $\Delta m^2/2E_\nu$, is much larger than that of matter term, $\sqrt{2}G_F N_f \varepsilon$, where $\Delta m^2 = 2.1 \times 10^{-3} \text{eV}^2$, $N_f \equiv N_d \sim 3N_e$, and $\varepsilon = 1.0$ are assumed. This means that $\nu_\mu \rightarrow \nu_\tau$ transition is mostly governed by 2-flavor standard oscillation below 1GeV and no significant contribution of NSI is expected. Note that the eigenvalue of the solar term(Δm_{21}^2 and θ_{12}) has a comparable size to the matter effects below 200MeV, which will be discussed later.

(2) $1< E_\nu <$30GeV

In this energy range the matter term competes with the vacuum term. The $\nu_\mu \rightarrow \nu_\tau$ transition is no longer dominated by the standard oscillation, but also sizably modified by the matter term. Modified oscillation parameters, effective mixing angle (Θ) and eigenvalue (Δm_{eff}^2) in the matter, for several $\varepsilon_{\mu\tau}$ and $\varepsilon_{\tau\tau} - \varepsilon_{\mu\mu}$ are presented in Figure 8.6. As shown in Figure 8.6, nonzero $\varepsilon_{\tau\tau} - \varepsilon_{\mu\mu}$ gives the supression of $\nu_\mu \rightarrow \nu_\tau$ transition due to the condition $\Theta < \theta_{23} \sim 45°$ and the magnitude of supression becomes larger as the neutrino energy increases, while nonzero $\varepsilon_{\mu\tau}$ affects the frequency of the oscillation, $\Delta m_{eff}^2 > \Delta m^2$. As seen in the left panel on Figure 8.3, maximum transition in the case of standard oscillation, i.e. $P(\nu_\mu \rightarrow \nu_\mu) \sim 0$, occurrs in the
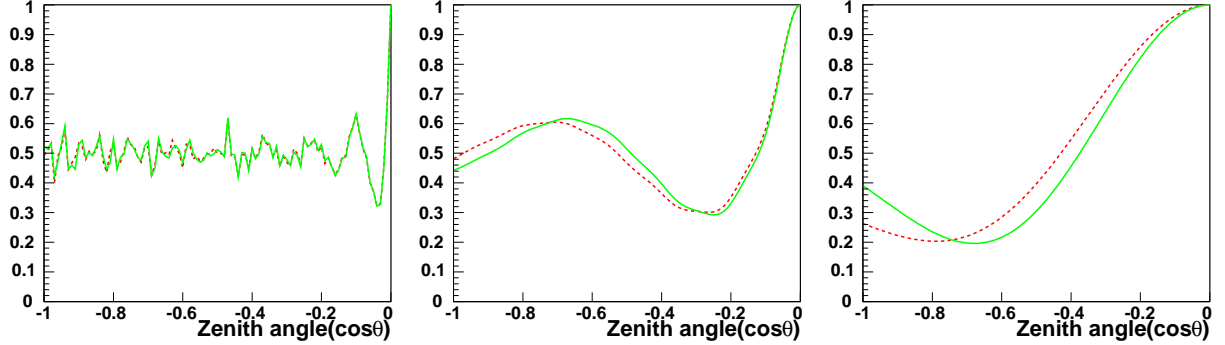
Figure 8.4: Survival probability of $\nu_\mu \to \nu_\mu$ for standard 2-flavor oscillation and the 2-flavor hybrid model as a function of the zenith angle of the neutrino direction. Solid curves (2-flavor hybrid model) and dashed curves (standard 2-flavor oscillation) indicate the average probability over neutrino energy: E_ν <1.4 GeV (left), $1.4 < E_\nu < 5.0$ GeV (center), and $5.0 < E_\nu < 30.0$ GeV (right). In all panels $\Delta m^2 = 2.1 \times 10^{-3} \text{eV}^2$ and $\theta = 45°$ are assumed. As for NSI parameters $\varepsilon_{\mu\tau}$=0.015 and $\varepsilon_{\tau\tau} - \varepsilon_{\mu\mu}$=0.05 are considered. Constant density $\rho = 5.0\text{g/cm}^3$ is assumed for simplicity.
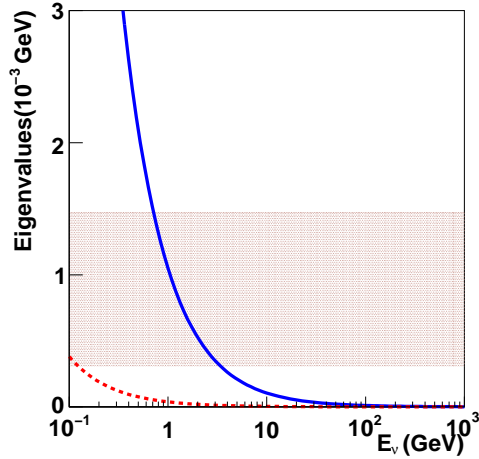
Figure 8.5: Eigenvalues of the vacuum term and matter term in eq.(8.2). Solid curve indicates the eigenvalue of the vacuum term, $\Delta m^2/2E_\nu$, and the hatched area represents the eigenvalue of the matter term $\sqrt{2}G_F N_f \varepsilon$, where $\Delta m^2 = 2.1 \times 10^{-3} \text{eV}^2$, $N_f \equiv N_d \sim 3N_e$, and $\varepsilon = 1.0$ are assumed. The hatched area ranges from the case with $\rho = 2.7\text{g/cm}^3$ (bottom edge) to the case with $\rho = 13\text{g/cm}^3$ (top edge). For reference, dashed curve indicates the eigenvalue of vacuum term with $\Delta m^2_{21} = 7.6 \times 10^{-5} \text{eV}^2$, which are discussed in the 3-flavor hybrid model analysis.

107
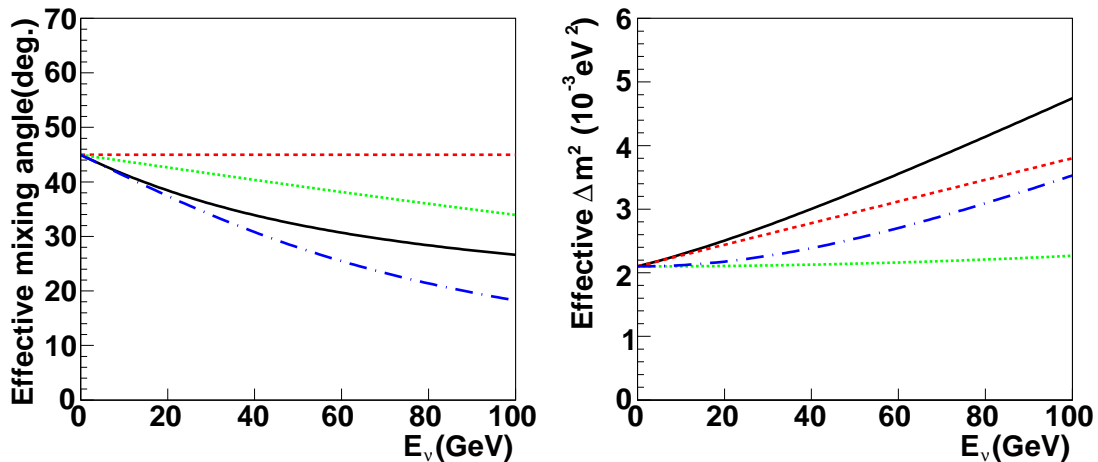
Figure 8.6: (Left) Effective mixing angle in matter. (Right) Effective mass squared difference in matter. In both panels, solid curves indicate the case with $\varepsilon_{\mu\tau}$(FCNC)=0.015 and $\varepsilon_{\tau\tau} - \varepsilon_{\mu\mu}$(NU)=0.05, dashed curves for $\varepsilon_{\mu\tau}$=0.015, dotted curves for $\varepsilon_{\tau\tau} - \varepsilon_{\mu\mu}$=0.015, dashed-dotted curves for $\varepsilon_{\tau\tau} - \varepsilon_{\mu\mu}$=0.05. As for vacuum parameters, $\theta_{23} = 45°$ and $\Delta m^2 = 2.1 \times 10^{-3}$eV^2 are assumed. $\rho = 5.0$g/cm^3 is assumed.

nearly upward direction at about 20GeV. On the other hand, once nonzero $\varepsilon_{\mu\tau}$ is considered the maximum transition can be realized even at larger zenith angles. This is recognized in the right panel of Figure 8.3 and Figure 8.4. If we focus on the zenith angle distributions, since this energy range corresponds to FC Multi-GeV, PC, and UPMU stopping samples, we expect that the magnitude of μ-like deficit becomes smaller due to $\varepsilon_{\tau\tau} - \varepsilon_{\mu\mu}$ and the shape of zenith angle distributions between near horizon and upward are modified because of $\varepsilon_{\mu\tau}$ in higher energy ν_μ-rich samples.

(3) $E_\nu >$30GeV

As indicated in the solid curve in Figure 8.5, vacuum oscillation has less of a leading effect in the $\nu_\mu \to \nu_\tau$ transition in this energy range, while a large transition is realized with an energy independent matter term when the neutrino propagates in the Earth sufficiently long. In other words, this is a different case from (2), $\varepsilon_{\mu\tau}$ plays the leading role in this energy range since the modified frequency of the oscillation has a comparable size to the path length, therefore a $\nu_\mu \to \nu_\tau$ transition driven by $\varepsilon_{\mu\tau}$ is expected. In contrast, $\varepsilon_{\tau\tau} - \varepsilon_{\mu\mu}$ takes a sub-leading effect because this effect is subject to the standard oscillation induced $\nu_\mu \to \nu_\tau$ transition which is less apparent in this energy range. Overall, these phenomena are expected to be visible in UPMU through samples which range from a few tens of GeV up to extreme high energy $\sim$ 100TeV.

Finally we summarize this discussion: $\varepsilon_{\mu\tau}$ gives a higher frequency, thus leads the $\nu_\mu \to \nu_\tau$ transition for shorter path lengths in matter, while $\varepsilon_{\tau\tau} - \varepsilon_{\mu\mu}$ suppresses the transition even at relevant energies.

8.3 Analysis Method

A value of χ^2 is evaluated at each grid point in the four-dimensional parameter space of $\sin^2 2\theta_{23}$, Δm^2, $\varepsilon_{\mu\tau}$, and $\varepsilon_{\tau\tau} - \varepsilon_{\mu\mu}$ in case without relative complex phase η. If we consider the phase η, χ^2 is calculated with five-dimensional parameter space. Note that $\varepsilon_{\mu\tau}$ is symmetrical between negative and positive value, then we only consider the positive value.

8.4 Result of 2-Flavor Non-Standard Interaction Analysis

First we mention the case when the relative phase η is not considered. As a result of the global scan on the four-dimensional oscillation parameter space, best-fit values are derived at

$$\sin^2 2\theta = 1.00, \quad \Delta m^2 = 2.2 \times 10^{-3} \text{eV}^2,$$
$$\varepsilon_{\mu\tau} = 1.0 \times 10^{-3}, \quad \varepsilon_{\tau\tau} - \varepsilon_{\mu\mu} = -2.7 \times 10^{-2}$$
$$\chi^2_{min} = 838.9 \; / \; 746.0 \text{ d.o.f.} \tag{8.12}$$

The best-fit values of the systematic uncertainty parameters ϵ_j obtained at the global minimum are summarized in Tables from 8.1 to 8.7.

Figure 8.7 shows the allowed regions of the neutrino oscillation parameters $(\sin^2 2\theta, \Delta m^2)$. The three contour curves correspond to the 68%, 90% and 99% confidence level (C.L.) allowed regions which are defined to be $\chi^2 = \chi^2_{min}$ +2.30, 4.61, and 9.21 respectively.

As for the case when the relative phase η is considered, a global scan on the five-dimensional oscillation parameter space gives best-fit values,

$$\sin^2 2\theta = 1.00, \quad \Delta m^2 = 2.2 \times 10^{-3} \text{eV}^2,$$
$$\varepsilon_{\mu\tau} = 6.9 \times 10^{-3}, \quad \varepsilon_{\tau\tau} - \varepsilon_{\mu\mu} = -1.9 \times 10^{-2}, \quad \cos\eta = -1.0$$
$$\chi^2_{min} = 837.5 \; / \; 745.0 \text{ d.o.f.} \tag{8.13}$$

No significant difference is found in the allowed neutrino oscillation parameter region between the two cases, with and without relative phase.

The minimum χ^2 value derived from the 2-flavor hybrid model is larger than that with the standard 2-flavor neutrino oscillation shown in Appendix B, even if two or three free parameters are additionally considerd. This can be understood by the difference in the "averaging method". As seen, for example, in the left panel of Figure 8.4, the oscillation probability varies frequently when $\Delta m^2 L/4E_\nu \gg 1$, and these frequent variations bring notchy allowed regions. In order to avoid such a problem, an "averaging method" is introduced, which takes $P(\nu_\mu \to \nu_\tau) = \sin^2 2\theta/2$ in the case that a oscillation probability frequently varies between 0 and 1. However it cannot be applied to the 2-flavor hybrid model as keeping the original mechanism because the probability equation is different between the two cases. Therefore a modified averaging method is introduced and this method gives a little bit larger χ^2 value. Considering the disparity of the averaging method, the difference of the minimum χ^2 value between the 2-flavor hybrid model and standard 2-flavor neutrino oscillation is less than 1, therefore the choice of averaging method can be negligible in the analysis.

The two allowed neutrino oscillation parameter regions, that of the the hybrid model in Figure 8.7 and standard oscillation in Appendix B, are consistent each other and also the difference of the minimum χ^2 is very small. Hence we can conclude that 2-flavor neutrino oscillation is a robust hypothesis for the atmospheric neutrinos and no significant contribution of NSI is found.
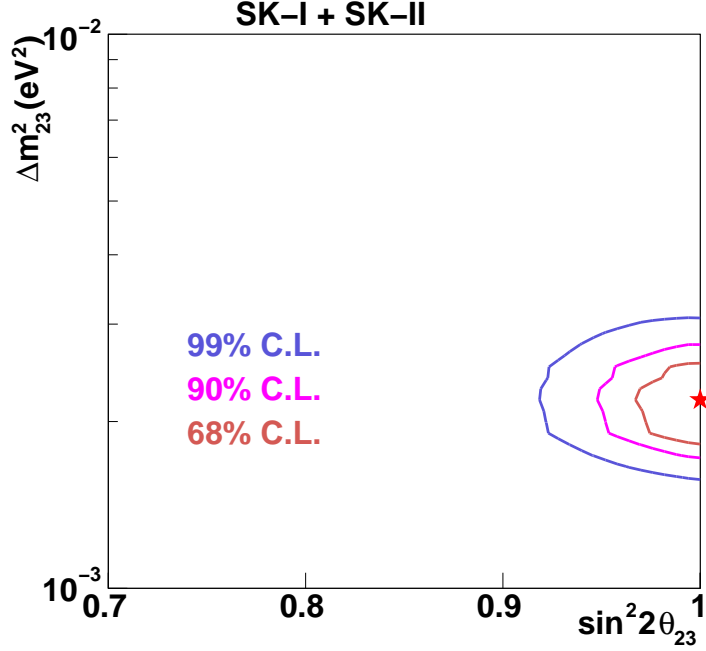
Figure 8.7: Allowed oscillation parameters assuming the 2-flavor hybrid model, where undisplayed parameters $\varepsilon_{\mu\tau}$ and $\varepsilon_{\tau\tau} - \varepsilon_{\mu\mu}$ are integrated out. The three contours correspond to the 68%, 90% and 99% C.L. allowed regions, respectively.

8.4.1 Limit on NSI parameters without relative phase

We present the allowed 2-flavor NSI paramters when relative phase η is not considered. Figure 8.8 shows the allowed regions of the NSI parameters $(\varepsilon_{\mu\tau}, \varepsilon_{\tau\tau} - \varepsilon_{\mu\mu})$, where undisplayed parameters $\sin^2 2\theta$ and Δm^2 are integrated out. Three contours correspond to the 68%, 90% and 99% confidence level (C.L.) allowed regions which are defined to be $\chi^2 = \chi^2_{min}$ +2.30, 4.61, and 9.21, respectively. Figures 8.9 and 8.10 show the $\chi^2 - \chi^2_{min}$ distributions as a function of $\varepsilon_{\mu\tau}$ and $\varepsilon_{\tau\tau} - \varepsilon_{\mu\mu}$, respectively, which are sliced at the best-fit position of other parameters. Limits on the NSI parameters in the $\nu_\mu - \nu_\tau$ sector at a 90 % C.L. are :

$$|\varepsilon_{\mu\tau}| < 1.1 \times 10^{-2}, \quad -4.9 \times 10^{-2} < \varepsilon_{\tau\tau} - \varepsilon_{\mu\mu} < 4.9 \times 10^{-2} \tag{8.14}$$

Systematic uncertainties are summarized in Tables from 8.1 to 8.7. Best-fit values are without parentheses.

8.4.2 Limit on NSI parameters with relative phase

Next we take the more general case when the relative phase η is considered. The allowed 2-flavor NSI parameters region is presented in Figure 8.11, where the relative phase η is scanned from 0 to 2π. Therefore a χ^2 value is calculated at each grid point in the five-dimensional parameter space including η.

Figure 8.11 shows the allowed regions of the NSI parameters $(\varepsilon_{\mu\tau}, \varepsilon_{\tau\tau} - \varepsilon_{\mu\mu})$, where the undisplayed parameters $\sin^2 2\theta$, Δm^2, and $\cos \eta$ are integrated out. The three contours correspond to the 68%, 90% and 99% confidence levels (C.L.) allowed regions with the same definition as
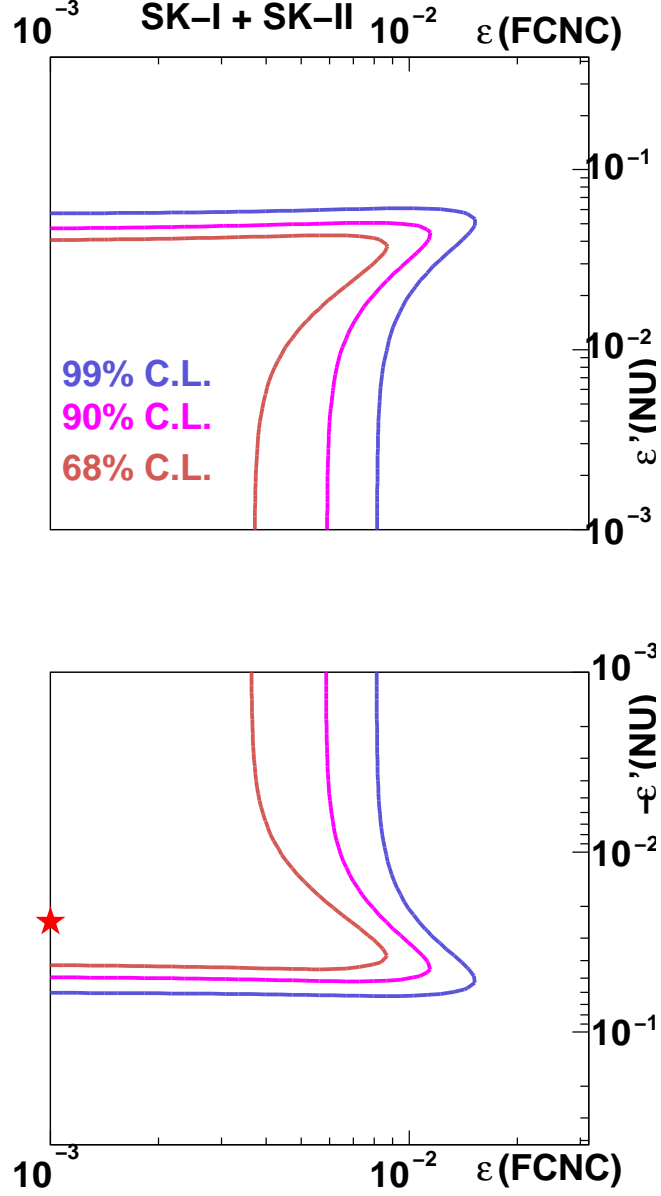
Figure 8.8: Allowed NSI parameters region assuming the 2-flavor hybrid model *without* the relative phase. The horizontal axis shows $\varepsilon_{\mu\tau}$ ($\equiv \varepsilon$, FCNC) and the vertical axis shows $\varepsilon_{\tau\tau} - \varepsilon_{\mu\mu}$ ($\equiv \varepsilon'$, NU). The undisplayed parameters $\sin^2 2\theta$ and Δm^2 are integrated out. The three contours correspond to the 68%, 90% and 99% C.L. allowed regions, respectively. Star represents the best-fit point for the NSI parameters.
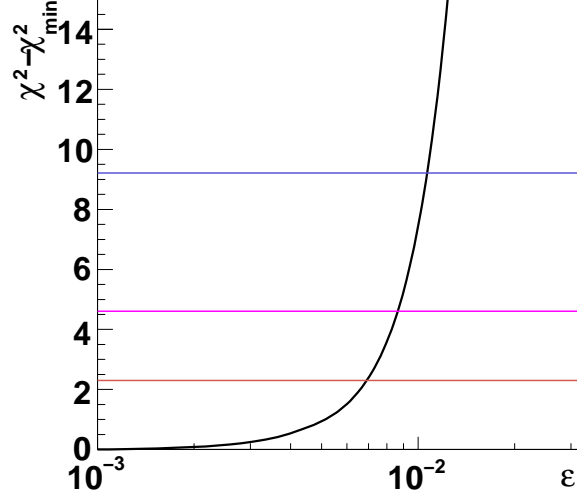
Figure 8.9: $\chi^2 - \chi^2_{min}$ distributions as a function of $\varepsilon_{\mu\tau}$ ($\equiv \varepsilon$) in the negative side of $\varepsilon_{\tau\tau} - \varepsilon_{\mu\mu}$ *without* the relative phase, where $\sin^2 2\theta$ and Δm^2 are integrated out. The three horizontal lines correspond to the 68%, 90% and 99% C.L..
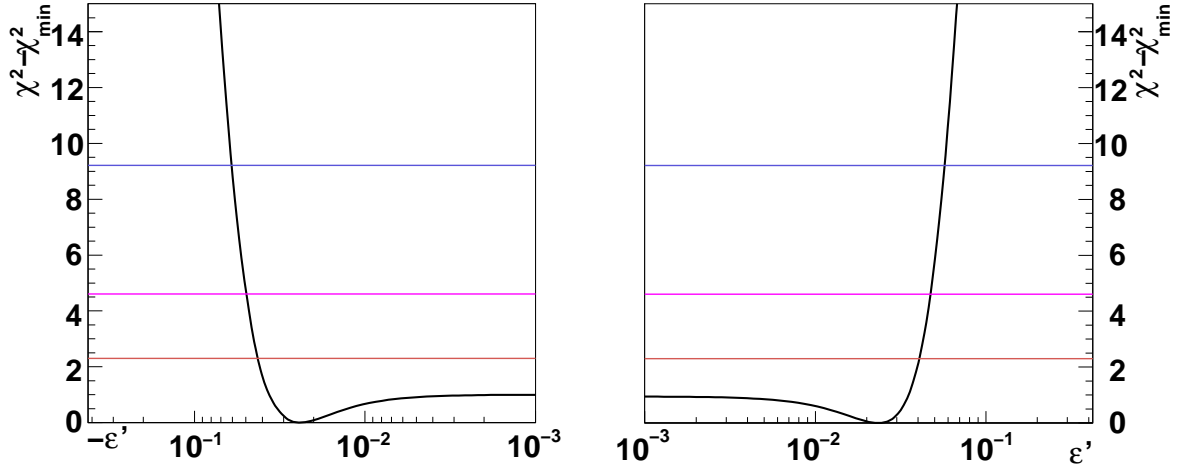
Figure 8.10: $\chi^2 - \chi^2_{min}$ distributions as a function of $\varepsilon_{\tau\tau} - \varepsilon_{\mu\mu}$ ($\equiv \varepsilon'$) *without* the relative phase, where $\sin^2 2\theta$ and Δm^2 are integrated out. The three horizontal lines correspond to the 68%, 90% and 99% C.L..

Figure 8.8. Figures 8.12 and 8.13 show the $\chi^2 - \chi^2_{min}$ distributions as a function of $\varepsilon_{\mu\tau}$ and $\varepsilon_{\tau\tau} - \varepsilon_{\mu\mu}$. The limit on the NSI parameters in the $\nu_\mu - \nu_\tau$ sector at a 90 % C.L. is :

$$|\varepsilon_{\mu\tau}| < 1.6 \times 10^{-2}, \quad -5.3 \times 10^{-2} < \varepsilon_{\tau\tau} - \varepsilon_{\mu\mu} < 4.9 \times 10^{-2} \tag{8.15}$$

Systematic uncertainties are summarized in Tables from 8.1 to 8.7. Best-fit values are within parentheses.

8.5 Discussion

At the end of this section, we discuss how NSI parameters are constranied by atmospheric neutrinos. As mentioned in Chapter 8.2, the NSI effects are expected to be visible in ν_μ-rich samples above a few GeV. In order to check it, we present the allowed NSI parameter region derived by sets of sub-samples in Figure 8.14, where the solid curve indicates the allowed NSI region given by UPMU through, the dashed curve for PC and UPMU stopping, and the dotted curve for FC Single-ring Multi-GeV and Multi-ring. The plane with negative $\varepsilon_{\tau\tau} - \varepsilon_{\mu\mu}$ is presented, since the minimum χ^2 is located in negative $\varepsilon_{\tau\tau} - \varepsilon_{\mu\mu}$ space. strongest constraint to $\varepsilon_{\mu\tau}$ is given by UPMU through, while $\varepsilon_{\tau\tau} - \varepsilon_{\mu\mu}$ is constrained by the other sub-samples: FC Single-ring Multi-GeV, FC Multi-ring, PC and UPMU stopping. Note that FC Sub-GeV samples are less effective to place a limit on NSI in the $\nu_\mu - \nu_\tau$ sector.

The Constraints to $\varepsilon_{\mu\tau}$ (FCNC) and $\varepsilon_{\tau\tau} - \varepsilon_{\mu\mu}$ (NU) make sense as follows: nonzero $\varepsilon_{\mu\tau}$ modifies the frequency of oscillation and the modified frequency leads to a $\nu_\mu \to \nu_\tau$ transition with a shorter path length in matter. Although, when neutrino energy is sufficiently small, the first octant of the transition can occur at a smaller zenith angle even without $\varepsilon_{\mu\tau}$ modification. Thus it is not possible to observe a clear inconsistency between standard oscillation and nonzero $\varepsilon_{\mu\tau}$ below $\sim$30GeV. In the energy region corresponding to the UPMU through samples, the first octant of standard oscillation is no longer found at any zenith angle, on the other hand the modified frequency by $\varepsilon_{\mu\tau}$ allows the $\nu_\mu \to \nu_\tau$ transition in the upward direction. Indeed, nonzero $\varepsilon_{\mu\tau}$ yields a deficit of UPMU through events, and results in a apparent conflict with the expected standard oscillation observation.

In Figure 8.15, colored boxes show the ratio of UPMU through events in three upward bins $(\cos\Theta = -1 \sim -0.7)$ to that in three horizon bins $(\cos\Theta = -0.3 \sim 0)$, we call it the *Up/Horizon ratio*, and the three contours are also displayed for reference. The negative $\varepsilon_{\tau\tau} - \varepsilon_{\mu\mu}$ plane is only presented due to the same reason as in Figure [**?**]. We can see the Up/Horizon ratio becomes smaller as $\varepsilon_{\mu\tau}$ increases due to the deficit of upward events, and results in a constraint on $\varepsilon_{\mu\tau}$. In contrast, we know that the $\varepsilon_{\tau\tau} - \varepsilon_{\mu\mu}$ induced supression of the $\nu_\mu \to \nu_\tau$ transition is found in any energy range, especially clear in the range $1 < E_\nu < 30$GeV. As shown in Figure 8.14, the ν_μ-rich higher energy samples of PC, UPMU stopping, and also UPMU through contribute to put a constraint on $\varepsilon_{\tau\tau} - \varepsilon_{\mu\mu}$. Moreover, in Figure 8.15 the Up/Horizon ratio grows larger as the absolute value of $\varepsilon_{\tau\tau} - \varepsilon_{\mu\mu}$ increases, however it is inconsistent with the observations.

Finally, we test how our limits are changed when the systematic uncertainty of K/π ratio is considered, which is effective to the fraction of UPMU stopping and through events. Figure 8.16 shows the allowed regions with two cases: (solid lines) with all of systematic uncertainties, and (dashed lines) K/π ratio uncertainty is neglected. $\varepsilon_{\mu\tau}$ is sensitive to the K/π ratio uncertainty since $\varepsilon_{\mu\tau}$ is mostly constrained by UPMU through events as well as UPMU stopping, as seen in Figure 8.14. On the other hand, the modification of $\varepsilon_{\tau\tau} - \varepsilon_{\mu\mu}$ is rather small. This makes sence as we remember $\varepsilon_{\tau\tau} - \varepsilon_{\mu\mu}$ is also constrained by the other sub-samples.
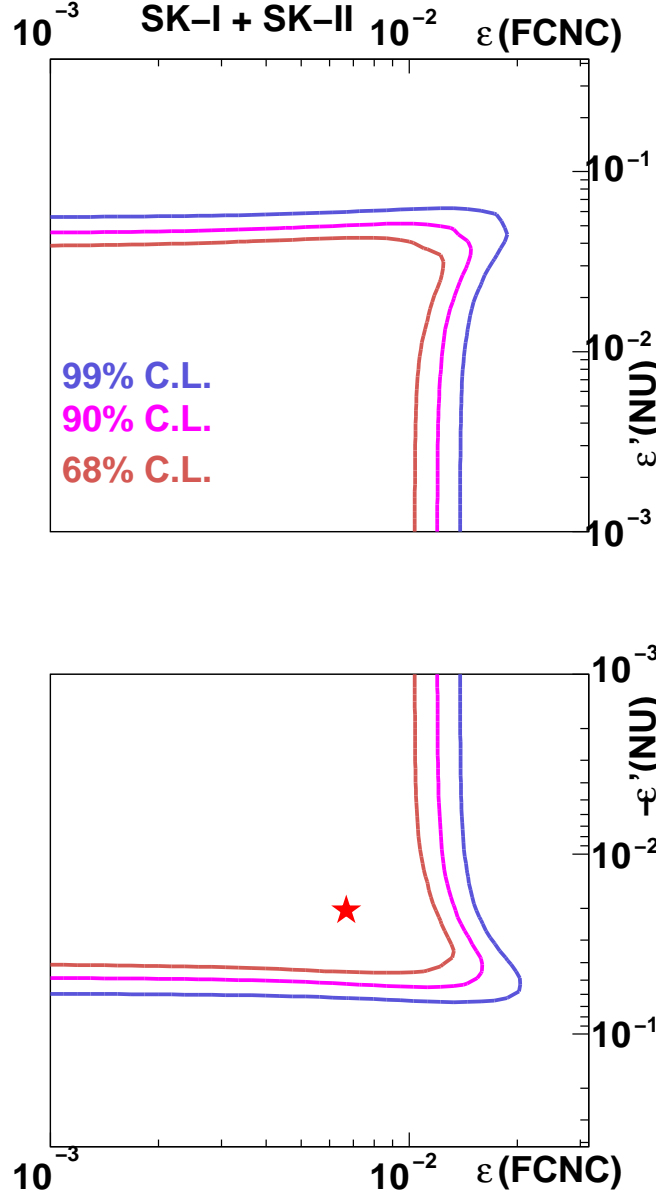
Figure 8.11: Allowed NSI parameters region assuming the 2-flavor hybrid model *with* the relative phase η. The horizontal axis shows $\varepsilon_{\mu\tau}$ ($\equiv \varepsilon$, FCNC) and the vertical axis shows $\varepsilon_{\tau\tau} - \varepsilon_{\mu\mu}$ ($\equiv \varepsilon'$, NU). The undisplayed parameters $\sin^2 2\theta$, Δm^2, and $\cos\eta$ are integrated out. The three contours correspond to the 68%, 90% and 99% C.L. allowed regions, respectively. Star represents the best-fit point for the NSI parameters.
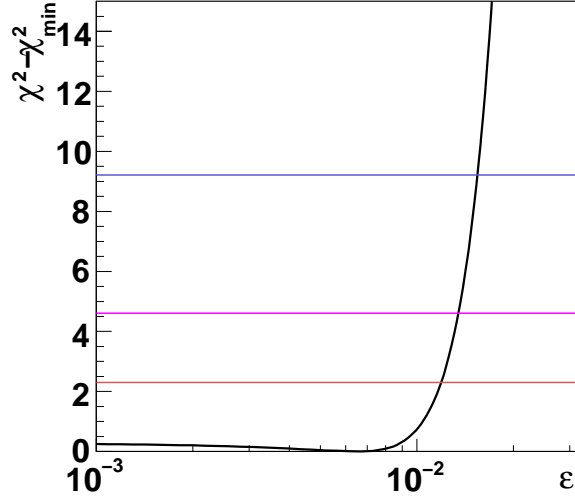
Figure 8.12: $\chi^2 - \chi^2_{min}$ distributions as a function of $\varepsilon_{\mu\tau}$ ($\equiv \varepsilon$) in the negative side of $\varepsilon_{\tau\tau} - \varepsilon_{\mu\mu}$ *with* the relative phase η, where $\sin^2 2\theta$, Δm^2, and $\cos \eta$ are integrated out. The three horizontal lines correspond to the 68%, 90% and 99% C.L..
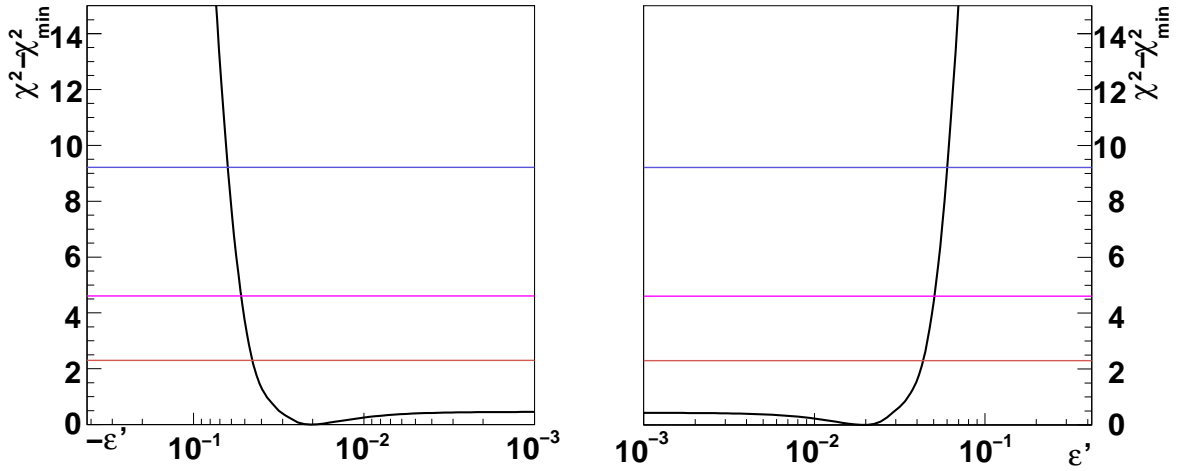

Figure 8.13: $\chi^2 - \chi^2_{min}$ distributions as a function of $\varepsilon_{\tau\tau} - \varepsilon_{\mu\mu}$ ($\equiv \varepsilon'$) *with* the relative phase η, where $\sin^2 2\theta$, Δm^2, and $\cos \eta$ are integrated out. The three horizontal lines correspond to the 68%, 90% and 99% C.L..
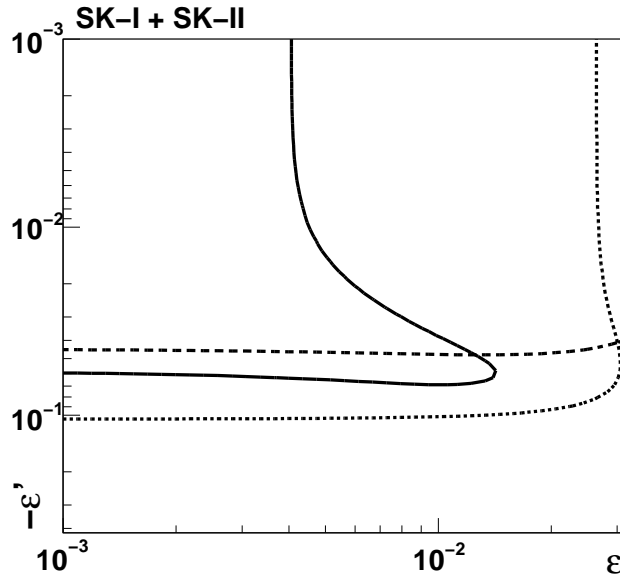
Figure 8.14: Allowed NSI parameters region derived by sets of sub-samples, where horizontal axis is $\varepsilon_{\mu\tau}$ ($\equiv \varepsilon$) and vertical axis is $\varepsilon_{\tau\tau} - \varepsilon_{\mu\mu}$ ($\equiv \varepsilon'$). Solid curve indicates the allowed region given by UPMU through, dashed curve by PC and UPMU stopping, dotted curve by FC Single-ring Multi-GeV and Multi-ring. Contour corresponds to $\chi^2 = \chi^2 + 2.31$.
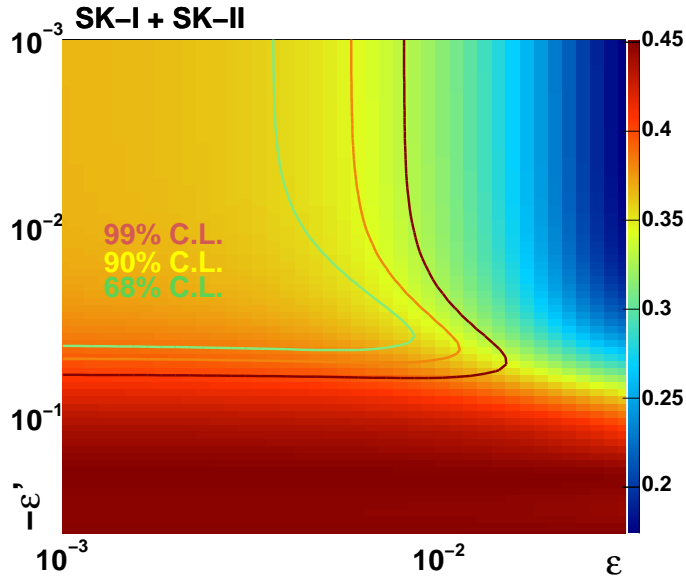
Figure 8.15: Colored boxes show the UP/Horizon ratio of UPMU through events, where horizontal axis is $\varepsilon_{\mu\tau}$ ($\equiv \varepsilon$) and vertical axis is $\varepsilon_{\tau\tau} - \varepsilon_{\mu\mu}$ ($\equiv \varepsilon'$). Three contours, same as in Figure 8.8, are displayed for reference.
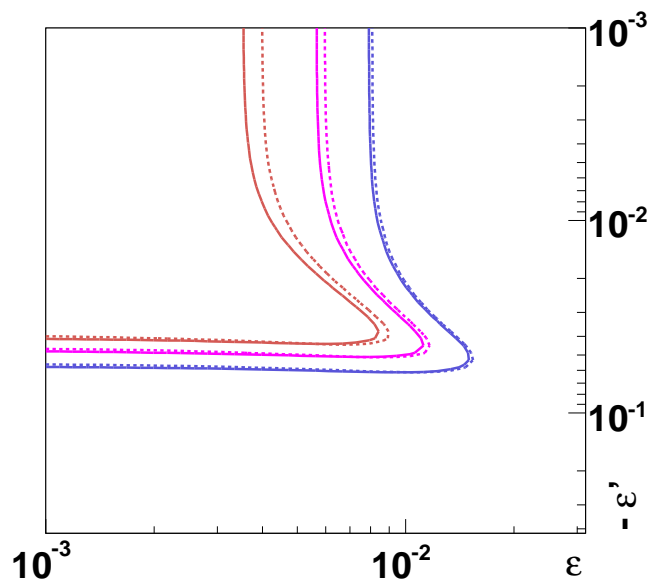
Figure 8.16: Allowed NSI parameters region, where horizontal axis is $\varepsilon_{\mu\tau}$ ($\equiv \varepsilon$) and vertical axis is $\varepsilon_{\tau\tau} - \varepsilon_{\mu\mu}$ ($\equiv \varepsilon'$). All of systematic uncertainties are considered in solid lines, while K/π ratio uncertainty is neglected in dashed lines.

			uncertainty (%)	best-fit (%)
(A1) Systematic uncertainties in neutrino flux				
Absolute normalization	$E_\nu < 1\,\mathrm{GeV}$		25.0	34.2 (33.1)
	$E_\nu > 1\,\mathrm{GeV}$		15.0	20.5 (17.5)
$(\nu_\mu + \overline{\nu}_\mu)/(\nu_e + \overline{\nu}_e)$	$E_\nu < 1\,\mathrm{GeV}$		2.0	-0.7 (-0.6)
	$1 < E_\nu < 10\,\mathrm{GeV}$		3.0	-1.3 (-1.3)
	$E_\nu > 10\,\mathrm{GeV}$		5.0[a]	7.0 (6.9)
$\nu_e/\overline{\nu}_e$	$E_\nu < 1\,\mathrm{GeV}$		5.0	3.1 (3.0)
	$1 < E_\nu < 10\,\mathrm{GeV}$		5.0	1.1 (1.1)
	$E_\nu > 10\,\mathrm{GeV}$		8.0[b]	-0.9 (-0.8)
$\nu_\mu/\overline{\nu}_\mu$	$E_\nu < 1\,\mathrm{GeV}$		2.0	-0.3 (-0.3)
	$1 < E_\nu < 10\,\mathrm{GeV}$		6.0	-0.2 (-0.1)
	$E_\nu > 10\,\mathrm{GeV}$		6.0[c]	1.2 (1.3)
Up/down	$< 400\,\mathrm{MeV}$	e-like	0.1	-0.05 (-0.05)
		μ-like	0.3	-0.1 (-0.2)
	$> 400\,\mathrm{MeV}$	e-like	0.8	-0.04 (-0.04)
		μ-like	0.5	-0.2 (-0.3)
	Multi-GeV	e-like	0.7	-0.3 (-0.4)
		μ-like	0.2	-0.1 (-0.1)
	Sub-GeV Multi-ring e-like		0.2	-0.1 (-0.1)
	Sub-GeV Multi-ring μ-like		0.2	-0.1 (-0.1)
	Multi-GeV Multi-ring e-like		0.3	-0.1 (-0.2)
	Multi-GeV Multi-ring μ-like		0.2	-0.1 (-0.1)
	PC		0.2	-0.1 (-0.1)
Horizontal/vertical	$< 400\,\mathrm{MeV}$	e-like	0.1	0.005 (0.005)
		μ-like	0.1	0.005 (0.005)
	$> 400\,\mathrm{MeV}$	e-like	1.4	0.07 (0.08)
		μ-like	1.9	0.1 (0.1)
	Multi-GeV	e-like	3.2	0.2 (0.2)
		μ-like	2.3	0.1 (0.1)
	Sub-GeV Multi-ring e-like		1.4	0.07 (0.08)
	Sub-GeV Multi-ring μ-like		1.3	0.07 (0.07)
	Multi-GeV Multi-ring e-like		2.8	0.1 (0.2)
	Multi-GeV Multi-ring μ-like		1.5	0.08 (0.08)
	PC		1.7	0.09 (0.09)

Table 8.1: Summary of systematic uncertainties in atmospheric neutrino flux. Values within(without) parentheses are without(with) relative phase η.

[a]Uncertainty linearly increases with $\log E_\nu$ from 5 % (10 GeV) to 30 %(1 TeV).
[b]Uncertainty linearly increases with $\log E_\nu$ from 8 %(100 GeV) to 20 %(1 TeV).
[c]Uncertainty linearly increases with $\log E_\nu$ from 6 %(50 GeV) to 40 %(1 TeV).

		uncertainty (%)	best-fit (%)
(A2) Systematic uncertainties in neutrino flux			
K/π ratio		5.0^a	-5.9 (-5.6)
L_ν (production height)		10.0	1.2 (1.6)
Sample-by-sample	FC Multi-GeV	5.0	-5.6 (-5.5)
	PC + upward stopping μ	5.0	-10.1 (-9.7)
Solar activity	SK-I	20.0	4.0 (4.0)
	SK-II	50.0	30.3 (30.3)

Table 8.2: Summary of systematic uncertainties in atmospheric neutrino flux (continued). Values within(without) parentheses are without(with) relative phase η.

---

^{a}Uncertainty is 20 % above $E_\nu =$ 1 TeV. The uncertainty increases linearly from 5% to 20% between 100GeV and 1TeV.

	uncertainty (%)	best-fit (%)
(B) Systematic uncertainties in neutrino interaction		
Quasi-elastic scattering and single meson production (M_A)	1.0^a	0.9 (1.1)
Quasi-elastic scattering for bound nucleon (total cross section)	1.0^b	4.3 (4.1)
Quasi-elastic scattering for bound nucleon ($\overline{\nu}/\nu$ ratio)	1.0^c	10.1 (10.0)
Quasi-elastic scattering for bound nucleon (ν_μ/ν_e ratio)	1.0^d	4.3 (4.0)
Single meson production (total cross section)	20.0	-2.1 (-2.0)
Single meson production ($\overline{\nu}/\nu$ ratio)	1.0^e	-3.1 (-3.1)
Single meson production ($\pi^0/\pi^\pm$ ratio)	40.0	-37.1 (-37.9)
Deep inelastic scattering ($E_\nu < 10\text{GeV}$)	1.0^f	1.3 (1.6)
Deep inelastic scattering (total cross section)	5.0	1.3 (1.2)
Coherent pion production (total cross section)	$100.0(50.0)^g$	15.4 (18.6)
NC/CC ratio	20.0	-23.9 (-23.5)
Nuclear Effect in ^{16}O nucleus	30.0	-24.2 (-23.0)
Nuclear Effect in pion spectrum	1.0^h	10.7 (10.5)
CC ν_τ interaction cross section	30.0	-10.9 (-10.2)
Hadron simulation	10.0	-3.7 (-3.7)

Table 8.3: Summary of systematic uncertainties in neutrino interactions. Values within(without) parentheses are without(with) relative phase η.

---

[a]Difference from the $M_A = 1.1\text{GeV/c}$ is set to be 1.0

[b]Difference from the Nieves model is set to 1.0

[c]Difference from the Nieves model is set to 1.0

[d]Difference from the Nieves model is set to 1.0

[e]Difference from the Hernandez model is set to 1.0

[f]Difference from CKMT parametrization is set to 1.0

[g]100% for CC ν_μ. 50% for CC ν_e and NC.

[h]Difference between NEUT and NUANCE is set to 1.0

			uncertainty (%)	best-fit (%)
(C) Systematic uncertainties in event selection for SK-I				
Reduction for FC event			0.2	0.03 (0.03)
Reduction for PC event			2.4	-0.8 (-0.7)
FC/PC separation			0.6	-0.01 (-0.01)
Non-ν background	Flasher for e-like	Sub-GeV	0.5	0.06 (0.05)
		Multi-GeV	0.2	0.02 (0.02)
	Cosmic ray for μ-like	Sub-GeV	0.1	-0.01 (-0.02)
		Multi-GeV	0.1	-0.01 (-0.02)
	PC		0.2	-0.03 (-0.04)
PC stop/through separation	OD top region		15.0	11.4 (11.5)
	OD barrel region		7.4	-0.6 (-0.5)
	OD bottom region		11.3	-7.3 (-7.3)
Reduction for UPMU event	UPMU stopping		1.8	0.5 (-0.1)
	UPMU through		0.3	0.09 (-0.02)
UPMU stopping/through separation			0.4	-0.03 (-0.04)
UPMU stopping energy cut			0.8	-0.08 (-0.08)
UPMU through showering/non-showering separation			2.8	-2.0 (-2.0)

Table 8.4: Summary of systematic uncertainties in event selection for SK-I. Values within(without) parentheses are without(with) relative phase η.

			uncertainty (%)	best-fit (%)
(D) Systematic uncertainties in event selection for SK-II				
Reduction for FC event			0.2	0.006 (0.007)
Reduction for PC event			4.8	-2.6 (-2.5)
FC/PC separation			0.5	0.06 (0.06)
Non-ν background	Flasher for e-like	Sub-GeV	0.3	-0.03 (-0.03)
		Multi-GeV	0.7	-0.07 (-0.07)
	Cosmic ray for μ-like	Sub-GeV	0.1	0.02 (0.02)
		Multi-GeV	0.1	0.02 (0.02)
	PC		0.7	0.1 (0.1)
PC stop/through separation	OD top region		19.0	-18.0 (-18.0)
	OD barrel region		14.0	-22.4 (-22.0)
	OD bottom region		18.0	-19.5 (-19.4)
Reduction for UPMU event	stopping μ		2.1	0.6 (-0.1)
	through-going μ		0.3	0.09 (-0.02)
UPMU stopping/through separation			0.4	-0.02 (-0.03)
UPMU stopping energy cut			1.5	-0.04 (-0.04)
UPMU through showering/non-showering separation			1.8	-0.5 (-0.4)

Table 8.5: Summary of systematic uncertainties in event selection for SK-II. Values within(without) parentheses are without(with) relative phase η.

			uncertainty (%)	best-fit (%)
(E) Systematic uncertainties in event reconstruction for SK-I				
Single-ring/Multi-ring separation	*Single-ring*			
	$< 400\,\mathrm{MeV}$	e-like	2.3	1.3 (1.3)
		μ-like	0.7	0.4 (0.4)
	$> 400\,\mathrm{MeV}$	e-like	0.4	0.2 (0.2)
		μ-like	0.7	0.4 (0.4)
	Multi-GeV	e-like	3.7	2.1 (2.1)
		μ-like	1.7	1.0 (1.0)
	Multi-ring			
	Sub-GeV	e-like	3.5	-2.0 (-2.0)
		μ-like	4.5	-2.6 (-2.6)
	Multi-GeV	e-like	3.1	-1.8 (-1.8)
		μ-like	4.1	-2.4 (-2.4)
Particle identification	*Single-ring*			
	Sub-GeV	e-like	0.1	0.006 (0.006)
		μ-like	-0.1	-0.006 (-0.006)
	Multi-GeV	e-like	0.2	0.01 (0.01)
		μ-like	-0.2	-0.01 (-0.01)
	Multi-ring			
	Sub-GeV	e-like	2.3	0.1 (0.1)
		μ-like	-3.9	-0.2 (-0.2)
	Multi-GeV	e-like	1.7	0.1 (0.1)
		μ-like	-2.9	-0.2 (-0.2)
Energy calibration for FC event			1.1	0.07 (0.07)
Up/down symmetry of energy calibration			0.6	0.08 (0.08)
π^0-like sample selection	$100< P_e <250\,\mathrm{MeV/c}$		11.2	-3.4 (-3.4)
	$250< P_e <400\,\mathrm{MeV/c}$		11.5	-3.5 (-3.5)
	$400< P_e <630\,\mathrm{MeV/c}$		23.4	-7.1 (-7.1)
	$630< P_e <1000\,\mathrm{MeV/c}$		19.1	-5.8 (-5.8)
	$1000< P_e <1330\,\mathrm{MeV/c}$		13.0	-4.0 (-4.0)
FC Sub-GeV two-ring π^0-like sample selection			2.0	-0.5 (-0.5)
Decay electron tagging (π^+decay)	e-like 0μedecay		1.5~1.7	0.1 (0.1)
	e-like 1μedecay		-4.4~-3.8	-0.3 (-0.3)
	μ-like 0μedecay		1.6~1.8	0.1 (0.1)
	μ-like 1μedecay		-1.5	-0.1(-0.1)
	μ-like 2μedecay		-6.4~-5.9	-0.5~-0.4 (-0.5~-0.4)
Decay electron tagging ($\mu \to e$ decay)			1.1	0.7 (0.7)

Table 8.6: Summary of systematic uncertainties in event reconstruction for SK-I.

			uncertainty (%)	best-fit (%)
(F) Systematic uncertainties in event reconstruction for SK-II				
Single-ring/Multi-ring separation	*Single-ring*			
	$< 400\,\mathrm{MeV}$	e-like	1.3	1.2 (1.2)
		μ-like	2.3	2.1 (2.1)
	$> 400\,\mathrm{MeV}$	e-like	1.7	1.6 (1.6)
		μ-like	0.7	2.4 (2.4)
	Multi-GeV	e-like	2.6	2.4 (2.4)
		μ-like	1.7	1.6 (1.6)
	Multi-ring			
	Sub-GeV	e-like	3.8	-3.5 (-3.5)
		μ-like	8.2	-7.6 (-7.6)
	Multi-GeV	e-like	1.9	-1.9 (-1.9)
		μ-like	0.8	-0.7 (-0.7)
Particle identification	*Single-ring*			
	Sub-GeV	e-like	0.5	0.08 (0.08)
		μ-like	-0.4	-0.07 (-0.07)
	Multi-GeV	e-like	0.1	0.02 (0.02)
		μ-like	-0.1	-0.02 (-0.02)
	Multi-ring			
	Sub-GeV	e-like	1.2	0.2 (0.2)
		μ-like	-2.2	-0.4 (-0.4)
	Multi-GeV	e-like	1.8	0.3 (0.3)
		μ-like	-3.4	-0.6 (-0.6)
Energy calibration for FC event			1.7	-1.7 (-1.7)
Up/down symmetry of energy calibration			0.6	-0.2 (-0.2)
π^0-like sample selection	$100< P_e <250\,\mathrm{MeV/c}$		7.5	-4.0 (-4.0)
	$250< P_e <400\,\mathrm{MeV/c}$		8.9	-4.8 (-4.8)
	$400< P_e <630\,\mathrm{MeV/c}$		17.5	-9.4 (-9.4)
	$630< P_e <1000\,\mathrm{MeV/c}$		10.7	-5.8 (-5.8)
	$1000< P_e <1330\,\mathrm{MeV/c}$		11.1	-6.0 (-6.0)
FC Sub-GeV two-ring π^0-like sample selection			2.0	-0.5 (-0.5)
Decay electron tagging (π^+decay)	e-like 0μedecay		1.2~1.7	-0.1 (-0.1)
	e-like 1μedecay		-4.2~-3.8	0.3 (0.3)
	μ-like 0μedecay		1.6~1.8	-0.1 (-0.1)
	μ-like 1μedecay		-1.5	0.1 (0.1)
	μ-like 2μedecay		-6.5~-5.9	0.4~0.5 (0.4~0.5)
Decay electron tagging ($\mu \to e$ decay)			1.1	-0.7 (-0.7)

Table 8.7: Summary of systematic uncertainties in event reconstruction for SK-II.

Chapter 9

Analysis with 3-Flavor Hybrid Model

Various direct limits on NSI with matter are available thanks to the neutrino scattering experiments. Among these experiments NuTeV gives a stringent limit on non-standard ν_μ interactions, while the constrains to non-standard ν_e or ν_τ interactions are still poor.

In order to obtain the limits on NSI in the $\nu_e - \nu_\tau$ sector, we extend the framework of 2-flavor hybrid model to the *3-flavor hybrid model* in which NSI in the $\nu_e - \nu_\tau$ sector coexist with 2-flavor $\nu_\mu \leftrightarrow \nu_\tau$ standard oscillation. The 3-flavor hybrid model allows the flavor transition for all flavored neutrinos through the NSI coupling between ν_e and ν_τ. Propagation of flavored neutrinos from their source to the detector is expressed in Figure 9.1.

The formalism we employ for this model is introduced in Chapter 9.1. Expected phenomena and analysis method are mentioned in Chapters 9.2 and 9.3, respectively. Results of this test are presented in Chapter 9.4. In the analysis, we consider the three-dimensional parameter space constructed by the NSI couplings, ε_{ee}, $\varepsilon_{e\tau}$, and $\varepsilon_{\tau\tau}$. Likewise, the effects of the other subdominant contributions to the size of such NSI paramters are studied assuming several possible scenarios, which include the nonzero θ_{13}, Δm_{12}^2 and θ_{12} (solar term), and so on.

9.1 Formalism

An evolution matrix can be obtained by diagonalizing the hamiltonian eq.(8.1) in terms of the leptonic mixing matrix in the matter U', and the effective eigenvalues $\hat{H} = \text{diag}(E_1, E_2, E_3)$. In the case of constant matter density, the evolution matrix is represented as

$$S_{\beta\alpha}(t, t_0) = \sum_{i=1}^{3} (U'_{\alpha i})^* U'_{\beta i} e^{-iE_i L}, \quad \alpha, \beta = e, \mu, \tau \tag{9.1}$$

where L is defined as $L \equiv t - t_0$. Therefore the neutrino oscillation probability under the effect of NSI can be expressed as

$$P_{\alpha\beta} = |S_{\beta\alpha}(t, t_0)|^2 \tag{9.2}$$

However more realistically, as seen in Figure 8.2, the matter density in the Earth ranges from about 2.5 to 13. So as to solve it, we divide the neutrino propagation length by several steps and derive the relevant evolution matrix. The oscillation probability can be calculated by the

125
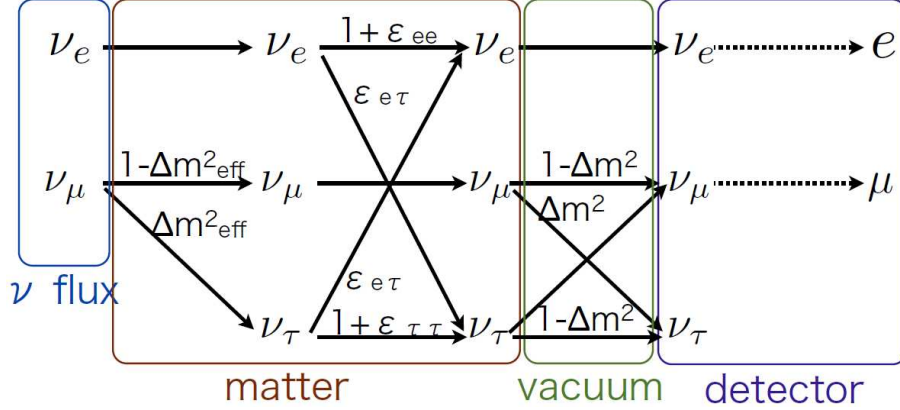
Figure 9.1: Propagation of the 3-flavor hybrid model in which 2-flavor $\nu_\mu \leftrightarrow \nu_\tau$ standard neutrino oscillations coexist with NSI in the $\nu_e - \nu_\tau$ sector.

product of each evolution matrix and its eigenvalues. Note that our interests lie in the $\nu_e - \nu_\tau$ sector, so the NSI parameters other than ε_{ee}, $\varepsilon_{e\tau}$, and $\varepsilon_{\tau\tau}$ are set to 0 in the calculation.

9.2 Expected Phenomena

In this chapter we describe expected phenomena driven by NSI. Similar to the case of the 2-flavor hybrid model, the relative effects of NSI in the hybrid model are expected to vary according to the neutrino energy. Survival and oscillation probabilities are demonstrated in Figure 9.2. Resonant peaks can be seen by the variation of the matter density as a function of the depth.

We discuss how NSI affects the atmospheric neutrino distributions in three energy ranges: (1) E_ν <1GeV, (2) 1< E_ν <15GeV, and (3) E_ν >15GeV.

(1) E_ν <1GeV

Because of the condition $\Delta m^2/4E_\nu \gg \sqrt{2}G_F N_f$, $\nu_\mu \rightarrow \nu_\tau$ transition is mainly caused by 2-flavor standard oscillation thus we can disregard NSI effects.

(2) 1< E_ν <15GeV

In this energy range, as we see in the 2-flavor hybrid model, the matter term has a sizable effect to modify the $\nu_\mu \rightarrow \nu_\tau$ transition. Moreover the existing poor limits on NSI in the $\nu_e \rightarrow \nu_\tau$ sector allow the large modification compared to the 2-flavor hybrid model.

Fisrt we mention the NSI modification to the $\nu_\mu \rightarrow \nu_e$ transition. This transition is unaffected in the 2-flavor hybrid model, i.e. exactly 0, due to the lack of coupling between ν_e and ν_μ, however in the 3-flavor hybrid model, $\nu_\mu \rightarrow \nu_e$ transition is allowed by a standard $\nu_\mu \rightarrow \nu_\tau$ transition together with a non-standard $\nu_\tau \rightarrow \nu_e$ transition due to $\varepsilon_{e\tau}$:

$$\nu_\mu \xrightarrow{\theta_{23}} \nu_\tau \xrightarrow{\varepsilon_{e\tau}} \nu_e \tag{9.3}$$

The top right panel of Figure 9.2 shows the oscillation probability with NSI, which is exactly 0 unless NSI is considered. The survival probability of $\nu_e \rightarrow \nu_e$ is presented in the top left panel

126
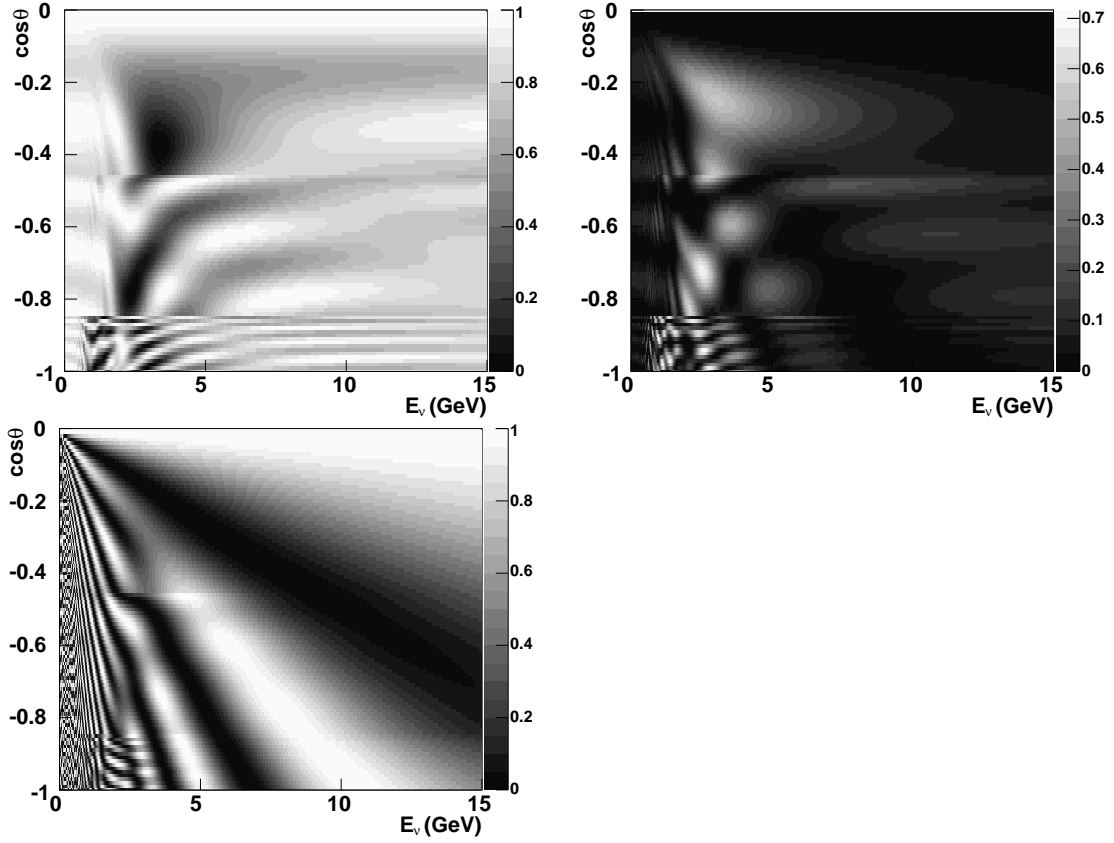
Figure 9.2: Survival and oscillation probabilities for the 3-flavor hybrid model. (Top left) Survival probability of $\nu_e \to \nu_e$. (Top right) Oscillation probability of $\nu_\mu \to \nu_e$. (Bottom) Survival probability of $\nu_\mu \to \nu_\mu$. In all panels, ε_{ee}=0.5, $\varepsilon_{e\tau}$=0.25 and $\varepsilon_{\tau\tau}$=0.05 are assumed, also standard oscillation parameters are fixed as the best-fit parameters given by 2-flavor NSI analysis. For simplicity, the propagation length of the neutrino is defined as $L \equiv -2R_{Earth}\cos\theta \sim -13000\cos\theta$ (km).
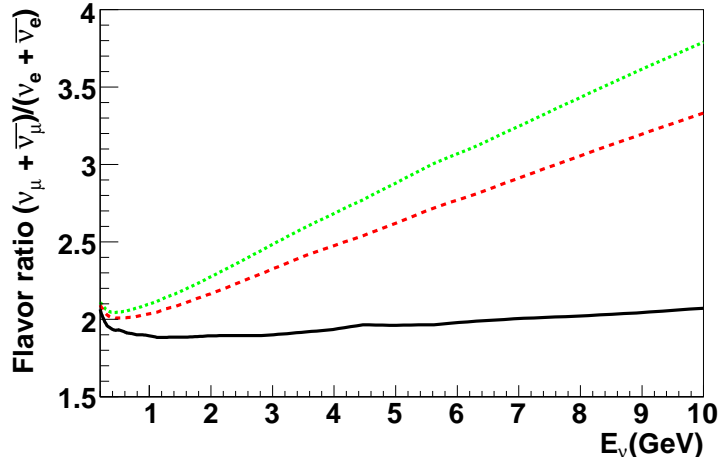
Figure 9.3: Flavor ratio $(\nu_\mu + \overline{\nu}_\mu)/(\nu_e + \overline{\nu}_e)$ as a function of neutrino energy, where calculation is based on the Honda flux. Solid curve indicates the ratio at the horizon ($\cos\theta = 0.$). Dashed and dotted curves indicate the ratio at $\cos\theta = -0.5$ and $\cos\theta = -1.0$, respectively.

of Figure 9.2. These two probabilites in association with neutrino flux yield the expected e-like distributions, namely, if we normalize by the ν_e flux (Φ_e) and also disregard the ν_μ contaminations, e-like distributions can be expressed as $P(\nu_e \to \nu_e) + (\Phi_\mu/\Phi_e)P(\nu_\mu \to \nu_e)$, where Φ_μ/Φ_e is the so called *Flavor ratio* shown in Figure 3.7. We notice that the flavor ratio grows with increasing neutrino enegy, and also this ratio is highly zenith angle dependent, which is shown in Figure 9.3. Focusing the near horizontal direction, the flavor ratio is approximately 2. Then if $P(\nu_e \to \nu_e) + 2P(\nu_\mu \to \nu_e) \lesssim 1$, number of ν_e events decrease. This case is realized when $\varepsilon_{e\tau}$ and $\varepsilon_{\tau\tau}$ have a large and also comparable values each other. As seen in the chain of eq.(9.3), $\nu_\mu \to \nu_e$ transition is decreased since $\nu_\mu \to \nu_\tau$ transition is suppressed by large $\varepsilon_{\tau\tau}$. Also, at the same time, $\nu_e \to \nu_\mu$ or ν_τ is caused by $\varepsilon_{e\tau}$. In contrast, focusing on upward direction, ν_e events increase effectively due to the condition $(\Phi_\mu/\Phi_e)P(\nu_\mu \to \nu_e) \gtrsim 1 - P(\nu_e \to \nu_e)$. This condition corresponds to large $\varepsilon_{e\tau}$ and ε_{ee}, because $\nu_\tau \to \nu_e$ transition is given by $\varepsilon_{e\tau}$, while $\nu_e \to \nu_\mu$ or ν_τ is suppressed due to ε_{ee}.

Therefore we expect that nonzero $\nu_e \to \nu_e$ probability leads the deficit of e-like events near the horizon, while $(\Phi_\mu/\Phi_e)P(\nu_\mu \to \nu_e)$ gives a sizable excess in upward e-like events. Indeed, zenith angle distributions of higher energy ν_e-rich samples in Figure 9.4 indicate our expectations, where $\varepsilon_{e\tau}$=0.4 is assumed to show these two phenomena simultaneously.

As for $\nu_\mu \to \nu_\tau$ transition, we mention the case with nonzero $\varepsilon_{\tau\tau}$, while other two parameters ε_{ee} and $\varepsilon_{e\tau}$ are assumed to be almost 0. This case can be reduced to the 2-flavor hybrid model with nonzero ε' and negligible ε, hence the comparable constraint with ε' is expected to be obtained for $\varepsilon_{\tau\tau}$. This case can be also realized when $\varepsilon_{ee} \gg \varepsilon_{e\tau}$, where $\nu_e \to \nu_\tau$ transition is highly suppressed, therefore phenomena in the $\nu_\mu - \nu_\tau$ sector become close to that of the 2-flavor hybrid model.

(3) $E_\nu >$15GeV

Above a few tens of GeV, the ν_e flux decreases so it allows us to neglect the $\nu_e \to \nu_\mu$ or ν_τ transition, corresponding to an e-like deficit, while an e-like excess due to the non-standard
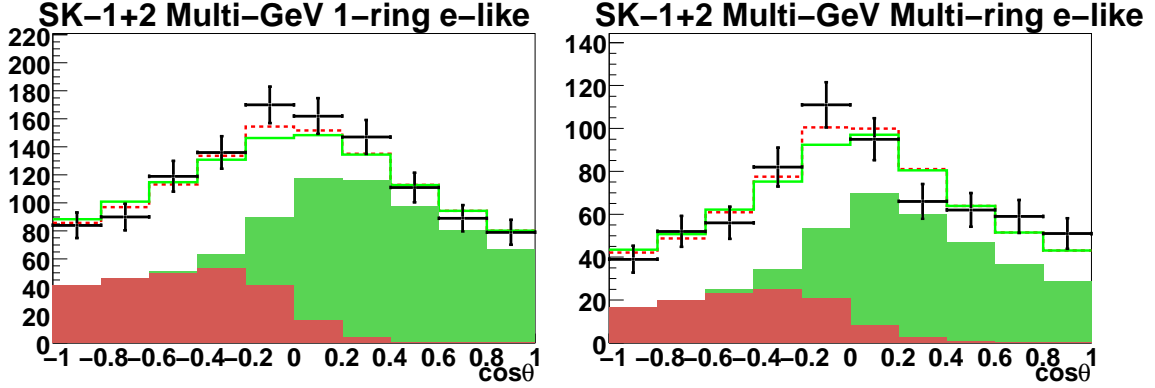
Figure 9.4: (Left) Zenith angle distribution of FC Single-ring Multi-GeV *e*-like sample. (Right) Zenith angle distribution of FC Multi-ring Multi-GeV *e*-like sample. In both panels, solid line indicates the 3-flavor hybrid model, dashed line 2-flavor standard oscillation, green hatched area unoscillated ν_e events, and red hatched area appearance of oscillated ν_μ events. Note that no systematic uncertainty is considered in the figure.

$\nu_\tau \to \nu_e$ transition can be clearly recognized thanks to the small ν_e flux. As for the $\nu_\mu - \nu_\tau$ sector, if we replace ε' with $\varepsilon_{\tau\tau}$, the case (3) of the 2-flavor hybrid model is applicable to this range.

Finally, we mention why atmospheric neutrinos are less sensitive for placing a limit on ε_{ee}. The reason is as follows: once $\varepsilon_{e\tau}$ and $\varepsilon_{\tau\tau}$ are constrained to quite a small value, the sizable element in the matter term is only in the (e, e) sector, i.e. ε_{ee}. It turns out that the matter term is disconnected from the standard oscillation and this condition allows ε_{ee} to have any value.

Let us summarize the above discussions: $\varepsilon_{e\tau}$ can be constrained by higher energy ν_e-rich samples near the horizon and in the upward direction, while $\varepsilon_{\tau\tau}$ can be constrained by the deficit in ν_μ-rich samples.

9.3   Analysis Method

Analysis procedure for the 3-flavor hybrid model is essentially common to that used for the 2-flavor hybrid model, however we neglect a complex relative phase for flavor changing couplings because other sub-dominant effects, for example nonzero θ_{13}, may have a larger effect on the size of allowed NSI.

A value of χ^2 is evaluated at each grid point in the three-dimensional parameter space of ε_{ee}, $\varepsilon_{e\tau}$, and $\varepsilon_{\tau\tau}$. As we mentioned in Chapter 9.2, atmospheric neutrinos are less sensitive to constrain ε_{ee}, then we set the bound to the ε_{ee} parameter space with the existing experimental limit given by the CHARM experiment, $-0.5 < \varepsilon_{ee} < 0.5$. Also $\varepsilon_{e\tau}$ is symmetrical between negative and positive value when neither θ_{13} nor solar term (Δm_{12}^2 and θ_{12}) are considered, therefore the evaluation is performed in the positive side of $\varepsilon_{e\tau}$.

2-flavor standard oscillation parameters are fixed as $(\sin^2\theta_{23}, \Delta m^2) = (0.5, 2.1 \times 10^{-3} \text{eV}^2)$, i.e. best-fit parameters given by the 2-flavor standard oscillation analysis in Appendix B. This condition is motivated by the result of the analysis with the 2-flavor hybrid model, in which

allowed oscillation parameters region is similar to that of 2-flavor standard oscillation analysis. Standard oscillation parameters in this hybrid model are assumed to take the fixed values. We later verify this assumption by comparing the allowed NSI parameter region derived by several different oscillation parameters.

9.4 Result of 3-Flavor Non standard interaction analysis

Our main results, allowed 3-flavor NSI paramters, are presented in Figure 9.5. In all panels, undisplayed NSI parameter is integrated out, for example in top left panel $\varepsilon_{\tau\tau}$ is integrated out. Three contours correspond to the 68%, 90% and 99% confidence level (C.L.) allowed regions which are defined to be $\chi^2 = \chi^2_{min}$ +2.30, 4.61, and 9.21, respectively. According to the bottom panel of Figure 9.5, limit on NSI parameters in the $\nu_e - \nu_\tau$ sector at a 90 % C.L. is :

$$|\varepsilon_{e\tau}| < 0.16, \quad -0.05 < \varepsilon_{\tau\tau} < 0.06 \tag{9.4}$$

Best-fit values are

$$\varepsilon_{ee} = -0.25, \quad \varepsilon_{e\tau} = 0.016, \quad \varepsilon_{\tau\tau} = 0.024 \tag{9.5}$$

$$\chi^2_{min} = 829.9 \ / \ 747 \text{ d.o.f.} \tag{9.6}$$

We only consider positive $\varepsilon_{e\tau}$ in this result, since $\varepsilon_{e\tau}$ is symmetrical between negative and positive value, which is explained in *Discussion* again.

Systematic uncertainties are summarized in Tables from 9.2 to 9.8.

Allowed NSI paramters regions with four sets of standard oscillation parameters are presented in Figure 9.6. Choise of the oscillation parameters is based on the standard 2-flavor oscillation analysis. Two points are chosen along the Δm^2 direction within 90% C.L. with fixed value $\sin^2\theta_{23}$=0.5, namely Δm^2=1.7×10^{-3}eV^2 and 2.7×10^{-3}eV^2. The other two points are chosen along the $\sin^2\theta_{23}$ direction within 90% C.L. with fixed value Δm^2=2.1×10^{-3}eV^2, $\sin^2\theta_{23}$=0.39 and $\sin^2\theta_{23}$=0.61. We compare the allowed NSI regions at totally four points.

Allowed parameters regions are summarized in Table 9.1. Sizable changes of allowed NSI parameters region are not found except for $(\sin^2\theta_{23}, \Delta m^2)$=(0.5, 2.7×10^{-3}eV^2) indicated by dahsed curve in Figure 9.6. Considering the difference of minimum χ^2 values between $(\sin^2\theta_{23}, \Delta m^2)$=(0.5, 2.1×10^{-3}eV^2) and (0.5, 2.7×10^{-3}eV^2), the latter allowed region shown by dashed curve could be changed smaller. Therefore the assumption of the fixing standard oscillation parameters is not significant in this analysis.

9.5 Discussion

We start the discussion with Figure 9.7, in which allowed NSI regions for five fixed ε_{ee} = -0.5, -0.25, 0., 0.25, and 0.5, are presented. In this figure, parabola-like distributions of allowed region as a function of $\varepsilon_{e\tau}$ are found except for $\varepsilon_{ee} = -0.25$. Especially the allowed region extends to negative $\varepsilon_{\tau\tau}$ values when $\varepsilon_{ee} = -0.5$, while they extend to the positive ones above $\varepsilon_{ee} = 0$. The parabola distributions can be explained as follows: For convenience, we introduce the eigenvalues of matter term, which are derived by diagonalizing the matter term. If we recall eq.(8.1) and $N_f \equiv N_d \sim 3N_e$, matter term including V_{MSW} can be expressed as
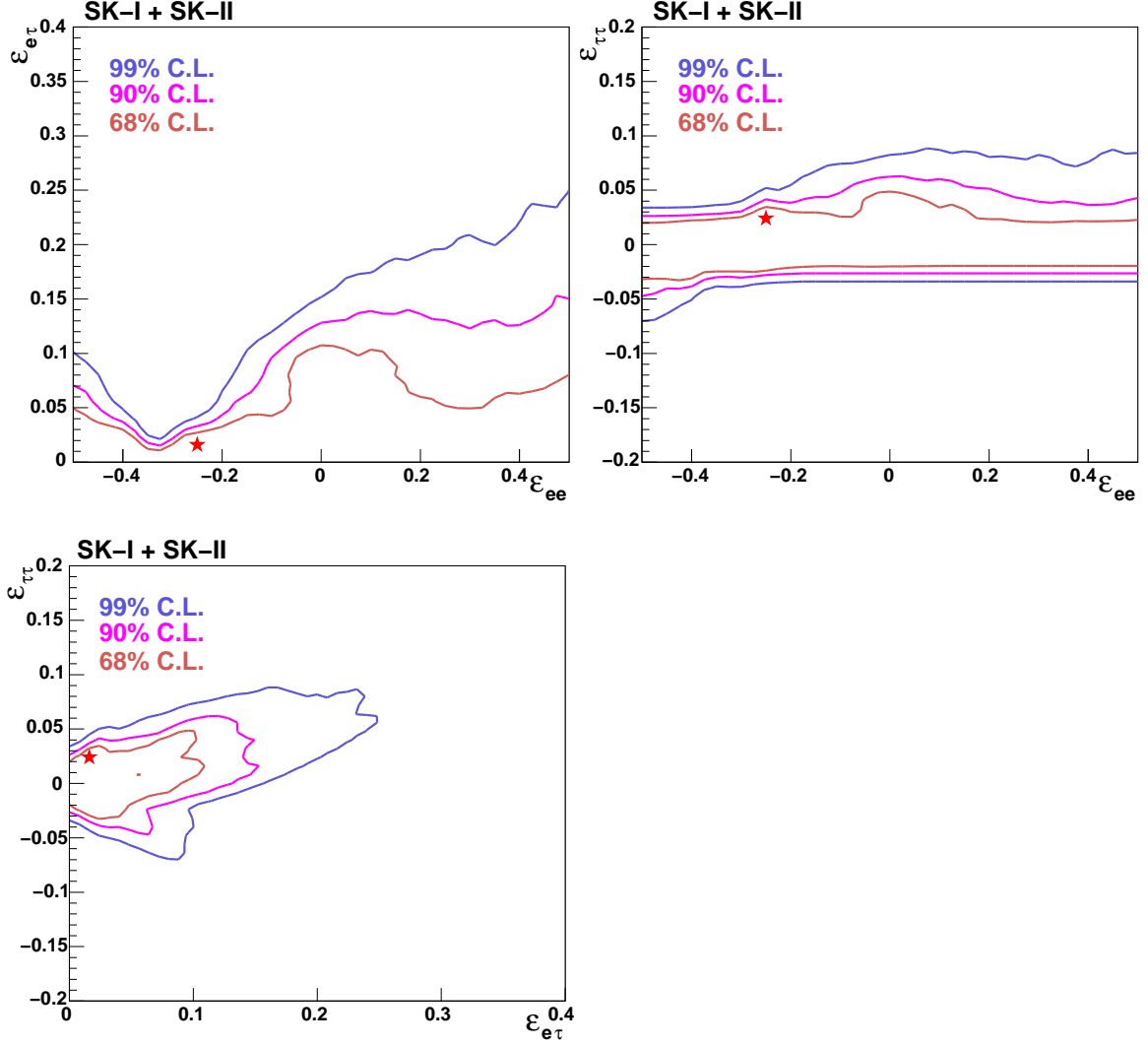
Figure 9.5: Allowed NSI parameters region. (Top left) ε_{ee} vs. $\varepsilon_{e\tau}$ space. (Top right) ε_{ee} vs. $\varepsilon_{\tau\tau}$ space. (Bottom) $\varepsilon_{e\tau}$ vs. $\varepsilon_{\tau\tau}$ space.

$\sin^2\theta_{23}$	$\Delta m^2(\text{eV}^2)$	Allowed $\varepsilon_{e\tau}$	Allowed $\varepsilon_{\tau\tau}$	Minimum χ^2 (747 d.o.f.)
0.50	2.1×10^{-3}	$|\varepsilon_{e\tau}| < 0.16$	$-0.05 < \varepsilon_{\tau\tau} < 0.06$	829.9
0.50	1.7×10^{-3}	$|\varepsilon_{e\tau}| < 0.15$	$-0.04 < \varepsilon_{\tau\tau} < 0.04$	836.1
0.50	2.7×10^{-3}	$|\varepsilon_{e\tau}| < 0.17$	$-0.06 < \varepsilon_{\tau\tau} < 0.09$	831.4
0.39	2.1×10^{-3}	$|\varepsilon_{e\tau}| < 0.14$	$-0.07 < \varepsilon_{\tau\tau} < 0.05$	834.0
0.61	2.1×10^{-3}	$|\varepsilon_{e\tau}| < 0.14$	$-0.03 < \varepsilon_{\tau\tau} < 0.06$	834.4

Table 9.1: Summary of NSI allowed parameters at the 90% C.L.. Our main result is in the first line.

131
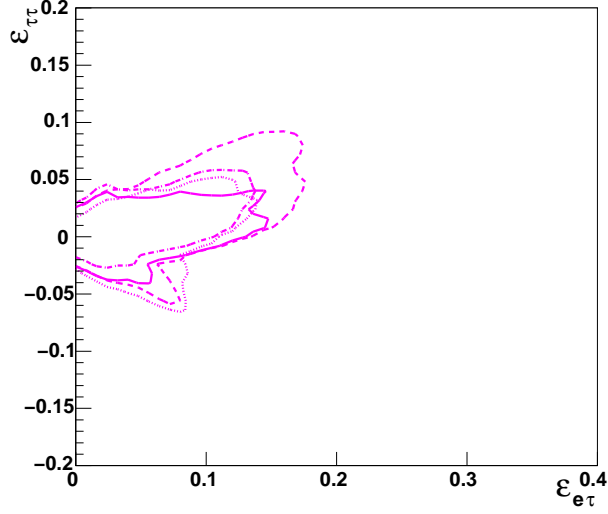
Figure 9.6: Allowed region in $\varepsilon_{e\tau}$ vs. $\varepsilon_{\tau\tau}$ space at the 90% C.L.. Solid curve is for the result with $(\sin^2\theta_{23}, \Delta m^2)=(0.5, 1.7\times10^{-3}\mathrm{eV}^2)$, dashed curve for $(0.5, 2.7\times10^{-3}\mathrm{eV}^2)$, dotted curve for $(0.39, 2.1\times10^{-3}\mathrm{eV}^2)$, and dashed-dotted curve for $(0.61, 2.1\times10^{-3}\mathrm{eV}^2)$.

(a) $\varepsilon_{ee} = -0.5$

(b) $\varepsilon_{ee} = -0.25$

(c) $\varepsilon_{ee} = 0.0$

(d) $\varepsilon_{ee} = 0.25$

(e) $\varepsilon_{ee} = 0.5$
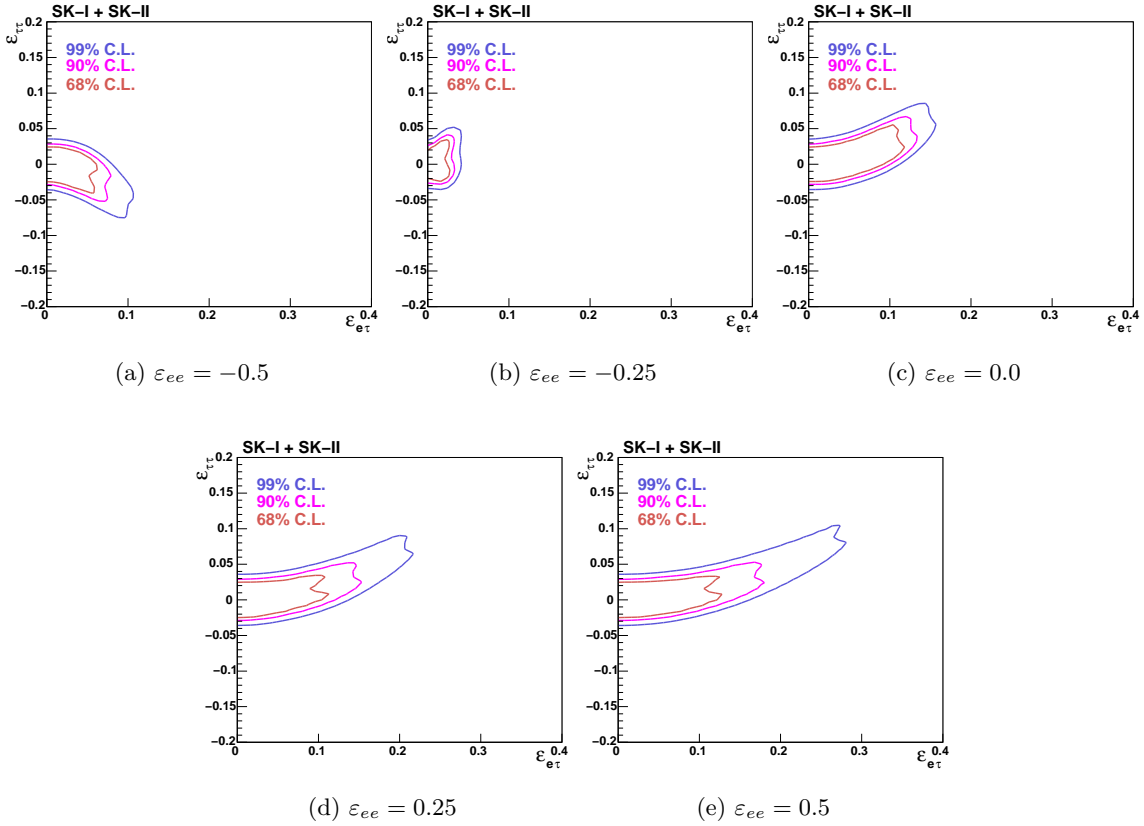
Figure 9.7: Allowed NSI parameters region for fixed ε_{ee}. $\Delta\chi^2$ is defined as the deviation from the minimum χ^2 value for each fixed ε_{ee}.

$$H_{matter} = \sqrt{2}G_F N_e \begin{pmatrix} 1 + 3\varepsilon_{ee} & 0 & 3\varepsilon_{e\tau} \\ 0 & 0 & 0 \\ 3\varepsilon_{e\tau} & 0 & 3\varepsilon_{\tau\tau} \end{pmatrix} \tag{9.7}$$

where we disregard complex relative phase for $\varepsilon_{e\tau}$.

We know that a matrix A defined as

$$A = \begin{pmatrix} \alpha & \beta \\ \beta & \gamma \end{pmatrix} \tag{9.8}$$

can be easily diagonalized in terms of eigenvectors P and rotation angle ω

$$P = \begin{pmatrix} \cos\omega & \sin\omega \\ -\sin\omega & \cos\omega \end{pmatrix}, \quad \tan 2\omega = \frac{2\beta}{\gamma - \alpha} \tag{9.9}$$

as

$$P^\dagger A P = \begin{pmatrix} \lambda_1 & 0 \\ 0 & \lambda_2 \end{pmatrix}, \quad \text{where} \quad \lambda_1 = \frac{\alpha \cos^2\omega - \gamma \sin^2\omega}{\cos^2\omega - \sin^2\omega}, \quad \lambda_2 = \frac{\gamma \cos^2\omega - \alpha \sin^2\omega}{\cos^2\omega - \sin^2\omega}. \tag{9.10}$$

Thus the diagonalization of the H_{matter} gives the eigenvalues $E'_{\nu_e,\nu_\mu,\nu_\tau}$ and rotation angle, i.e. mixing angle in matter, θ' as:

$$E'_{\nu_e} = \frac{3\sqrt{2}G_F N_e}{2}\left[\frac{1}{3} + \varepsilon_{ee} + \varepsilon_{\tau\tau} + \sqrt{\left(\frac{1}{3} + \varepsilon_{ee} - \varepsilon_{\tau\tau}\right)^2 + 4\varepsilon_{e\tau}^2}\right] \tag{9.11}$$

$$E'_{\nu_\mu} = 0 \tag{9.12}$$

$$E'_{\nu_\tau} = \frac{3\sqrt{2}G_F N_e}{2}\left[\frac{1}{3} + \varepsilon_{ee} + \varepsilon_{\tau\tau} - \sqrt{\left(\frac{1}{3} + \varepsilon_{ee} - \varepsilon_{\tau\tau}\right)^2 + 4\varepsilon_{e\tau}^2}\right] \tag{9.13}$$

$$\tan 2\theta' = \frac{2|\varepsilon_{e\tau}|}{1/3 + \varepsilon_{ee} - \varepsilon_{\tau\tau}} \tag{9.14}$$

Note that $\varepsilon_{e\tau}$ is included as $|\varepsilon_{e\tau}|$ in $\tan 2\theta'$. Therefore, the oscillation probability is symmetrical between negative and positive $\varepsilon_{e\tau}$.

We first consider the case in which both E'_{ν_e} and E'_{ν_τ} are larger than the eigenvalue of vacuum term, i.e. $E'_{\nu_e}, E'_{\nu_\tau} > \Delta m^2/4E_\nu$, which corresponds to $1/3 + \varepsilon_{ee}, \varepsilon_{\tau\tau} \gg \varepsilon_{e\tau}$. In this case, $\nu_\mu \to \nu_e$ transition is quite small due to $E'_{\nu_e} > \Delta m^2/4E_\nu$. However, at the same time, $\nu_\mu \to \nu_\tau$ transition is also suppressed by large $\varepsilon_{\tau\tau}$. This is clearly inconsistent with the observation, therefore this scenario is strongly excluded.

In addition to that case, we have another case where NSI parameters are allowed to have a sizable value and also significant discrepancy between NSI and standard oscillation is not found. This scenario is realised when $E'_{\nu_e} > \Delta m^2/4E_\nu > E'_{\nu_\tau}$. In this case, thanks to $E'_{\nu_e} > \Delta m^2/4E_\nu$, transition from ν_e to ν_μ or ν_τ is suppressed, thus it is approximately possible to regard the 3-flavor hybrid model as the 2-flavor hybrid model. If we assume $E'_{\nu_\tau} = 0$ for simplicity, we obtain the following relation:

$$\varepsilon_{\tau\tau} = \frac{3\varepsilon_{e\tau}^2}{1 + 3\varepsilon_{ee}} \tag{9.15}$$

133
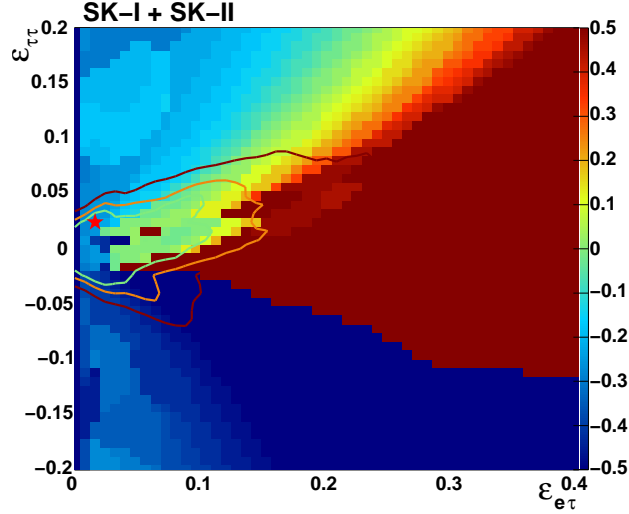
Figure 9.8: Allowed NSI parameters region, ε_{ee} and $\varepsilon_{e\tau}$ at the 68%, 90% and 99% C.L. from inside. Colored boxes in each grid indicate the value of ε_{ee}.

Suppose ε_{ee} is fixed, this relation yields the parabolic χ^2 distribution as seen in Figure 9.7. In other words, atmospheric neutrinos are rather insensitive to constrain NSI parameters as long as one keeps the reration in eq.(9.15), because the frequency of the transition from ν_μ to the other flavored neutrinos is unaffected. In fact, NSI parameters on the parabola distribution in Figure 9.7 mostly satisfy eq.(9.15).

Besides the origin of parabolic χ^2 distribution, the relation (9.15) yields the correlation of the sign of allowed NSI parameters between ε_{ee} and $\varepsilon_{\tau\tau}$. Namely if $1 + 3\varepsilon_{ee}$ is negative, $\varepsilon_{\tau\tau}$ should also be negative, since $3\varepsilon_{e\tau}^2$ is always positive. The correlation is recognized in right panel of Figure 9.5, where allowed region ranges to negative $\varepsilon_{\tau\tau}$ when ε_{ee} is below about -0.3, while the area changes from negative to positive $\varepsilon_{\tau\tau}$ as ε_{ee} increases. This can be more clearly seen in Figure 9.8, in which negative $\varepsilon_{\tau\tau}$ is constrained by negative ε_{ee}, and this is also true for positive ε_{ee} and $\varepsilon_{\tau\tau}$.

If $E'_{\nu_e} > \Delta m^2 / 4E_\nu > E'_{\nu_\tau}$ is satisfied, the frequency of ν_μ disapearance induced by the hybrid model, i.e. $\nu_\mu \to \nu_e$ or ν_τ transition, is same as that of 2-flavor $\nu_\mu \to \nu_\tau$ standard oscillation. Nevertheless, effective mixing angle in matter is still under the effect of NSI through the NSI mixing angle θ'. θ' leads $\nu_\mu \to \nu_e$ transition and suppresses $\nu_\mu \to \nu_\tau$ transition. Therefore the inconsistency of higher energy e-like samples between NSI and observation contributes to constrain θ'. Phenomena due to the nonzero θ' corresponds to the deficit of e-like events in near the horizon and excess in the upward direction given by $\varepsilon_{e\tau}$, as we discussed in chapter 9.2. Our expectation that θ' can be constrained by the disapearance and appearance of ν_e events is certainly consistent $\theta' \sim 0$, which is equivalent to $\tan 2\theta' \sim 0$, in other words, $\varepsilon_{e\tau} \sim 0$.

To see more detail, we present the allowed NSI parameters regions derived by sets of sub-samples in Figure 9.9, where FC Sub-GeV samples are not displayed because of their small sensitivity. Higher energy ν_μ-rich samples indicated by solid curve (UPMU through) and dashed curve (PC and UPMU stopping) show parabolic χ^2 distributioins, which can be understood as follows: Once the relation eq.(9.15) is satisfied, the frequency of $\nu_\mu \to \nu_e$ or ν_τ is similar to that of $\nu_\mu \to \nu_\tau$ in vacuum term. Futhermore, UPMU and PC samples can not distinguish whether
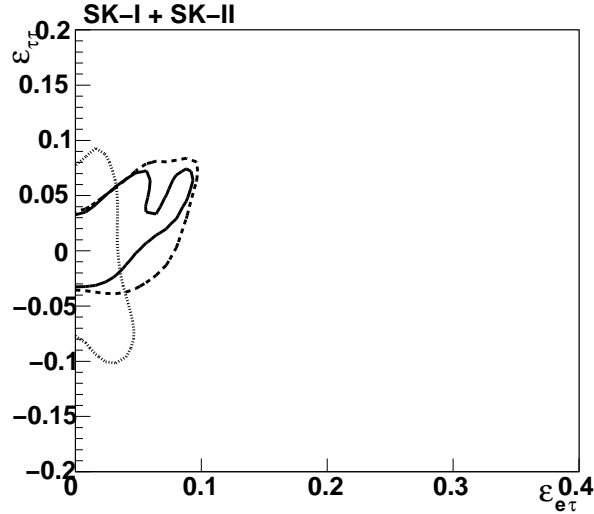
Figure 9.9: Allowed NSI parameters derived by a set of sub-samples with $\varepsilon_{ee} = -0.25$. Solid curve indicates the allowed region given by UPMU through going, dashed curve by PC and UPMU stopping, and dotted curve by FC Single-ring Multi-GeV and Multi-ring. Contour corresponds to $\chi^2 = \chi^2_{min} + 3.53$ (68% C.L.).

$\theta' \sim 0$ or not because of no sensitivity to the e-like distributions. Figure 9.10 shows the allowed NSI parameter region derived by UPMU through events (solid curve) and the UP/Horizon ratio (colored boxes) introduced in chapter 8.5. Indeed, the UP/Horizon ratios outside of the parabola area disagree with that of standard oscillation which is equivalent to $\varepsilon_{e\tau} \sim \varepsilon_{\tau\tau} \sim 0$.

In contrast, allowed region derived by FC Single-ring Multi-GeV and Multi-ring (dotted curve) seems to constrain $\varepsilon_{e\tau}$ rather than other sub-samples. It means that higher energy ν_e-rich samples constrain $\varepsilon_{e\tau}$.

9.6 Results with the uncertainty of matter density and sub-dominant effects

There are several scenarios including sub-dominant effects possibly affecting the size of allowed NSI parameters. One is the systematic uncertainty of the matter density in the Earth, others are the sub-dominant oscillation parameters. In this section, we investigate how our limits can be modified when these parameters are taken into account.

9.6.1 Effect of the uncertainty of matter density profile

First, we consider the systematic uncertainty of the matter density in the Earth. It is known that the variation of matter density along the neutrino propagation changes the oscillation probabilities and it results in the systematic uncertainty of the limit on NSI. In order to estimate the relaxations of the constraints, we derive limits on NSI assuming three cases: (1) matter density is decreased by 10%, (2) original PREM prediction, i.e. results presented in the previous chapters, and (3) matter density is increased by 10%. Systematic uncertainty of matter density, $\pm 10\%$, is motivated by the studies in geophysics [148, 149].

135
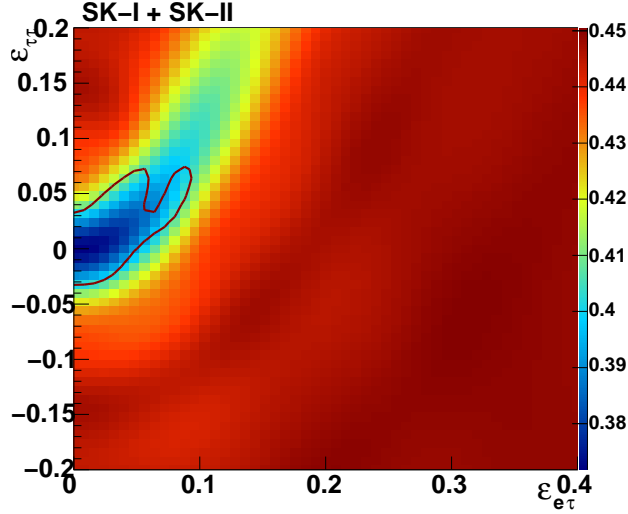
Figure 9.10: Allowed NSI parameters with $\varepsilon_{ee} = -0.25$. Solid curve indicates the allowed region given by UPMU through going, where contour corresponds to $\chi^2 = \chi^2_{min} + 3.53$, i.e. the 68% C.L.. Colored boxes show UP/Horizontal ratio defined as the ratio of upward 3 bins ($\cos\Theta = -1 \sim -0.7$) to horizontal 3 bins ($\cos\Theta = -0.3 \sim 0$).

Results of three cases are presented in Figure 9.11, where dashed curve indicates the result with 10% decreased density and dotted curve indicates the one with 10% increased density. Solid curve is the original result, same as Figure 9.5. These curves show the allowed regions at the 90% C.L.. According to the bottom panel of Figure 9.11, the limits on $\varepsilon_{e\tau}$ or $\varepsilon_{\tau\tau}$ are rather insensitive to the variation of matter density, however we notice that the limits on $\varepsilon_{e\tau}$ and $\varepsilon_{\tau\tau}$ are derived at the bound of parameter space, $\varepsilon_{ee} = 0.5$. In contrast, if we see top two panels, variations of allwed NSI parameters are maximum at $\varepsilon_{ee} \sim 0.2$. Therefore, according to the variation at $\varepsilon_{ee} \sim 0.2$, we estimate the systematic uncertainties to be at most 0.03 for $\varepsilon_{e\tau}$ and 0.02 for $\varepsilon_{\tau\tau}$.

9.6.2 Effect of nonzero θ_{13}

Next, we consider nonzero θ_{13}, which is expected to be quite small compared to θ_{23} or θ_{12}. Thanks to the smallness of θ_{13}, in the previous analysis, we neglected the effects of θ_{13}. However θ_{13} has similar effects to $\varepsilon_{e\tau}$ in matter, then θ_{13} possibly interferes with $\varepsilon_{e\tau}$. We test the scenario with nonzero θ_{13}, assuming $\sin^2\theta_{13} = 0.04$, corresponding to the upper limit derived by the CHOOZ experiment [150]. Note that nonzero θ_{13} breaks the symmetry between positive $\varepsilon_{e\tau}$ and negative $\varepsilon_{e\tau}$.

Results with two cases, normal hierarchy $\Delta m^2 > 0$ and inverted hierarchy $\Delta m^2 < 0$, are presented in Figure 9.12. Allowed parameters at the 90% C.L. are

$$-0.16 < \varepsilon_{e\tau} < 0.10, \qquad -0.03 < \varepsilon_{\tau\tau} < 0.04, \quad \text{(Normal hierarchy)} \qquad (9.16)$$

$$-0.14 < \varepsilon_{e\tau} < 0.13, \qquad -0.03 < \varepsilon_{\tau\tau} < 0.04, \quad \text{(Inverted hierarchy)} \qquad (9.17)$$

First we focus on normal hierarchy and compare it to the result with $\theta_{13} = 0$ (see Figure 9.5). Comparison of two results in the positive side of $\varepsilon_{e\tau}$ indicates that nonzero θ_{13} contributes
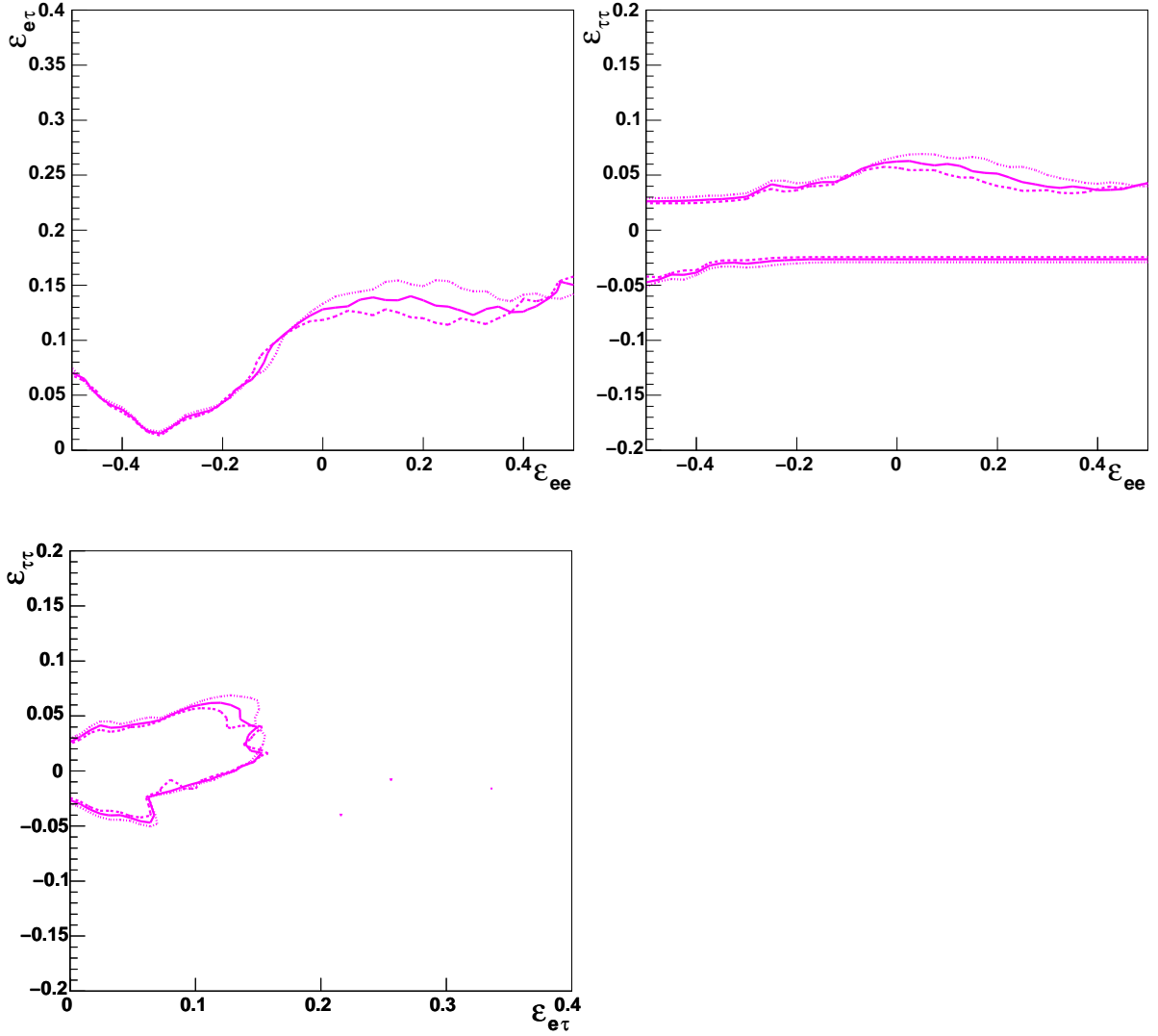
Figure 9.11: Allowed NSI parameters region with the uncertainty of matter density profile. (Top left) ε_{ee} vs. $\varepsilon_{e\tau}$ space. (Top right) ε_{ee} vs. $\varepsilon_{\tau\tau}$ space. (Bottom) $\varepsilon_{e\tau}$ vs. $\varepsilon_{\tau\tau}$ space. In all panels, solid curve, dashed curve, and dotted curve indicate the original PREM matter densty, 10% decreased density, and 10% increased density, respectively. Contours are at the 90% C.L..
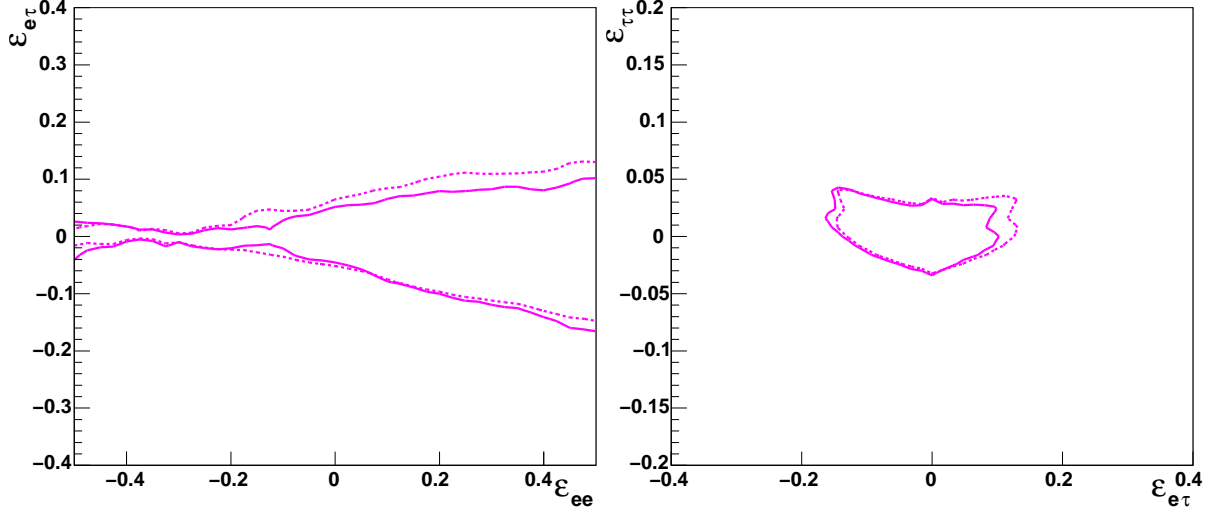
Figure 9.12: Allowed NSI parameters region with nonzero θ_{13}. (Left) ε_{ee} vs. $\varepsilon_{e\tau}$ space. (Right) $\varepsilon_{e\tau}$ vs. $\varepsilon_{\tau\tau}$ space. In both panels, $\sin^2\theta_{13}$=0.04, upper limit by the CHOOZ experiment [150], is considered. Solid curve and dashed curve indicate normal hierarchy and inverted hierarchy, respectively. Contours are at the 90% C.L..

to constrain $\varepsilon_{e\tau}$ more tightly. This can be understood by the comparison between $\nu_\mu \to \nu_e$ transition driven by θ_{13} and the effects of $\varepsilon_{e\tau}$. Assuming standard 3-flavor oscillation with normal hierarchy, the effective mixing angle in matter Θ_{23} is mostly equal to θ_{23} when $\theta_{12} = 0$, while Θ_{13} is modified by V_{MSW}. Θ_{13} is approximately expressed as

$$\Theta_{13} \sim \theta_{13} + \phi, \quad \tan 2\phi \sim \frac{a\sin 2\theta_{13}}{\Delta m_{31}^2 - a\cos 2\theta_{13}} \tag{9.18}$$

where a is the product of amplitude of matter term and neutrino energy, $2\sqrt{2}G_F N_e E_\nu$. Thus Θ_{13} depends on neutrino energy as shown in Figure 9.13. Since $\sin^2\Theta_{13}$ is not suppressed at $E_\nu \sim 10\mathrm{GeV}$, $\nu_\mu \to \nu_e$ transition is arised by θ_{23} together with Θ_{13}. As a result, this $\nu_\mu \to \nu_e$ transition will increase number of higher energy ν_e events in upward. We have to notice that the excess is purely caused by standard oscillation with nonzero θ_{13} and V_{MSW}, and also this is similar with the effects of $\varepsilon_{e\tau}$. In other words, $\varepsilon_{e\tau}$ is restricted to give upward excess, since nonzero θ_{13} occupies a room of ν_e-rich samples once allowed for $\varepsilon_{e\tau}$. It means that nonzero θ_{13} contributes to constrain $\varepsilon_{e\tau}$.

In Figure 9.12, we also see that normal hierarchy (solid curve) has stronger limit on positive $\varepsilon_{e\tau}$ rather than inverted hierarchy (dashed curve), while this is reversed for negative $\varepsilon_{e\tau}$. This difference comes from the sign of the matter term, $\pm\sqrt{2}G_F N_e$, which is positive for neutrinos and negative for anti-neutrinos. For convenience, we define the hierarchy of Δm^2 and sign of matter term as $(\Delta m^2, \sqrt{2}G_F N_e) = (\pm, \pm)$, for example $(+, -)$ for anti-neutrino oscillation with normal hierarchy. If we see Figure 9.13, $(+, +)$ and $(-, -)$ are represented by solid curves, while $(+, -)$ and $(-, +)$ are expressed by dashed curves. Namely, $(+, +)$ and $(-, -)$ give large upawrd excess in ν_e-rich samples rather than $(+, -)$ or $(-, +)$, since solid curves have large mixing angle at $E_\nu = 5 - 10\mathrm{GeV}$

For simplicity, we discuss only in the positive side of $\varepsilon_{e\tau}$. In case of normal hierarchy,
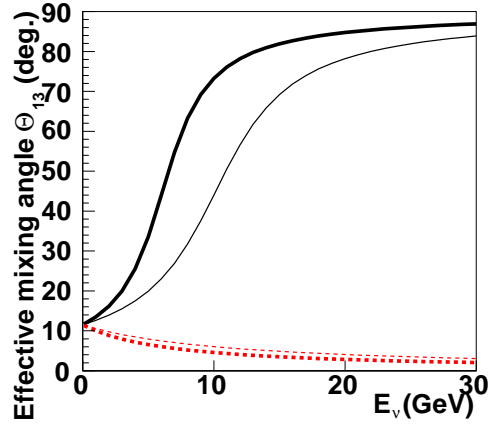
Figure 9.13: Effective mixing angle Θ_{13} for neutrino in the matter, corresponding to θ_{13} in vacuum. $\sin^2\theta_{13} = 0.04$ and constant matter density are assumed. Solid curves indicate the angle with normal hierarchy and dashed curves indicate that with inverted hierarchy. For both curves, thick curves are for $\rho = 5.0\text{g/cm}^3$ and thin curves are for $\rho = 3.0\text{g/cm}^3$. These angles are also applicable to anti-neutrinos by interchanging $\nu \leftrightarrow \overline{\nu}$ and normal hierarchy $\leftrightarrow$ inverted hierarchy. Note that no NSI is considered in this figure.

neutrino events have $(+,+)$, then it gives an excess in upward ν_e-rich samples. To the contrary, for inverted hierarchy, the excess is caused by anti-neutrinos due to $(-,-)$. In the energy range $E_\nu = 1 \sim 15\text{GeV}$, number of neutrino events is at least factor~ 2 larger than anti-neutrino events, because of the atmospheric neutrino flux $(\Phi(\nu) > \Phi(\overline{\nu}))$ and also neutrino-nucleus corss sections $(\sigma(\nu) > \sigma(\overline{\nu}))$. As a result, neutrino events are expected to have larger contributions to the excpected phenomena in atmospheric neutrinos rather than anti-neutrino events.

The excess in upward going events is more enhanced in normal hierarchy than inverted hierarchy, because, in normal hierarchy, large contribution is given by ν_μ, not by $\overline{\nu}_\mu$. In other words, normal hierarchy occupies a room of ν_e-rich samples rather than inverted hierarchy. Figure 9.14 shows zenith angle distributions of FC Single-ring Multi-GeV e-like samples. Left panel and right panel show normal hierarchy and inverted hierarchy, respectively, where expectations of 2-flavor standard oscillation, 3-flavor standard oscillation, and the 3-flavor hybrid model are displayed. If we normalize 3-flavor standard and hybrid model by 2-flavor oscillation, the magnitudes of the transition relative to 2-flavor oscillation is derived as in Figure 9.15. We can see that the upward excess are caused by $(+,+)$ and $(-,-)$, while $(+,-)$ and $(-,+)$ have smaller effects. Thus $\varepsilon_{e\tau}$ is constrained more tightly for normal hierarchy. This discussion is also true for negative $\varepsilon_{e\tau}$. In this case, sign of the matter term is reversed and an upawrd excess is given by $(+,-)$ and $(-,+)$. Therefore the tighter constraint to $\varepsilon_{e\tau}$ is obtained with inverted hierarchy rather than with normal hierarchy.

9.6.3 Effect of nonzero Δm_{12}^2 and θ_{12}

The oscillation parameters Δm_{12}^2 and θ_{12} have been measured by solar neutrino experiments, Super-Kamiokande [151] and SNO [152], and by KamLAND [153] using nuclear reactor anti-neutrinos, then we call Δm_{12}^2 and θ_{12} as *Solar term* in the following text. Results from the global analysis with their results, solar term is measured with high precision, and the combined
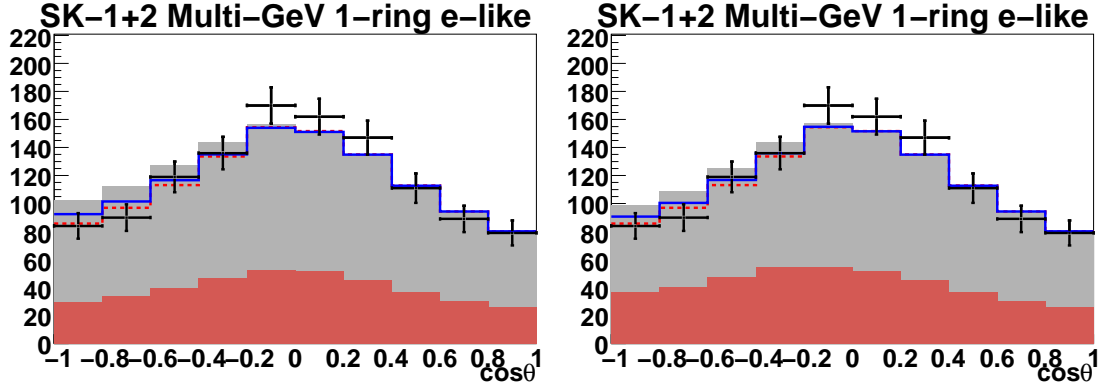
Figure 9.14: Zenith angle distribution for FC Single-ring Multi-GeV e-like samples. Left panel shows normal hierarchy ($\Delta m^2 = 2.1 \times 10^{-3} \text{eV}^2$), while right panel shows inverted hierarchy ($\Delta m^2 = -2.1 \times 10^{-3} \text{eV}^2$). In both panels, crosses with error are for data, solid lines for 3-flavor standard oscillation, and dashed lines for 2-flavor standard oscillation. Oscillation parameters are assumed to be $(\sin^2\theta_{23}, |\Delta m^2|) = (0.5, 2.1 \times 10^{-3} \text{eV}^2)$. $\sin^2\theta_{13} = 0.04$ is additionaly considerd only in 3-flavor oscillation. Gray hatched area indicates the 3-flavor hybrid model with $\sin^2\theta_{13} = 0.04$. Especially the component of anti-neutrino is shown by red hatched area.
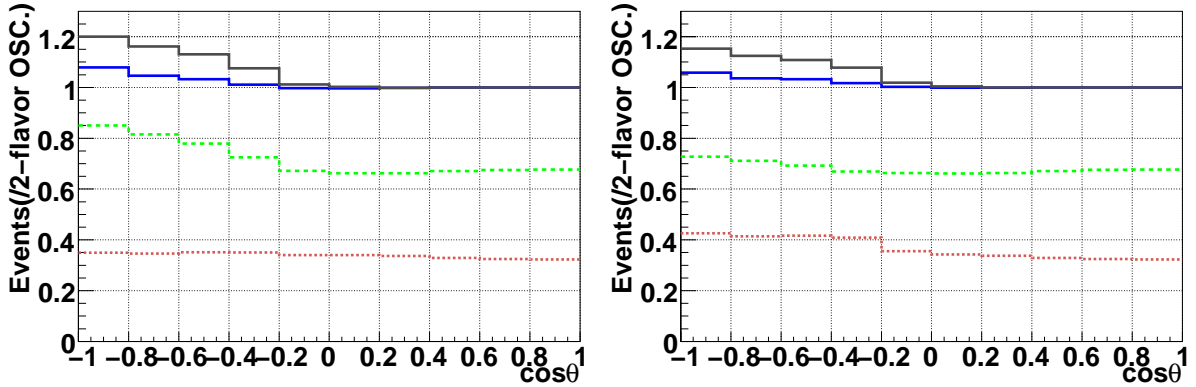
Figure 9.15: Number of FC Single-ring Multi-GeV e-like samples normalized by 2-flavor standard oscillation as a function of zenith angle, where $(\sin^2\theta_{23}, |\Delta m^2|) = (0.5, 2.1 \times 10^{-3} \text{eV}^2)$ is assumed. Left panel shows normal hierarchy, while right panel shows inverted hierarchy. Blue solid line indicates the ratio of 3-flavor standard oscillation and gray solid line indicates the 3-flavor hybrid model. For the 3-flavor hybrid model, the contribution of neutrino is shown by dashed line and that of anti-neutrino is shown by dotted line.
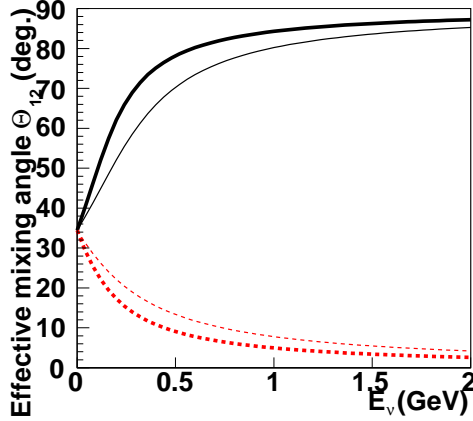
Figure 9.16: Effective mixing angle Θ_{12} in the matter, corresponding to θ_{12} in vacuum. $\sin^2\theta_{12} = 0.32$ ($\tan^2\theta_{12} = 0.47$) and constant matter density are assumed. Solid curve indicates the angle with neutrino and dashed curve indicates that with anti-neutrino. For both curves, thick curves are for $\rho = 5.0\text{g/cm}^3$ and thin curves are for $\rho = 3.0\text{g/cm}^3$. Note that no NSI is considered in this figure.

result [153] is

$$\Delta m_{21}^2 = 7.59^{+0.21}_{-0.21} \times 10^{-5}\text{eV}^2, \quad \tan^2\theta_{12} = 0.47^{+0.06}_{-0.05} \tag{9.19}$$

We focus on the effects of solar term in atmospheric neutrinos observation. First if we neglect V_{MSW}, $\nu_e \to \nu_\mu$ transition appears below $E_\nu \sim 2\text{GeV}$. While in actual case, the probability of $\nu_e \to \nu_\mu$ transition gets smaller due to V_{MSW} as increase of neutrino energy. It is explained as follows: If we see Figure 8.5, vacuum term $\Delta m_{12}^2/4E_\nu$ indicated by dashed curve competes with matter term even in low energy. Therefore the effective mixing angle Θ_{12} grows up rapidly due to the matter effect, as shown in Figure 9.16, and transitions of ν_e to other flavored neutrinos are suppressed. Effective mixing angle Θ_{12} is approximately expressed as

$$\Theta_{12} \sim \theta_{12} + \varphi, \quad \tan 2\varphi \sim \frac{a\sin 2\theta_{12}}{\Delta m_{21}^2 - a\cos 2\theta_{12}} \tag{9.20}$$

where a is defined as $2\sqrt{2}G_F N_e E_\nu$. $\nu_e \to \nu_\mu$ transition is still visible in Sub-GeV samples, while it fades out above $E_\nu \sim 400\text{MeV}$. Hereafter, we investigate the effects of solar term to the size of allowed NSI.

With unoscillated neutrino fluxes $\Phi(\nu_e)$ and $\Phi(\nu_\mu)$, e-like distribution is expressed as $\Phi(\nu_e)P(\nu_e \to \nu_e) + \Phi(\nu_\mu)P(\nu_\mu \to \nu_e)$. If we normalize by $\Phi(\nu_e)$, relative e-like distribution to that of standard 2-flavor oscillation is expressed as $P(\nu_e \to \nu_e) + \Phi(\nu_\mu)/\Phi(\nu_e)P(\nu_\mu \to \nu_e)$, where $\Phi(\nu_\mu)/\Phi(\nu_e)$ is approximately 2 in Sub-GeV region. Thus e-like distributions are mainly controled by $\nu_\mu \to \nu_e$ transition.

In Figure 9.17, we present $\nu_\mu \to \nu_e$ oscillation probability with three cases: (1) standard $\nu_\mu \to \nu_e$ oscillation with solar term, (2) the hybrid model without solar term, and (3) the hybrid model with solar term. This figure indicates that the hybrid model without solar term gives $\nu_\mu \to \nu_e$ transition due to nonzeo $\varepsilon_{e\tau}$ (top left panel), however, once solar term is considerd as in bottom panel, this transition is governed by vacuum solar term below 100MeV, and is suppressed by the interference between vacuum and matter term in $E_\nu = 100 \sim 300\text{MeV}$, while
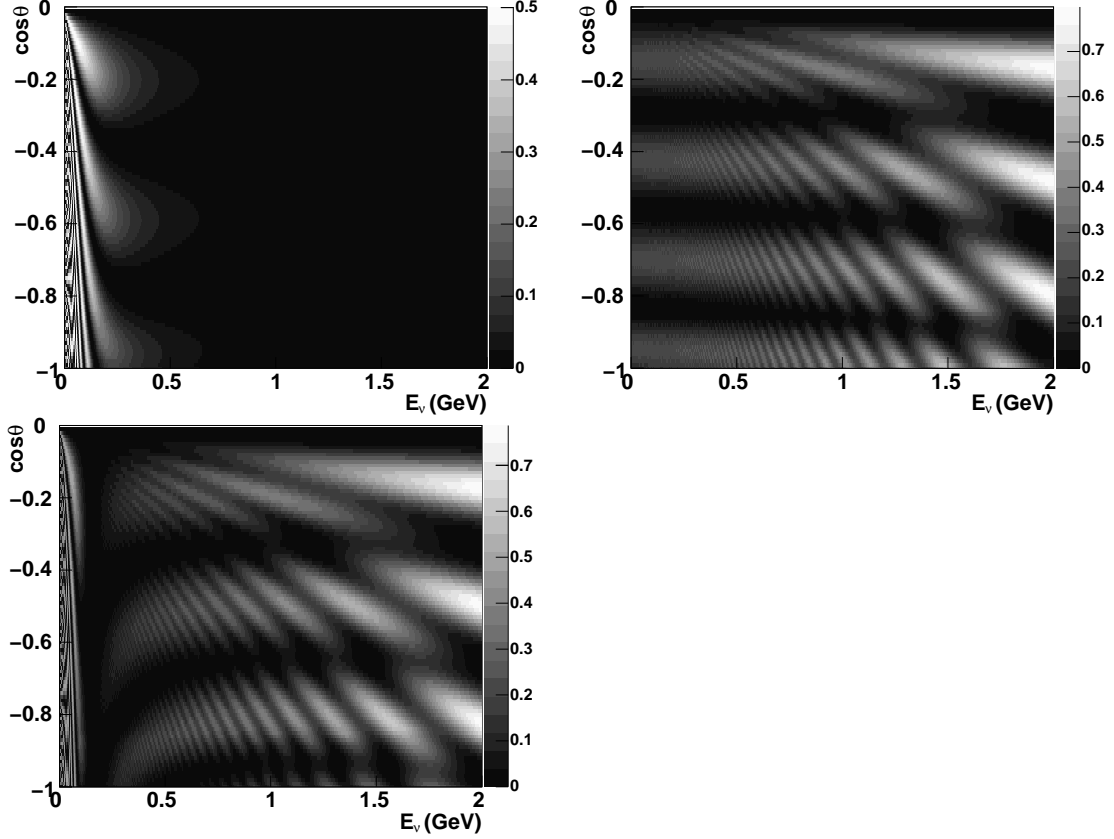
Figure 9.17: Oscillation probabilities of $\nu_\mu \to \nu_e$. (Top left) Standard oscillation with solar term, $\Delta m_{31}^2, \Delta m_{21}^2, \theta_{23}$, and θ_{12}. (Top right) The hybrid model without solar term, $\Delta m_{31}^2, \theta_{23}$, and $\varepsilon_{e\tau}$. (Bottom) The hybrid model with solar term, $\Delta m_{31}^2, \Delta m_{21}^2, \theta_{23}, \theta_{12}, \varepsilon_{e\tau}$. In this figure, $\Delta m_{31}^2 = 2.1 \times 10^{-3} \mathrm{eV}^2$, $\Delta m_{21}^2 = 7.6 \times 10^{-5} \mathrm{eV}^2$, $\sin^2 \theta_{23} = 0.5, \sin^2 \theta_{12} = 0.32$ are assumed. As for NSI, $\varepsilon_{e\tau} = 0.2$ is assumed. For simplicity, we assume the matter density of constant $\rho = 5.0 \mathrm{g/cm}^3$.

the transition is recovered again due to matter term $\varepsilon_{e\tau}$ above 300MeV. The importance what we notice here is that we do not use e-like events with reconstructed momentum below 100MeV in the analysis to avoid electrons from muon decay. This means that, in the hybrid model, solar term is expected to act as the suppression of $\nu_\mu \to \nu_e$ transition in the energy range we are interested in. In other words, NSI parameters are allowed to have larger values when solar term is considerd compared to without solar term. Indeed, analysis results in Figure 9.18 and Figure 9.5 are consistent with our expectations. Limits on NSI parameters are slightly looser than that without solar term. Allowed parameters at the 90% C.L. are

$$-0.16 < \varepsilon_{e\tau} < 0.18, \quad -0.05 < \varepsilon_{\tau\tau} < 0.06 \tag{9.21}$$
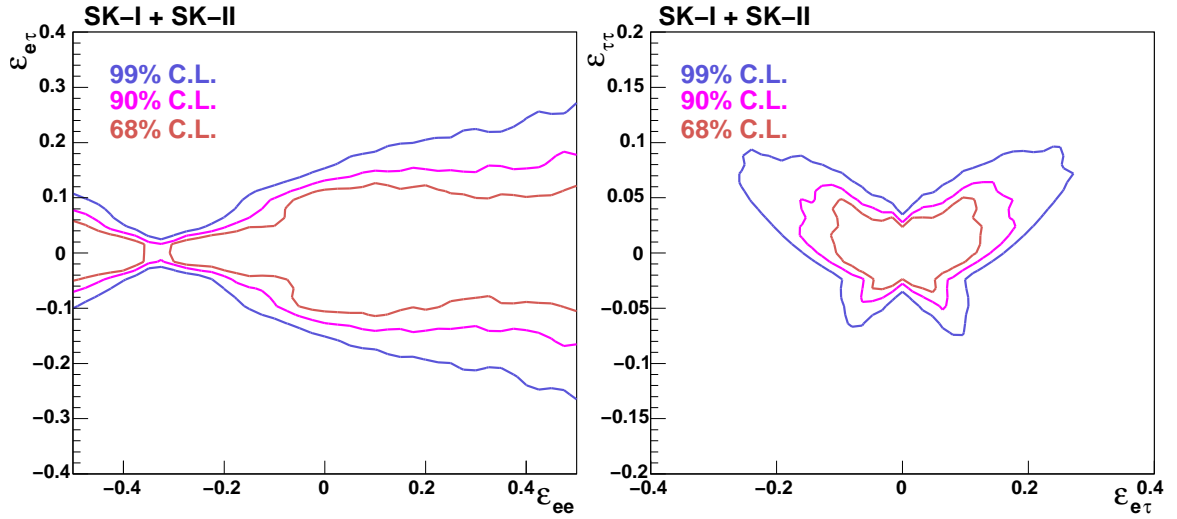
Figure 9.18: Allowed NSI parameters region with solar term. (Left) ε_{ee} vs. $\varepsilon_{e\tau}$ space. (Right) $\varepsilon_{e\tau}$ vs. $\varepsilon_{\tau\tau}$ space. In both panels, $\sin^2\theta_{12}=0.32$ and $\Delta m_{21}^2=7.6\times10^{-5}\mathrm{eV}^2$, best-fit parameters given by the global analysis [154], are considered.

			uncertainty (%)	best-fit (%)
(A1) Systematic uncertainties in neutrino flux				
Absolute normalization	$E_\nu < 1\,\mathrm{GeV}$		25.0	35.0
	$E_\nu > 1\,\mathrm{GeV}$		15.0	19.3
$(\nu_\mu + \overline{\nu}_\mu)/(\nu_e + \overline{\nu}_e)$	$E_\nu < 1\,\mathrm{GeV}$		2.0	-0.6
	$1 < E_\nu < 10\,\mathrm{GeV}$		3.0	-1.9
	$E_\nu > 10\,\mathrm{GeV}$		5.0[a]	4.7
$\nu_e/\overline{\nu}_e$	$E_\nu < 1\,\mathrm{GeV}$		5.0	2.9
	$1 < E_\nu < 10\,\mathrm{GeV}$		5.0	1.1
	$E_\nu > 10\,\mathrm{GeV}$		8.0[b]	0.07
$\nu_\mu/\overline{\nu}_\mu$	$E_\nu < 1\,\mathrm{GeV}$		2.0	-0.2
	$1 < E_\nu < 10\,\mathrm{GeV}$		6.0	-0.4
	$E_\nu > 10\,\mathrm{GeV}$		6.0[c]	1.3
Up/down	$< 400\,\mathrm{MeV}$	e-like	0.1	-0.05
		μ-like	0.3	-0.1
	$> 400\,\mathrm{MeV}$	e-like	0.8	-0.04
		μ-like	0.5	-0.2
	Multi-GeV	e-like	0.7	-0.3
		μ-like	0.2	-0.1
	Sub-GeV Multi-ring e-like		0.2	-0.1
	Sub-GeV Multi-ring μ-like		0.2	-0.1
	Multi-GeV Multi-ring e-like		0.3	-0.1
	Multi-GeV Multi-ring μ-like		0.2	-0.1
	PC		0.2	-0.1
Horizontal/vertical	$< 400\,\mathrm{MeV}$	e-like	0.1	0.005
		μ-like	0.1	0.005
	$> 400\,\mathrm{MeV}$	e-like	1.4	0.08
		μ-like	1.9	0.1
	Multi-GeV	e-like	3.2	0.2
		μ-like	2.3	0.1
	Sub-GeV Multi-ring e-like		1.4	0.08
	Sub-GeV Multi-ring μ-like		1.3	0.07
	Multi-GeV Multi-ring e-like		2.8	0.2
	Multi-GeV Multi-ring μ-like		1.5	0.08
	PC		1.7	0.09

Table 9.2: Summary of systematic uncertainties in atmospheric neutrino flux.

[a]Uncertainty linearly increases with $\log E_\nu$ from $5\,\%$ ($10\,\mathrm{GeV}$) to $30\,\%$($1\,\mathrm{TeV}$).
[b]Uncertainty linearly increases with $\log E_\nu$ from $8\,\%$($100\,\mathrm{GeV}$) to $20\,\%$($1\,\mathrm{TeV}$).
[c]Uncertainty linearly increases with $\log E_\nu$ from $6\,\%$($50\,\mathrm{GeV}$) to $40\,\%$($1\,\mathrm{TeV}$).

		uncertainty (%)	best-fit (%)
(A2) Systematic uncertainties in neutrino flux			
K/π ratio		5.0^a	-7.5
L_ν (production height)		10.0	0.3
Sample-by-sample	FC Multi-GeV	5.0	-5.1
	PC + upward stopping μ	5.0	-10.3
Solar activity	SK-I	20.0	3.1
	SK-II	50.0	32.1

Table 9.3: Summary of systematic uncertainties in atmospheric neutrino flux (continued).

^{a}Uncertainty is 20 % above $E_\nu =$1 TeV. The uncertainty increases linearly from 5% to 20% between 100GeV and 1TeV.

	uncertainty (%)	best-fit (%)
(B) Systematic uncertainties in neutrino interaction		
Quasi-elastic scattering and single meson production (M_A)	1.0^a	0.8
Quasi-elastic scattering for bound nucleon (total cross section)	1.0^b	5.3
Quasi-elastic scattering for bound nucleon ($\overline{\nu}/\nu$ ratio)	1.0^c	8.9
Quasi-elastic scattering for bound nucleon (ν_μ/ν_e ratio)	1.0^d	5.0
Single meson production (total cross section)	20.0	3.2
Single meson production ($\overline{\nu}/\nu$ ratio)	1.0^e	-3.4
Single meson production ($\pi^0/\pi^\pm$ ratio)	40.0	-35.9
Multi-pion production ($E_\nu < 10$GeV)	1.0^f	-0.6
Multi-pion production (total cross section)	5.0	1.9
Coherent pion production (total cross section)	$100.0(50.0)^g$	24.2
NC/CC ratio	20.0	-0.8
Nuclear Effect in ^{16}O nucleus	30.0	-22.9
Nuclear Effect in pion spectrum	1.0^h	9.3
CC ν_τ interaction cross section	30.0	-15.9
Hadron simulation	10.0	-2.2

Table 9.4: Summary of systematic uncertainties in neutrino interactions.

^{a}Difference from the $M_A = 1.1$GeV/c is set to be 1.0
^{b}Difference from the Nieves model is set to 1.0
^{c}Difference from the Nieves model is set to 1.0
^{d}Difference from the Nieves model is set to 1.0
^{e}Difference from the Hernandez model is set to 1.0
^{f}Difference from CKMT parametrization is set to 1.0
^{g}100% for CC ν_μ. 50% for CC ν_e and NC.
^{h}Difference between NEUT and NUANCE is set to 1.0

			uncertainty (%)	best-fit (%)
(C) Systematic uncertainties in event selection for SK-I				
Reduction for FC event			0.2	0.04
Reduction for PC event			2.4	-0.8
FC/PC separation			0.6	-0.01
Non-ν background	Flasher for e-like	Sub-GeV	0.5	0.07
		Multi-GeV	0.2	0.03
	Cosmic ray for μ-like	Sub-GeV	0.1	-0.01
		Multi-GeV	0.1	-0.01
	PC		0.2	-0.03
PC stop/through separation	OD top region		15.0	11.3
	OD barrel region		7.4	-0.6
	OD bottom region		11.3	-7.1
Reduction for UPMU event	stopping μ		1.8	0.1
	through-going μ		0.3	0.02
UPMU stopping/through separation			0.4	-0.04
UPMU stopping energy cut			0.8	-0.08
UPMU through showering/non-showering separation			2.8	-1.7

Table 9.5: Summary of systematic uncertainties in event selection for SK-I.

			uncertainty (%)	best-fit (%)
(D) Systematic uncertainties in event selection for SK-II				
Reduction for FC event			0.2	0.007
Reduction for PC event			4.8	-2.6
FC/PC separation			0.5	0.05
Non-ν background	Flasher for e-like	Sub-GeV	0.3	-0.01
		Multi-GeV	0.7	-0.03
	Cosmic ray for μ-like	Sub-GeV	0.1	0.02
		Multi-GeV	0.1	0.02
	PC		0.7	0.2
PC stop/through separation	OD top region		19.0	-18.0
	OD barrel region		14.0	-22.4
	OD bottom region		18.0	-19.2
Reduction for UPMU event	stopping μ		2.1	-0.2
	through-going μ		0.3	-0.02
UPMU stopping/through separation			0.4	-0.02
UPMU stopping energy cut			1.5	-0.04
UPMU through showering/non-showering separation			1.8	-0.3

Table 9.6: Summary of systematic uncertainties in event selection for SK-II.

			uncertainty (%)	best-fit (%)
(E) Systematic uncertainties in event reconstruction for SK-I				
Single-ring/Multi-ring separation	*Single-ring*			
	$< 400\,\mathrm{MeV}$	e-like	2.3	1.4
		μ-like	0.7	0.4
	$> 400\,\mathrm{MeV}$	e-like	0.4	0.2
		μ-like	0.7	0.4
	Multi-GeV	e-like	3.7	2.2
		μ-like	1.7	1.0
	Multi-ring			
	Sub-GeV	e-like	3.5	-2.1
		μ-like	4.5	-2.7
	Multi-GeV	e-like	3.1	-1.9
		μ-like	4.1	-2.5
Particle identification	*Single-ring*			
	Sub-GeV	e-like	0.1	-0.01
		μ-like	-0.1	0.01
	Multi-GeV	e-like	0.2	-0.02
		μ-like	-0.2	0.02
	Multi-ring			
	Sub-GeV	e-like	2.3	0.07
		μ-like	-3.9	-0.1
	Multi-GeV	e-like	1.7	0.05
		μ-like	-2.9	-0.1
Energy calibration for FC event			1.1	0.1
Up/down symmetry of energy calibration			0.6	0.06
π^0-like sample selection	$100 < P_e < 250\,\mathrm{MeV/c}$		11.2	-3.4
	$250 < P_e < 400\,\mathrm{MeV/c}$		11.5	-3.5
	$400 < P_e < 630\,\mathrm{MeV/c}$		23.4	-7.1
	$630 < P_e < 1000\,\mathrm{MeV/c}$		19.1	-5.8
	$1000 < P_e < 1330\,\mathrm{MeV/c}$		13.0	-4.0
FC Sub-GeV two-ring π^0-like sample selection			2.0	-0.5
Decay electron tagging (π^+decay)	e-like 0μedecay		1.5~1.7	0.1
	e-like 1μedecay		-4.4~-3.8	-0.3
	μ-like 0μedecay		1.6~1.8	0.1
	μ-like 1μedecay		-1.5	-0.1
	μ-like 2μedecay		-6.4~-5.9	-0.5~-0.4
Decay electron tagging ($\mu \to e$ decay)			1.1	0.7

Table 9.7: Summary of systematic uncertainties in event reconstruction for SK-I.

			uncertainty (%)	best-fit (%)
(F) Systematic uncertainties in event reconstruction for SK-II				
Single-ring/Multi-ring separation	*Single-ring*			
	< 400 MeV	e-like	1.3	1.3
		μ-like	2.3	2.3
	> 400 MeV	e-like	1.7	1.7
		μ-like	0.7	0.7
	Multi-GeV	e-like	2.6	2.7
		μ-like	1.7	1.8
	Multi-ring			
	Sub-GeV	e-like	3.8	-4.0
		μ-like	8.2	-8.5
	Multi-GeV	e-like	1.9	-1.9
		μ-like	0.8	-0.8
Particle identification	*Single-ring*			
	Sub-GeV	e-like	0.5	0.08
		μ-like	-0.4	-0.07
	Multi-GeV	e-like	0.1	0.02
		μ-like	-0.1	-0.02
	Multi-ring			
	Sub-GeV	e-like	1.2	0.2
		μ-like	-2.2	-0.4
	Multi-GeV	e-like	1.8	0.3
		μ-like	-3.4	-0.6
Energy calibration for FC event			1.7	-1.6
Up/down symmetry of energy calibration			0.6	-0.2
π^0-like sample selection	100< P_e <250 MeV/c		7.5	-4.0
	250< P_e <400 MeV/c		8.9	-4.8
	400< P_e <630 MeV/c		17.5	-9.4
	630< P_e <1000 MeV/c		10.7	-5.8
	1000< P_e <1330 MeV/c		11.1	-6.0
FC Sub-GeV two-ring π^0-like sample selection			2.0	-0.3
Decay electron tagging (π^+decay)	e-like 0μedecay		1.2∼1.7	-0.1
	e-like 1μedecay		-4.2∼-3.8	0.3
	μ-like 0μedecay		1.6∼1.8	-0.1
	μ-like 1μedecay		-1.5	0.1
	μ-like 2μedecay		-6.5∼-5.9	0.4∼0.5
Decay electron tagging ($\mu \to e$ decay)			1.1	-0.7

Table 9.8: Summary of systematic uncertainties in event reconstruction for SK-II.

Chapter 10

Discussions

As a result of the study using SK-I and SK-II atmospheric neutrino data, we obtained the constraints on NSI parameters by means of the robustness of the implementation of 2-flavor $\nu_\mu \leftrightarrow \nu_\tau$ neutrino oscillations to the atmospheric neutrinos. We compare our results to the existing results derived from the neutrino scattering experiments, the CHARM and NuTeV experiment, where the cross section ratio for the deep inelastic scattering is measured. First, cross section formulae are introduced in Chapter 10.1, and next, existing results from the CHARM and NuTeV experiment are reviewed. Finally our results are compared to those results.

10.1 Deep inelastic scattering

If we discuss under the tree level, neutral current neutrino scattering off a quark is expressed as

$$\begin{aligned}
\frac{d\sigma}{dy}(\nu q, \bar{\nu}\bar{q}) &= \frac{G_F^2}{\pi} s[g_L^2 + g_R^2(1-y)^2] \\
\frac{d\sigma}{dy}(\bar{\nu} q, \nu\bar{q}) &= \frac{G_F^2}{\pi} s[g_L^2(1-y)^2 + g_R^2]
\end{aligned} \tag{10.1}$$

where $s \simeq 2m_N E_\nu$, y is the Bjorken scaling, and g_L, g_R are the neutral current couplings as summarized in Table 10.1. m_N is the nucleon mass.

Cross section for the neutrino scattering off nucleon is derived from eq.(10.1),

$$\begin{aligned}
\frac{d\sigma}{dxdy}(\nu N) &= \frac{G_F^2}{\pi} s[g_L^2 xq(x) + g_R^2 x\bar{q}(x) + (g_R^2 xq(x) + g_L^2 x\bar{q}(x))(1-y)^2] \\
\frac{d\sigma}{dxdy}(\bar{\nu} N) &= \frac{G_F^2}{\pi} s[g_R^2 xq(x) + g_L^2 x\bar{q}(x) + (g_L^2 xq(x) + g_R^2 x\bar{q}(x))(1-y)^2]
\end{aligned} \tag{10.2}$$

	g_L	g_R
u	$\frac{1}{2} - \frac{2}{3}\sin^2\theta_W$	$-\frac{2}{3}\sin^2\theta_W$
d	$-\frac{1}{2} + \frac{2}{3}\sin^2\theta_W$	$\frac{1}{3}\sin^2\theta_W$

Table 10.1: Neutral current couplings. θ_W is the Weinberg angle.

where x is the Bjorken scaling and $q(x)$, $\bar{q}(x)$ are the parton distribution function. Integration over x and y gives the total cross section,

$$
\begin{aligned}
\sigma(\nu N) &= \frac{G_F^2}{\pi} s \left[\left(g_L^2 + \frac{g_R^2}{3} \right) \int x q(x) dx + \left(\frac{g_L^2}{3} + g_R^2 \right) \int x \bar{q}(x) dx \right] \\
\sigma(\bar{\nu} N) &= \frac{G_F^2}{\pi} s \left[\left(\frac{g_L^2}{3} + g_R^2 \right) \int x q(x) dx + \left(g_L^2 + \frac{g_R^2}{3} \right) \int x \bar{q}(x) dx \right]
\end{aligned}
\tag{10.3}
$$

Suppose a target of the scattering is isoscalar nucleus and parton disutibution functions for u-quark and d-quark are denoted as $u(x)$ and $d(xa)$, respectively, neutral current couplings g_L, g_R are relpaced with,

$$
\begin{aligned}
g_L^2 \int x q(x) dx &\rightarrow \frac{1}{2} \left[(g_L^2(u) U + g_L^2(d) D) + (U \leftrightarrow D) \right] \equiv \tilde{g}_L^2 \frac{U + D}{2} \\
g_R^2 \int x q(x) dx &\rightarrow \frac{1}{2} \left[(g_R^2(u) U + g_R^2(d) D) + (U \leftrightarrow D) \right] \equiv \tilde{g}_R^2 \frac{U + D}{2} \\
U &= \int x u(x) dx, \quad D = \int x d(x) dx \\
\tilde{g}_L^2 &= g_L^2(u) + g_L^2(d), \quad \tilde{g}_R^2 = g_R^2(u) + g_R^2(d)
\end{aligned}
\tag{10.4}
$$

The total cross sections eq.(10.3) are expressed as

$$
\begin{aligned}
\sigma_{NC}(\nu N) &\equiv \sigma(\nu N) = \frac{G_F^2}{\pi} s \left[\tilde{g}_L^2 \left(Q + \frac{\bar{Q}}{3} \right) + \tilde{g}_R^2 \left(\frac{Q}{3} + \bar{Q} \right) \right] \\
\sigma_{NC}(\bar{\nu} N) &\equiv \sigma(\bar{\nu} N) = \frac{G_F^2}{\pi} s \left[\tilde{g}_L^2 \left(\frac{Q}{3} + \bar{Q} \right) + \tilde{g}_R^2 \left(Q + \frac{\bar{Q}}{3} \right) \right] \\
Q &\equiv \frac{U + D}{2}
\end{aligned}
\tag{10.5}
$$

Using the same method, charge current total cross sections are given as

$$
\begin{aligned}
\sigma_{CC}(\nu N) &= \frac{G_F^2}{\pi} s \left(Q + \frac{\bar{Q}}{3} \right) \\
\sigma_{CC}(\bar{\nu} N) &= \frac{G_F^2}{\pi} s \left(\frac{Q}{3} + \bar{Q} \right)
\end{aligned}
\tag{10.6}
$$

10.2   CHARM experiment

The CHARM neutrino detector is a fine-grained calorimeter followed by an iron spectrometer with a troidal magnetic field. The calorimeter is surrounded by a magnetized iron frame and has a sampling step correnponding to one radiation length or 0.22 absorption length with other detecting elements, scintillators, propotional drift tubes and streamer tubes. The CHARM detector was exposed to the neutrino beam in 1982. Neutrino beam was produced as follows: The 400GeV proton beam was extracted from the CERN SPS and dumped onto thick copper targets in the direction of the neutrino detector. Electron neutrinos with equal contributions of neutrinos and anti-neutrinos were produced mainly from neutral kaon decay.

The CHARM collaboration measured the follwing combination of $\nu_e N$ and $\bar{\nu}_e N$ cross section [156]:

$$R^e = \frac{\sigma(\nu_e N \to \nu X) + \sigma(\bar{\nu}_e N \to \bar{\nu} X)}{\sigma(\nu_e N \to e X) + \sigma(\bar{\nu}_e N \to \bar{e} X)} = \tilde{g}_L^2 + \tilde{g}_R^2 = 0.406 \pm 0.140 \tag{10.7}$$

where the couplings $\tilde{g}_L$ and $\tilde{g}_R$ are taken from eq.(10.4). The eq.(10.7) does not depend on any specific model beyond the standard model nor neutrino energy, thus we can compare it to our results.

In order to investigate NSI in the CHARM result, we extend the couplings $\tilde{g}_L$ and $\tilde{g}_R$ to that with NSI parameters,

$$\tilde{g}_L^2 \to (g_L(u) + \varepsilon_{ee}^{uL})^2 + \sum_{\alpha \neq e} |\varepsilon_{\alpha e}^{uL}|^2 + (g_L(d) + \varepsilon_{ee}^{dL})^2 + \sum_{\alpha \neq e} |\varepsilon_{\alpha e}^{dL}|^2$$

$$\tilde{g}_R^2 \to (g_R(u) + \varepsilon_{ee}^{uR})^2 + \sum_{\alpha \neq e} |\varepsilon_{\alpha e}^{uR}|^2 + (g_R(d) + \varepsilon_{ee}^{dR})^2 + \sum_{\alpha \neq e} |\varepsilon_{\alpha e}^{dR}|^2 \tag{10.8}$$

According to this result, together with the corresponding couplings given by the standard model, $(\tilde{g}_L)_{SM}^2 = 0.3042$ and $(\tilde{g}_R)_{SM}^2 = 0.0301$, the limits on flavor diagonal NSI and flavor changing NSI off d-quark are

$$-0.5 < \varepsilon_{ee}^{dL} < 0.5, \qquad |\varepsilon_{\tau e}^{dP}| < 0.5 \quad (P = L, R) \tag{10.9}$$

10.3 NuTeV experiment

The NuTeV detector consisted of an 18m long, 690ton steel-scintillator target, followed by an iron-toroid spectrometer. The target calorimeter was composed of 168 (3m×3m×5.1cm) steel plates interspersed with liquid scintillation counters (spaced every two plates) and drift chambers (spaced every four plates). High-purity ν and $\bar{\nu}$ beams are provided by the Sign Selected Quadrupole Train (SSQT) beam line at the Fermilab Tevatron. Neutrinos are produced from the decay of pions and kaons resulting from interactions of 800GeV protons in a BeO target.

The NuTeV collaboration measures the cross section ratios of the neutrino-nucleon interactions. The ratios for an isoscalar target and at leading order are given by

$$R(\nu) \equiv \frac{\sigma(\nu N \to \nu X)}{\sigma(\nu N \to \mu X)} = \tilde{g}_L^2 + r\tilde{g}_R^2 \tag{10.10}$$

$$R(\bar{\nu}) \equiv \frac{\sigma(\bar{\nu} N \to \bar{\nu} X)}{\sigma(\bar{\nu} N \to \bar{\mu} X)} = \tilde{g}_L^2 + \frac{1}{r}\tilde{g}_R^2 \tag{10.11}$$

$$r = \frac{\sigma(\bar{\nu} N \to \bar{\mu} X)}{\sigma(\nu N \to \mu X)} \tag{10.12}$$

The effective couplings $\tilde{g}_L$, $\tilde{g}_R$ are the same style in eq.(10.8), with changing $e \to \mu$ in the coefficients of the neutral current NSI.

The values of these couplings reported by NuTeV are [155]

$$\tilde{g}_L^2 = 0.3005 \pm 0.0014, \qquad \tilde{g}_R^2 = 0.0310 \pm 0.0011 \tag{10.13}$$

Because of the same reason as we mentioned above, these results can be compared with our results. Accompanied with the standard model prediction, $(\tilde{g}_L)_{SM}^2 = 0.0301$ and $(\tilde{g}_L)_{SM}^2 =$

0.3042, the constraints at 90% C.L. to left-handed NSI are

$$|\varepsilon_{\mu\mu}^{dL}| < 0.003 \tag{10.14}$$

$$|\varepsilon_{\tau\mu}^{dL}| < 0.05 \tag{10.15}$$

For diagonal right-handed NSI at 90% C.L. allowed regions are

$$-0.008 < \varepsilon_{\mu\mu}^{dR} < 0.015 \tag{10.16}$$

while for flavor changing intearctions,

$$|\varepsilon_{\tau\mu}^{dR}| < 0.05 \tag{10.17}$$

10.4   Comparison with the existing results

As a result of the 2-flavor hybrid model with relative phase, more general case than that without relative phase, the constraints to NSI in the $\nu_\mu - \nu_\tau$ sector are written as

$$|\varepsilon_{\mu\tau}| < 1.6 \times 10^{-2}, \quad -5.3 \times 10^{-2} < \varepsilon_{\tau\tau} - \varepsilon_{\mu\mu} < 4.9 \times 10^{-2} \quad (90\% \text{ C.L.}) \tag{10.18}$$

As for 3-flavor hybrid model, results are given as

$$|\varepsilon_{e\tau}| < 0.16, \quad -0.05 < \varepsilon_{\tau\tau} < 0.06 \quad (90\% \text{ C.L.}) \tag{10.19}$$

If we combine the limit on $\varepsilon_{\tau\tau} - \varepsilon_{\mu\mu}$ with that on $\varepsilon_{\tau\tau}$, limit on $\varepsilon_{\mu\mu}$ can be extracted as

$$-9.9 \times 10^{-2} < \quad \varepsilon_{\mu\mu} \quad < 0.11 \quad (90\% \text{ C.L.}) \tag{10.20}$$

As explained in Chapter 1.3, the NSI coupling $\varepsilon_{\alpha\beta}^{fP}$ ($f = e, u, d$ $P = L, R$) corresponds to the standard model NC coupling $g_P(f)$, so $\varepsilon_{\alpha\beta}^{fP}$ itself has no dependence on the matter density nor the neutrino energy. Therefore, we can compare the limits on $\varepsilon_{\alpha\beta}^{fP}$ from the atmospheric neutrinos with that from the neutrino scattering experiments. However, the measurement of NSI using atmospheric neutrinos cannot distinguish the constraints between left-handed and right-handed fermions, since NSI is not detected as the cross section, but appeared in neutrino propagation through the matter of the Earth. Thus our detectable NSI parameter with d-quark is taken as $\varepsilon_{\alpha\beta} = \varepsilon_{\alpha\beta}^{dL} + \varepsilon_{\alpha\beta}^{dR}$. Considering the difference in the detections, the limits are compared in the two-dimentional space of $\varepsilon_{\alpha\beta}^{dL}$ and $\varepsilon_{\alpha\beta}^{dR}$. Figure 10.1 shows the constraints on the NSI parameters. Note that no constrant on $\varepsilon_{\tau\tau}^{dP}$ is available from the other experiments.
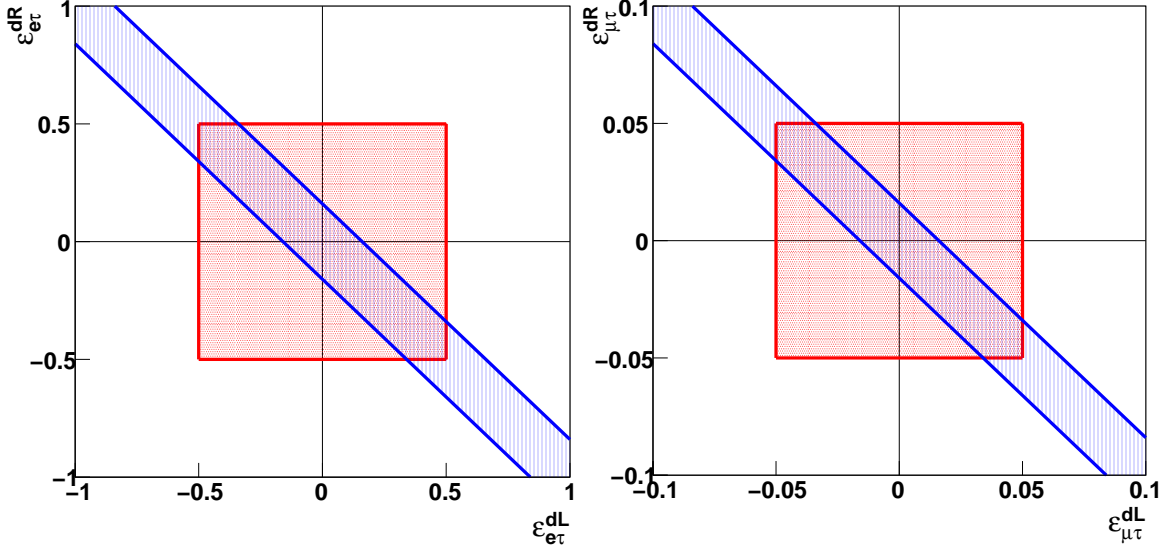
(a) Constraints on $\varepsilon_{e\tau}^{dL}$ and $\varepsilon_{e\tau}^{dR}$

(b) Constraints on $\varepsilon_{\mu\tau}^{dL}$ and $\varepsilon_{\mu\tau}^{dR}$
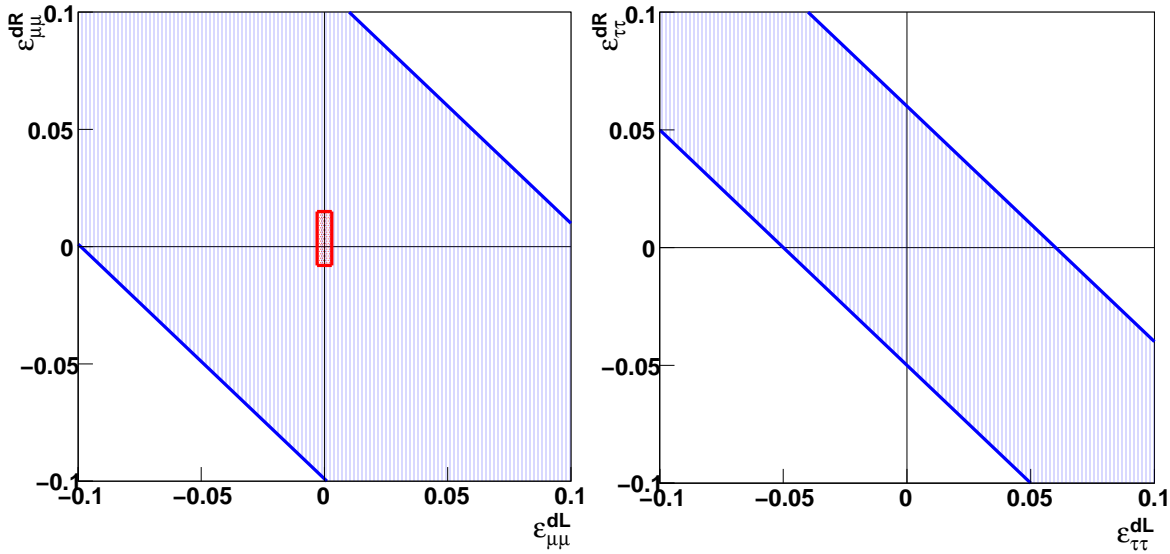
(c) Constraints on $\varepsilon_{\mu\mu}^{dL}$ and $\varepsilon_{\mu\mu}^{dR}$

(d) Constraints on $\varepsilon_{\tau\tau}^{dL}$ and $\varepsilon_{\tau\tau}^{dR}$

Figure 10.1: Constraints on the NSI parameters. Brue hatched areas indicate the allowed parameter region obtained in this analysis. Red hatched areas indicate the existing results. For both areas the hatched region corresponds to the 90% C.L.. Existing limit on the panel (a) is derived from the CHARM experiment [156], while that on the panel (b) and (c) are derived from the NuTeV experiment [155].

Chapter 11

Conclusions

We studied non-standard neutrino interactions (NSI) with the matter in the Earth, where NSI consisted of either flavor changing neutral current (FCNC) and lepton non universality (NU). Considering that atmospheric neutrinos were well explained by neutrino oscillations, it was assumed that neutrino oscillations had the dominant contribution and NSI had the subdominant contribution in the atmospheric neutrino data.

We analyzed atmospheric neutrino data to examine

(1) How neutrino oscillations are robust to the atmospheric neutrino data.

(2) What amount of NSI is included in the atmospheric neutrino data. If we would not able to obtain the signal of NSI, we derive the constraints to them.

where NSI was allowed to arise through the parameters $\varepsilon_{\alpha\beta}$ (FCNC) and $\varepsilon_{\alpha\alpha}$ (NU). The analysis was performed with two schemes: (i) 2-flavor $\nu_\mu \leftrightarrow \nu_\tau$ oscillation with NSI in the $\nu_\mu - \nu_\tau$ sector, and (ii) 2-flavor $\nu_\mu \leftrightarrow \nu_\tau$ oscillation with NSI in the $\nu_e - \nu_\tau$ sector.

Scheme (i) assumed that the flavor transition was only occurred between ν_μ and ν_τ, whereas ν_e flux was kept as is. In this scheme, in order to investigate (1) and (2), we set two oscillation parameters and two (or three if relative phase η was considerd) NSI parameters as free parameters. As a result of the analysis without relative phase using SK-I and SK-II atmospheric neutrino data, minimum χ^2 value $\chi^2_{min} = 838.9/746$ d.o.f. at the best-fit position $(\sin^2 2\theta, \Delta m^2, \varepsilon, \varepsilon') = (1.00, 2.2 \times 10^{-3} \text{eV}^2, 1.0 \times 10^{-3}, -2.7 \times 10^{-2})$ was obtained. No possible signal of NSI was found, while we constrained the NSI parameters,

$$|\varepsilon_{\mu\tau}| < 1.1 \times 10^{-2}, \quad -4.9 \times 10^{-2} < \varepsilon_{\tau\tau} - \varepsilon_{\mu\mu} < 4.9 \times 10^{-2} \quad (90\% \text{ C.L.}) \tag{11.1}$$

As for the case with non vanishing relative phase, $\chi^2_{min} = 837.5/745$ d.o.f. at the best-fit position $(\sin^2 2\theta, \Delta m^2, \varepsilon, \varepsilon', \cos\eta) = (1.00, 2.2 \times 10^{-3} \text{eV}^2, 6.9 \times 10^{-3}, -1.9 \times 10^{-2}, -1.0)$ was obtained. Constraints to the NSI parameters were

$$|\varepsilon_{\mu\tau}| < 1.6 \times 10^{-2}, \quad -5.3 \times 10^{-2} < \varepsilon_{\tau\tau} - \varepsilon_{\mu\mu} < 4.9 \times 10^{-2} \quad (90\% \text{ C.L.}) \tag{11.2}$$

No significant difference was found in the allowed neutrino oscillation parameters region between scheme (i) and standard neutrino oscillation. Therefore neutrino oscillations were proven to be robust to the atmospheric neutrino data even though NSI existed simultaneously.

On the other hand, scheme (2) allowed the flavor transition among all flavored neutrinos. In this scheme we fixed the neutrino oscillation parameters as the best-fit values from the analysis with only standard neutrino oscillation, then this scheme purposed to examine (2). As a result, no signal of NSI was given by the SK-I and SK-II data, while we obtained the constraints to NSI

$$|\varepsilon_{e\tau}| < 0.16, \quad -0.05 < \varepsilon_{\tau\tau} < 0.06 \quad (90\% \text{ C.L.}) \tag{11.3}$$

Best-fit position was $(\sin^2 2\theta, \Delta m^2, \varepsilon_{ee}, \varepsilon_{e\tau}, \varepsilon_{\tau\tau})=(1.00, 2.1 \times 10^{-3}\text{eV}^2, -0.25, 0.016, 0.024)$ and minimum χ^2 value was $\chi^2_{min} = 829.9/747$ d.o.f.

Limit on $\varepsilon_{\mu\mu}$ was extracted from the combination of the limit on $\varepsilon_{\tau\tau} - \varepsilon_{\mu\mu}$ and that on $\varepsilon_{\tau\tau}$,

$$-9.9 \times 10^{-2} < \quad \varepsilon_{\mu\mu} \quad < 0.11 \quad (90\% \text{ C.L.}) \tag{11.4}$$

Our constraints to the NSI parameters were compared with the existing limits derived from the neutrino scattering experiments, the CHARM and NuTeV experiment.

We concluded that we achieved the purposes, check the robustness of neutrino oscillations and investigation of NSI, based on the first experimental approach assuming the existence of NSI together with neutrino oscillations.

Bibliography

[1] M. Honda *et al.*, Phys. Rev. D **64**, 053001 (2001).

[2] M. Honda *et al.*, Phys. Rev. D **70**, 043008 (2004).

[3] M. Honda *et al.*, Phys. Rev. D **75**, 043006 (2007).

[4] K.S. Hirata *et al.*, Phys. Lett. B **205**, 416 (1988).

[5] K.S. Hirata *et al.*, Phys. Lett. B **280**, 146 (1992).

[6] Y. Fukuda *et al.*, Phys. Lett. B **335**, 237 (1994).

[7] D. Casper *et al.*, Phys. Rev. Lett. **66**, 2561 (1991).

[8] R. Becker-Szendy *et al.*, Phys. Rev. D **46**, 3720 (1992).

[9] M. C. Sanchez *et al.*, Phys. Rev. D **68**, 113004 (2003).

[10] The MACRO collaboration, Phys. Lett. B **434**, 451 (1998).

[11] Y.Fukuda *et al.*, Phys. Rev. Lett. **82**, 2644 (1999).

[12] S. Hatakeyama *et al.*, Phys. Rev. Lett **81**, (1998).

[13] S.L. Glashow, Nucl. Phys. **22**, 579 (1961).

[14] S. Weinberg, Phys. Rev. Lett. **19**, 1264 (1967).

[15] A. Salam, In *Proceedings of the 8th Nobel Symposium on Elementary particle theory, relativistic groups and analyticity*, edited by N. Svartholm (1969).

[16] Z. Maki, M. Nakagawa, and S. Sakata, Prog. Theo. Phys. **28**, 870 (1962).

[17] Y. Fukuda *et al.*, Phys. Lett. **81**, 1562 (1998).

[18] Y. Ashie *et al.*, Phys. Rev. Lett. **93**, 101801 (2004).

[19] J. Raaf, Talk at the 23-th International Conference on Neutrino Physics and Astro physics(Neutrino08), http://www2.phys.canterbury.ac.nz/ jaa53/

[20] M. H. Ahn *et al.*, Phys. Rev. D **74**, 072003 (2006).

[21] H. Gallagher, Talk at the 23-th International Conference on Neutrino Physics and Astro physics(Neutrino08), http://www2.phys.canterbury.ac.nz/ jaa53/

[22] P. Lipari and M. Lusignoli, Phys. Rev. D, **60**, 013003 (1999).

[23] J. Schechter and J.W.F. Valle, Phys. Rev. D, **22**, 2227 (1980).

[24] Dziewonski and Anderson, Phys. Earth. Planet. Int. **25**, 297-356 (1981).

[25] M. C. Gonzalez-Garcia *et al.*, Nucl. Phys. B, **573**, 3 (2000).

[26] L. Wolfenstein, Phys. Rev. D **17**, 2369 (1978).

[27] S. P. Mikheev and A. Y. Smirnov, Nuovo Cimento Soc. Ital. Fis. **9C**, 17 (1986).

[28] S. P. Mikheev and A. Y. Smirnov, Sov. J. Nucl. Phys. **42**, 913 (1985).

[29] M. Zito, J. Phys. Conf. Ser. **110**, 082023 (2008).

[30] I. Frank and I.Tamm, C. R. Acad. Sci. USSR **14**, 109 (1937).

[31] H. Kume *et al.*, Nucl. Inst. and Meth. **205**, 443 (1983).

[32] A. Suzuki *et al.*, Nucl. Inst. and Meth. A **329**, 299 (1993).

[33] R. Claus *et al.*, Nucl. Inst. and Meth. A **261**, 540 (1987).

[34] S. Fukuda *et al.*, Nucl. Inst. Meth. Phys. Res. Sect. A **501**, 418 (2003).

[35] Y. Takeuchi *et al.*, Phys. Lett. **452**, 418 (1999).

[36] H. Ikeda *et al.*, Nucl. Inst. and Meth. A **320**, 310 (1992).

[37] T. Tanimori *et al.*, IEEE Trans. Nucl. Sci. **NS-36**, 497 (1989).

[38] J. George, Ph.D. Thesis, University of Washington (1998).

[39] G.Battistoni *et al.*, Astropart.Phys. **19** 269 (2003) [Erratum-ibid. **19** 291 (2003)]. (http://www.mi.infn.it/ battist/neutrino.html)

[40] G. Barr *et al.*, Phys. Rev. D **70**, 0423006 (2004).

[41] L.V. Volkova, Sov. J. Nucl. Phys. **31**, 784 (1980).

[42] T. Sanuki *et al.*, Astrophys. J. **545** 1135 (2000).

[43] J.Alcarez *et al.*, Phys. Lett. B **490** 27 (2000).

[44] W.R. Webber, R.L. Golden and S.A. Stephens, In *Proceedings of the 20th International Cosmic Ray Conference* (1987).

[45] E.S. Seo *et al.*, Astrophys. J. **378** 763 (1991).

[46] P. Pappini *et al.*, In *Proceedings of the 23rd International Cosmic Ray Conference* (1993).

[47] M. Boezio *et al.*, Astrophys. J. **518** 457 (1999).

[48] W. Menn *et al.*, Astrophys. J. **533** 281 (2000).

[49] M.J. Ryan, J.F. Ormes and V.K. Balasubrahmanyan, Phys. Rev. Lett. **28** 985 (1972).

[50] K. Asakamori *et al.*, Astrophys. J. **502** 985 (1998).

[51] I.P. Ivanenko *et al.*, In *Proceedings of the 23rd International Cosmic Ray Conference* (1993).

[52] Y. Kawamura *et al.*, Phys. Rev. D **40** 729 (1989).

[53] A.V. Apanasenko *et al.*, Astropart. Phys. **16** 13 (2001).

[54] http://modelweb.gsfc.nasa.gov/atmos/usstandard.html.

[55] See http://www.ngdc.noaa.gov/IAGA/vmod/igrf.html.

[56] K. Hänssget and J. Ranft, Comput. Phys. **39** 37 (1986).

[57] S. Roesler, R. Engel, and J. Ranft, Phys. Rev. D **57** 2889 (1998).

[58] M.Motoki *et al.*, Astropart.Phys. **19** 113 (2003).

[59] P. Achard *et al.*(L3 Collaboration), Phys. Lett. B **598**, 15 (2004).

[60] M. Honda *et al.*, Phys. Rev. D **75**, 043005 (2007).

[61] S. Haino *et al.*(BESS Collaboration), Phys. Lett. B **594**, 35 (2004).

[62] T. Sanuki *et al.*, Phys. Lett. B **541**, 234 (2002).

[63] O. C. Allkofer *et al.*, Nucl. Phys. B **259**, 1 (1985).

[64] S. Matsuno *et al.*, Phys. Rev. D **29**, 1 (1984).

[65] G. Battistoni *et al.*, Astopart. Phys. **12**, 315 (2000).

[66] Y. Hayato, Nucl. Phys. Proc. Suppl. **112**, 171 (2002).

[67] G. Mitsuka, AIP Conf. Proc. **967**:208-211 (2007), AIP Conf. Proc. **981**:262-264 (2008).

[68] C. H. Llewellyn Smith, Phys. Rep. **3**, 261 (1972).

[69] R. Gran, E. J. Jeon *et al.*, Phys. Rev. D **74**, 052002 (2006).

[70] A.A. Aguilar-Arevalo *et al.*, Phys. Rev. Lett. **100**, 032301 (2008).

[71] F. Sanchez, Talk at Fifth International Workshop on Neutrino-Nucleus Interactions in the Few-GeV Region(NuInt07), http://conferences.fnal.gov/nuint07/

[72] J. Reich *et al.*, Nucl. Instrum. Method A **440**, 535 (2000). H. Abele *et al.*, Nucl. Instrum. Method A **440**, 499 (2000).

[73] D.E. Groom *et al.*, Eur. Phys. J. C **5**, 1 (2000).

[74] P.E. Bosted *et al.*, Phys. Rev. C **51**, 409 (1995).

[75] E.J. Barish *et al.*, Phys. Rev. C **65**, 051001 (2002).

[76] A. Bodek *et al.*, hep-ex/0708.1827

[77] V. Bernard *et al.*, J. Phys. G: Nucl. Part. Phys. **28**, R1-R5 (2002).

[78] R. A. Smith and E. J. Moniz, Nucl. Phys. B **43**, 605 (1972). [Erratum-ibid. B **101**, 547 (1975).]

[79] O. Benhar *et al.*, Phys. Rev. D **72**, 053005 (2005).

[80] J. Nieves *et al.*, Phys. Rev. C **70**, 055503 (2004).

[81] H. Nakamura *et al.*, Nucl. Phys. B (Proc. Suppl.) **112**, 197 (2002).

[82] C.H. Albright *et al.*, Phys. Rev. D **14**, 1780 (1976).

[83] K. Abe *et al.*, Phys. Rev. Lett. **56**, 1107 (1986).

[84] S. Barish *et al.*, Phys. Rev. D **16**, 3103 (1977).

[85] S. Bonetti *et al.*, Nouvo Cimento **38**, 260 (1977).

[86] M. Pohl *et al.*, Nuovo Cimento **26**, 332 (1979);
N. Arimenise *et al.*, Nucl. Phys. B **152**, 365 (1979).

[87] A.S. Vovenko *et al.*, Yad. Fiz. **30**, 1014 (1979).

[88] S. Belikov *et al.*, Z. Phys. **320**, 625 (1985).

[89] J.Brunner *et al.*, Z. Phys. C **45**, 551 (1990).

[90] D. Rein and L.M. Sehgal, Ann. of Phys. **133**, 1780 (1981).

[91] R. Feynman *et al.*, Phys. Rev. D **3**, 2706 (1971).

[92] K.S. Kuzmin, V.V. Lyubushkin and V.A. Naumov, Mod. Phys. Lett. A **19**, 2815 (2005).

[93] C. Berger and L.M. Sehgal, Phys. Rev. D **76**, 113004 (2007).

[94] D. Rein, Z. Phys. C **35**, 43 (1987).

[95] T. Kitagaki *et al.*, Phys. Rev. D **34**, 2554 (1986).

[96] S.K. Singh, M.J. Vicente-Vacas and E.Oset, Phys. Lett. B **416**, 23 (1998).

[97] H. Faissne *et al.*, Phys. Lett. B **125**, 230 (1983).

[98] W. Krenz *et al.*, Nucl. Phys. B **135**, 45 (1978).

[99] C.H. Albright and C. Jarlskog, Nucl. Phys. B **84**, 467 (1975).

[100] M. Glück, E. Reya and A. Vogt, Eur. Phys. J. C **5**,461 (1998).

[101] A. Bodek and U.K. Yang, hep-ex/0308007

[102] P. Musset and J.P. Vialle, Phys. Rep. C **39**, 1 (1978).

[103] J.E. Kim *et al.*, Rev. Mod. Phys. **53**, 211 (1981).

[104] S.J. Barish *et al.*, Phys. Rev. **D17**, 1 (1978).

[105] S. Barlag *et al.*, Z. Phys. C **11**, 283 (1982).

[106] T. Sjöstrand *et al.*, CERN-TH-7112-93 (1994).

[107] D. Rein and L.M. Sehgal, Nucl. Phys. B **233**, 29 (1983).

[108] M. Hasegawa *et al.*, Phys. Rev. Lett. **95**, 252301 (2005).

[109] D. Rein and L.M. Sehgal, Phys. Lett. B. **657**, 207 (2007).

[110] A. Kartavtsev, E. A. Paschos, and G. J. Gounaris, Phys. Rev. D **74**, 054007 (2006).

[111] L. Alvarez-Ruso *et al.*, Phys. Rev. C **75**, 055501 (2007).

[112] K. Hiraide *et al.*, Phys. Rev. D **78**, 112004 (2008).

[113] J. L. Raaf, Ph.D. thesis, University of Cincinnati (2005).

[114] H. Faissner *et al.*, Phys. Lett. B **125**, 230 (1983).

[115] E. Isiksal, D. Rein, and J. G. Morfin, Phys. Rev. Lett. **52**, 1096 (1984).

[116] R. Woods and D. Saxon, Phys. Rev. **95**, 577 (1954).

[117] Jager and Vries, Atomic Data and Nuclear Data Tables **14**, 5 (1974).

[118] L. Salcedo *et al.*, Nucl. Phys. A **484**, 557 (1988).

[119] G. Rowe *et al.*, Phys. Rev. C **18**, 584 (1978).

[120] D. Ashery *et al.*, Phys. Rev. C **23**, 2173 (1981).

[121] C. Ingram *et al.*, Phys. Rev. C **27**, 1578 (1983).

[122] B. R. Martin and M. K. Pidcock, Nuc. Phys. B **126**, 266 (1977).

[123] B. R. Martin and M. K. Pidcock, Nuc. Phys. B **126**, 285 (1977).

[124] J. S. Hyslop *et al.*, Phys. Rev. D **46**, 961 (1992).

[125] D. A. Sparrow, Proc. of the Conf. on the intersection between partivle and nuclear physics, 1019 (1984).

[126] H. W. Bertini *et al.*, Phys. Rev. C **6**, 631 (1972).

[127] S. J. Lindenbaum *et al.*, Phys. Rev. **105**, 1874 (1957).

[128] V. Ammosov, Talk at NuInt01 workshop at KEK, Tsukuba, Japan (2001).

[129] GEANT, CERN Program Library Long Writeup W5013 (1994).

[130] C. Zeitnitz and T.A. Gabriel, Nucl. Inst. and Meth. A **349**, 106 (1994).

[131] M. Nakahata *et al.*, J. Phys. Soc. Jpn. **55**, 3786 (1986).

[132] E. Bracci *et al.*, CERN/HERA 72-1 (1972).

[133] A.S. Carrol *et al.*, Phys. Rev. C **14**, 635 (1976).

[134] A. Morel *et al.*, Luminology and Oceanography 22, **709**, (1977).

[135] D. Groom *et al.*, Atomic Data and Nuclear Data Tables **78**, 044 (201).

[136] P. Lipari and T. Stanev, Phys. Rev. D **44**, 3543 (1991).

[137] T. Shiabata, Master Thesis, Niigata University (2002).

[138] R. P. MacDonald *et al.*, Phys. Rev. D **78**, 032010 (2008).

[139] P. Hanggi *et al.*, Phys. Lett. B **51**, 119 (1974).

[140] M. Yamada *et al.*, Phys. Rev. D **44**, 617 (1991).

[141] Hirokazu Ishino, PhD Thesis, University of Tokyo, (1999).

[142] S.Baker and R.D. Cousins, Nucl. Inst. and Meth. **221**, 437 (1984).

[143] G.L. Fogli *et al.*, Phys. Rev. D **66**, 053010 (2002).

[144] G. Ambrosini *et al.*, Phys. Lett. B **420**, 225 (1998).

[145] D. Casper, Nucl. Phys. Proc. Suppl. **112**, 161 (2002).

[146] M. G. Ollsen and G. B. Yodh, Phys. Rev. **145**, 1309 (1966).

[147] M. C. Gonzalez-Garcia and M. Maltoni Phys. Rev. D **70**, 033010 (2004).

[148] D. N. Krasnoshchekov *et al.*, Nature **435**, 483-487 (2005).

[149] X. Song and D. V. Helmberger, J. Geophys. Res. **100**(B7), 9817, (1995).

[150] M. Apollonio *et al.*, Phys. Lett. B **466**, 415 (1999).

[151] J. Hosaka *et al.*, Phys. Rev. D **73**, 112001 (2006).

[152] B. Aharmim *et al.*, Phys. Rev. D **72**, 052010 (2005).

[153] S. Abe *et al.*, Phys. Rev. Lett. **100**, 221803, (2008).

[154] S. Abe *et al.*, hep-ex 0801.4589, (2008).

[155] G. P. Zeller *et al.*, Phys. Rev. Lett, **88**, 091802, (2002).

[156] J. Dorenbosh *et al.*, Phys. Lett. B **180**, 303 (1986).

[157] A. E. Hedin, J. Geophys. Res. **96**, 1159 (1991),

[158] E. Hernandez *et al.*, Phys. Rev. D **76**, 033005 (2007).

[159] A. Capella *et al.*, Phys. Lett. B **337**, 358 (1994). M.H.Reno, Phys. Rev. D **74**, 033001 (2006).

[160] K. Hagiwara *et al.*, Nucl. Phys. B **668**, 364 (2003).

[161] Particle Data Group, C. Caso *et al.*, Eur. Phys. C **3**, 1 (1998).

[162] S. Desai, Ph.D. Thesis, Boston University.

[163] E. R. Davies, *Machine Vision: Theory, Algorithms, Practicalities*, Academic Press, San Diego (1997).

[164] S. Desai *et al.*, Astopart. Phys. **29**, 42 (2008).

Appendix A

Systematic Uncertainties

A.0.1 Atmospheric Neutrino Flux

- Anti-neutrino/neutrino ratio
  The systematic uncertainty of the relativity between neutrino flux and anti-neutrino flux comes from π^+/π^- and K^+/K^- ratio in hadronic interaction of the flux calculation. The uncertainties of $\bar{\nu}_e/\nu_e$, shown in the left panel on Figure A.1, are estimated to be 5% below 1 GeV and 5% from 1 GeV to 10 GeV. The uncertainties of $\bar{\nu}_\mu/\nu_\mu$ are estimated to be 2% below 1 GeV and 6% from 1 GeV to 10 GeV as shown in the right panel on Figure A.1. The variations of both ratios are within 10% below 100 GeV, while it increases almost linearly above 100 GeV. This can be explained as that π's are the major source of atmospheric neutrino below 100 GeV, however the contribution of K's grows up above 100 GeV, where the different K production model is employed in each flux model. The anti-neutrino/neutrino ratio uncertainty is divided into three terms: E_ν <1 GeV, 1 GeV< E_ν <10 GeV, and E_ν >10 GeV.

- Up/down ratio
  As described in Section 3.2, the neutrino flux below a few GeV has up/down asymmetry due to the rigidity cutoff by the geomagnetic field, while it becomes up/down symmetric above a few GeV. The systematic uncertainty of up/down ratio is caused by the treatment of the geomagnetic field in the flux calculation. However, the uncertainty does not directly affect the zenith angle distributions, because the up/down asymmetry in low energy is largely washed out due to the poor angular correlation in neutrino interactions. The systematic uncertainties of up/down ratio are estimated by the comparison of the zenith angle distributions using flux calculations.

- Horizontal/vertical ratio
  The systematic uncertainty of horizontal/vertical ratio is caused by the difference in the 3-dimensional calculation method in each flux model below 3 GeV of neutrino energy, while, above 3 GeV, it arise due to the predicted K/π ratio in hadronic interactions in the atmosphere. The magnitude of the uncertainty in the horizontal/vertical ratio is a function of energy, however is assumed to be fully correlated.

- Neutrino flight length
  An uncertainty of the altitude where atmospheric neutrinos are produced affects the neu-
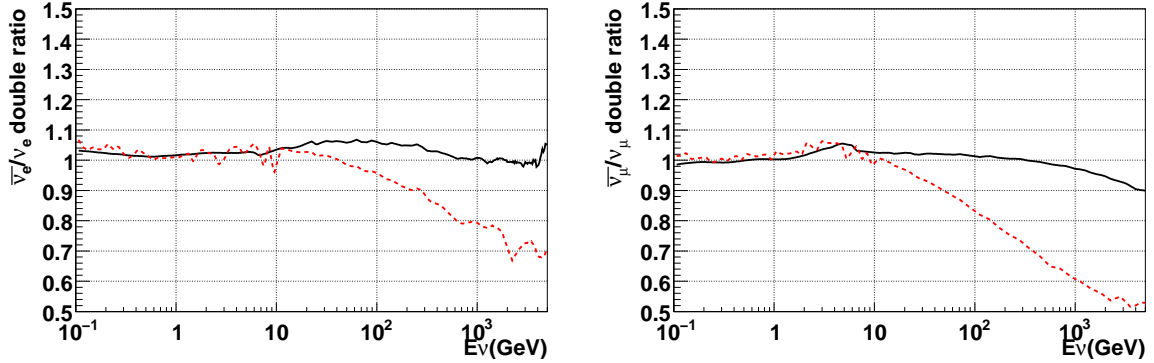
Figure A.1: Anti-neutrino/neutrino double ratio for $\overline{\nu}_e/\nu_e$ (left panel) and $\overline{\nu}_\mu/\nu_\mu$ (right panel). Double ratio is defined as $(\overline{\nu}/\nu)_{\text{Fluka or Bartol}}/(\overline{\nu}/\nu)_{\text{Honda}}$. Solid(dashed) line indicates the double ratio with the Fluka(Bartol) flux.

trino oscillation probabilities. The uncertainty of the production altitude, distance from the surface of the Earth to the production point, is negligible for upward-going neutrinos passing through the Earth because the production altitude is much shorter than the neutrino propagation length in the matter of Earth. However, for downward-going and horizontally-going neutrinos, the uncertainty of the production altitude has sizable effect to the calculation the oscillation probability. The systematic uncertainty is estimated by the flux calculations which are carried out with the 10% enhanced and reduced density structure of atmosphere, as shown in Figure A.2. The uncertainty of air density profile 10% is given by the comparison between US-standard'76 and MSISE90 [157]. The variation of neutrino flux due to the increased or decreased density is considered as the systematic uncertainty.

- Solar activity
  The primary cosmic ray flux is affected by the solar activity changing in 11 year period and the atmospheric neutrino flux calculations consider the solar activity. ± 1 year of uncertainty is assigned to the modulation of solar activity.

A.0.2 Neutrino Interactions

- Axial vector mass(M_A) in quasi-elastic scattering and single meson production
  Quasi-elastic scattering and single meson production have a dependence on the axial vector mass M_A which is set to be 1.21GeV/c as described in Section 3.3. M_A is included with the style of $-1.23(1 - Q^2/M_A^2)^{-1/2}$, therefore the uncertainty should be considered as a function of Q^2. Figure A.3 shows the ratio of Q^2 spectrum with $M_A = 1.11$GeV/c to that with $M_A = 1.21$GeV/c. Fitted curve of this ratio is considered as the systematic uncertainty of M_A.

- Quasi-elastic scattering for bound nucleon (Total cross section)
  The CCQE cross section for bound nucleon is simulated based on the Smith and Monitz model. The systematic uncertainty of the CCQE cross section is estimated by the comparison between the Smith and Monitz model and the Nieves model [80], and is set to

165
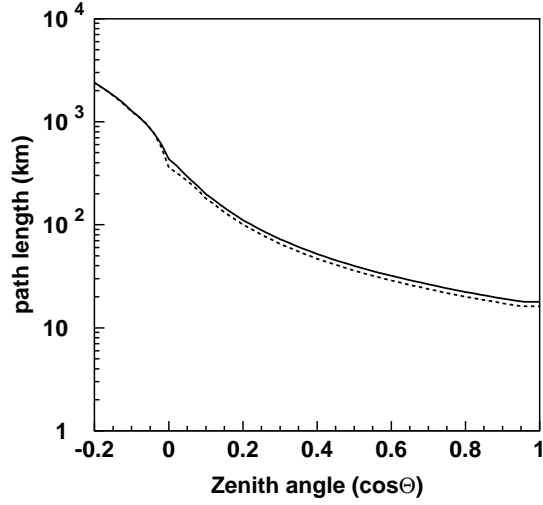
Figure A.2: Neutrino flight length as a function of zenith angle. Solid curve shows the flight length used in our analysis and dashed curve shows that for the compressed density structure of atmosphere by 10%.
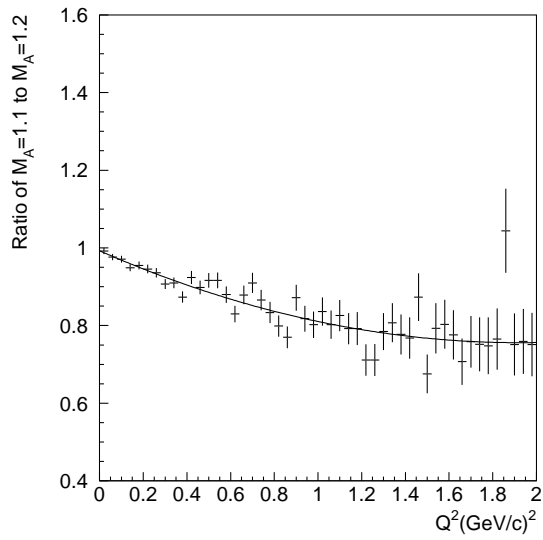

Figure A.3: The ratio of Q^2 spectrum with $M_A = 1.11\mathrm{GeV/c}$ to that of with $M_A = 1.21\mathrm{GeV/c}$. Dot and error bar show the expectation of Monte Carlo events and the fitted curve is considered as the systematic uncertainty.
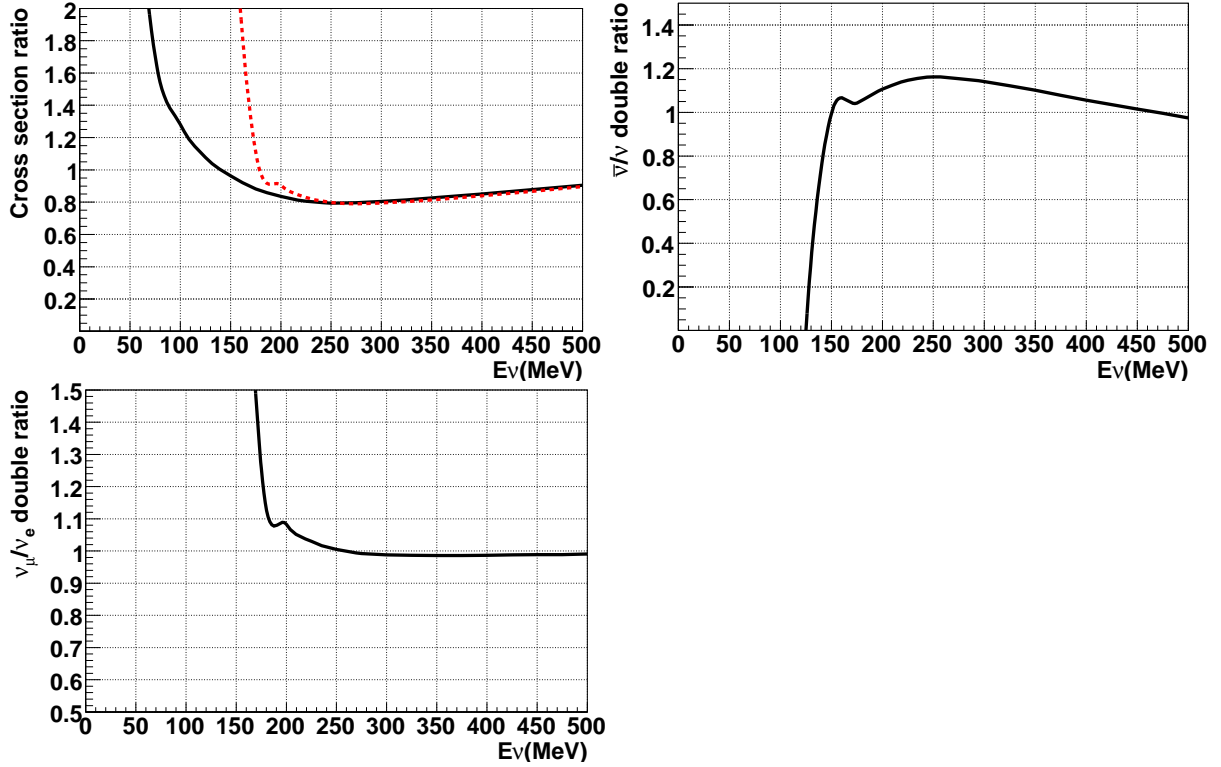
Figure A.4: Top left: The ratio of the CCQE cross section, the Nieves model normalized by the Smith and Monitz model, for $\nu_e + \overline{\nu}_e$ (solid curve) and for $\nu_\mu + \overline{\nu}_\mu$ (dahsed curve). Top right: $(\overline{\nu}_e + \overline{\nu}_\mu)/(\nu_e + \nu_\mu)$ ratio. Bottom: $(\nu_\mu + \overline{\nu}_\mu)/(\nu_e + \overline{\nu}_e)$ ratio.

be 1σ. In the Nieves model the motion of target nucleon in nucleus, so called nuclear effects, is considered using highly sophisticated way. Top left panel of Figure A.4 shows the calculated CCQE cross section of the Nieves model normalized by Smith and Monitz model.

- Quasi-elastic scattering for bound nucleon ($\overline{\nu}/\nu$ ratio)
  The uncertainty of $\overline{\nu}/\nu$ ratio in CCQE cross section is estimeted using the same approach as that for CCQE total cross section. The top right panel of Figure A.4 shows the calculated CCQE cross section of $\overline{\nu}/\nu$ ratio of the Nieves model normalized by the Smith and Monitz model.

- Quasi-elastic scattering for bound nucleon (ν_μ/ν_e)
  The uncertainty of ν_μ/ν_e ratio in CCQE cross section is estimeted by the comparison using two models. The ratio of Nieves model to the Smith and Monitz model is shown in the bottom of Figure A.4.

- Single meson production (Total cross section)
  Estimation of systematic uncertainties related to the single meson production is carried out by using single π production because of the statistics. It means that the uncertainties estimated using single π production are also applied to the other single meson productions, η or K. The uncertainty of the single meson production cross section is estimated to
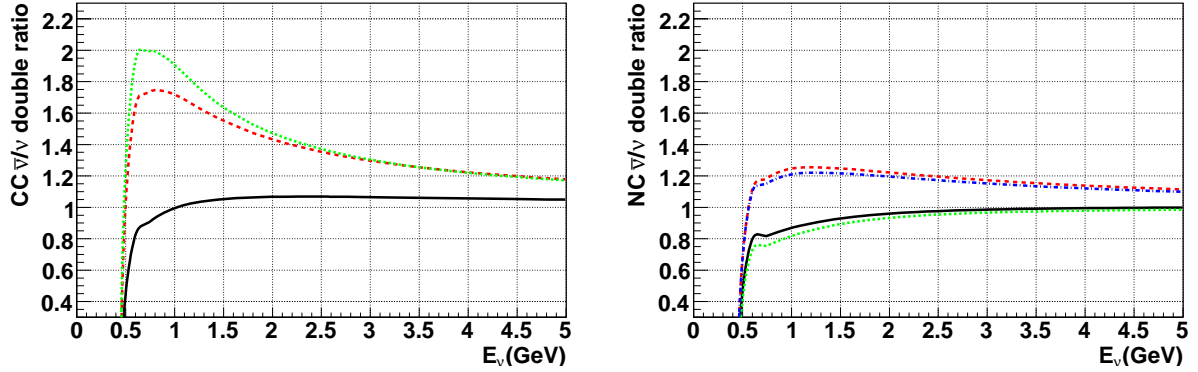
Figure A.5: The $\overline{\nu}/\nu$ ratio of the Hernandez model normalized by the Smith and Monitz model. Left panel shows charged current interactions and right panel shows neutral current interactions. For the detail, see the text.

be 20 % according to the agreement between Monte Carlo simulation and experimental results of the $\nu_\mu p \to \mu^- p\pi^+$ reaction, which is the dominant mode among the single meson productions and various exmerimental results are available. The π^0 emitting interaction has an additional uncertainly caused by the poor understanding of the π^0 interaction compared to that with charged π.

- Single meson production ($\overline{\nu}/\nu$ ratio)
  The uncertainty of $\overline{\nu}/\nu$ in single meson production cross section is estimeted by the comparison of the Rein and Sehgal model, used as default in our simulation, and the Hernandez model [158] which includes the recent progresses in the theoretical studies. Figure A.5 shows the $\overline{\nu}/\nu$ ratio of the Hernandez model normalized by the Rein and Sehgal model. Left panel shows CC interactions: $\nu_\mu p \to \mu^- p\pi^+$ (solid curve), $\nu_\mu n \to \mu^- p\pi^0$ (dashed curve), and $\nu_\mu n \to \mu^- n\pi^+$ (dotted curve). Right panel shows NC interactions: $\nu_\mu p \to \nu_\mu p\pi^0$ (solid curve), $\nu_\mu p \to \nu_\mu n\pi^+$ (dashed curve), $\nu_\mu n \to \nu_\mu n\pi^0$ (dotted curve), and $\nu_\mu n \to \nu_\mu p\pi^-$ (dash-dot curve). Energy dependent difference between two models are adopted to the systematic uncertainties.

- Single meson production ($\pi^0/\pi^\pm$)
  Understanding of the interaction emitting π^0 is relatively poorer than that with charged π due to the small statistics of the experimental results as seen in Figure 3.10, so the predicted cross section has large variation among theoretical models. To estimate the uncertainty of the single π^0 production, the Rein and Sehgal model is compared with the Hernandez model. The Figure A.6 shows the ratio of the CC single pion ν_μ cross section of the Hernandez model normalized by the Rein and Sehgal model, $\nu_\mu p \to \mu^- p\pi^+$ (solid curve), $\nu_\mu n \to \mu^- p\pi^0$ (dashed curve), and $\nu_\mu n \to \mu^- n\pi^+$ (dotted curve). According to the comparison, 40% should be reasonably adopted to the uncertainty of π^0 emitting interactions relative to the $\pi^\pm$ emitting interactions.

- Deep inelastic scattering (Model dependence in lower energy region)
  For neutrino energy above 50 GeV, the calculation for deep inelastic scattering agree with the experimental measurement within 5 %. However, in the lower energy region the

168
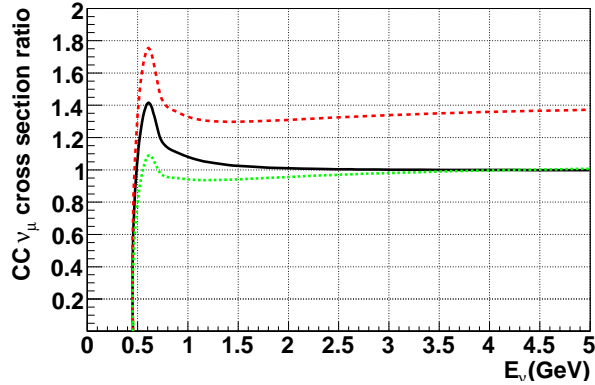
Figure A.6: The ratio of the predicted cross section by the Hernandez model to that of the Rein and Sehgal model for CC ν_μ interactions. For the detail, see the text.

uncertainty gets larger. Estimation of the systematic uncertainty is carried out by taking the difference between our default model and CKMT parametrization [159]. The difference in these two models depends on Q^2 and is quite large in a few GeV energy region. The difference of the these two models is assumed to be 1σ.

- Deep inelastic scattering (Total cross section)
  The uncertainty in the deep inelastic scattering cross section at high energy ($\geq$ a few tens of GeV) is estimated to be 5 % according to the agreement between measurements and expectation.

- Coherent pion production
  The systematic uncertainty of coherent pion production is estimated based on the comparison of the Rein and Sehgal model and experimental results. As for NC interaction, several experimental results are available, and the difference between our simulation and the experimental results is within about 50%. Thus the uncertainty for NC intearction is estimated to be 50%, and it is also applied to CC ν_e interaction because lepton mass, here electron mass, is negligible in a few GeV region. However, it can not be capable to the CC ν_μ interaction due to no evidence for the existing of this mode derived from the K2K result, so 100% uncertainty is considered for CC ν_μ interaction.

- NC/CC ratio
  The systematic uncertainty in the NC/CC ratio is estimated to be 20 %, which is caused by the poor understanding of NC interactions.

- Nuclear effects in ^{16}O nucleus
  Nuclear effects in ^{16}O nucleus affects the angular correlation between incident neutrino and emitted mesons. Our predicted cross section and experimental results are shown in Figure 3.15. The systematic uncertainty of nuclear effects in ^{16}O nucleus, the mean free path of hadrons produced via neutrino interactions, is estimated to be 30 % according to the agreement between experimental results and our prediction.

- Charged current ν_τ interaction

169

The systematic uncertainty in the ν_τ cross sections for CC interactions is estimated to be 30 % by comparing two models of NEUT and Hagiwara *et al.* [160].

A.0.3 Event Selections

- FC and PC reduction
  Details of FC and PC reduction are described in Chapter 5.1 and Appendix C. The uncertainty of the FC and PC reduction efficiencies are estimated by the comparison of the distributions between data and Monte Carlo events as changing the cut variables. The uncertainty is estimated to be 0.2 % (0.2 %) and 2.4 % (4.8 %) for FC and PC reduction of SK-I (SK-II), respectively.

- Non-neutrino background
  The possible sources of background in FC μ-like and PC samples are cosmic ray muons, while in FC e-like samples, flasher PMTs and neutron from the rock are majour sources. The estimated contamination of the background is summarized in Table 8.4 and 8.5.

- UPMU reduction
  The methods of the reduction for UPMU events are described in Appendix C.3. The systematic uncertainty is estimated by the comparison of cut variables between data and Monte Carlo events. The estimated uncertainties are 1.8 % (2.1 %) for UPMU stopping and 0.3 % (0.3 %) for UPMU through for SK-I (SK-II). Uncertainties for UPMU stopping and UPMU through are assumed to be correlated.

- UPMU stopping/through separation
  The UPMU events are separated by the number of hit OD PMTs within 8 m from the exit position, we call it NHITEX. The systematic uncertainty for the stopping/through separation is estimated to be 0.4 % and 0.4 % for SK-I and SK-II, respectively.

A.0.4 Event Reconstructions

- Ring counting
  The ring counting process is described in Appendix D.2. The systematic uncertainty of Single-ring and Multi-ring separation is derived by several uncertainties such as water transparency and detector calibration. The uncertainties are estimated by the comparison of ring counting likelihood distributions between data and Monte Carlo events.

- Energy calibration
  The absolute energy scale is calibrated with several calibration sources as described in Section 4.5 and the systematic uncertainty is estimated to be 1.1 % for SK-I and 1.7 % for SK-II.

- Up/down symmetry of energy calibration
  The difference in the energy scale for upward-going and downward-going events is measured by using decay electrons from cosmic ray stopping muons (see Figure 4.20). The up/down asymmetry of the energy scale is estimated to be 0.6 % both for SK-I and SK-II.

Appendix B

Atmospheric Neutrino Analysis

B.1   2-Flavor $\nu_\mu \leftrightarrow \nu_\tau$ Oscillation Analysis

$\nu_\mu \leftrightarrow \nu_\tau$ oscillation analysis is performed SK-I and SK-II FC+PC+UPMU combined data set. As the result of the global scan on the oscillation parameter grid, the minimum χ^2 value, $\chi^2_{min} = 832.8/748$ d.o.f., is obtained at $(\sin^2 2\theta, \Delta m^2) = (1.02, 2.1 \times 10^{-3}\,\mathrm{eV^2})$, where θ is the mixing angle and $\Delta m^2 = m_3^2 - m_2^2$ is the difference of the squared mass of ν_3 and ν_2. When only the grid in physical region is considerd, $\chi^2_{min} = 834.3/748$ d.o.f. is obtained at $(\sin^2 2\theta, \Delta m^2) = (1.00, 2.1 \times 10^{-3}\,\mathrm{eV^2}$. Assuming no oscillation, χ^2 value takes 1395.6 for 747 d.o.f.. The hypothesis of no oscillation is strongly rejected.

Figure B.1 shows the contour plots of the allowed regions of the neutrino oscillation parameters $(\sin^2 2\theta, \Delta m^2)$. Three contours correspond to the 68%, 90% and 99% confidence levels (C.L.) allowed regions which are defined to be $\chi^2 = \chi^2_{min} +3.34$, 5.75, and 10.41 based on the minimum in the physical region, respectively. These intervals are derived by using the 2-dimensional Gaussian approximation from the minimum in the unphysical region [161]. The 90 % allowed parameter region is :

$$1.7 \times 10^{-3}\,\mathrm{eV^2} \quad < \quad \Delta m^2 < 2.7 \times 10^{-3}\,\mathrm{eV^2} \tag{B.1}$$

$$0.95 \quad < \quad \sin^2 2\theta \tag{B.2}$$

Figure B.2 shows the $\chi^2 - \chi^2_{min}$ distributions as a function of $\sin^2 2\theta$ and Δm^2, which are sliced at $\Delta m^2 = 2.1 \times 10^{-3}\,\mathrm{eV^2}$ and $\sin^2 2\theta = 1.00$.

Zenith angle and momentum distributions are shown in Figures from 6.8 to 6.12 in Chapter 6. The data (dots and errors) are compared with the Monte Carlo expectation without oscillations (dashed lines) and the best-fit expectation for 2-flavor $\nu_\mu \leftrightarrow \nu_\tau$ oscillations (solid lines). The 2-flavor $\nu_\mu \leftrightarrow \nu_\tau$ oscillation hypothesis provides a consistent explanation to all data samples.
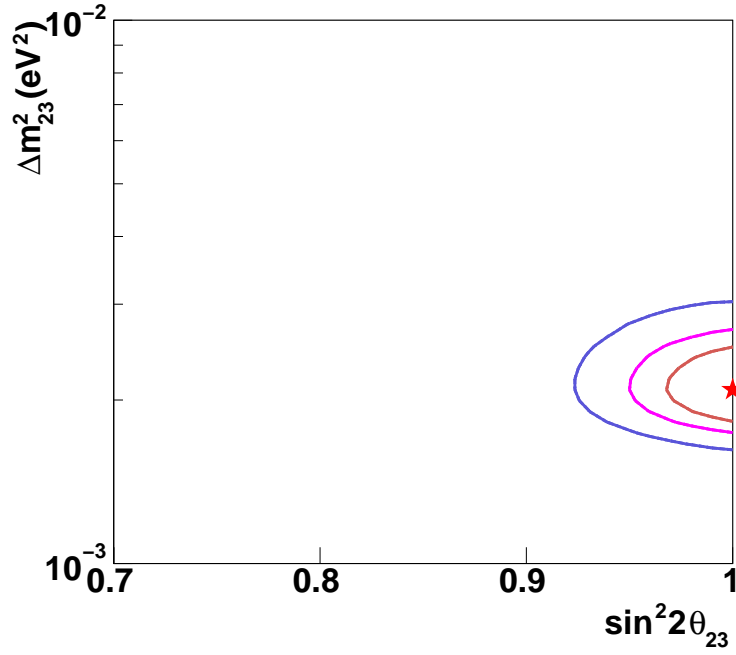
Figure B.1: Allowed oscillation parameters for 2-flavor $\nu_\mu \leftrightarrow \nu_\tau$ oscillations. The horizontal axis shows $\sin^2 2\theta$ and the vertical axis shows Δm^2. Three contours correspond to the 68 %, 90 %, and 99 % C.L. allowed regions, respectively.
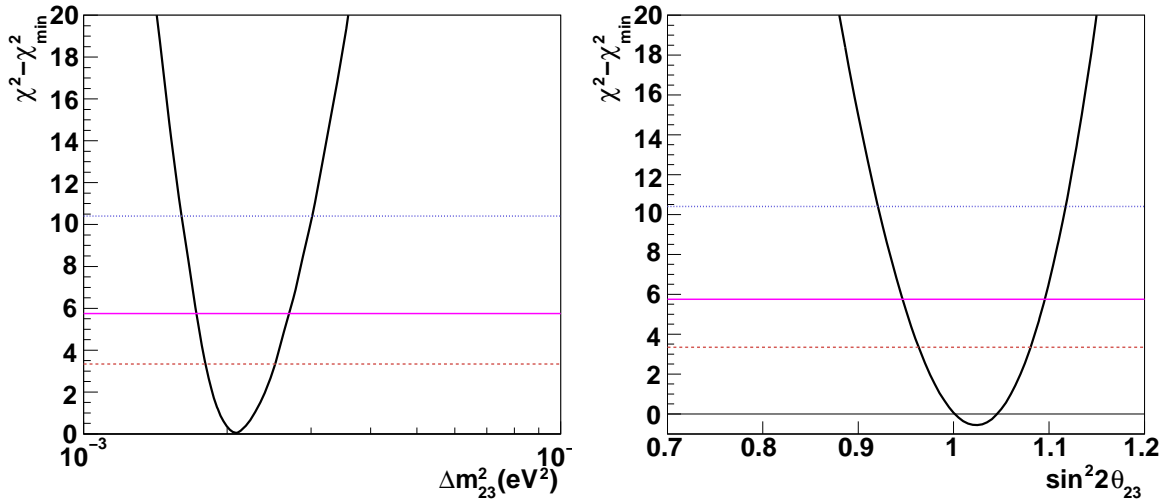

Figure B.2: $\chi^2 - \chi^2_{min}$ distributions as a function of Δm^2 (left) and $\sin^2 2\theta$ (right), in which χ^2_{min} is the minimum value of χ^2 in physical parameter region. $\sin^2 2\theta$ is set to be 1.00 in the left-hand figure and Δ^2_m is set be $2.1 \times 10^{-3} \mathrm{eV}^2$ in the right-hand figure. Three horizontal lines correspond to the 68 % (dotted line), 90 % (solid line) and 99 % (dashed line) C.L. intervals, respectively.

Appendix C

Data Reduction

In this section the procedures of the data reduction for FC, PC and UPMU events are described.

C.1   Reduction for Fully Contained Sample

There are five steps in FC reduction process. The main background sources are cosmic ray muons, low energy events from radio isotopes and electrical noise events.

C.1.1   First Reduction

The selection criteria of the FC 1st reduction are the following :

(1) PE_{300} should be ≥ 200 p.e.s (100 for SK-II).
  PE_{300} is the maximum number of total p.e.s observed by the ID PMTs in a sliding 300 nsec time window.

and

(2) $NHITA_{800}$ should be ≤ 50 or OD trigger is off.
  $NHITA_{800}$ is the number of hit OD PMTs in a fixed 800 nsec time window from -400 nsec to $+400$ nsec before and after the trigger timing.

and

(3)   TDIFF should be $> 100\,\mu$sec
  TDIFF is a time interval to the previous event.

Criterion (1) rejects the low energy background events from radio isotopes. Figure C.1 shows the PE_{300} distributions for the raw data and the FC final events. The 200 p.e.s (100 p.e.s for SK-II) corresponds to 22 MeV/c of electron momentum. Since the events which have visible energy below 30 MeV are not used in the analysis, this cut is safe. Criterion (2) removes the cosmic ray muon events. Figure C.2 shows the $NHITA_{800}$ distributions for the raw data, FC atmospheric neutrino Monte Carlo events and the FC final events. Criterion (3) removes the electron events from the decay of the cosmic ray muons stopped in the ID. The events within 30 μsec after the selected events by the above criteria are selected to keep the decay electrons.

173
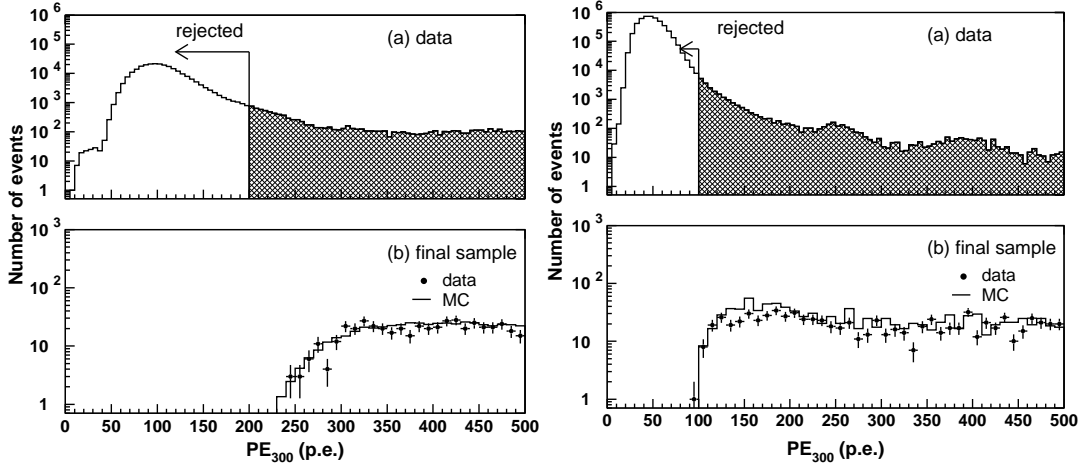
Figure C.1: PE_{300} distribution for (a) the raw data and (b) the final FC data and atmospheric neutrino Monte Carlo events (no oscillation) in FC final samples for SK-I (left) and SK-II (right). The number of the Monte Carlo events in (b) is normalized to that of the data. The selection criterion is shown by arrows.

These events are attached to the fully contained event candidates as sub-events and not counted as a primary atmospheric neutrino event. These cuts reduce the data size from 10^6 events/day to 3000 (2200) events/day for SK-I (SK-II).

C.1.2 Second Reduction

In the second reduction, the low energy events and cosmic ray muons are rejected. The selection criteria of the FC 2nd reduction are the following :

(1) $NHITA_{800}$ should be ≤ 25 if $PE_{tot} < 100,000$ p.e.s (50,000 for SK-II) or OD trigger is off.

and

(2) PE_{max}/PE_{300} should be < 0.5.
        PE_{max} is the maximum number of p.e.s observed by an ID PMT.

Criterion (1) is to reject cosmic ray muons by tighter threshold than the 1st reduction as shown in Figure C.2 by solid lines. The second cut removes the low energy events and electrical noise events, which have one larger hit signal from a single PMT. Figure C.3 shows the PE_{max}/PE_{300} distributions for the data after the 1st reduction, FC atmospheric neutrino Monte Carlo events and the FC final events. A PMT sometimes flashes because of a discharge around the dynode structure. The flashing PMT tends to record a very large charge. The flasher events due to such a noisy PMT are rejected further in the next step. The event rate is 200 (280) events/day for SK-I (SK-II) after the FC 2nd reduction.

174
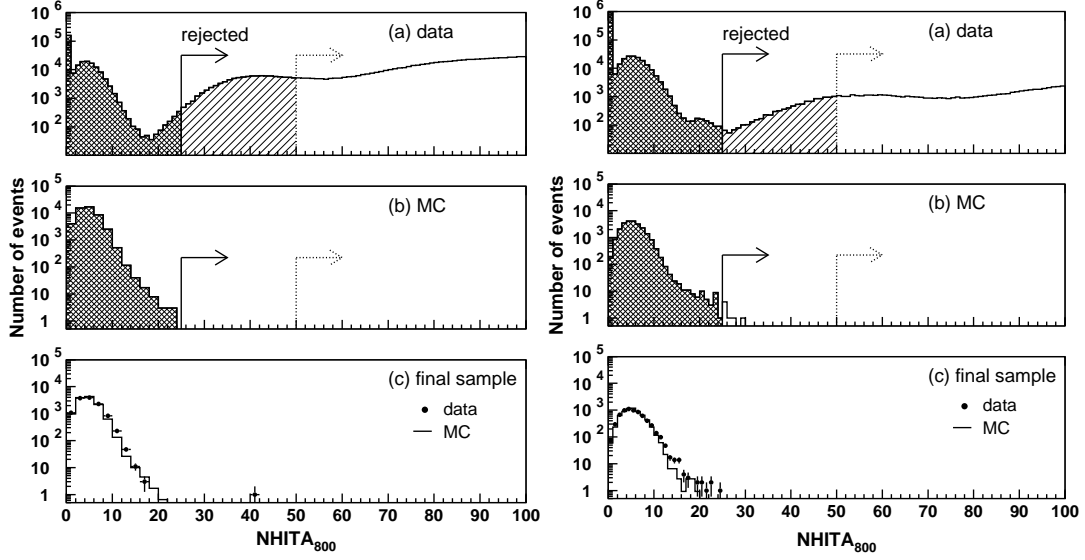
Figure C.2: NHITA$_{800}$ distributions for (a) the raw data, (b) fully contained atmospheric neutrino Monte Carlo events whose vertex position is more than 2 m away from the ID wall and (c) final samples of the data and the Monte Carlo events for SK-I (left) and SK-II (right). The number of the Monte Carlo events in (c) is normalized to that of the data. The arrows written by dotted (solid) lines show the selection criteria in the FC 1st (2nd) reduction.
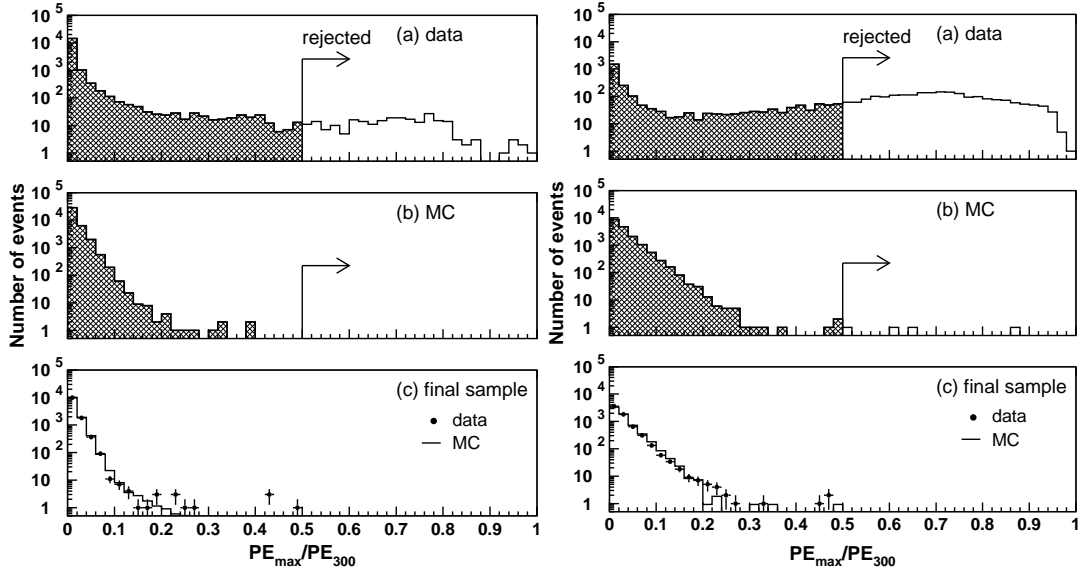

Figure C.3: PE$_{max}$/PE$_{300}$ distribution for (a) the data after the FC 1st reduction, (b) fully contained atmospheric neutrino Monte Carlo events and (c) final samples of the data and the the Monte Carlo events for SK-I (left) and SK-II (right). The number of the Monte Carlo events in (c) is normalized to that of the data. The selection criteria are shown by arrows.

175

C.1.3 Third Reduction

After the 1st and 2nd reduction steps, remaining background events are mostly noise events and cosmic ray muons which have a small number of OD hits.

Through-going muon cut

The through-going muons are very energetic and deposit a lot of charge in the ID. To eliminate these events, a special through-going muon fitter is applied if the number of p.e.s in any single PMT is larger than 230 p.e.s. This fitter selects the entrance point, which is the point of the earliest hit PMT with some neighboring hit PMTs and the exit point, which is defined the center of the saturated ID PMTs. Then, if the goodness of the fit is greater than 0.75, and the number of hit OD PMTs around the reconstruted muon entrance or exit point is more than 9, the events are rejected as through-going muons. In SK-II, the condition to apply a special through-going muon fitter is modified to additionally require that number of hit ID PMTs exceeds 1000. The rejection criteria are summarized :

(1) $PE_{max} > 230$ p.e.s (and NHIT > 1000 for SK-II)

and

(2)   goodness of through-going muon fit > 0.75

and

(3) $NHITA_{in} \geq 10$ or $NHITA_{out} \geq 10$
$NHITA_{in}$ ($NHITA_{out}$) is the number of hit OD PMTs located within 8 m from the entrance (exit) point in a fixed 800 nsec time window.

The goodness of through-going muon fit is defined as :

$$goodness \quad = \quad \frac{1}{\sum_i \dfrac{1}{\sigma_i^2}} \times \sum_i \frac{1}{\sigma_i^2} \exp\left(-\frac{(t_i - T_i)^2}{2(1.5 \times \sigma_i)^2}\right) \tag{C.1}$$

where t_i and σ_i are the observed hit time of the i-th PMT and its resolution, and T_i is the hit time expected from the entering time of muon and its track. Figure C.4 and C.5 show the number of hit OD PMTs near the entrance and the exit points for the data after the 2nd reduction, the FC atmospheric neutrino Monte Carlo events and the FC final events satisfying the above criteria (1) and (2).

Stopping muon cut

To eliminate stopping muons, a stopping muon fitter is applied, which finds the entrance point in the similar way as through-going muon fit. The events satisfying the following criteria are classified as stopping muons and removed :

(1) $NHITA_{in} \geq 10$
or
$NHITA_{in} \geq 5$ if   goodness of stopping muon fit > 0.5
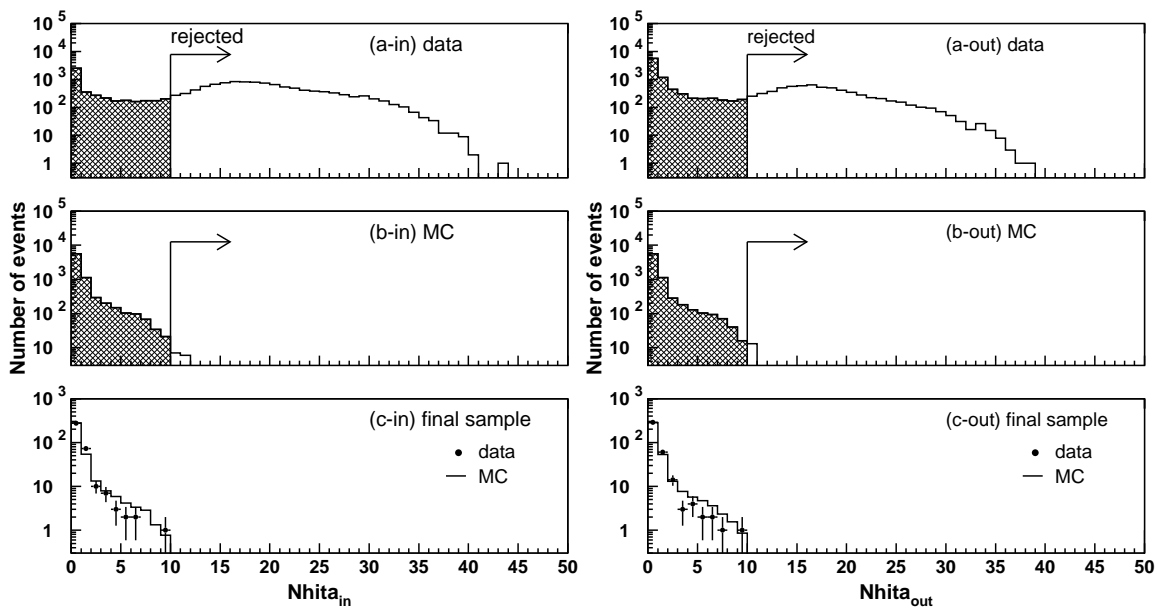
Figure C.4: Number of hit OD PMTs within 8 m of the entrance point (left) of muons and within 8 m of the exit position (right) for (a) the data after FC 2nd reduction, (b) fully contained atmospheric neutrino Monte Carlo events and (c) final samples for SK-I. The number of the Monte Carlo events in (c) is normalized to that of the data. The selection criteria are shown by arrows.
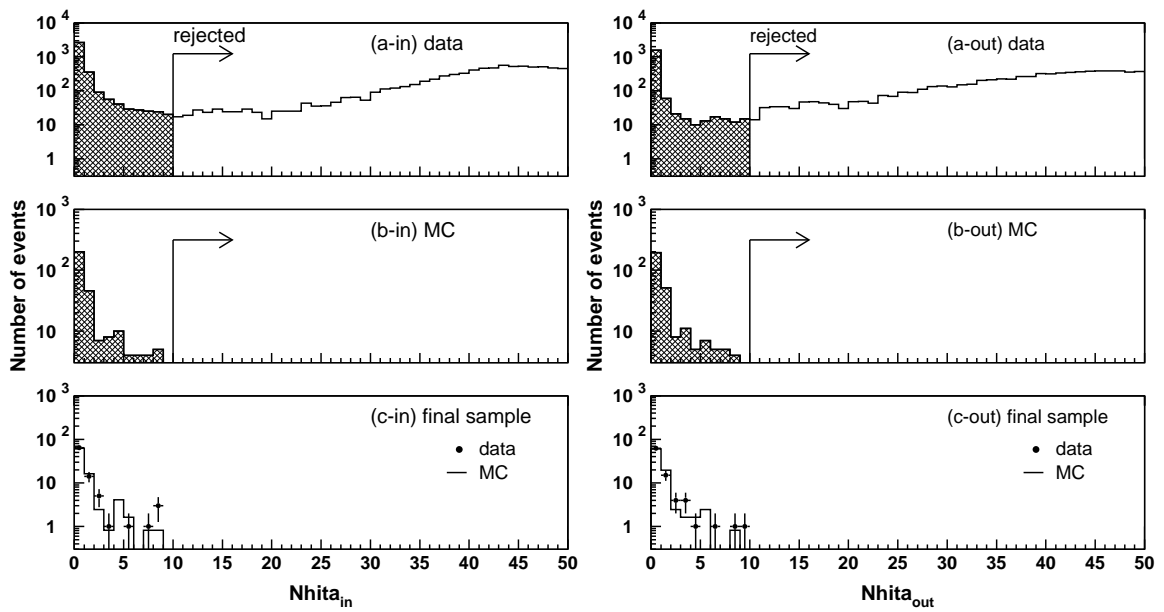
Figure C.5: Number of hit OD PMTs within 8 m of the entrance point (left) of muons and within 8 m of the exit position (right) for (a) the data after FC 2nd reduction, (b) fully contained atmospheric neutrino Monte Carlo events and (c) final samples for SK-II. The number of the Monte Carlo events in (c) is normalized to that of the data. The selection criteria are shown by arrows.

178
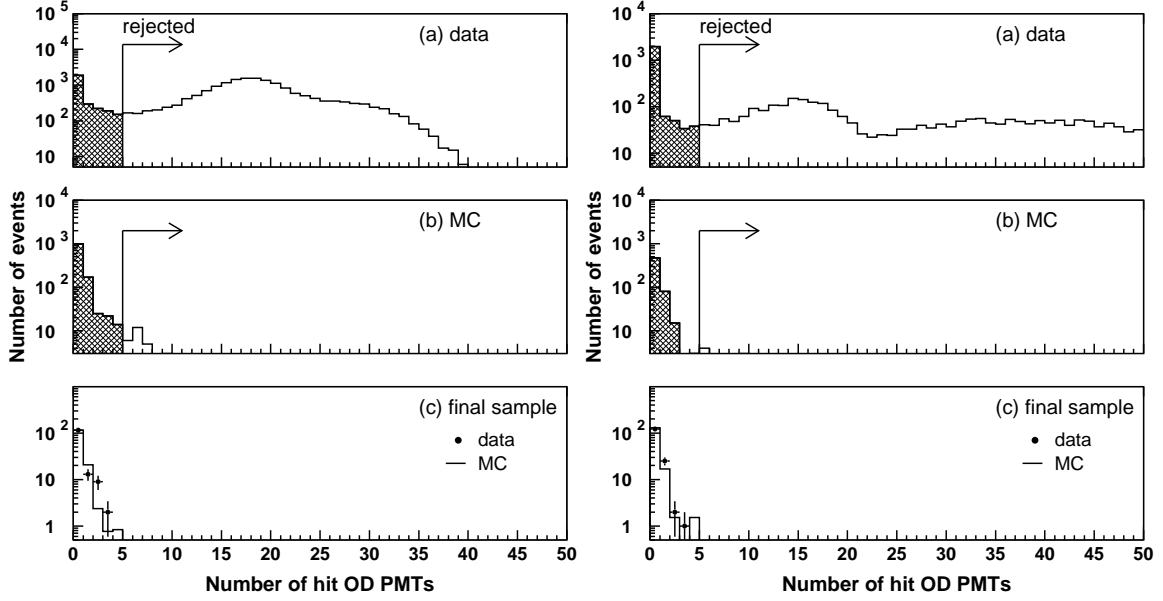
Figure C.6: Number of hit OD PMTs near the entrance point of muons for (a) the data after FC 2nd reduction, (b) fully contained atmospheric neutrino Monte Carlo events and (c) final samples satisfying a condition, goodness > 0.5 for SK-I (left) and SK-II (right). The number of the Monte Carlo events in (c) is normalized to that of the data. The selection criteria are shown by arrows.

$NHITA_{in}$ is the number of hit OD PMTs located within 8 m from the entrance point in a fixed 800 nsec time window.

The direction of muon is reconstructed to maximize the total number of p.e.s inside the cone with a half opening angle 42°. The goodness definition is same as that of through-going muon fit. Figure C.6 shows $NHITA_{in}$ distributions for the data after the 2nd reduction, the FC atmospheric neutrino Monte Carlo events and the FC final events satisfying the condition, goodness > 0.5.

Cable hole muons

On top of the detector tank, there are twelve cable holes to take signal and HV supply cables out. Four holes out of twelve are directly above the ID and block the OD. Cosmic ray muons going through these holes would not leave any OD signal and could be detected as contained neutrino events. To eliminate this mis-identification possibility, a set of veto counters (2 m × 2.5 m plastic scintillation counters) were installed in April, 1997 (see Figure C.7). The rejection criteria for cable hole muons are :

(1)   One veto counter hit

and

(2) $L_{veto} < 4$ m
 L_{veto} is the distance from the cable hole to the the reconstructed vertex.

179
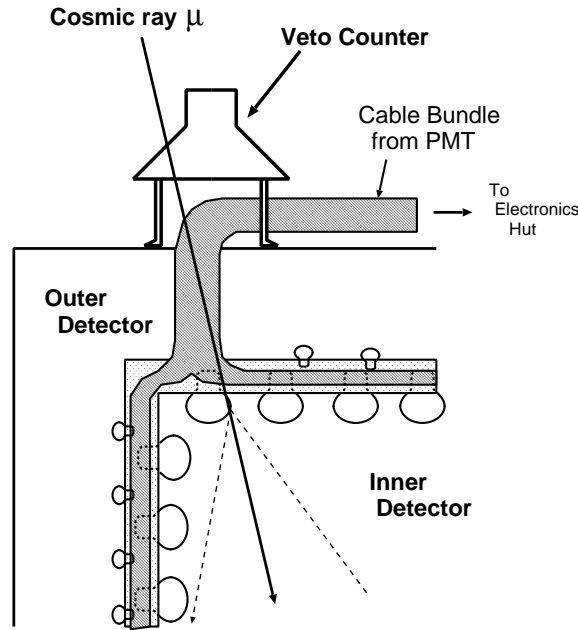
Figure C.7: A schematic view of a cable-hole muon and a veto counter.

Figure C.8 shows the reconstructed vertex distribution for the FC 1-ring μ-like events before and after the installation of veto counters. Cable hole muons are well eliminated by veto counters as shown in this figure.

Flasher event cut

Flasher events usually have a broad hit timing distribution compared with that of the neutrino events. The cut criteria to eliminate these flasher events for SK-I are :

(1) $NMIN_{100} \geq 14$
        or
        $NMIN_{100} \geq 10$ if   the number of hit ID PMTs < 800
        $NMIN_{100}$ is the minimum number of hit ID PMTs in a sliding 100 nsec time
        window from +300 nsec to +800 nsec after the trigger.

For SK-II, the cut criteria are :

(1) $NMIN_{100} \geq 20$

Figure C.9 shows the timing distribution of (i) a typical flashing PMT event and (ii) a typical FC neutrino event and the time window for $NMIN_{100}$ is shown by arrows.

Figure C.10 and C.11 shows $NMIN_{100}$ distributions for the data after the 2nd reduction, the FC atmospheric neutrino Monte Carlo events and the FC final events.
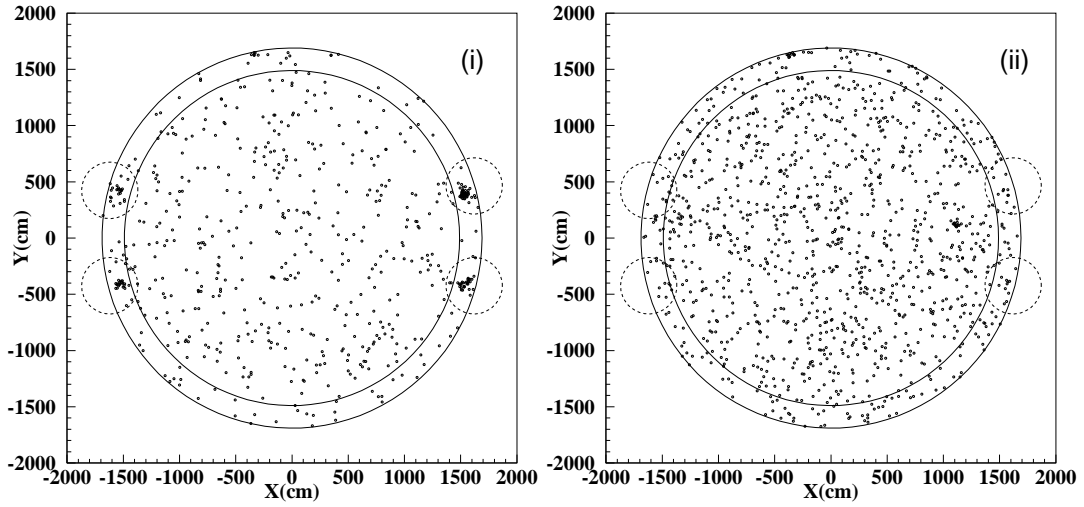
Figure C.8: Reconstructed vertex distribution for the fully contained 1-ring μ-like events (i) before the installation of the veto counters and (ii) after installation. The outer solid circle shows the ID wall and the inner solid circle shows the fiducial volume (2 m from the wall). Small dashed circles indicate the positions of the veto counters. Four clusters are clearly seen around cable holes for data without veto counters, while no cluster is visible for data after the installation.
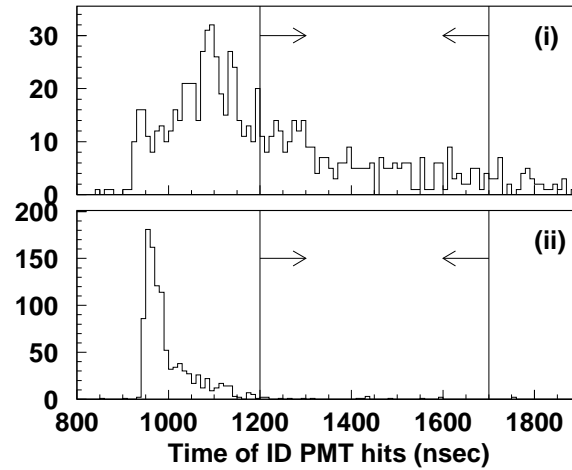
Figure C.9: The timing distribution of (i) a typical flashing PMT event and (ii) a typical FC neutrino event. The arrows show the time window for counting $NMIN_{100}$.

181
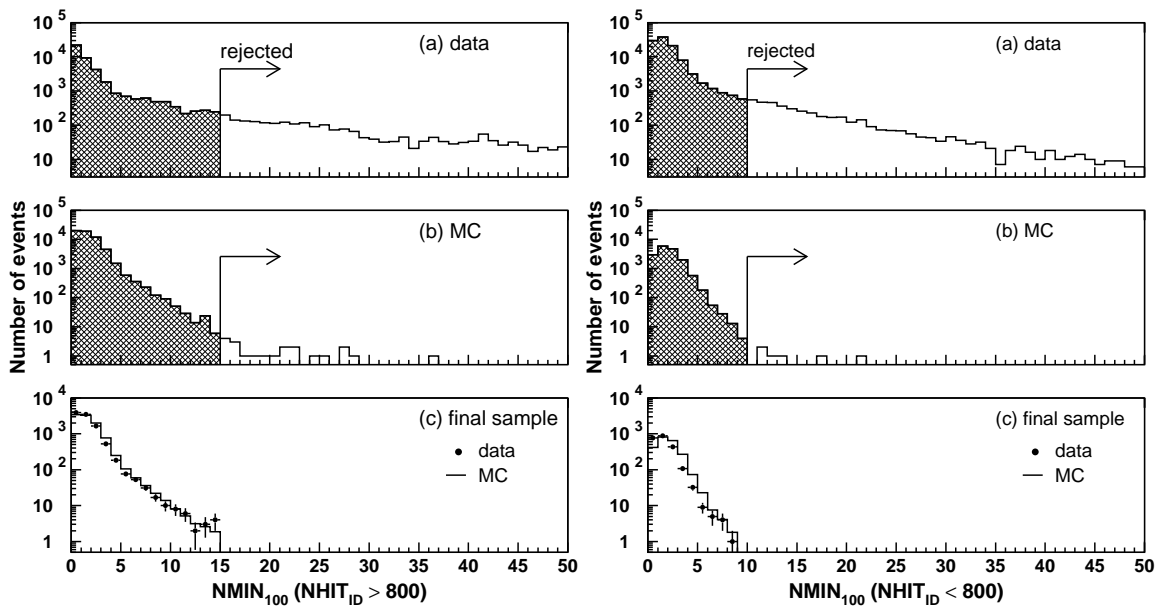
Figure C.10: $NMIN_{100}$ distributions (left) for the events with more than 800 hit PMTs in the ID and (right) less than 800 hit PMTs for SK-I. Three figures show (a) the data after FC 2nd reduction, (b) fully contained atmospheric neutrino Monte Carlo events and (c) final samples, respectively. The number of the Monte Carlo events in (c) is normalized to that of the data. The selection criteria are shown by arrows.

182
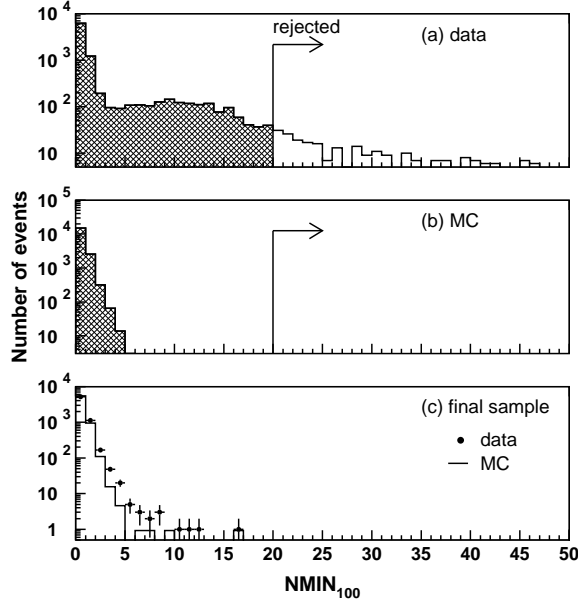
Figure C.11: $NMIN_{100}$ distributions for SK-II. Three figures show (a) the data after FC 2nd reduction, (b) fully contained atmospheric neutrino Monte Carlo events and (c) final samples, respectively. The number of the Monte Carlo events in (c) is normalized to that of the data. The selection criteria are shown by arrows.

Accidental coincidence events cut

The accidental coincidence occurs when a low energy event forms the trigger and a cosmic ray muon event follows in a single trigger gate. These events are not rejected in the former reduction because of the absence of the OD activities on the trigger timing and the large number of total p.e.s in the ID due to the muons. The accidental coincidence events are removed by the following cuts :

(1) $NHITA_{off} \geq 20$
        $NHITA_{off}$ is the number of hit OD PMTs in a fixed 500 nsec off-timing window
        from +400 nsec to +900 nsec after the trigger timing.

and

(2) $PE_{off} > 5000$ p.e.s (2500 for SK-II)
        PE_{off} is the number of p.e.s observed by ID PMTs in a fixed 500 nsec off-timing
        window from +400 nsec to +900 nsec.

Low energy events cut

The remaining low energy events are from the decay of radio isotopes and the electrical noise. Events satisfying the following criteria are removed as low energy background events :

(1) $NHIT_{50} < 50$ (25 for SK-II)
        $NHIT_{50}$ is the number of hit ID PMTs in a sliding 50 nsec time window.

183

where NHIT$_{50}$ is counted after subtracting the time of flight (TOF) of each observed photon assuming all photons are generated at a point. The vertex is determined as the position at which the timing residual distribution is peaked. NHIT$_{50}$=50 corresponds to visible energy of 9 MeV and is low enough not to lose efficiency for contained neutrino events with E$_{vis}$ >30 MeV.

After the FC third reduction, the event rate is 45 (21) events/day for SK-I (SK-II).

C.1.4   Fourth Reduction

In the fourth reduction, an intelligent pattern matching algorithm is used to further remove the remaining flasher events. Flasher events usually repeat with similar hit patterns in the detector in the course of hours and days. These repeated events are not likely to be caused by neutrinos. Figure C.12 shows the scatter plots of N$_{match}$ and the maximum value of the estimator r for the data after the FC 3rd reduction and atmospheric neutrino Monte Carlo events. For the Monte Carlo events, the data which were removed as flasher events in this reduction stage are mixed, and the estimator r is calculated. The cut criteria are also shown in Figure C.12.

The algorithm of the pattern matching is as follows :

(1)   Divide the ID wall into 1450 patches of 2 m×2 m square.

(2)   Compute the correlation factor r by comparing the total charge in each patch of two events, A and B. The correlation is defined as :

$$r = \frac{1}{N} \sum_i \frac{\left(Q_i^A - \langle Q^A \rangle\right) \times \left(Q_i^B - \langle Q^B \rangle\right)}{\sigma_A \times \sigma_B} \qquad \text{(C.2)}$$

where N is the number of the patches, and $\langle Q^{A(B)} \rangle$ and $\sigma_{A(B)}$ are the averaged charge and its standard deviation for event A and B, respectively.

(3)   Calculate the distance (DIST$_{max}$)between the PMTs with the maximum pulse heights in the two compared events

(4)   If DIST$_{max}$ < 75 cm, an offset value is added to r :r=r+0.15.

(5)   If r exceeds the threshold(r_{th}), events A and B are recognized as matched events. r_{th} is defined as :

$$r > r_{th} = 0.168 \times \log_{10}((\text{PE}_{tot}^A + \text{PE}_{tot}^B)/2.) + 0.130, \qquad \text{(C.3)}$$

where PE$_{tot}$ is the total number of p.e.s observed in the ID.

(6)   Repeat the above calculation over 10,000 events around the target event and count the number of matched events.

(7)   Remove the events with large correlation factor r, or large number of matched events.

The event rate after the fourth reduction is 18 events/day for both SK-I and SK-II.

C.1.5   Fifth Reduction

The remaining background events are removed by several criteria specialized for each kind of background events.
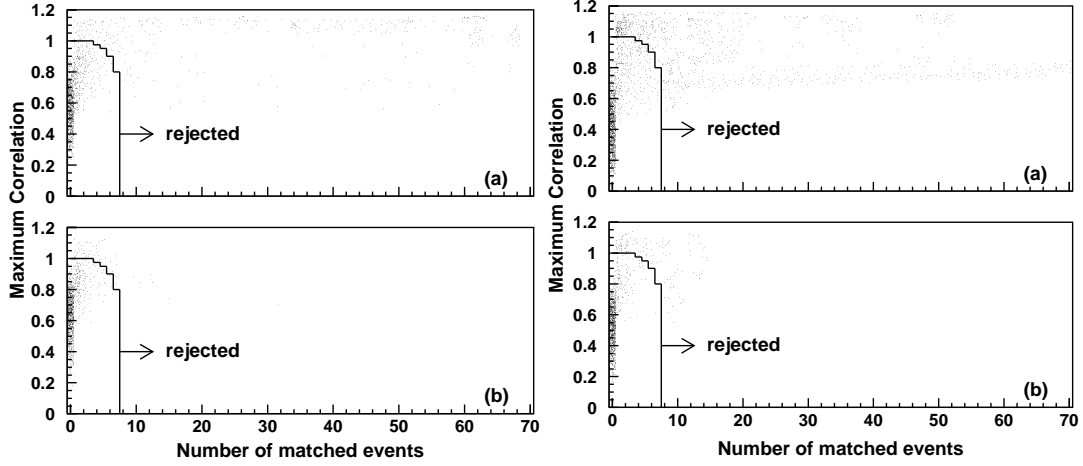
Figure C.12: Scatter plots of N_{match} and the maximum value of the estimator r for (a) the data after the FC 3rd reduction and (b) atmospheric neutrino Monte Carlo events for SK-I (left) and SK-II (right). The cut criteria are shown by arrows.

Stopping muon cut

The remaining stopping muons are rejected by tighter criteria than those in the third reduction stage. Events satisfying the following criteria are rejected :

(1) $NHITA_{in} \geq 5$
  $NHITA_{in}$ is the number of hit OD PMTs located within 8 m from the entrance point in a sliding 200 nsec time window from -400 nsec to $+400$ nsec.

The entrance position in the OD is estimated by a backward extrapolation from the reconstructed vertex determined by TDC-fit (see Section **??**). Figure C.13 shows $NHITA_{in}$ distributions for the data after the 4th reduction, the FC atmospheric neutrino Monte Carlo events and the FC final events.

Invisible muon cut

Invisible muon events are caused by cosmic ray muons with momenta less than the Cherenkov threshold and the subsequent decay electrons being observed. These events are characterized by a low energy signal from decay electron and a signal in the OD before the trigger timing. Events which satisfy the following cut criteria are rejected as invisible muons :

(1) $PE_{tot} < 1000$ p.e.s (500 for SK-II)
  PE_{tot} is the total number of p.e.s observed in the ID.

and

(2) $NHITAC_{early} > 4$
  $NHITAC_{early}$ is the maximum number of hit PMTs in the OD hit cluster in a sliding 200 nsec time window from -8800 nsec to -100 nsec.

185
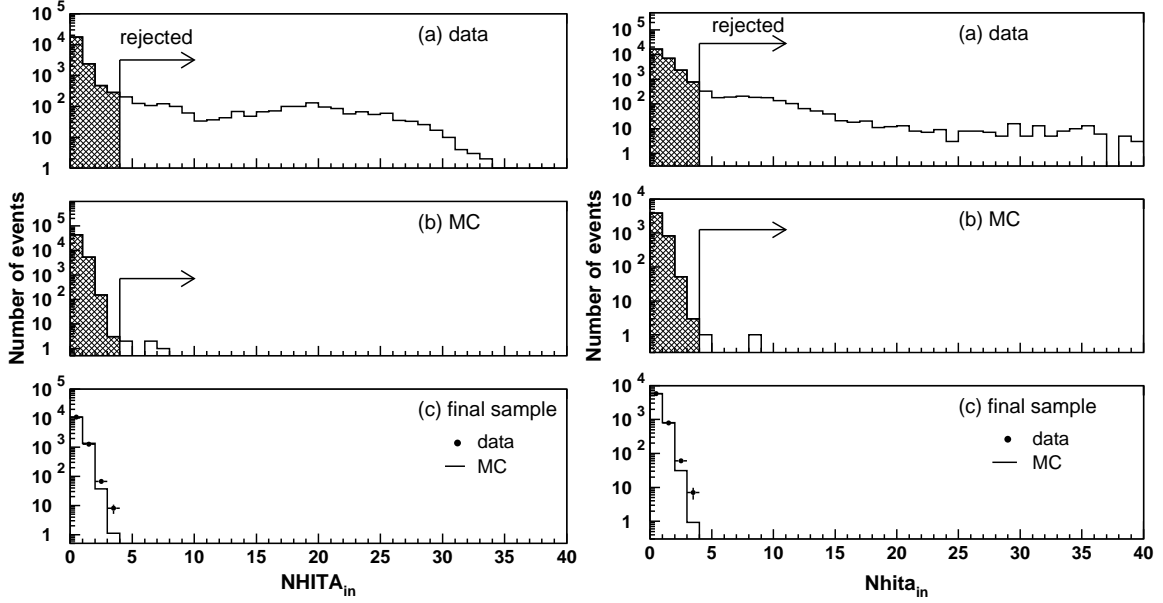
Figure C.13: NHITA$_{in}$ distribution for (a) the data after FC 4th reduction and (b) fully contained atmospheric neutrino Monte Carlo events, and (c) final samples. The number of the Monte Carlo events in (c) is normalized to that of the data for SK-I (left) and SK-II (right). The selection criteria are shown by arrows.

and

(3)   NHITAC$_{early}$ + NHITAC$_{500}$ > 9   if   DIST$_{clust}$ < 500 cm
        NHITAC$_{early}$ > 9   otherwise

> NHITAC$_{500}$ is the number of hit PMTs in the OD hit cluster in a fixed 500 nsec time window from -100 nsec to $+400$ nsec.
> DIST$_{clust}$ is a distance between two OD hit clusters, which are used for the NHITAC$_{early}$ and the NHITAC$_{500}$.

Figure C.14 shows the NHITAC$_{early}$ distribution for the data after the FC 4th reduction, fully contained atmospheric neutrino Monte Carlo events and final samples, satisfying criterion (1) and DIST$_{clust}$ > 500 cm. Although the number of hit PMTs in off-timing window for data is larger than that for the Monte Carlo simulation, the cut is safe for FC sample.

Coincidence muon cut

The remaining accidental coincidence muon events are removed by :

(1)   PE$_{500}$ < 300 p.e.s (150 for SK-II)
        PE$_{500}$ is the total number of p.e.s observed in the ID in a fixed 500 nsec time window from -100 nsec to $+400$ nsec.

and
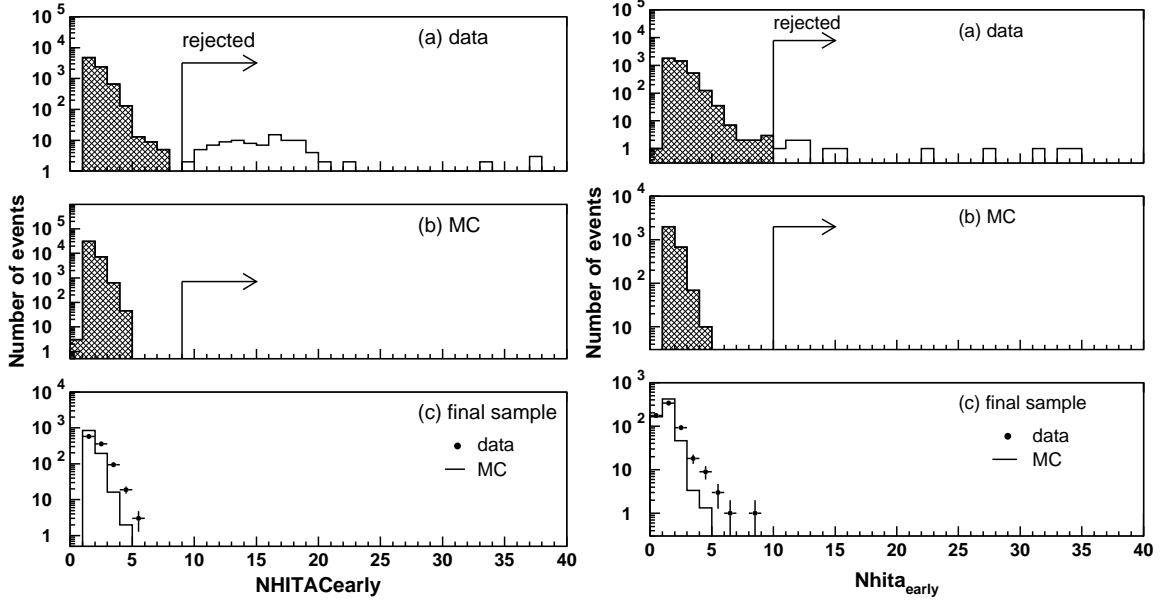
Figure C.14: NHITAC$_{\text{early}}$ distribution for (a) the data after FC 4th reduction and (b) fully contained atmospheric neutrino Monte Carlo events, and (c) final samples, satisfying criterion (1) and DIST$_{\text{clust}}$ > 500 cm for SK-I (left) and SK-II (right). The number of the Monte Carlo events in (c) is normalized to that of the data. The selection criteria are shown by arrows.

(2)   PE$_{\text{late}} \geq 20$ p.e.s
PE$_{\text{late}}$ is the maximum number of hit OD PMTs in a 200 nsec sliding time window from +400 nsec to +1600 nsec.

Figure C.15 shows the PE$_{\text{late}}$ distribution for the data after the FC 4th reduction, fully contained atmospheric neutrino Monte Carlo events and final samples, satisfying the criterion (1). The cut is safe for FC sample.

Long-tail flasher cut

This is a stricter version of flasher cut in the FC 3rd reduction stage. Events satisfying the following criterion are removed as flasher events :

(1)   NMIN$_{100}$ > 5   if the goodness of point fit < 0.4
NMIN$_{100}$ is the minimum number of the hit ID PMTs in a sliding 100 nsec time window from +300 nsec to +800 nsec.

For SK-II, in addition to the criteria above, the extra cuts are applied :

(3)   Goodness of point fit < 0.3

and

(4)   NHITMIN$_{100}$ < 6

See Section **??** for the explanation of point fit.

After the fifth reduction, the FC event rate is 16 events/day for both SK-I and SK-II.

187
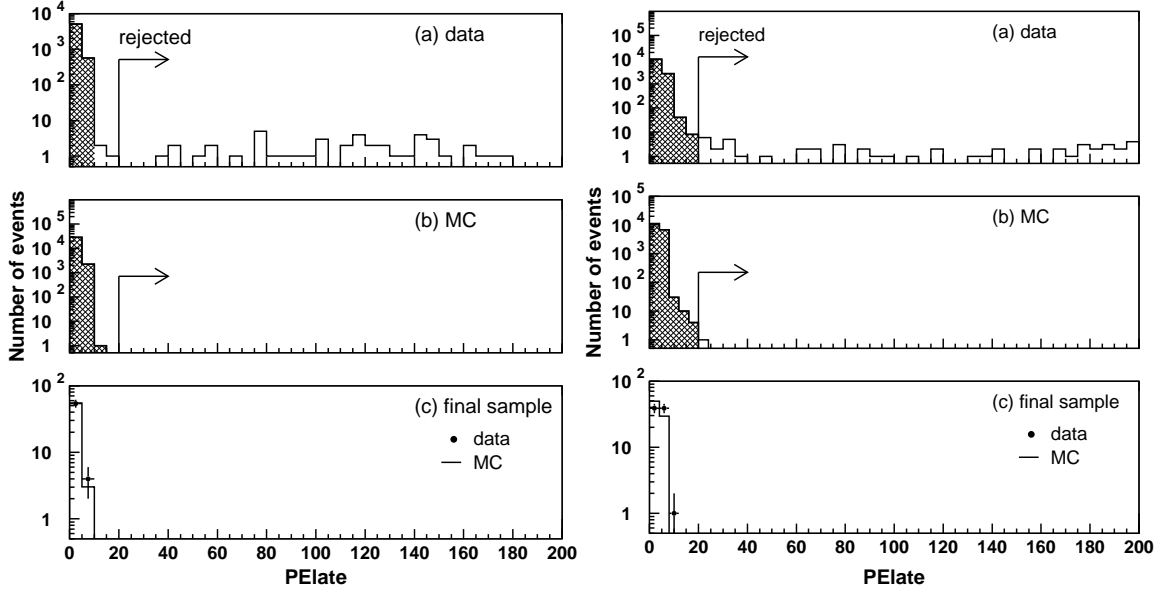
Figure C.15: PE$_{\text{late}}$ distribution for (a) the data after FC 4th reduction and (b) fully contained atmospheric neutrino Monte Carlo events, and (c) final samples, satisfying criterion (1) for SK-I (left) and SK-II (right). The number of the Monte Carlo events in (c) is normalized to that of the data. The selection criteria are shown by arrows.

C.1.6   FC Reduction Summary

Finally, the fully contained neutrino events are selected by applying the FC event cuts :

- Vertex of neutrino interactions should be inside the fiducial volume (2 m from the ID PMT surface).

- The number of hit PMTs in the highest charge OD cluster (NHITAC) should be less than 10 (16 for SK-II).

- Visible energy (E$_{vis}$) should be greater than 30 MeV.

The detection efficiencies in each reduction step are estimated by the atmospheric neutrino events as shown in Table C.1. The detection efficiency for final events is estimated to be 98.8 % and 99.5 % for SK-I and SK-II, respectively. The systematic uncertainty of FC reduction is estimated to be 0.2 % for both SK-I and SK-II. The event rate of FC events for real data is shown in Figure C.30 and is 8.18±0.07 (8.26±0.10) events/day for SK-I (SK-II).

The main sources of the background for FC events are cosmic ray muons, flasher events and neutrons from the rock around the detector. These background events are largely rejected by requiring fiducial volume cut. The contaminations of the backgrounds are estimated as shown in Table C.2.

Reduction step	SK-I (%)	SK-II (%)
1st reduction	100.00	100.00
2nd reduction	100.00	99.94
3rd reduction	99.92	99.76
4th reduction	99.33	99.45
5th reduction	99.30	99.37
Final cut	98.84	99.51

Table C.1: The detection efficiency in the each reduction step for SK-I and SK-II for events whose true vertices are in the fiducial volume, NHITAC less than 10 (16 for SK-II) and E_{vis} larger than 30 MeV. In the last line, the fitted vertex is used.

SK-I	Sub-GeV ($E_{vis} < 1330 MeV/c$)		Multi-GeV ($E_{vis} \geq 1330 MeV/c$)	
	e-like(%)	μ-like(%)	e-like(%)	μ-like(%)
Cosmic ray μ	—	0.07	—	0.09
Flashing PMT	0.42	—	0.16	—
Neutron event	0.1	—	0.1	—
SK-II	Sub-GeV		Multi-GeV	
	e-like(%)	μ-like(%)	e-like(%)	μ-like(%)
Cosmic ray μ	—	0.01	—	0.07
Flashing PMT	0.27	—	0.65	—
Neutron event	0.1	—	0.1	—

Table C.2: Summary of the estimated upper limit of the contamination of each background.

C.2 Reduction for Partially Contained Sample

Since PC events have the OD activities by its definition, the reduction scheme is different from that that of FC events and it is rather difficult to eliminate cosmic ray muon backgrounds. There are five steps in PC reduction process.

C.2.1 First Reduction

The aim of the 1st reduction is to reject the through-going cosmic ray muons and low energy events. The selection criteria of the PC 1st reduction are as follows :

(1) PE_{tot} should be ≥ 1000 p.e.s (500 for SK-II).
        PE_{tot} is the number of p.e.s observed in the ID.

and

(2)   TWIDA should be ≤ 260 nsec (170 nsec for SK-II).
        TWIDA is the width of the hit timing distribution in the OD PMTs.

and

(3)   NCLSTA should be ≤ 1 (only for SK-I).
        NCLSTA is the number of the hit clusters in the OD.

Exiting particles in the PC sample, mostly muons, must have at least 2 m track length in the ID, which corresponds to the momentum loss of 500 MeV/c for muons. In criterion (1), PE_{tot} should be larger than 1000 p.e.s (500 for SK-II), which corresponds to 310 MeV/c for muons. The second criteria rejects the through-going muons. The through-going muon events have a broad hit timing distribution and two hit clusters around the entrance and exit point in the OD. Figure C.16 shows the TWIDA distribution for the raw data, partially contained atmospheric neutrino Monte Carlo events and final samples. Since the reflected photon in the OD is increased and the quantum efficiency of OD PMTs is increased in SK-II, the hit timing becomes broad. Therefore TWIDA is redefined by the counted hit OD PMTs with the threshold of 2 p.e.s in SK-II (it was 0 p.e. in SK-I) and the cut criterion for TWIDA is tuned. The hit cluster means the spatial cluster of neighboring hit PMTs. A hit cluster is formed around the PMT which detects more than 8 p.e.s and the clusters within 8 m are merged.

The event rate after the PC 1st reduction is 14000 (36000) events/day for SK-I (SK-II).

C.2.2 Second Reduction

In the second reduction, another clustering algorithm of OD hit is used to reject the remaining through-going muons and the stopping muons. The OD (ID) walls are divided into 11×11 (21×21) patches and the charge observed in each patch is counted. The clusters are formed by looking for the charge gradient to the neighboring patches. The algorithm is illustrated in Figure C.17. Events satisfying the following criteria remain after the PC 2nd reduction for SK-I :

(1)   NCLSTA2 should be ≤ 1
        NCLSTA2 is the number of the OD hit clusters including more than 6 hit PMTs.
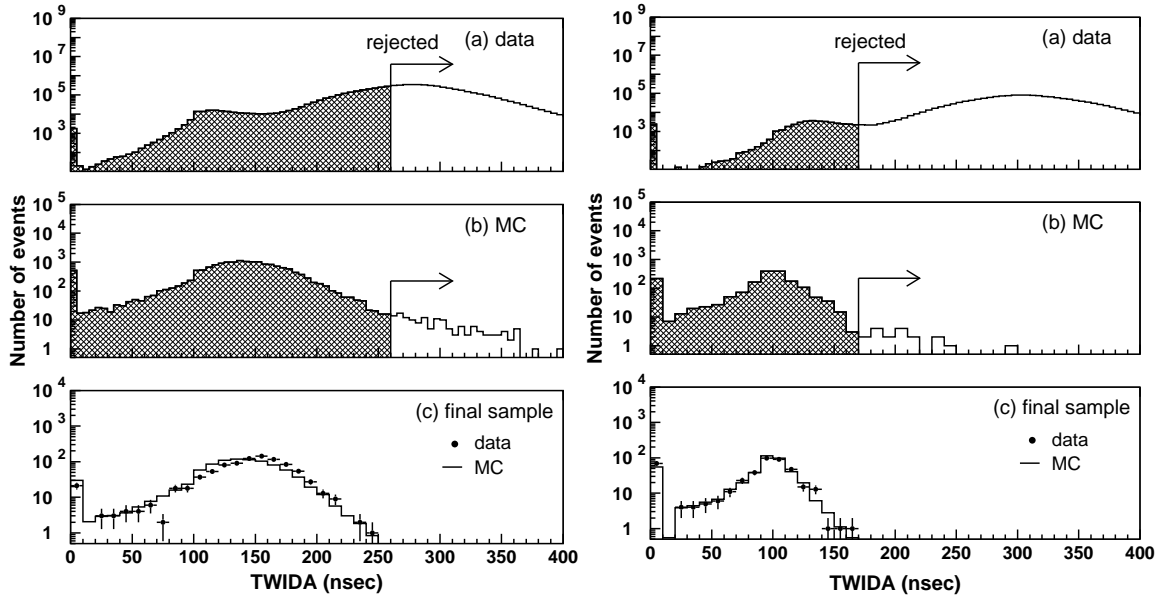
Figure C.16: TWIDA distributions for (a) the raw data, (b) partially contained atmospheric neutrino Monte Carlo events whose vertex position is more than 2 m away from the ID wall and (c) final samples of the data and the Monte Carlo events for SK-I (left) and SK-II (right). The number of the Monte Carlo events in (c) is normalized to that of the data. The selection criteria are shown by arrows.
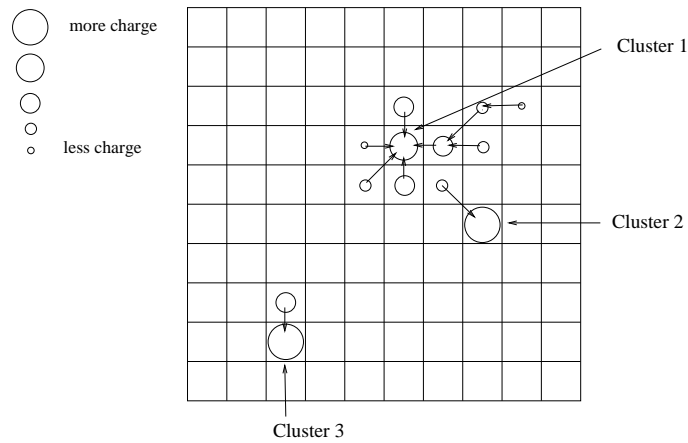

Figure C.17: A schematic view of the algorithm to find hit clusters in the PC 2nd reduction. The circles represent the charge observed in each patch. The size of the circle is proportional to the number of p.e.s. The arrows represent the vector charge gradient, which point to the highest charge among the neighboring patches.

191

and

(2) $NHITAC_{min}$ should be < 7
$NHITAC_{min}$ is the minimum number of hit PMTs among top (or bottom) and side regions in the OD hit cluster.

and

(3) PE_{200} should be > 1000 p.e.s   if $NCLSTA2 = 1$
PE_{200} is the number of the observed p.e.s within 200 cm from the highest charge PMT in the ID hit cluster closest to the OD hit cluster.

For SK-II, the criteria are tuned to keep the reduction efficiency.

(1) $NCLSTA2(2)$ should be ≤ 1
$NCLSTA2(2)$ is the number of the 2nd OD hit clusters including more than 10 hit PMTs.

and

(2) $NHITA_{endcap} < 20$ or $NHITA_{endcap} < MAX(NHITA_{side})$
$MAX(NHITA_{side})$ is defined as :
$MAX(NHITA_{side} = \exp(5.8\text{-}0.023\times NHITA_{side})$ if $NHITA_{side} < 75$
$MAX(NHITA_{side} = \exp(4.675\text{-}0.008\times NHITA_{side})$ if $NHITA_{side} \geq 75$
$NHITA_{endcap}$ is the number of OD hit PMTs in the top and bottom region.
$NHITA_{side}$ is the number of hit OD PMTs in the side region.

(3) $NHITAC2 < 12 + 0.085 \times PE_{200}$
$NHITAC2$ is the number of the OD hit PMTs in the 2nd cluster.

Criteria (2) for both SK-I and SK-II reject corner clipping muons, which left the hit PMTs in both top (or bottom) and side regions in the OD. Figure C.18 shows the $NHITAC_{min}$ distributions for the data, atmospheric neutrino Monte Carlo events after the PC 1st reduction and final samples for SK-I. Figure C.19 shows the scatter plots of the $NHITA_{endcap}$ and the $NHITA_{side}$ for the same samples. In criteria (3) for SK-I and SK-II, the number of p.e.s in the ID hit cluster located behind the OD hit cluster is used to reject the stopping muons. Figure C.20 shows the scatter plots of the NCLSTA2 and the PE_{200} for the data, atmospheric neutrino Monte Carlo events after the PC 1st reduction and final samples for SK-I. Figure C.21 shows the scatter plots of the NHITAC2 and the PE_{200} for the data, atmospheric neutrino Monte Carlo events after the PC 1st reduction and final samples for SK-II.

The event rate after the PC 2nd reduction is 2000 (5500) events/day for SK-I (SK-II).

C.2.3   Third Reduction

In the third reduction flasher events and cosmic ray stopping muons are rejected. The flasher events are rejected by the same way as that in the FC 3rd reduction, in which the broad timing distribution of the flasher events is used for cut. Events which satisfy the following criteria are rejected as flasher events for both SK-I and SK-II :
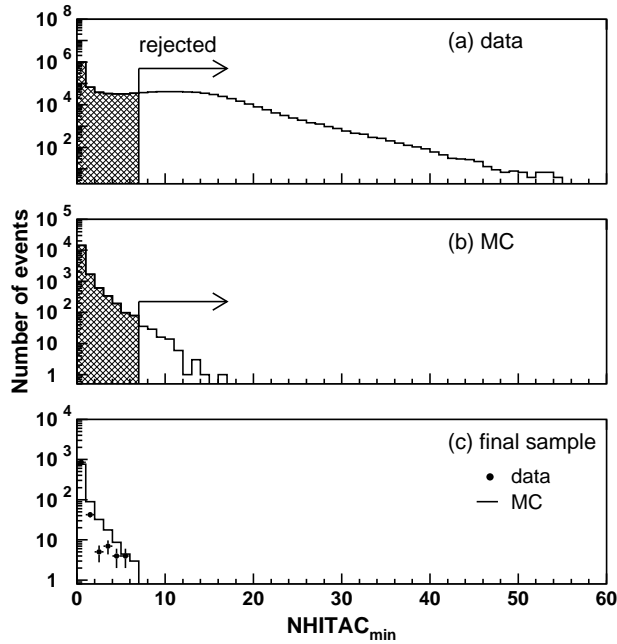
Figure C.18: $\text{NHITAC}_{\text{min}}$ distributions for (a) the data, (b) partially contained atmospheric neutrino Monte Carlo events after the PC 1st reduction and (c) final sample of the data and the Monte Carlo events for SK-I. The selection criteria are shown by arrows.
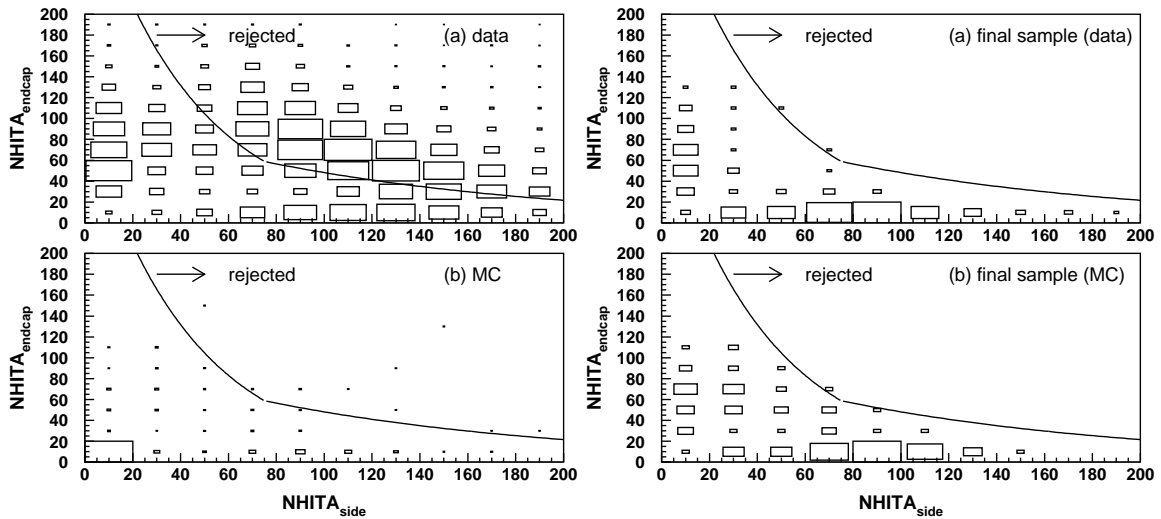
Figure C.19: Scatter plots of $\text{NHITA}_{\text{endcap}}$ and $\text{NHITA}_{\text{side}}$ for (a) the data and (b) partially contained atmospheric neutrino Monte Carlo events after the PC 1st reduction and (c) final samples of the data and (d) the Monte Carlo events for SK-II. The size of the boxes shows the number of the events in each bin. The cut criteria are shown by the lines and arrows.
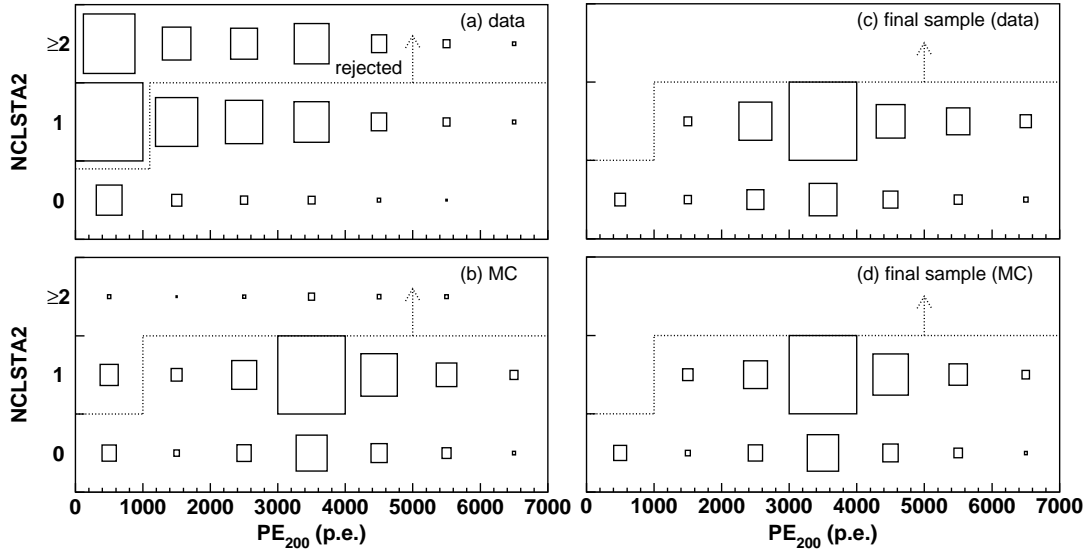
Figure C.20: Scatter plots of NCLSTA2 and PE$_{200}$ for (a) the data and (b) partially contained atmospheric neutrino Monte Carlo events after the PC 1st reduction and (c) final samples of the data and (d) the Monte Carlo events for SK-I. The size of the boxes shows the number of the events in each bin. The cut criteria are shown by the dashed lines and arrows.
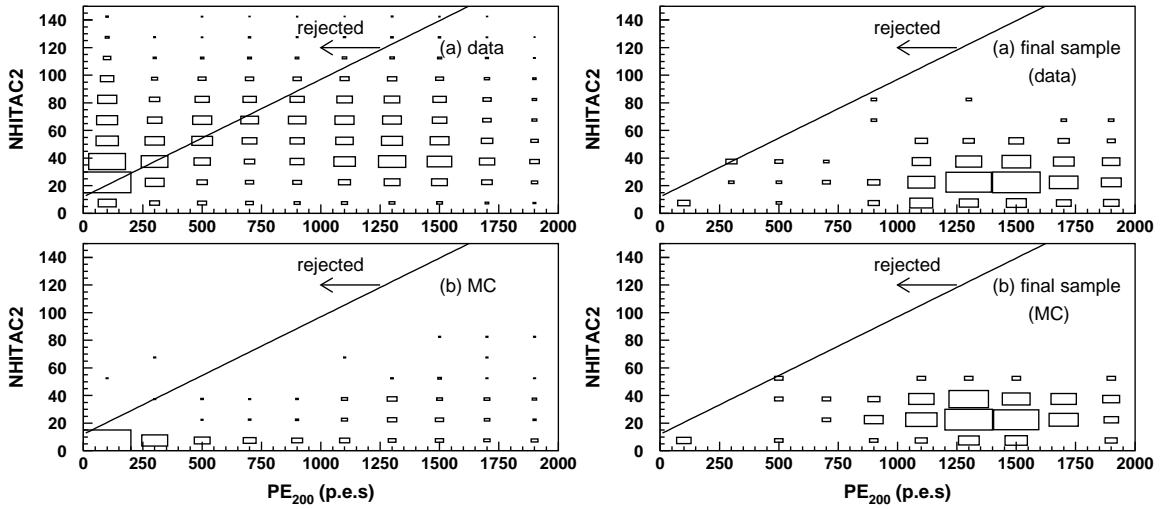

Figure C.21: Scatter plots of NHITAC2 and PE$_{200}$ for (a) the data and (b) partially contained atmospheric neutrino Monte Carlo events after the PC 1st reduction and (c) final samples of the data and (d) the Monte Carlo events for SK-II. The size of the boxes shows the number of the events in each bin. The cut criteria are shown by the lines and arrows.

194
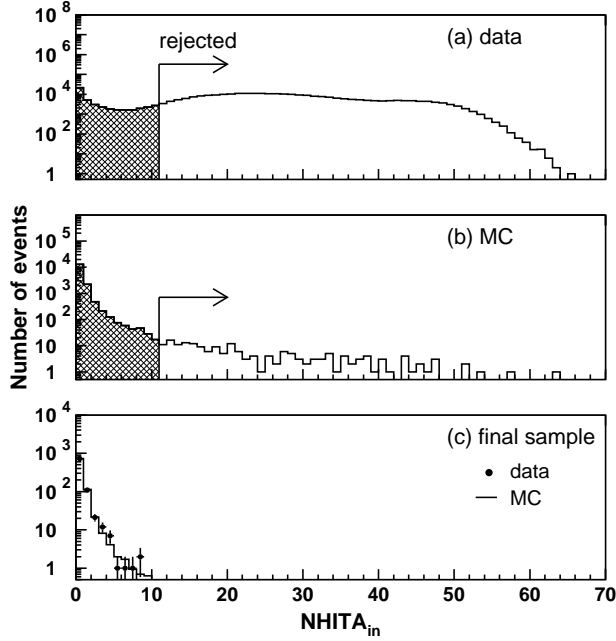
Figure C.22: NHITA$_{in}$ distributions for (a) the data and (b) atmospheric neutrino Monte Carlo events after the PC 2nd reduction and (c) final samples. The number of the Monte Carlo events in (c) is normalized to that of the data for SK-I. The selection criteria are shown by arrows.

(1)   NMIN$_{100}$ > 14
       or
       NMIN$_{100}$ > 9   if   the number of hit ID PMTs < 800 (400 for SK-II)
       NMIN$_{100}$ is the minimum number of hit ID PMTs in a sliding 100 nsec time
       window from +300 nsec to +800 nsec.

The stopping muon events are removed by the number of the hit OD PMTs near the entrance position. Simple vertex and direction fitter called point fit is applied. The vertex position is determined by point fit as the point where the timing residual distribution of hit PMTs has the sharpest peak assuming the photons are emitted from a point source (see Section ??). The direction of the ring is determined by summing up the charge weighted vector for all PMTs, and the entrance position is estimated by a backward extrapolation from the reconstructed vertex. Events satisfying the following criteria are rejected as stopping muons for both SK-I and SK-II :

(2)   NHITA$_{in}$ > 10
       NHITA$_{in}$ is the number of hit OD PMTs located within 8 m from the entrance
       point in a fixed 500 nsec time window.

The NHITA$_{in}$ distributions for the data and atmospheric neutrino Monte Carlo events for SK-I after the PC 2nd reduction, and final samples are shown in Figure C.22.

The event rate after the PC 3rd reduction is 100 (200) events/day for SK-I (SK-II).

C.2.4 Fourth Reduction

The PC 4th reduction rejects further cosmic ray muons, which pass through the PC 3rd reduction due to the relatively small OD activities. The two types of event reconstruction tools are used in this reduction stage, that is a point fit and a though going muon fit. The through

going muon fit determines the entrance point as the position of the earliest hit cluster in the ID. For the PC events, the entrance point can not be correctly determined by the through-going muon fit because they are generated inside the ID, and the goodness tends to be worse compared with the through-going muon events. On the other hand, the vertex position and the direction can be reasonably well estimated by the point fit for both the PC events and the cosmic ray muons. The selection criteria in the PC 4th reduction are as follows for SK-I and SK-II :

(1) $\vec{d}_{\text{pfit}} \cdot \vec{d}_{\text{PMT}}$ should be > -0.8
       $\vec{d}_{\text{pfit}}$ is the reconstructed direction by point fit, and $\vec{d}_{\text{PMT}}$ is the direction from the reconstructed vertex to the earliest saturated PMT.

and

(2)   DCORN should be $> 150\,\text{cm}$
       DCORN is the distance from the reconstructed vertex by the point fit to the nearest fringe of the ID.

and

(3)   TLMU should be $> 30\,\text{m}$ if   goodness of through-going muon fit > 0.85
       TLMU is the track length of a muon estimated from the entrance and the exit points by the through going muon fit.

The criterion (1) rejects the cosmic ray stopping muons which have the entrance point in opposite direction to the reconstructed direction by point fit. The second criterion aims to reject corner clipping muons. The distribution for SK-I of the $\vec{d}_{\text{pfit}} \cdot \vec{d}_{\text{PMT}}$ and the DCORN are shown in Figure C.23 and Figure C.24, respectively. Through-going muons which have long track length are rejected by the third cut. Figure C.25 shows the scatter plots of the TLMU and the goodness of the through-going muon fit for the data and atmospheric neutrino Monte Carlo events after the PC 3rd reduction, and final samples for SK-I. The events in the upper-right box region are rejected as through-going muons.

The event rate after the PC 4th reduction is 20 events/day for both SK-I and SK-II.

C.2.5   Fifth Reduction

The aim of the 5th reduction stage is the final rejection of the remaining background events for the PC sample. This is done by some elaborate criteria specialized for each background source. The event rate after the PC 5th reduction is 1 events/day for both SK-I and SK-II.

Low energy event cut

Events satisfying the following criteria are removed as the remaining low energy background events :

(1) $\text{PE}_{\text{tot}} < 3000\,\text{p.e.s}$ (1500 for SK-II)
       PE_{tot} is the total number of p.e.s observed in the ID.

The requirement of total photoelectrons $> 3000\,\text{p.e.s}$, which corresponds to muon momentum of $500\,\text{MeV}/c$, is safe for PC events because the exiting muons must have at least momentum of $700\,\text{MeV}/c$ to reach the OD.
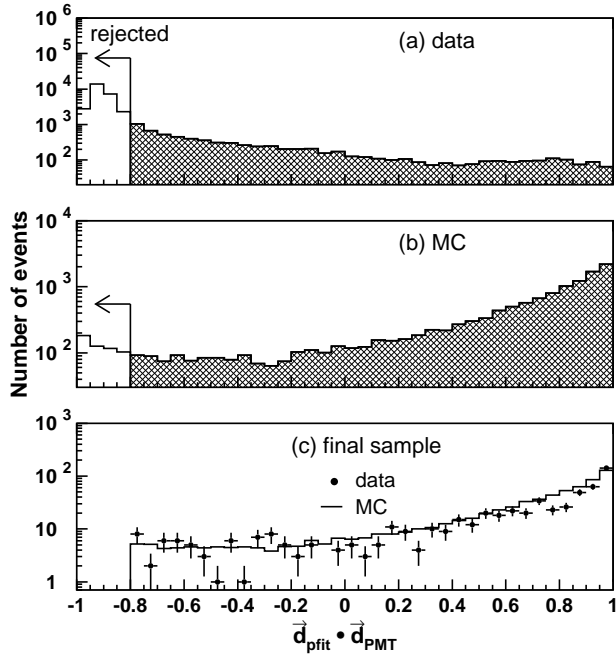
Figure C.23: $\vec{d}_{\mathrm{pfit}}\cdot\vec{d}_{\mathrm{PMT}}$ distributions for (a) the data and (b) partially contained atmospheric neutrino Monte Carlo events after the PC 3rd reduction and (c) final samples. The number of the Monte Carlo events in (c) is normalized to that of the data for SK-I. The selection criteria are shown by arrows.
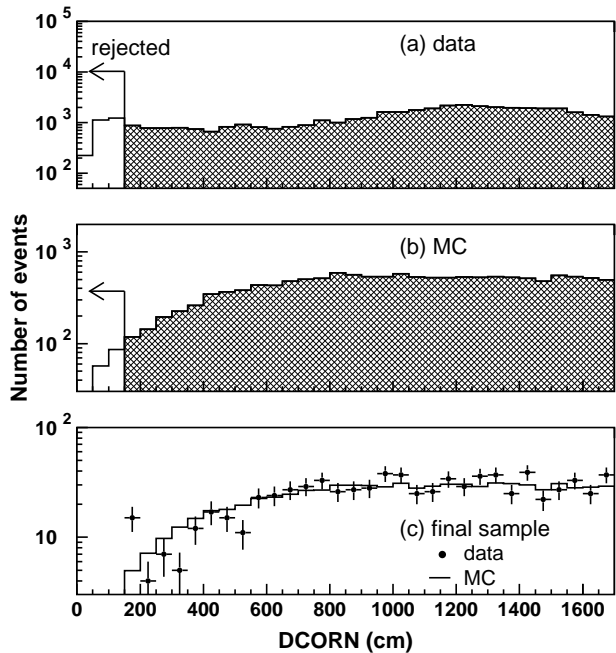

Figure C.24: DCORN distributions for for (a) the data and (b) partially contained atmospheric neutrino Monte Carlo events after the PC 3rd reduction and (c) final samples. The number of the Monte Carlo events in (c) is normalized to that of the data for SK-I. The selection criteria are shown by arrows.
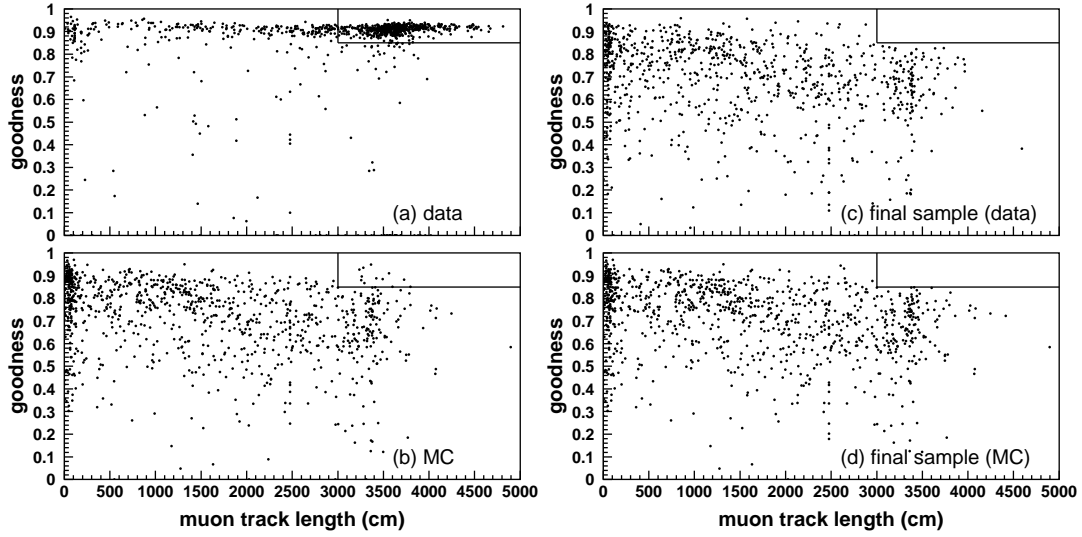
Figure C.25: Scatter plots of muon track length and goodness of through-going muon fit for (a) the data and (b) partially contained atmospheric neutrino Monte Carlo events after the PC 3rd reduction, and (c) final samples of the data and (d) the Monte Carlo for SK-I. The events in the upper-right box region are rejected as through-going muons.

Through-going muon cut

The remaining through-going muons are removed by investigating the existence of two OD hit clusters and the existence of hit OD PMTs near the entrance and the exit points. The first cut uses the OD hit cluster information obtained by the algorithm in the PC 2nd reduction. Events satisfying the following criteria are removed as through-going muons :

(1) $DIST_{clust} > 20\,m$
       $DIST_{clust}$ is the distance between the highest charge OD hit cluster and the second highest one.

and

(2) $PEAC_{2nd} \geq 10\,p.e.s$
       $PEAC_{2nd}$ is the number of p.e.s detected in the second highest charge OD hit cluster.

and

(3) $NCLSTA5 \geq 2$
       NCLST5 is the number of OD hit clusters which contain more than 9 hit PMTs.

In criterion (3), the same clustering algorithm as that in the PC 2nd reduction with different parameters is used. The OD wall is divided into 6×6 instead of 11×11 in the PC 5th reduction to avoid the boundary effect of the patches.

198

Some cosmic ray muons enters from the edge on top, passes along the ID wall and exits from the edge of the bottom. These through-going muon events tend to pass through the former reduction criteria because the light collection efficiency around the edge of the OD is not good and the event reconstruction is not so accurate for these events. To reject these events, the number of hit OD PMTs and the observed p.e.s in $8\,\mathrm{m}$ radius spheres centered at the top and the bottom edges or fringes are used. Events satisfying the following criteria are rejected as through-going muons :

(1) $\mathrm{NHITA_{top}} \geq 7$ and $\mathrm{NHITA_{bottom}} \geq 7$
        $\mathrm{NHITA_{top}}$ ($\mathrm{NHITA_{bottom}}$) is the maximum number of hit OD PMTs in a $8\,\mathrm{m}$
        radius sphere centered at the top (bottom) edge.

and

(2) $\mathrm{PEA_{top}} \geq 10\,\mathrm{p.e.s}$ and $\mathrm{PEA_{bottom}} \geq 10\,\mathrm{p.e.s}$
        $\mathrm{PEA_{top}}$ ($\mathrm{PEA_{bottom}}$) is the number of p.e.s in OD detected in the same sphere
        as that for the $\mathrm{NHITA_{top}}$ ($\mathrm{NHITA_{bottom}}$)

and

(3) $0.75 < \mathrm{TDIFFA} \times c/40\,\mathrm{m} < 1.5$
        TDIFFA is a time interval between the averaged hit timing in the top and the
        bottom spheres.

The remaining through-going muons are removed by the number of hit OD PMTs near the entrance and the exit points. The vertex position and the ring direction are reconstructed by a precise fit (MS-fit) using the Cherenkov ring pattern (see Section D.4). The entrance and the exit points on the detector wall are estimated by an extrapolation. The cut criteria for both SK-I and SK-II are as follows :

(1) $\mathrm{NHITA_{in}} \geq 5$ and $\mathrm{NHITA_{out}} \geq 5$
        $\mathrm{NHITA_{in}}$ ($\mathrm{NHITA_{out}}$) is the number of hit OD PMTs within $8\,\mathrm{m}$ from the
        entrance (exit) point.

and

(2) $0.75 < \mathrm{TDIFFA} \times c/\mathrm{TRACK} < 1.5$
        TRACK is distance between the entrance and exit point estimated using the
        vertex position and the ring direction reconstructed by MS-fit.

Stopping muon cut

Three types of stopping muon cuts are applied. In the first cut, the number of hit OD PMTs near the entrance position is counted. The entrance position of the stopping muons are estimated by reconstructing the vertex position and direction using MS-fit and back extrapolating to the wall. Events satisfying the following criteria are rejected as stopping muons :

(1) $\mathrm{NHITA_{in}} \geq 10$
        $\mathrm{NHITA_{in}}$ is the number of OD hit PMTs within $8\,\mathrm{m}$ from the reconstructed
        entrance.

In the second stopping muon cut, the opening angles between the OD hit cluster and the ring estimated by two different fitters, TDC-fit and MS-fit are compared. In case of the stopping muon event, the opening angle is expected to be large, while it is small for th PC event. The cut criterion is the following :

(1) $\Theta_{\text{TDC-fit}} > 90°$ or $\Theta_{\text{MS-fit}} > 90°$

$\Theta_{\text{TDC-fit}}$ ($\Theta_{\text{MS-fit}}$) is the opening angle between the direction to the OD hit cluster and the ring direction reconstructed by TDC-fit (MS-fit).

In the third stopping muon cut, the charge inside a $42°$ cone in the ID is used. The vertex and direction are determined by stopping muon fit, which estimate the entrance as the position of the earliest hit cluster in the ID. The entrance position can not be reconstructed correctly for the PC events since the vertex of the PC events are not on the wall. Events satisfying the following criteria are rejected as stopping muons :

(1)   goodness of stopping muon fit > 0

and

(2) $\text{PE}_{\text{cone}}/\text{PE}_{\text{tot}} \geq 0.6$
        PE_{cone} is the number of p.e.s observed by ID PMTs located inside a $42°$ cone.
        PE_{tot} is the total number of p.e.s observed in the ID.

and

(3) $\text{NHITA}_{\text{in}} > 6$
        NHITA_{in} is the number of hit OD PMTs within $8\,\text{m}$ from the entrance position.

These cut criteria are common for SK-I and SK-II.

Cable hole muon cut

The veto scintillation counters are placed over the four cable holes on top of the detector. Unlike the FC event selection, simple condition that only requiring veto counter hit is inapplicable for the PC event selection. Cut criteria rejecting for cable hole muons are as follows and common for SK-I and SK-II :

(1)   One veto counter hit.

and

(2) $\vec{d}_{\text{ring}} \cdot \vec{d}_{\text{veto-vertex}} > -0.8$
        $\vec{d}_{\text{ring}}$ is the reconstructed ring direction by TDC-fit, and $\vec{d}_{\text{vertex-veto}}$ is the direction from the hit veto counter to the reconstructed vertex.
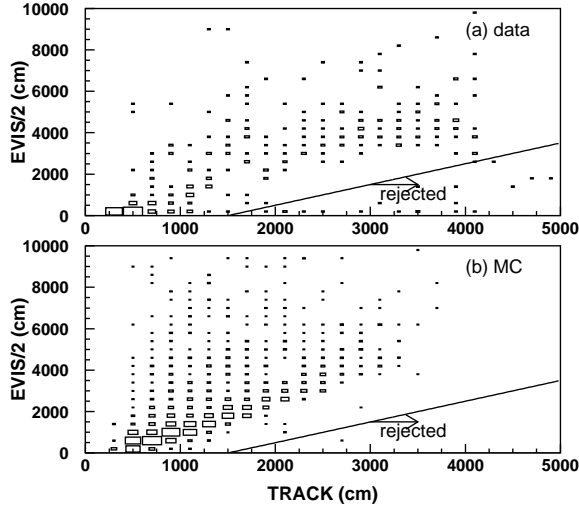
Figure C.26: Scatter plots of $E_{vis}/2$ and TRACK for (a) the data and (b) atmospheric neutrino Monte Carlo events after the PC 4th reduction for SK-II. The selection criteria are shown by arrows.

Corner clipping muon cut

The corner clipping muon events are rejected in the PC 2nd and 3rd reduction steps. In this reduction step, the remaining corner clipping muon events. The corner clipping muon events have a small hit cluter in the ID, then the vertices are occasionally mis-reconstructed inside the ID. As a result, the track length from the vertex to the exit point reconstructed by MS-fit is large, while the track length which is estimated by the visible energy using the energy loss of muons $\sim 2\,\mathrm{MeV/cm}$ is small. This cut is applied in SK-II and the cut criterion for rejecting corner clipping events is the following :

(1) $E_{vis}/2\,(\mathrm{MeV/cm}) < \mathrm{TRACK} - 1500$ if $\mathrm{TRACK} > 15\,\mathrm{m}$
$E_{vis}/2$ is the estimated track length by the visible energy and TRACK is the track length from the vertex to the exit point estimated from the vertex point and the direction by MS-fit.

Figure C.26 shows the scatter plots of $E_{vis}/2$ and TRACK.

C.2.6   PC Reduction Summary

Finally, the fully contained neutrino events are selected by applying the PC event cuts :

- Vertex of neutrino interactions should be inside the fiducial volume ($2\,\mathrm{m}$ from the ID PMT surface).

- The number of hit PMTs in the highest charge OD cluster (NHITAC) should be larger than 9 (15 for SK-II).

- Visible energy (E_{vis}) should be greater than $350\,\mathrm{MeV}$.

The detection efficiency in each reduction step is estimated by the atmospheric neutrino Monte Carlo events as shown in Table C.3. The systematic uncertainty of PC reduction is estimated to be $2.4\,\%$ and $4.8\,\%$ for SK-I and SK-II, respectively.

Reduction step	SK-I (%)	SK-II (%)
1st reduction	99.0	98.6
2nd reduction	96.7	93.4
3rd reduction	95.7	92.3
4th reduction	89.9	84.6
5th reduction	88.7	82.6

Table C.3: The detection efficiencies in the each reduction step for SK-I and SK-II for events whose true vertices are in the fiducial volume, NHITAC larger than 9 (15 for SK-II) and E_{vis} larger than 350 MeV. In the last line, the fitted vertex is used.

The remaining background for PC sample is cosmic ray muons. After all reduction process, the remaining events are scanned by physicists and the contamination of background is estimated to be 0.2 % and 0.7 % for SK-I and SK-II, respectively. The event rate of PC events for real data is shown in Figure C.30 and is 0.61±0.02 (0.53±0.03) events/day for SK-I (SK-II) as shown in Figure C.30.

C.3   Reduction for Upward-Going Muon Sample

Finally, we mention the reduction processes for UPMU events.

C.3.1   Charge cut

In the first reduction, the low energy events and extremely high energy events are rejected :

(1) PE_{tot} should be > 8000 p.e.s (3000 for SK-II)

and

(2) PE_{tot} should be < 1,750,000 p.e.s (800,000 for SK-II) PE_{tot} is the total number of p.e.s observed in the ID.

PE_{tot}=8000 p.e.s corresponds to muon momentum of 1 GeV/c and to track length of 3.5 m. The requirement for final sample is track length longer than 7 m and the criterion is safe. At very high ID charge corresponding to $\sim$ 1,750,000 p.e.s, the ID electronics is saturated and the muon fitters cannot work.

C.3.2   Zenith angle cut

In order to reject the downward-going muon cosmic ray muons, seven different fitters specialized to fit stopping muons, through-going muon events and muon events with Bremsstrahlung are used. The algorithm of the zenith angle cut is as following :

(1) Apply a muon fitter.

(2) If the event is classified as upward and the goodness of fit is above the threshold, the event is saved.

(3) If the event is classified as downward and the goodness of fit is above the threshold, the event is rejected.

(4) If the event is classified as horizontal with the goodness of fit above the threshold, or if the goodness of fit is below the threshold, the judgment is suspended.

(5) Go to (1) and apply the next muon fitter.

This sequence continues until the event has passed through all the fitters or has been classified. If no fitter gives a goodness above the threshold, the event is rejected, while if at least one fitter classifies the event as horizontal, the event is saved. Detailed description about the seven muon fitters and the definition of the goodness can be found in [162].

All events from the output of the upward-going muon reduction are passed through the precise fitter which is described in D.9. The direction reconstructed by the precise fitter is used to select upward-going events by the criterion for $\cos\Theta < 0$.

C.3.3 Scanning

In order to eliminate the background events such as horizontal-going, corner clipping or bremsstrahlung cosmic ray muons and noise events, the selected events as upward are scanned by physicists using a visual display and upward-going muon events are selected one by one. All events are checked by two independent scanners not to miss neutrino events. The possibility to miss a upward-going event is at most 1 % by a scanner. Therefore, the efficiency of scanning is estimated to be almost 100 %. About a half of the events remaining after all the automated reduction steps are rejected by this final scan. We note that the scanners only check that the reconstructed vertex and direction is not largely wrong. The reconstruction results in the previous stage are used in the final physics analysis.

C.3.4 Efficiency and Background for Upward-Going Muon Sample

The final samples of the upward going muons are required the following conditions :

- The reconstructed particle direction is upward.

- The reconstructed track length should be greater than 7 m.

The second criterion is to keep the quality of the event reconstruction. The systematic error for the track length cut is estimated to be 1.8 % and 2.1 % for SK-I and SK-II, respectively.

The reduction efficiency of the upward stopping and through-going muon events are estimated by the upward-going muon Monte Carlo events to be 102 % (101 %) for stopping muons and 96 % (94 %) for through-going muon events for SK-I (SK-II). Efficiency higher than 100 % for upward stopping muons is due to a slight bias in the separation of stopping and through-going muons, causing a small fraction of the more numerous through-going muons to be misidentified as stopping muons. The systematic uncertainty in the data reduction process for upward-going sample is estimated by comparing the distribution of each cut variable of the data with that of

the Monte Carlo events. The estimated errors are 0.3 % (0.3 %) for upward stopping muons and 1.8 % (2.1 %) for upward through-going muons for SK-I (SK-II).

The final samples of upward-going muons contain cosmic ray muon background in the most horizontal bin ($-0.1 < \cos\Theta < 0$). Some of the down-going cosmic ray muons are fitted to be upward-going because of the fitter resolution and multiple Coulomb scattering of muons in the neaby rock. Figure C.27 shows the zenith versus azimuth directions for the upward going muon sample. Clusters of cosmic ray downward muons are seen in the regions zenith angle $\cos\Theta > 0$ (downward) and azimuth angle around $\phi = 120°$, $180°$ and $270°$ because the rock of the mountain covered over the detector is thin for these directions. In order to estimate the contamination of the background events, the upward going muon samples are divided into two azimuth angle regions. Figure C.28 shows the azimuth angle distributions for upward going muon samples, in which region (2) shows the thinner mountain direction, which is defined as $60° < \phi < 310°$ for stopping muons and $60° < \phi < 240°$ for through-going muons and region (1) shows the thicker mountain direction.

Figure C.29 shows the zenith angle distributions for upward-going muon samples, in which region (1) and (2) are normalized by the coverage of the azimuth angle. While the zenith angle distributions are almost flat for upward going events ($\cos\Theta < 0$), the number of events in the region (2) exponentially increase with the cosine of zenith angle for downward-going ($\cos\Theta > 0$). The contaminations of the cosmic ray muons into the upward-going direction are estimated by an extrapolation from the upward direction in the region (2) with ($exponential + constant$) function. The numbers of background events in the range of $-0.1 < \cos\Theta < 0$ are estimated to be 40.3±13.7 for upward stopping muon and 14.4±7.2 for upward through-going muon for SK-I, respectively. For SK-II, 19.4±6.3 events for upward stopping muons and 9.0±5.2 events for through-going muons are estimated. The errors represent the statistical uncertainties of the fitting. The event rate of upward going muon events before background subtraction is shown in Figure C.30. The event rate after background subtractio is 0.25±0.01 (0.25±0.02) events/day for stopping muon events and 1.12±0.03 (1.06±0.04) events/day for through-going muon events for SK-I (SK-II).
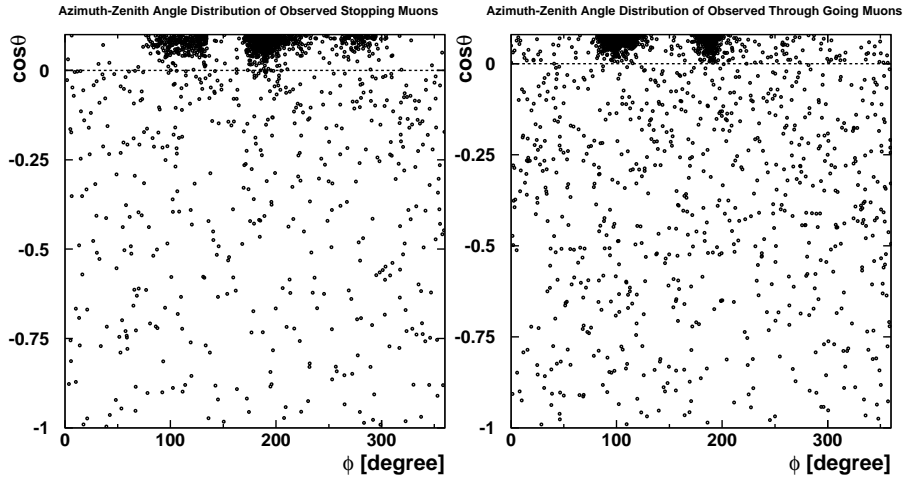
Figure C.27: Scatter plots of the zenith angle and the azimuth angle of the muon directions for stopping (left) and through-going muon data (right) for SK-I. Vertical axis shows the cosine of zenith angle and horizontal axis shows the azimuth angle of the muon direction.
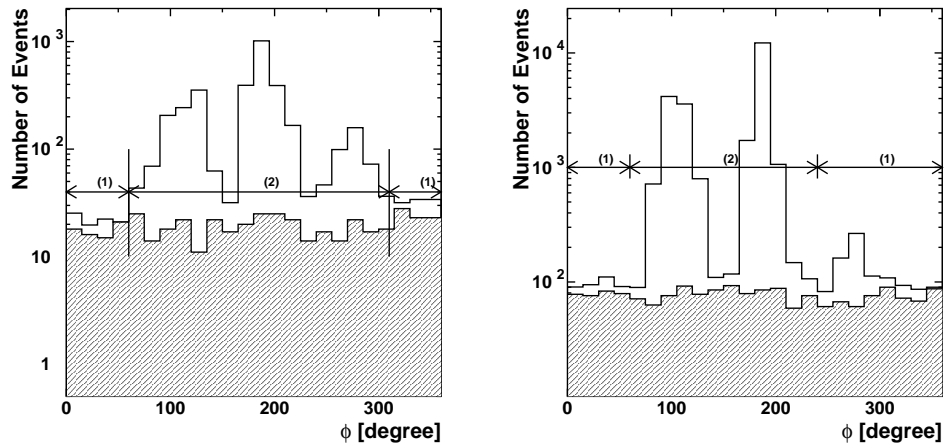
Figure C.28: Azimuth angle distributions for stopping (left) and through-going muons (right) for SK-I. Region (2) shows the thinner-mountain direction and region (1) shows the thicker-mountain direction. White histograms show the distributions of downward-going muons ($0 < \cos\Theta < 0.1$) and the hatched histograms show the upward-going muons ($\cos\Theta < 0$). Peaks due to the contamination from cosmic ray muons are seen in region (2) for downward-going muons.
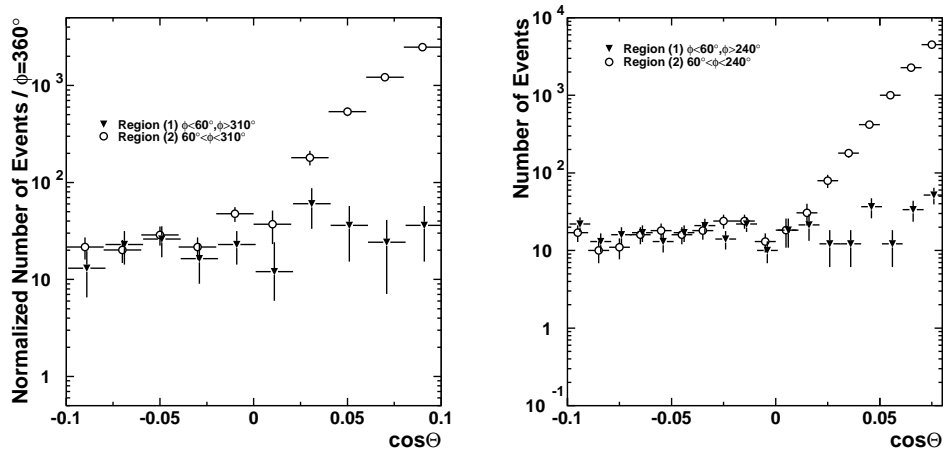
Figure C.29: Zenith angle distributions for stopping muons (left) and through-going muons (right) for SK-I. Reverse triangles show those for region (1) (thicker-mountain direction) and open circles show those for region (2) (thinner-mountain region).
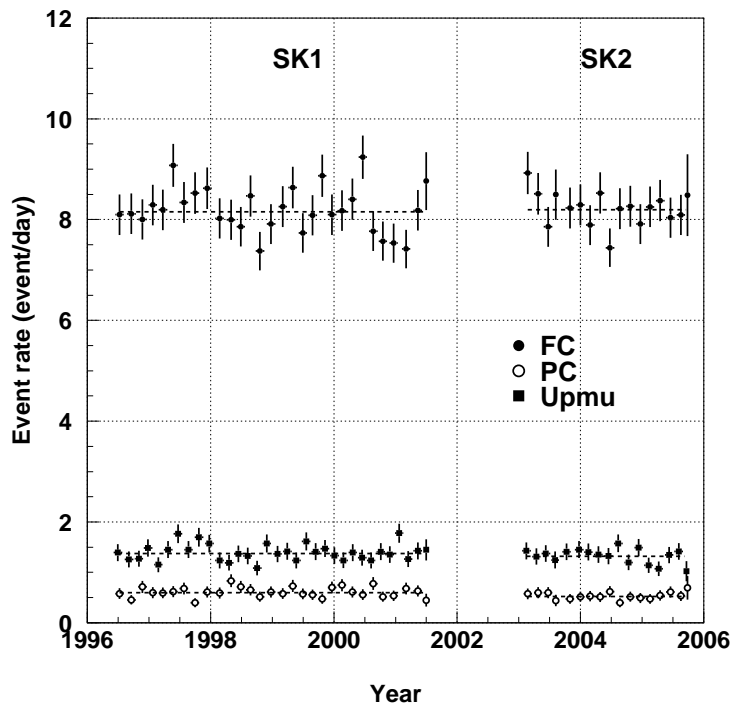

Figure C.30: The event rate for FC, PC and upward-going muon events as a function of the elapse days from 1996. The dashed line shows the averaged event rate for each sample.

Appendix D

Event Reconstruction

Event reconstruction processes are applied to the atmospheric neutrino events which pass through the data reduction processes. The common programs are applied for both the observed data and the atmospheric neutrino Monte Carlo events. The event reconstruction process is fully automated.

The reconstruction process for FC, PC, and UPMU events are described in this chapter.

D.1 Vertex Reconstruction

First, the vertex is estimated using timing information of the PMTs. The procedure has three steps.

(1) Point-fit   : roughly find the vertex using the timing information

(2) Ring edge search   : find Cherenkov ring edge

(3) TDC-fit   : fit precisely using (1) and (2) results

These steps are described below.

D.1.1 Point-Fit

The vertex fitter searches for the position where the timing residuals of the entire hit PMTs are approximately equal. The time residual of the ith PMT, t_i, is calculated by subtracting the time of flight of the photons from the hit timing of the ith PMT, t_i^0:

$$t_i = t_i^0 - \frac{n}{c} \times |\overrightarrow{P_i} - \overrightarrow{O}| \tag{D.1}$$

where n is the refractive index in water, O is the assumed vertex position, and P_i is the position of the ith PMT. To estimate the vertex, we use the estimator G_p for the goodness of the fitting:

$$G_p = \frac{1}{N} \sum_i \exp\left(-\frac{1}{2}\left(\frac{t_i - t0}{1.5 \times \sigma}\right)^2\right) \tag{D.2}$$

where N is the number of hit PMTs, σ is the typical timing resolution of a PMT (2.5 nsec), and $t0$ is the offset value of the time residual which is properly set in the fitting. The factor 1.5 in the denominator is chosen to optimize the fitter performance. G_p takes a value between 0 and 1. The fitter searches for the vertex position with which G_p takes the maximum value.
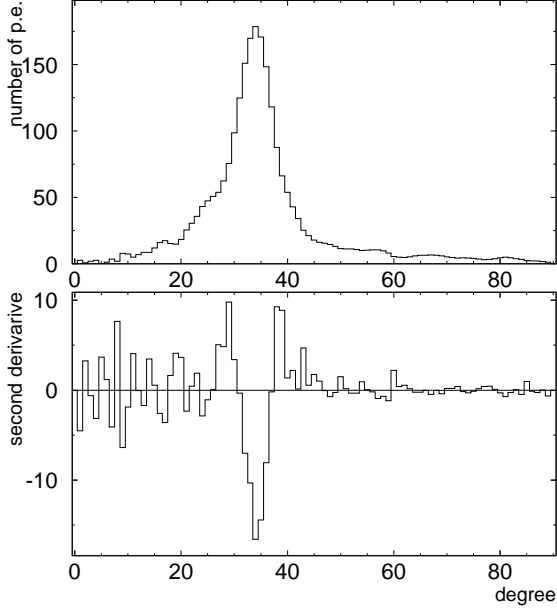
Figure D.1: Upper figure shows the typical $PE(\theta)$ distribution and lower figure shows the second derivative of $PE(\theta)$.

D.1.2 Ring Edge Finding

In this step, the edge of a Cherenkov ring is estimated. The information of the Cherenkov ring is used in the precise vertex fitter in the next step. The procedures of this step are as follows:

1. Make the angular distribution of the p.e.s, $PE(\theta)$, as a function of the opening angle θ between the assumed ring direction and the Cherenkov photon direction. The PMT acceptance and the transparency of water are taken into account in this calculation.

2. Obtain the Cherenkov opening angle θ_{edge} which satisfies the following criteria:

   - $\left. \dfrac{d^2 PE(\theta)}{d^2 \theta} \right|_{\theta_{\mathrm{edge}}} = 0$

   - $\theta_{\mathrm{edge}} > \theta_{\mathrm{peak}}$ where θ_{peak} is the angle at which $PE(\theta)$ has a peak

   If there are several θ_{edge} candidates, the θ_{edge} nearest to θ_{peak} is selected.

3. Calculate the estimator, Q, which is defined as:

$$Q = \frac{\int_0^{\theta_{\mathrm{edge}}} d\theta PE(\theta)}{\sin \theta_{\mathrm{edge}}} \times \left(\left. \frac{dPE(\theta)}{d\theta} \right|_{\theta_{\mathrm{edge}}} \right)^2 \times \exp \left(-\frac{(\theta_{\mathrm{edge}} - \theta_{\mathrm{exp}})^2}{2\sigma_\theta^2} \right) \qquad \text{(D.3)}$$

where θ_{exp} and σ_θ are the opening angle and its resolution of the Cherenkov cone expected from the p.e.s in the assumed Cherenkov ring, respectively.

Fig. D.1 shows the typical $PE(\theta)$ distribution and its second derivative. Q is maximized by changing the direction of the ring. These three steps are iterated until the maximum Q is found.
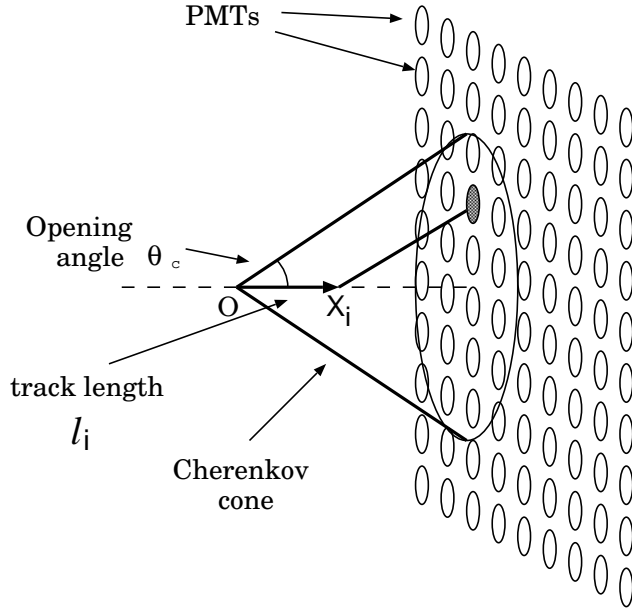
Figure D.2: Schematic view of Cherenkov radiation. The Cherenkov photons to the ith PMT were emitted at X_i. l_i is the track length of the charged particle from the vertex.

D.1.3 TDC-Fit

The final step is a precise vertex fitting using the results of the previous steps. In this procedure, the track length of the charged particle and the scattered Cherenkov photons are considered.

The time residual is calculated as:

$$t_i = \begin{cases} t_i^0 - \frac{1}{c} \times |\overrightarrow{X_i} - \overrightarrow{O}| - \frac{n}{c} \times |\overrightarrow{P_i} - \overrightarrow{X_i}| & \text{Inside the Cherenkov ring} \\ t_i^0 - \frac{n}{c} \times |\overrightarrow{P_i} - \overrightarrow{O}| & \text{Outside the Cherenkov ring} \end{cases} \tag{D.4}$$

where $\overrightarrow{P_i}$ is the position of the ith PMT, X_i is the estimated point at which the photons were emitted to the ith PMT, and n is the refractive index of water. Fig. D.2 shows the schematic view of the Cherenkov radiation.

We define the estimators, G_I and G_O, for the inside and outside of the Cherenkov ring, respectively. G_I is defined as follows:

$$G_I = \sum_i \frac{1}{\sigma_i^2} \exp\left(-\frac{1}{2} \cdot \left(\frac{t_i - t0}{1.5 \cdot \sigma}\right)^2\right) \tag{D.5}$$

where σ_i is the timing resolution of the ith PMT as a function of q_i (see Fig. **??**), σ is the timing resolution averaged over all hit PMTs, and t_i and $t0$ are the time residual of the ith PMTs and its offset, respectively.

For the PMTs outside the Cherenkov ring, the effect of the scattered light is considered. We

define the estimators, G_{O_1} and G_{O_2} according to the time residual of the PMTs:

$$G_{O_1} = \sum_i \frac{1}{\sigma_i^2} \left(\max \left[\exp\left(-\frac{1}{2} \cdot \left(\frac{t_i - t0}{1.5 \cdot \sigma}\right)^2 \right), G_{\text{scatt}}(t_i, t0) \right] \times 2 - 1 \right)$$

$$\text{(for } t_i > t0 \text{ PMTs)} \quad \text{(D.6)}$$

$$G_{O_2} = \sum_i \frac{1}{\sigma_i^2} \left(\exp\left(-\frac{1}{2} \cdot \left(\frac{t_i - t0}{1.5 \cdot \sigma}\right)^2 \right) \times 2 - 1 \right) \qquad \text{(for } t_i \leq t0 \text{ PMTs)} \quad \text{(D.7)}$$

where

$$G_{\text{scatt}}(t_i, t0) = \frac{R_q}{1.5^2} \times \exp\left(-\frac{1}{2} \cdot \left(\frac{t_i - t0}{1.5 \cdot \sigma}\right)^2 \right) + \left(1 - \frac{R_q}{1.5^2} \right) \exp\left(-\frac{t_i - t0}{60 nsec} \right) \quad \text{(D.8)}$$

$$R_q = \frac{\displaystyle\sum_{\theta < \theta_c + 3.0} q_i}{\displaystyle\sum_{\theta < 70°} q_i} \qquad : \text{Fractional p.e.s detected within Cherenkov ring} \qquad \text{(D.9)}$$

The numerical factors in Eqs.(D.5-D.9) are optimized by a Monte Carlo simulation study.

Finally, the estimator of the fitting, G_T, is defined as:

$$G_T = \frac{G_I + G_{O_1} + G_{O_2}}{\displaystyle\sum_i \frac{1}{\sigma_i^2}} \qquad \text{(D.10)}$$

The vertex position which maximizes G_T is defined to be the best fit vertex position by TDC-fit.

D.1.4   Performance of TDC-fit

Figures D.3 and D.4 show the resolution of TDC-fit estimated by atmospheric neutrino Monte Carlo events. The resolution is defined as the distance where 68% of the total events are covered. For SK-I, the resolutions are estimated to be 62 cm, 56 cm, 82 cm for FC single-ring, FC multi-ring μ-like, and PC events, respectively. As for SK-II, the resolutions are estimated to be 61 cm, 75 cm, 91 cm for FC single-ring, FC multi-ring μ-like, and PC events, respectively.

The event reconstruction process starts from the vertex fitting. The vertex position is reconstructed using the timing information of hit PMTs in three steps.

D.2   Ring Counting

Once the event vertex and the first Cherenkov ring is found, a ring counting algorithm is applied to search for any other Cherenkov rings in the event.

D.2.1   Ring Candidate Search

Cherenkov ring candidates are searched by an algorithm using a Hough transformation [163]. Figure D.5 illustrates the basic concept to find other possible rings, in which a spherical coordinate centered on the vertex position is considered. The shaded circle in this figure represents the
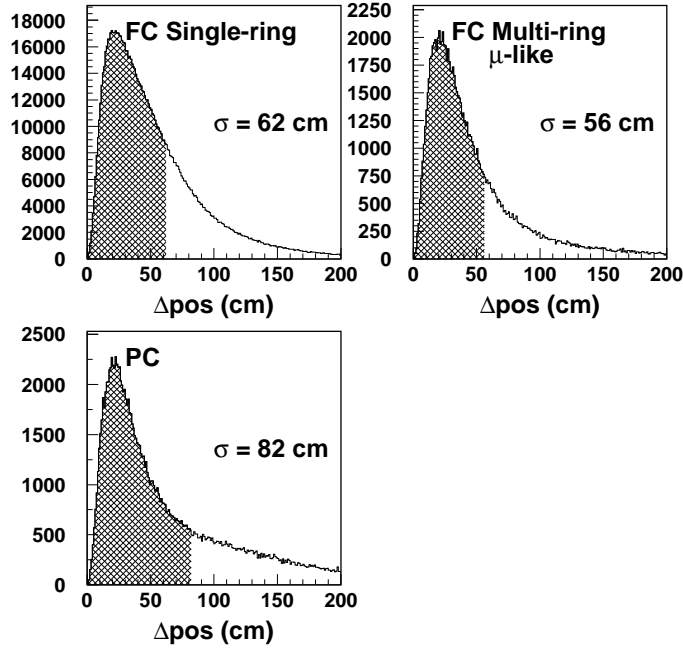
Figure D.3: The vertex resolution of TDC-fit for SK-I. (Left) FC single-ring samples (Center) FC multi-ring μ-like samples. (Right) PC samples. Resolutions are estimated from atmospheric neutrino Monte Carlo events. Hatched regions show the 68% of total events.
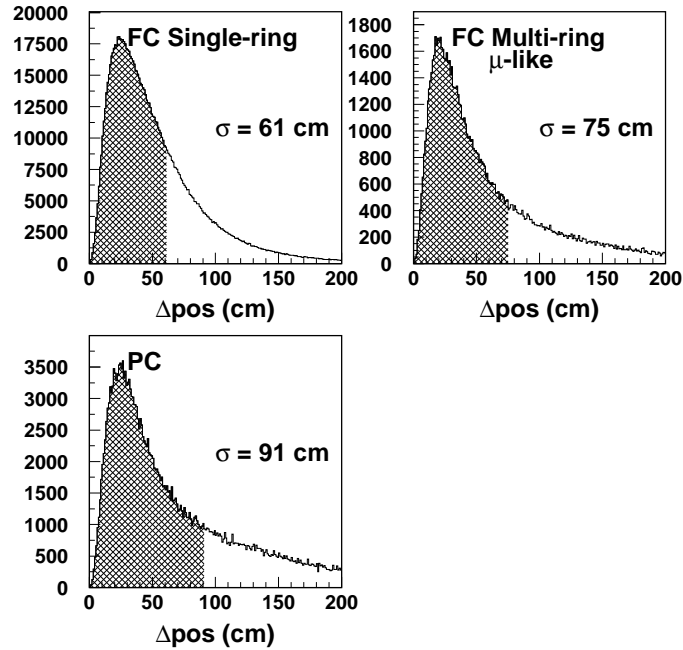
Figure D.4: The vertex resolution of TDC-fit for SK-II. (Left) FC single-ring samples. (Center) FC multi-ring μ-like samples. (Right) PC samples. Resolutions are estimated from atmospheric neutrino Monte Carlo events. Hatched regions show the 68% of total events.
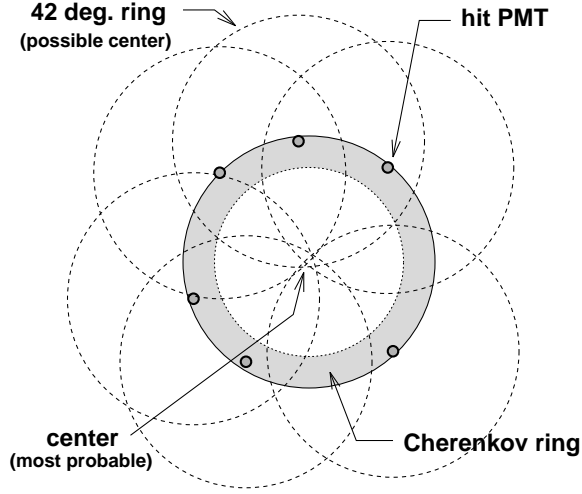
Figure D.5: A basic idea of finding ring candidates is shown. By drawing rings around the hit PMT with Cherenkov opening angle of $42\,^\circ$ from the vertex, the center of the actual Cherenkov ring can be identified.

Cherenkov ring image projected to a plane perpendicular to the ring direction. Hit PMTs are picked up and virtual circles (dashed line) centered on the position of the hit PMT are drawn with $42\,^\circ$ half angle. As a result of this procedure, the direction of a Cherenkov ring is identified as a intersection point of these circles. In practice, instead of drawing virtual circles, expected charge distribution function $f(\theta)$ with the weight of the observed charge is mapped on a (Θ, Φ) plane for each hit PMT. As a result of this Hough transformation method, ring center candidates are visible as the peaks of charge on the map. A typical charge map is shown in Figure D.6. The two peaks correspond to the directions of Cherenkov rings.

D.2.2   Ring Candidate Test

The ring candidates are tested by a likelihood method. When N rings are already found in the event, the test whether the $(N+1)$-th ring candidate is true or not by the likelihood function. The likelihood function for the assumption of $N+1$ rings is defined as :

$$L_{N+1} = \sum_i \log \left(prob \left(q_i^{\mathrm{obs}} \, , \, \sum_{n=1}^{N+1} \alpha_n \cdot q_{i,n}^{\mathrm{exp}} \right) \right) \tag{D.11}$$

where hit PMTs inside $N+1$ Cherenkov rings is summed up. q_i^{obs} is the observed p.e.s in the i-th PMT and $\alpha_n \cdot q_{i,n}^{\mathrm{exp}}$ is the expected p.e.s in the i-th PMT from the n-th ring. The L^{N+1} is maximized by changing the scale factors α_n $(n=1\ , \cdots\ , N+1)$ with a constraint of lower
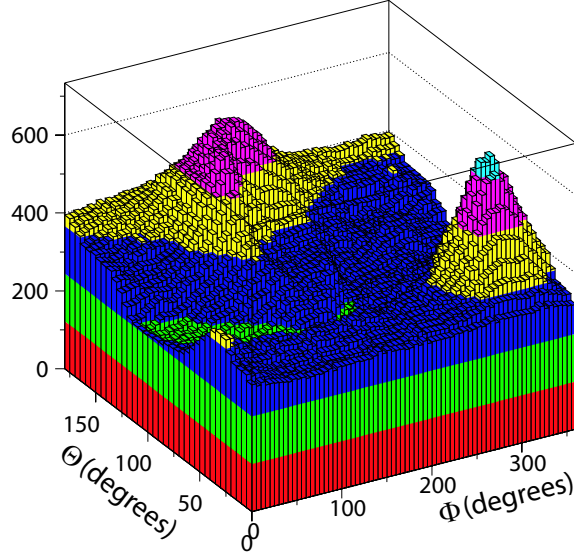
Figure D.6: A charge map from Hough transformation algorithm for a typical two ring events. The peaks are the direction of the Cherenkov rings.

momentum limit. The probability function in Equation (D.11) is defined by :

$$
prob\,(q_i^{\mathrm{obs}}\,,\,q_i^{\mathrm{exp}}) =
\begin{cases}
\dfrac{1}{\sqrt{2\pi}\,\sigma}\exp\left(-\dfrac{(q_i^{\mathrm{obs}}-q_i^{\mathrm{exp}})^2}{2\,\sigma^2}\right) & \text{(for } q_i^{\mathrm{exp}} > 20 \text{ p.e.)} \\[2ex]
\begin{array}{l}\text{Probability obtained by the probability density distribution} \\ \text{function based on the convolution of a single p.e. distribution} \\ \text{and a Poisson distribution (for } q_i^{\mathrm{exp}} < 20 \text{ p.e.)}\end{array}
\end{cases}
\tag{D.12}
$$

where σ is the resolution for q_{exp}. If no candidate satisfies $L^{N+1} \geq L^N$, the number of rings is determined to be N and the ring counting procedure is finalized. For the ring candidates satisfying $L^{N+1} \geq L^N$, following four evaluation functions are calculated :

F_1 : The difference $L(N+1) - L(N)$ corrected for the total p.e.s. When the difference is larger, the candidate is more likely to be true.

F_2 : The average of the expected p.e.s near the edge of the Cherenkov ring from the $(N+1)$-th ring, Q_{edge}. The charge from the other rings is not included in the calculation. When the Q_{edge} is larger, the candidate is more likely to be true.

F_3 : The average of the expected p.e.s outside the $(N+1)$-th ring, Q_{out}. The charge from the other rings is not included in the calculation. When the Q_{edge}-Q_{out} is larger, the candidate is more likely to be true.

213

F_4 : The residual p.e.s from the expectaion with N rings are calculated. Then the residual-charge weighted vector from all PMTs are calculated. When the absolute value of the vector sum is large, the candidate is more likely to be true.

F_5 : The difference in p.e's between the peak of a candidate ring and the average of inside and outside the ring. The larger F_5 is, the more probable the candidate is to be a true ring.

F_6 : The azimuthal symmetry of a ring with respect to the direction of the ring. A single-ring event is more symmetric than a multi-ring event. F_6 is only used to separated single and multi ring events.

The final evaluation function is determined by the probability density functions (PDFs) and log likelihood method, and written as:

$$F = \sum_i^6 log\left[(\mathcal{P}_i)\right] \tag{D.13}$$

$$= \sum_i^6 \{log\left[(\mathcal{P}_i)_{N+1}\right] - log\left[(\mathcal{P}_i)_N\right]\} \tag{D.14}$$

where $\mathcal{P}_i$ is the probability density function for i-th evaluation function, and $\mathcal{P}_{N+1}$ and $\mathcal{P}_N$ are the probability for $(N + 1)$-ring and N-ring events. Figure D.7 shows the distribution of the final evaluation function for SK-I and SK-II.

D.3 Particle Identification

Particle identification(PID) procedure estimates the particle types of the reconstructed Cherenkov rings using their patterns and the opening angles. The Cherenkov rings are categorized into 2 types: shower type which we call 'e-like', and non-shower type which we call 'μ-like'.

D.3.1 Estimation of the Particle Type

We define a likelihood function L_l for the electron assumption ($l = e$) and the muon assumption ($l = \mu$). The definition of L_l for the nth ring is:

$$L_l(n) = \prod_{\substack{i \\ \theta_{i,n} < 1.5\theta_{c,n}}} prob\left(q_i^{\mathrm{obs}}, q_{i,n}^{\mathrm{exp},l} + \sum_{n' \neq n} q_{i,n'}^{\mathrm{exp},l}\right) \tag{D.15}$$

where q_i^{obs} is the observed p.e.s for the ith PMT and $q_{i,n}^{\mathrm{exp,l}}$ is the expected p.e.s from the nth ring assuming the particle type is l ($l = e$ or μ). The function $prob(q_i^{\mathrm{obs}}, q_i^{\mathrm{exp,l}})$ is the same function as used in the Ring-Counting procedure (defined by Eq.(**??**)). The product in Eq.(D.15) is made for the PMTs whose opening angle from the nth ring direction is within 1.5 times the estimated Cherenkov opening angle of the nth ring. The calculation of the expected p.e.s are described in
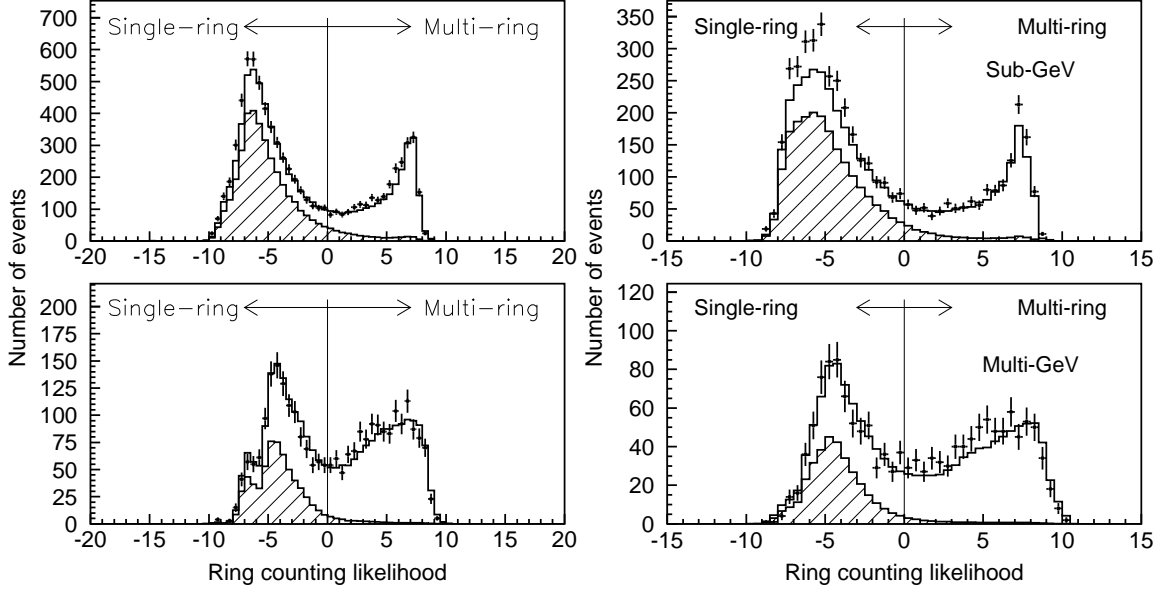
Figure D.7: The ring-counting likelihood distributions for FC Sub-GeV events (top) and Multi-GeV events (bottom) of data (dot) and the Monte Carlo events (solid line) assuming 2-flavor $\nu_\mu \leftrightarrow \nu_\tau$ oscillation assumed with $(\sin^2 2\theta, \Delta m^2) = (1.00, 2.5 \times 10^{-3}\,\mathrm{eV}^2)$ for SK-I (left two panels) and SK-II (right two panels). The hatched histograms show the CCQE interactions.

the following subsections. L_l is maximized by changing the direction and the opening angle of the nth ring while $q_{i,n'}^{\mathrm{exp},l}$ $(n' \neq n)$ are fixed.

In order to combine the information of Cherenkov ring pattern and Cherenkov opening angle, the likelihood L_l is transformed into the χ^2 function:

$$\chi_l^2(n) = -2\ln L_l(n) - \mathrm{const.} \tag{D.16}$$

The probability from the Cherenkov pattern is written as:

$$P_l^{\mathrm{pattern}}(n) = \exp\left(-\frac{1}{2}\frac{\left(\chi_l^2(n) - \chi_{min}^2\right)^2}{\sigma_{\chi^2}^2}\right) \tag{D.17}$$

where $\chi_{min}^2 = \min[\chi_e^2, \chi_\mu^2]$, σ_{χ^2} is $\sqrt{2N_D}$, and N_D is the number of PMTs which were used in the calculation of L_l.

The probability from the Cherenkov opening angle is written as:

$$P_l^{\mathrm{angle}}(n) = \exp\left(-\frac{1}{2}\frac{\left(\theta_{c,n} - \theta_n^{\mathrm{exp},l}\right)^2}{\sigma_\theta^2}\right) \tag{D.18}$$

where $\theta_{c,n}$ is the reconstructed Cherenkov opening angle of the nth ring, $\theta_n^{\mathrm{exp},l}$ is the expected opening angle for particle type l(electron or muon), σ_θ is the resolution of the estimated Cherenkov angle.

The total probability is defined as the product of $P_{\text{pattern}}(n)$ and $P_{\text{angle}}(n)$:

$$P_l^{\text{total}}(n) = P_l^{\text{pattern}}(n) \times P_l^{\text{angle}}(n) \tag{D.19}$$

where suffix l is e or μ.

If $P_e^{\text{total}}(n) > P_\mu^{\text{total}}(n)$, the nth ring is determined as e-like and vise versa. For multi-ring events, we adopt the ring pattern probability P^{pattern} only, because the performance of the reconstruction of Cherenkov angle is relatively poor than in the case of single ring events.

D.3.2   The Expected p.e. Distribution for Electrons

The expected p.e. distributions for electrons are made using a Monte Carlo simulation. In advance, we calculate the expected p.e. distribution, $Q_e^{\text{exp}}(p_e, \theta)$, which will be detected by a circular area of 50 cm diameter(same size as the 20 inch diameter PMTs) on a hypothetical spherical surface with the radius R^{sph}=16.9m(radius of the inner tank). $Q_e^{\text{exp}}(p_e, \theta)$ is given as a function of electron momentum p_e (MeV/c) and the opening angle θ from the electron direction.

The expected p.e. for the ith PMT due to the nth ring is calculated as:

$$q_{i,n}^e = \alpha_{n,e} \times Q_e(p_e, \theta_{i,n}) \times \left(\frac{R^{\text{sph}}}{r_i}\right)^{1.5} \times \exp\left(-\frac{r_i}{\lambda}\right) \times f(\Theta_i) \tag{D.20}$$

where

$q_{i,n}^e$	:	expected p.e.s for the ith PMT due to the nth ring
$\alpha_{n,e}$	:	normalization factor
$\theta_{i,n}$	:	opening angle between the nth ring direction and the
		direction from the vertex to the ith PMT
r_i	:	distance from the vertex to the ith PMT
Θ_i	:	angle of photon arriving direction relative to
		the ith PMT's facing direction
$f(\Theta_i)$	:	correction function of the PMT acceptance
λ	:	attenuation length of light in water (see Section **??**)

The factor $(R^{\text{sph}}/r_i)^{1.5}$ takes into account the r_i dependence of the intensity of the Cherenkov light. The index 1.5 was determined by a Monte Carlo study.

D.3.3   The Expected p.e. Distribution for Muons

The expected p.e. distribution for a muon is analytically calculated by the following equation:

$$q_{i,n}^\mu = \left(\alpha_{n,\mu} \times \frac{\sin^2\theta_{i,n}}{r_i\left(\sin\theta_{i,n} + r_i\frac{d\theta}{dx}|_{x=x_i}\right)} + q_i^{\text{knock}}\right) \times \exp\left(-\frac{r_i}{\lambda}\right) \times f(\Theta_i) \tag{D.21}$$
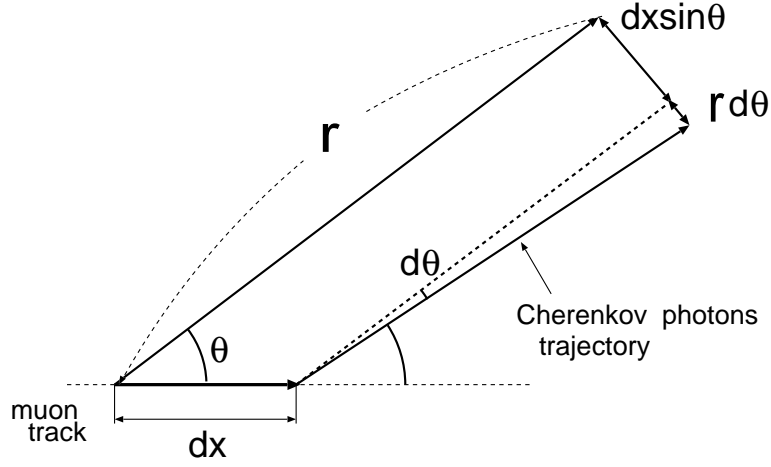
Figure D.8: Schematic view of Cherenkov radiation from a muon. Cherenkov opening angle θ changes as the muon momentum changes due to the energy loss in water. The Cherenkov photons are emitted into the region $dx \cdot \sin\theta + r \cdot d\theta$ during the muon propagation dx.

where

$$
\begin{array}{rcl}
q_{i,n}^{\mu} & : & \text{expected p.e.s for the } i\text{th PMT due to the } n\text{th ring} \\
\alpha_{n,\mu} & : & \text{normalization factor} \\
q_i^{\text{knock}} & : & \text{observed p.e.s for the } i\text{th PMT due to the knock-on electrons} \\
x & : & \text{distance from the vertex along the muon trajectory} \\
x_i & : & \text{distance from the vertex to the Cherenkov emission point} \\
& & \text{for the } i \text{ th PMT} \\
r_i, \theta_{i,n}, \lambda, \Theta_i, f(\Theta) & : & \text{same quantities as in Eq.(D.20)}
\end{array}
$$

The numerator $\sin^2\theta$ in Eq.(D.21) comes from the number of emitted Cherenkov photons to the direction $\theta_{i,n}$ (see Eq.(??)). The denominator $r_i(\sin\theta + r_i\frac{d\theta}{dx})$ comes from the area where Cherenkov photons are emitted to. Fig. D.8 shows the schematic view of the Cherenkov photon emission. The area changes due to the decreasing of the Cherenkov opening angle caused by the energy loss of the muon.

q_i^{knock} is the contribution from the knock on electrons which is estimated by a Monte Carlo simulation.

D.3.4 The Expected p.e. Distribution for Scattered Light

A PMT hit by the scattered light can be distinguished from a PMT hit by direct photons using the timing information. The 'Off timing' hit PMTs are chosen by the criteria:

$$t_{peak} - 30\text{nsec} < t_i' < t_{peak} + 2\sigma_i + 5\text{nsec} \qquad : \text{direct photons} \tag{D.22}$$

$$t_{peak} + 2\sigma_i + 5\text{nsec} < t_i' \qquad : \text{scattering photons} \tag{D.23}$$

where t_i' is the time residual for the ith PMT defined in Eq.(D.4), t_{peak} is the time at peak position of the time residual distribution, and σ_i is the measured timing resolution as a function
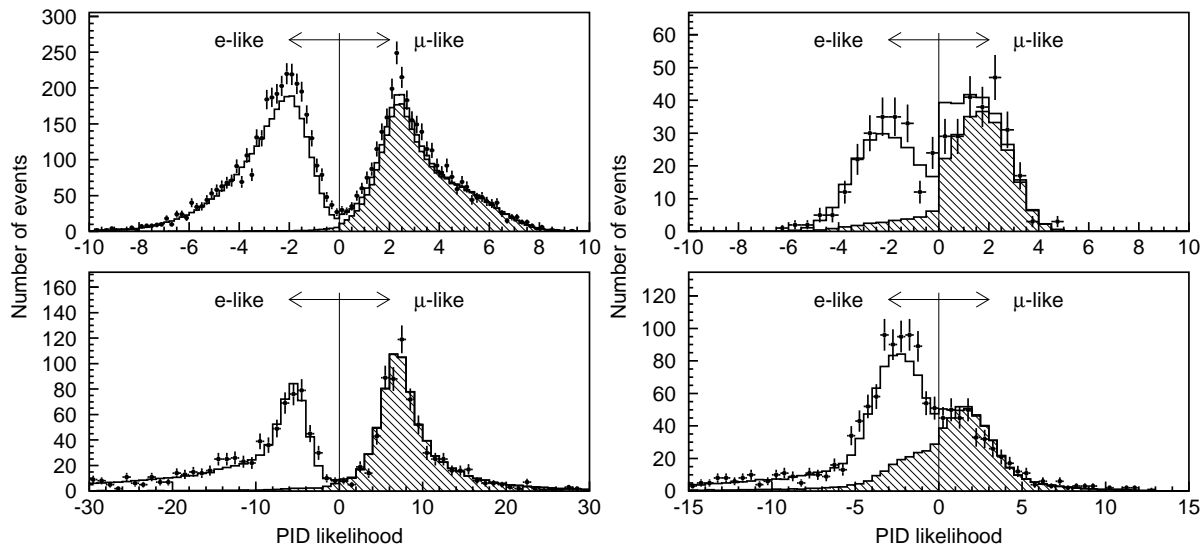
Figure D.9: The PID likelihood distributions of SK-I for Sub-GeV single-ring (left top), Multi-GeV single-ring (left bottom), Sub-GeV multi-ring (right top) and Multi-GeV multi-ring events (right bottom). Dot with cross and solid line indicate the data and Monte Carlo events respectively. In the Monte Carlo events 2-flavor $\nu_\mu \leftrightarrow \nu_\tau$ oscillation is considered with the parameter $(\sin^2 2\theta, \Delta m^2) = (1.00, 2.5 \times 10^{-3}\,\text{eV}^2)$. The hatched area indicates CC ν_μ interactions.

of observed p.e.s as shown in Fig. **??**.

The number of p.e.s due to the scattered photons, q_i^{scatt}, is estimated from the 'Off timing' PMTs and added to the expected p.e.s for the ith PMT:

$$q_i^{\text{exp},l} = q_i^l(\text{direct}) + q_i^{\text{scatt}} \tag{D.24}$$

where the suffix l represents e or μ.

D.3.5 Performance of Particle Identification

The performance of PID is estimated by a Monte Carlo study. Figures D.9 and D.10 show the PID parameter $\sqrt{-\log P_e} - \sqrt{-\log P_\mu}$ distributions for SK-I and SK-II final sample, respectively. Sub-GeV sample is defined as the events with visible energy below 1.33 GeV, and Multi-GeV sample is defined as the events with visible energy over 1.33 GeV. The peaks in e-like and μ-like events are clearly separated. Fig. D.11 shows the PID efficiency for CCQE events which are identified as single ring, and a function of the charged lepton momentum. The efficiency is very high for all energy region, and the misidentification probabilities are estimated to be 0.5% for CCQE ν_e events and 1.2% for CCQE ν_μ events.

D.4 Precise Vertex Reconstruction

For single-ring events, the vertex resolution in the longitudinal directions fitted by vertex fitting algorithm described in Section D.1 is not optimized since it only uses the timing information. This can be improved by re-fitting the vertex position using the ring pattern. The
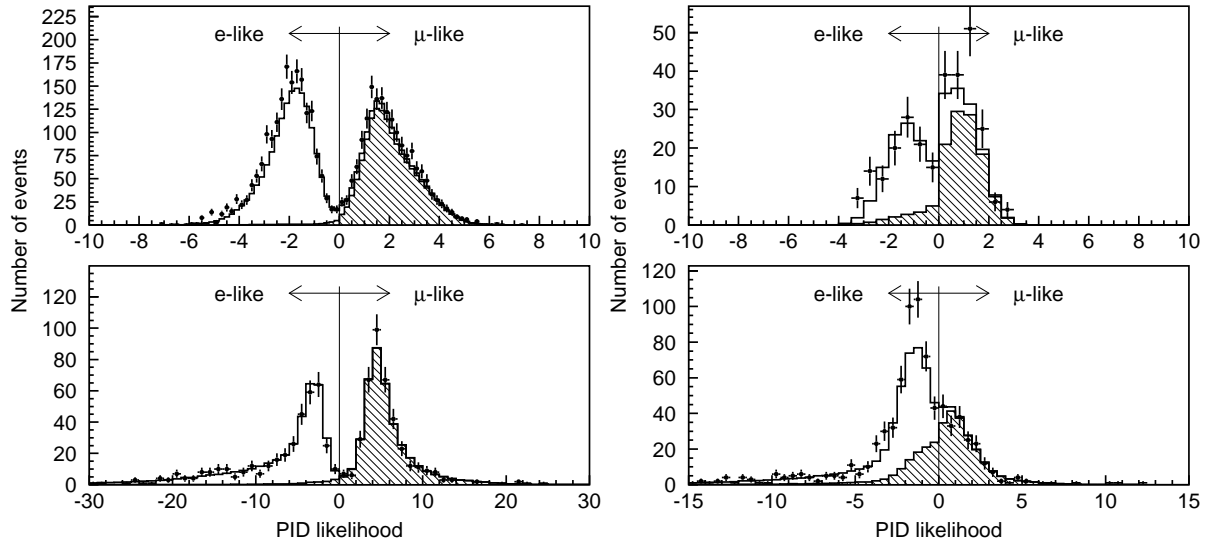
Figure D.10: The PID likelihood distributions of SK-II for Sub-GeV single-ring (left top), Multi-GeV single-ring (left bottom), Sub-GeV multi-ring (right top) and Multi-GeV multi-ring events (right bottom). Dot with cross and solid line indicate the data and Monte Carlo events respectively. In the Monte Carlo events 2-flavor $\nu_\mu \leftrightarrow \nu_\tau$ oscillation is considered with the parameter $(\sin^2 2\theta, \Delta m^2) = (1.00, 2.5 \times 10^{-3}\,\mathrm{eV}^2)$. The hatched area indicates CC ν_μ interactions.
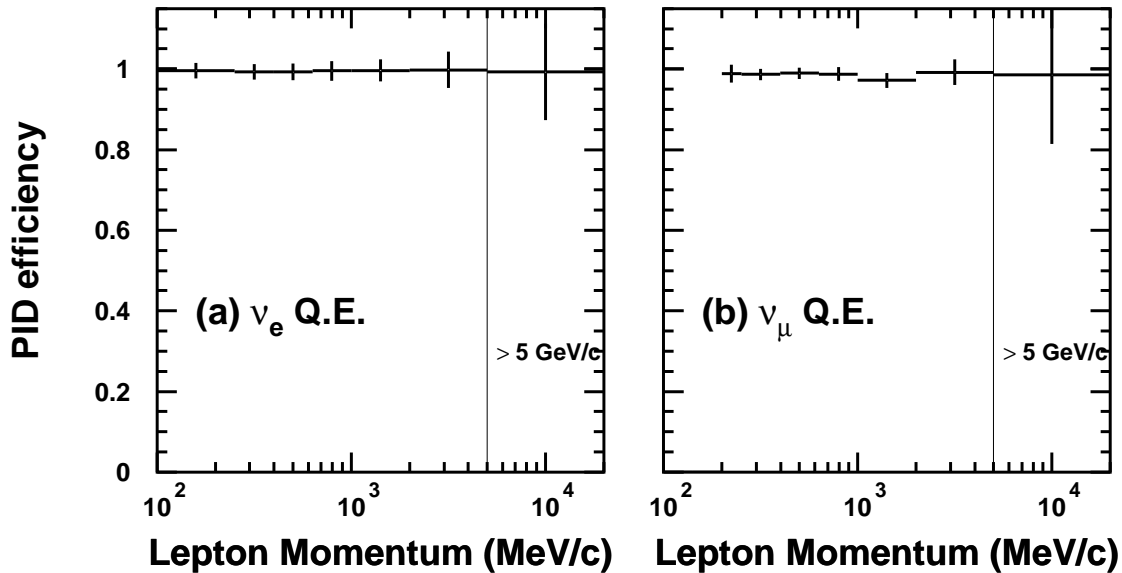

Figure D.11: The PID efficiency for CC quasi-elastic single-ring event as a function of charged lepton momentum for (a) ν_e and (b) ν_μ.

	SK-I(cm)	SK-II(cm)
FC Sub-GeV		
single-ring		
e-like	27	32
μ-like	26	31
FC Multi-GeV		
single-ring		
e-like	49	47
μ-like	24	27
multi-ring		
μ-like	56	75
PC	56	64

Table D.1: The vertex resolutions for SK-I and SK-II. The resolution is defined as the width where 68 % of the events are included. Note that the resolution for FC multi-ring samples are exactly same as the one after TDC-fit, since multi-ring events skip the precise vertex reconstruction processes.

MS-fit modifies the vertex position and the particle direction by using the PID likelihood, and the vertex position is adjusted parallel to the particle direction using the first vertex fitter with the timing information. This process is iterated until the changes in the vertex position and the particle direction is less than 5 cm and 0.5 degrees. The vertex resolution for single-ring events is approximately 30 cm.

The performance of the fitting algorithm, TDC-fit or MS-fit, is examined by applying it to the atmospheric neutrino Monte Carlo sample. Figure D.12 and D.13 show the distance between the true vertex and the reconstructed vertex for FC single-ring events, FC multi-ring μ-like events and PC events for SK-I and SK-II. The vertex resolutions are summarized in Tables D.1. The resolution is defined as the width where 68 % of the events are included.

D.5   Decay Electron Search

Improvements of the selection efficiency of μ-like event is achieved by requirng the detection of the electron produced by the muon decay (decay electron). In this section the detection method of the decay electrons followed by the primary events is described. Decay electron search consists of several criteria so as to detect three types of decay electrons :

- sub-event type
  Decay electrons observed as a separate event (sub-event) as shown in Figure D.15.

- primary-event type
  Decay electrons observed in the same event as primary event.

- split type
  Decay electrons occurred around the end of timing window, therefore the event is recorded
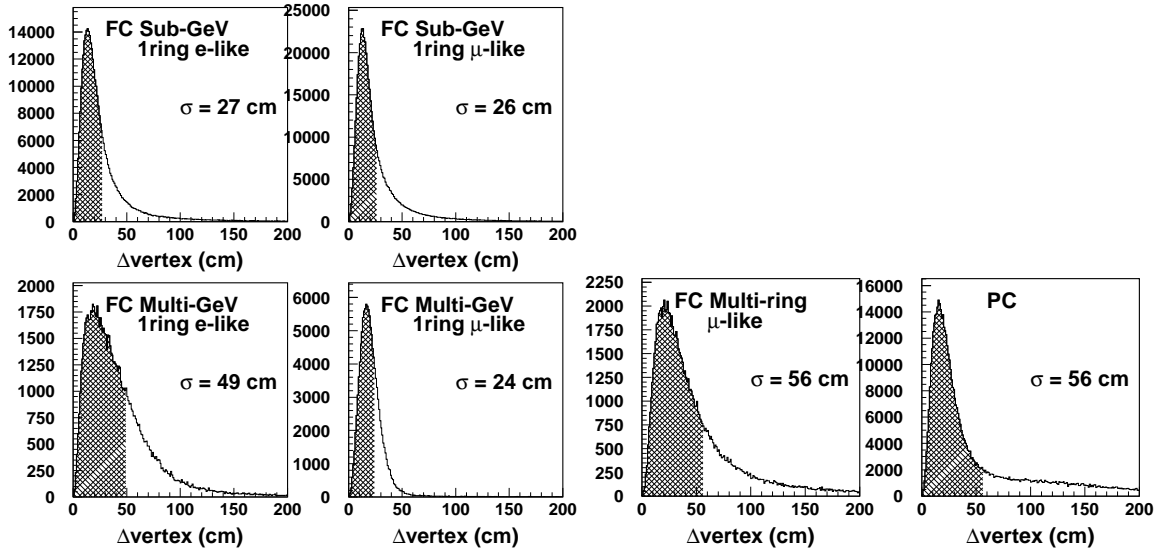
Figure D.12: Distance between the true vertex and the reconstructed vertex for FC single-ring events, FC multi-ring μ-like events and PC events in the atmospheric neutrino Monte Carlo sample for SK-I.
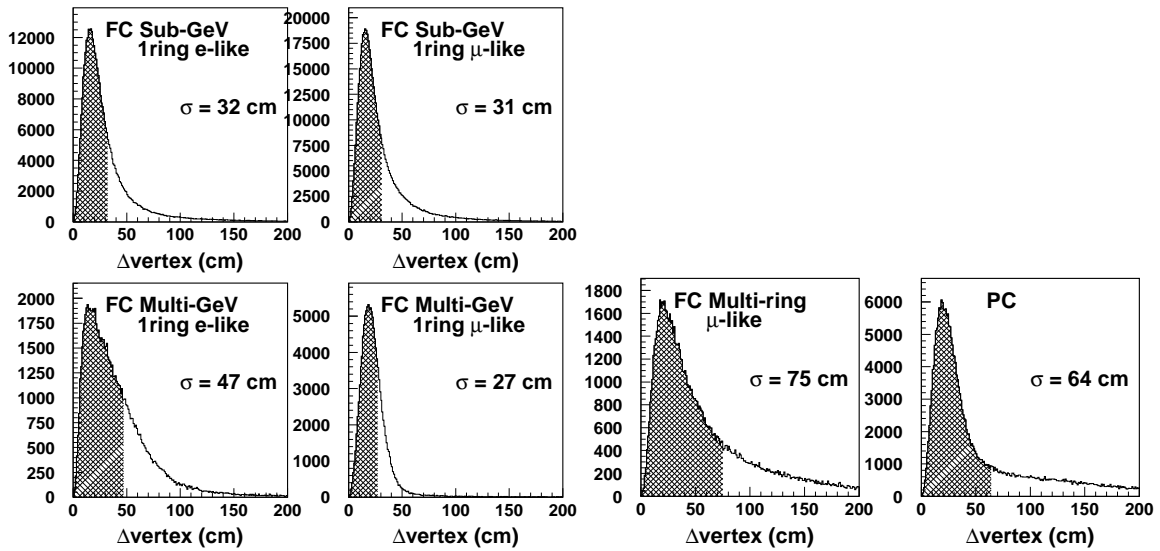

Figure D.13: Distance between the true vertex and the reconstructed vertex for FC single-ring events, FC multi-ring μ-like events and PC events in the atmospheric neutrino Monte Carlo sample for SK-II.
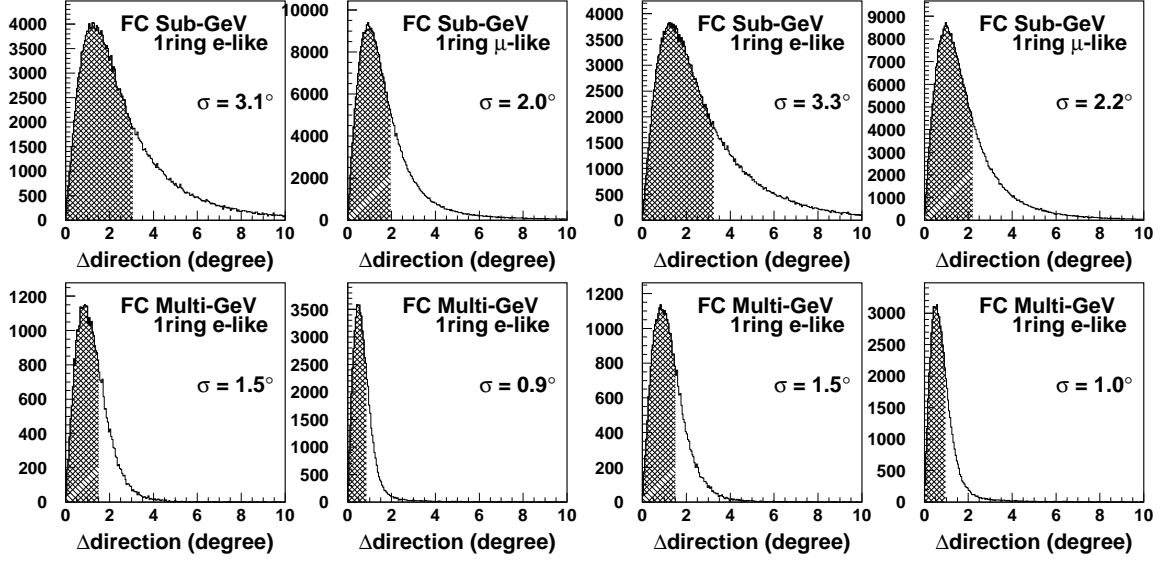
Figure D.14: Angular difference between the true electron or muon direction and the reconstructed direction for CC quasi-elastic scattering events in the atmospheric neutrino Monte Carlo events. The left four panels show for SK-I and the right four show for SK-II.

separately in the primary event and the sub-event.

For sub-event type events, the following criteria are required :

(1)   The time interval from a primary event(Δt) is $< 30\,\mu$sec.

(2)   The total number of hit PMTs is greater than 50 (25 for SK-II).

(3)   The goodness of vertex fit is greater than 0.5.

(4)   The number of hit PMTs in a 50 nsec time window is greater than 30 (15 for SK-II).

(5)   The total number of photoelectrons is less than 2000 (1000 for SK-II).

(6)   The number of hit PMTs in a 50 nsec time window (N_{50}) is greater than 60 (30 for SK-II).

For primary-event type, another peak after the primary event is searched with the additional coditions requring more than 20 hits in 30 nsec window above the background level. Additional conditions are as follows :

(7)   The number of hit PMT in a 30 nsec time window is greater than 40 (20 for SK-II). This is addopted to primary-event type and split type.

and

(8) $0.1\,\mu$sec $< \Delta$t $< 0.8\,\mu$sec or $1.2\,\mu$sec $< \Delta$t $< 30\,\mu$sec. This is addopted to all types.
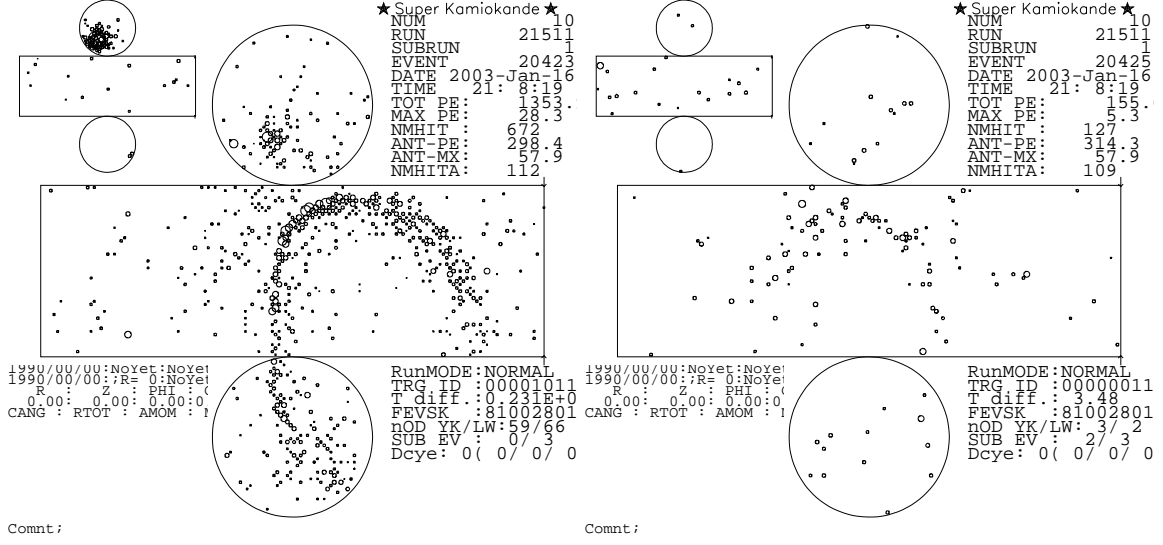
Figure D.15: An event display of a sub-event type decay electron. The left figure shows the primary event (cosmic ray stopping muon) and the right figure shows the following decay electron event. The time difference between two events is about $3.5\,\mu$sec.

N_{50}=60 (30 for SK-II) corresponds to about $11\,$MeV of electron energy. Criterion (1) rejects the gamma emission from μ^- captured on ^{16}O nuclei. Criterion (8) rejects the decays in the inefficient time interval around $1\,\mu$sec. The efficiency of detecting these electrons are $80\,\%$ and $63\,\%$ for μ^+ and μ^-, respectively.

D.6   Momentum Reconstruction

The momentum estimation is based on the relation between the number of observed Cherenkov photons inside a cone with half opening angle of $70°$ and the momentum of the particles. In order to determine the momentum for individual rings, the observed p.e.s in hit PMTs are separated to the contribution from each ring. The separation of the observed p.e.s is carried out based on the expected p.e. distribution from each ring as a function of the opening angle θ and uniform in azimuthal angle ϕ. The observed p.e.s in the i-th PMT from the n-th ring are estimated as :

$$q_{i,n}^{\mathrm{obs}} = q_i^{\mathrm{obs}} \times \frac{q_{i,n}^{\mathrm{exp}}}{\sum_{n'} q_{i,n'}^{\mathrm{exp}}} \tag{D.25}$$

where $q_{i,n}^{\mathrm{obs}}$ is the fractional p.e.s from the n-th ring in the i-th PMT, q_i^{obs} is the observed p.e.s in the i-th PMT and $q_{i,n}^{\mathrm{exp}}$ is the expected p.e.s .

To calculate the total number of p.e.s inside the $70°$ cone, the number of p.e.s in each PMT is corrected for the light attenuation in water and the acceptance of the PMT as follows :

$$RTOT_n = \frac{G_{\mathrm{MC}}}{G_{\mathrm{data}}} \left[\alpha \times \sum_{\substack{\theta_{i,n}<70° \\ -50\mathrm{nsec}<t_i<250\mathrm{nsec}}} \left(q_{i,n}^{\mathrm{obs}} \times \exp\left(\frac{r_i}{L}\right) \times \frac{\cos\Theta_i}{f(\Theta_i)} \right) - \sum_{\theta_{i,n}<70°} S_i \right] \tag{D.26}$$

where

α	:	normalization factor
$G_{\text{data}}, G_{\text{MC}}$	:	relative PMT gain parameter for the data and the Monte Carlo simulation
$\theta_{i,n}$	:	opening angle between the n-th ring direction and the i-th PMT direction
Θ_i	:	angle of photon arriving direction relative to the ith PMT facing direction
t_i	:	TOF subtracted hit timing of the i-th PMT position
L	:	light attenuation length in water
r_i	:	distance from the vertex position to the i-th PMT
$f(\Theta)$	:	correction function for the PMT acceptance
S_i	:	expected p.e.s for the i-th PMT from scattered photons

The summation is restricted inside the time window from -50 nsec to +250 nsec around the peak of the TOF subtracted hit timing distribution to reject the effect from muon decay electrons. For the attenuation length in water L, the continuous measurement using cosmic ray through-going muons (Section 4.4.2) is used to correct the time variation for the observed data. Fig. **??** shows the estimated momentum resolution for electrons and muons. The momentum resolution is approximately described as:

$$\sigma_p = \begin{cases} 0.6 + \frac{2.6}{\sqrt{p(\text{GeV}/c)}}\,\% & \text{for electron} \\ 1.7 + \frac{0.7}{\sqrt{p(\text{GeV}/c)}}\,\% & \text{for muon} \end{cases} \tag{D.27}$$

The resolution is defined as 1 σ width of the Gaussian fit.

D.7 Ring Number Correction

After the momentum reconstruction, the residual of a reconstruction is corrected by erasing the mis-reconstructed rings with number of rings >2 among all of ring candidates. Ring number correction process, suppose it aims to erase i-th ring, requires the criteria below :

(1-1) $p_i < p_j; i \neq j$
,where p_i is the momentum of i-th ring.

(1-2) $\theta_{ij} < 30°$
,where θ_{ij} is opening angle between the i-th and j-th rings.

(1-3) $p_i \cos\theta_{ij} < 60\,\text{MeV/c}$
,where $p_i \cos\theta_{ij}$ is the momentum of i-th ring projected perpendicularly to j-th ring.
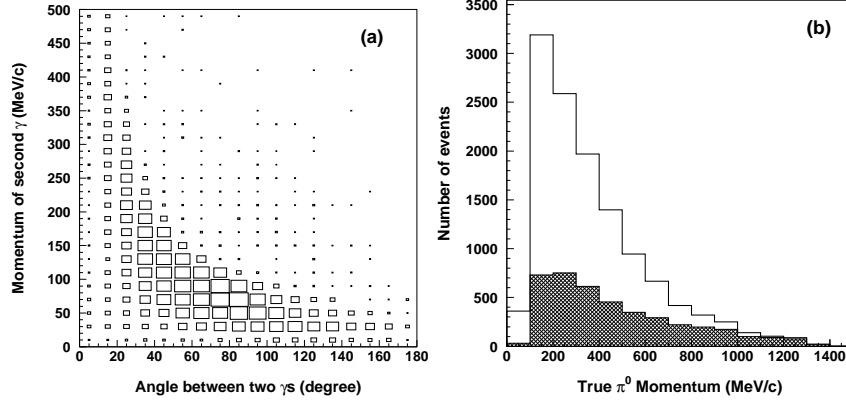
Figure D.16: (a) The scatter plot between the true momentum of the second gamma and the true opening angle between two gammas for NC1π^0 events in the atmospheric Monte Carlo events. (b) The distribution of the true π^0 momentum for NC1π^0 events in the atmospheric Monte Carlo events. The hatched region shows the NC1π^0 identified as single-ring e-like events.

or

(2-1) $p_i < 40\,\mathrm{MeV/c}$

(2-2) $p_i/p_{\mathrm{tot}} < 0.05$
    ,where p_{tot} is the total momentum for all rings.

D.8 π^0 Reconstruction

A π^0 immedeately decays into two γ's and can be identified as a π^0 event by the reconstruction algorism described in Section 4.5.2. However some events are classified as single-ring e-like event when one γ is missed by the standard reconstruction algorism. Mis-identification of γ ray from π^0 decay can be occurred by following reasons :

1. The energies of two γ's are highly asymmetric and the energy of the second γ ($\mathrm{E}_{\gamma 2}$) is too small to be reconstructed as a ring.

2. The two rings of γ's are overlapped and reconstructed as one ring when the opening angle between two γ's is small.

Relation of the opening angle between two γ's and the momentum of the second γ is shown in Figure D.16, where plotted events are the expected NC single π^0 events. Figure D.16(b) shows the momentum distribution of the expected NC single π^0 events. The hatched region indicates the mis-identified events as single-ring e-like which amounts to 33% of the total events.

The π^0 fitter reconstructs the second gamma-ray by comparing the observed charge distribution on PMTs with the expected charge distribution of two gamma-rays, where existence of two Cherenkov rings is assumed. The two gamma-rays are supposed to be emitted at one vertex and the direction of the more energetic gamma-ray is fixed on the direction derived from the precise vertex reconstruction. The best-fitted combination of two gamma-rays is determined by

225

varying the direction of the second gamma-ray and the fraction of energy shared among the two gamma-rays.

The expected charge distribution for the i-th PMT is calculated as follows :

$$q_i^{\mathrm{exp}} = \alpha_e \times Q^{\mathrm{exp}}(\theta_i, p_\gamma, r_i) \times \left(1 - \frac{r_i}{\sqrt{r_i^2 + R_{PMT}^2}} \right) \times \frac{1}{\exp(r_i/L)} \times f(\Theta_i) + q_i^{\mathrm{scatt}} \qquad (\mathrm{D.28})$$

where

α_e	:	normalization factor
Q^{exp}	:	expected photon distribution from a gamma-ray as a function of θ_i, p_γ and r_i
θ_i	:	opening angle between the i-th PMT direction and the ring direction
p_γ	:	initial gamma-ray momentum
r_i	:	distance from the vertex to the i-th PMT
R_{PMT}	:	radius of PMT$\sim$25 cm
L	:	light attenuation length in water
$f(\Theta_i)$	:	correction for the PMT acceptance as a function of the photon incidence angle Θ_i
q_i^{scatt}	:	expected p.e.s for the i-th PMT from scattered photons

The factors of $\left(1 - r_i / \sqrt{r_i^2 + R_{PMT}^2} \right)$ and $\exp(\text{-}r_i/L)$ are introduced to correct the solid angle and light attenuation, respectively. Q^{exp} is the expected photon distribution as a function of the photon incident angle Θ_i, the initial gamma-ray momentum p_γ and the distance from the vertex to the i-th PMT r_i.

A log likelihood method is adopted to determine the best-fitted configuration of two gamma-rays. The likelihood is defined as :

$$L = \sum_{i=1} log \left(prob \left(q_i^{\mathrm{obs}}, q_i^{\mathrm{exp}} \right) \right) \qquad (\mathrm{D.29})$$

The q_i^{exp} is optimized to derive the minimum likelihood value by changing the direction of the second gamma and the momentum fraction for the second gamma. The reconstruction process is iterated once again after the first process with finer stepping size to improve the fitting performance for such events as two rings are almost overlapped. These events give a narrow L distribution in the direction of the first ring and smallest L between the first wide fit and the second narrow fit is chosen as a fitting result.

Figure D.17 shows the reconstructed invariant mass (M_{inv}) distribution from two gamma rays of NC single π^0 events. M_{inv} is defined as :

$$M_{inv} = \sqrt{2E_{\gamma 1} E_{\gamma 2}(1 - \cos \theta_{\gamma\gamma})}. \qquad (\mathrm{D.30})$$

The mean value of the reconstructed invariant mass is $135.9 \, \mathrm{MeV}/c^2$ and $133.7 \, \mathrm{MeV}/c^2$ and the resolution of the invariant mass is $23.6 \, \mathrm{MeV}/c^2$ and $20.8 \, \mathrm{MeV}/c^2$ for SK-I and SK-II, respectively.
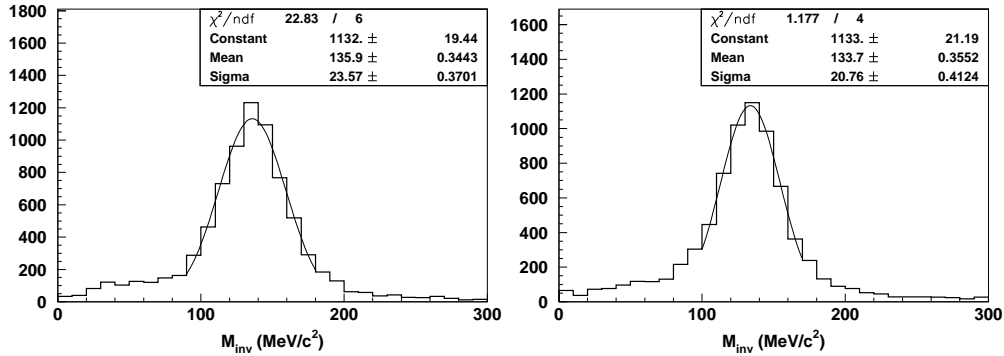
Figure D.17: The invariant mass distributions for NC1π^0 events with the line of the Gaussian fit for SK-I (left) and SK-II (right).

D.9 Event Reconstruction for Upward-Going Muon Sample

Among the upward through-going muon events, some of them are accompanied with an electromagnetic shower. The typical energy of these muons are higher than that for non-showering upward through-going muons. Figure D.18 shows the primary neutrino energy distributions for these events.

Therefore, the upward through going muons are separated to non-showering and showering events. Details of the criteria to separate them can be found in [164]. The event reconstruction algorithm for upward-going muons is different from that for FC and PC events. The same program is used for both observed data and atmospheric neutrino Monte Carlo events which pass through the data reduction process. The reconstruction is based on MS-fit (see Section D.4) with the assumption that the particle is a muon and the vertex is at the inner detector surface. However, when the muon produces an electromagnetic shower, almost all the ID PMTs are hit or the Cherenkov ring cannot observed. For these events, the information of OD hit is used to determine the particle direction. The angular resolution is 2.0° (2.3°) for stopping muon events for SK-I (SK-II), 1.3° (1.6°) for non-showering muon events for SK-I (SK-II) and 1.5° (2.7°) for showering muon events for SK-I (SK-II) as shown in Figure D.19.
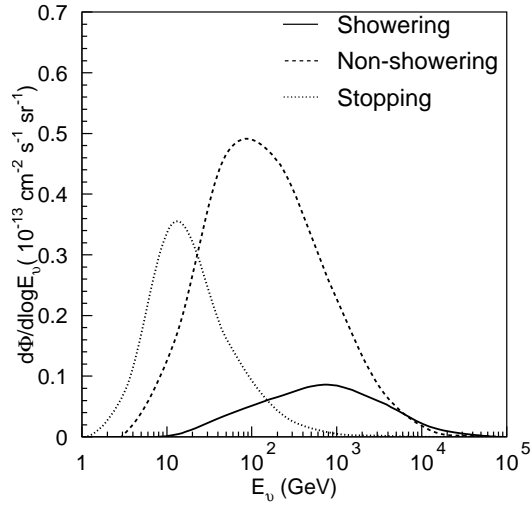
Figure D.18: The energy spectrum of primary neutrino for upward stopping (dotted line), non-showeing (dashed line) and showering (solid line) muon events.
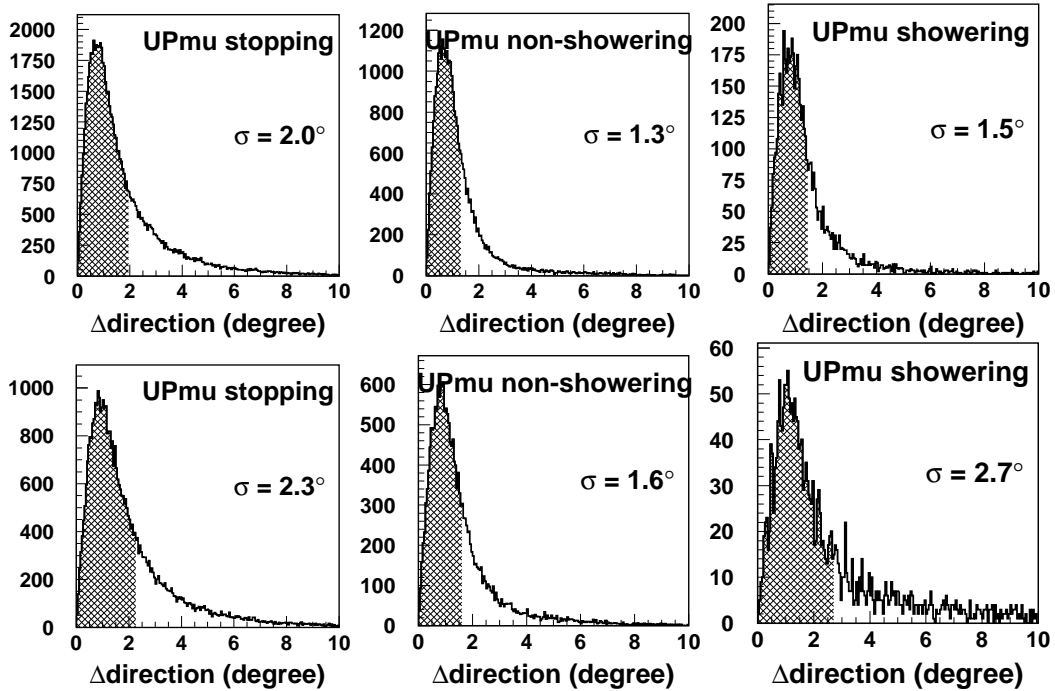

Figure D.19: Angular difference between the true direction and the reconstructed direction for upmu stopping event, upmu non-showering events and upmu showering events in the atmospheric neutrino Monte Carlo sample. The upper three panels are for SK-I and the bottom three are for SK-II.